

N6 9-40131
NASA CR-106331

**CASE FILE
COPY**

**APPLICATIONS OF RADIOISOTOPES AND
SUBLIMING MATERIALS FOR ATTITUDE
CONTROL OF SMALL SOLAR PROBES**

by

**Philip T. Choong
Edward A. Mason**

T 69-2

May, 1969

**CENTER FOR SPACE RESEARCH
MASSACHUSETTS INSTITUTE OF TECHNOLOGY**



**APPLICATIONS OF RADIOISOTOPES AND
SUBLIMING MATERIALS FOR ATTITUDE
CONTROL OF SMALL SOLAR PROBES**

by

**Philip T. Choong
Edward A. Mason**

T 69-2

May, 1969

for

**National Aeronautics and Space Administration
Contract No. NGL 22-009-019**

APPLICATIONS OF RADIOISOTOPES AND SUBLIMING MATERIALS
FOR ATTITUDE CONTROL OF SMALL SOLAR PROBES

by

Philip Tsi-Shien Choong

Submitted to the Department of Nuclear Engineering on
May 15, 1969 in partial fulfillment of the requirements for
the degree of Doctor of Philosophy.

ABSTRACT

A numerical procedure for calculating the molecular flow parameters from direct physical approach has been developed. The procedure has the merits of being accurate and flexible in comparison with the integral equation approach, yet it has the simplicity of Monte Carlo method. In particular, the effects of subliming surface reflection, channel wall reflection and molecular collision in cylindrical channels are taken into account in the non-obstruction factor calculations. The same procedure is extended to compute the mass and thrust non-obstruction factors for conic channels. The resultant molecular non-obstruction factors and the evaporation coefficients are employed in the transient thermal analyses of an erecting shell and a subliming microthruster proposed for orientation and despinning of a small solar probe. Transient numerical solutions of zero to two dimension heat conduction equations for both the non-linear and moving boundary conditions are involved in the analyses. The geometry of a microthruster utilizing the subliming material and radioisotopes is optimized by the above numerical procedure. Alpha-emitting radioisotopes, in addition to supplying the heat and thrust for a microthruster, are found to improve the performance of an erecting shell designed to damp out undesired precessional motions by significantly increasing the optimum spin rate. Finally, the applications of the erecting shell and the subliming microthruster to the attitude control of the MIT's Sunblazer appear very attractive in several aspects. Their future roles in the attitude control of small solar probes are discussed in some detail.

Thesis Supervisor: Edward A. Mason
Professor of
Nuclear Engineering

ACKNOWLEDGEMENT

It is a great pleasure to thank Professor Kent Hansen for many fruitful discussions on various numerical problems. The generous suggestions on related topics from Professor J. V. Harrington, Messrs R. Baker, C. Peterson and Miss S. L. Hsia are sincerely acknowledged.

This work was financially supported by the NASA grant (NGL 22-009-019) administered by the Center for Space Research at M.I.T. All numerical computations were carried out at the M.I.T. Information Processing Center.

TABLE OF CONTENTS

Title	1
Abstract	2
Acknowledgement	3
Table of Contents	4
List of Figures	9
List of Tables	13
1 Summary	14
1.1 Introduction	14
1.2 Thermal Analysis of Erecting Shell	15
1.3 Studies on Subliming Microthruster	18
1.4 Molecular Flow Parameters	20
1.5 Applications to Sunblazer	22
1.6 Conclusions	23
2 Introduction	41
2.1 Introductory Remarks	41
2.2 Probe Orbit Considerations	42
2.3 Spacecraft Dynamics Considerations	44
2.3.1 General	44
2.3.2 Restoring vane	45
2.3.3 Erecting shell	46
2.3.4 Despin microthruster	48
2.4 Rarefied Gas Dynamics Considerations	49
2.4.1 Evaporation coefficient	49
2.4.2 Molecular flow	50
3 Sublimation and Rarefied Gas Flow Parameters	55

3.1	Introduction	55
3.2	Molecular Non-obstruction Factor (Modified Clausing Factor)	56
3.2.1	Introduction	56
3.2.2	Vapor-wall collision effects	56
3.2.3	Description of numerical approach (TUBNOF)	59
3.2.4	Calculations of wall adsorption effect	61
3.2.5	Calculations of channel-wall reflection effect	62
3.2.6	Calculations of subliming surface reflection effect	63
3.2.7	Calculations of molecular collision effect	65
3.3	Evaporation Coefficient Theory	69
3.3.1	Introduction	69
3.3.2	Evaporation dependence on reflection	70
3.3.3	Ratio of recoil pressure to vapor pressure	72
3.4	Evaporation Coefficient Calculation Techniques	74
3.4.1	Introduction	74
3.4.2	Extraction from mass-flow data	74
3.4.3	Extraction from recoil-pressure data	76
4	Transient Thermal Analysis of Erecting Shell	86
4.1	Introduction	86
4.2	Strip Approximation Method	87
4.2.1	Description of strip model	87
4.2.2	Bare thin shell system	88
4.2.3	Optimum spin rate	90
4.2.4	Radioisotope-heated thin shell system	91
4.3	Thin Shell Approximation Method	92

4.3.1 Description of Thin Shell model	92
4.3.2 Semi-implicit numerical solution	93
4.3.3 Subliming material coated shell system	94
4.3.4 Approximate analytical solution	95
4.4 Thin Shell Approximation Method	99
4.5 Comparison of Results	101
5 Performance Analysis of Microthruster	121
5.1 Microthruster Design Considerations	121
5.2 Radioisotope Applications	122
5.2.1 Radioisotope properties	122
5.2.2 Radioisotope-doping for fast despin	124
5.2.3 Radioisotopic decay for long term spin-control	124
5.2.4 Radioisotopic heating of nozzle wall	127
5.3 Cylindrical-cup Microthruster	128
5.3.1 Description of governing equation	128
5.3.2 Explicit solution of temperature distribution	129
5.3.3 Implicit solution of temperature distribution	130
5.3.4 Comparison of results	131
5.3.5 Thrust non-obstruction factor	132
5.4 Chopped-cone Microthruster	133
5.4.1 Introduction	133
5.4.2 Optimum cone angle calculation	134
5.4.3 ADI solution of temperature distribution	136
5.4.4 Performance parameters	138
6 Applications to Sunblazer-type Solar Probe	159
6.1 Spacecraft Dynamics	159
6.1.1 Passive attitude control system	159

6.1.2 Euler's dynamical equations	161
6.1.3 Effect of various moments on precession	162
6.1.4 Despin rate	164
6.1.5 Erecting rate	165
6.2 Possible Applications	167
6.2.1 Introduction	167
6.2.2 Passive systems for inferior orbit probes	167
6.2.3 Semi-passive system for inferior orbit probes	168
6.2.4 Active system for superior orbit probes	170
7 Conclusions and Recommendations	181
7.1 Conclusions	181
7.2 Recommendations for Further Studies	183
Appendix	
A Approximate analytic solution of t - θ parabolic partial differential equation	185
B Approximate analytic solution of optimum rate	188
C Graphical explanations for the numerical solution of NSHELL	192
D Recoil pressure of photons, nuclear decay and sublimed particles	194
E Derivation of the relations between recoil pressure and reflection	196
F Geometrical relations for specular particle reflection in space	198
F.1 Cylindrical wall	198
F.2 Chopped cone wall	198
G Derivation of particle flux due to sublimation	199
H Descriptions of computer programs for thermal analysis of the erecting shell	200
H.1 Strip approximation (STRIP)	200

H.2	Thin shell approximation (NSHELL)	200
H.3	Thick shell approximation (KSHELL)	201
H.4	Optimum spin rate (OPTSPN)	201
I	Space curve traced by conic-particle beams on cylindrical tube wall	203
I.1	Inlet sublimation	203
I.2	Channel wall reemission	203
J	Descriptions of computer programs for thermal analysis of microthruster	205
J.1	Cylindrical tube-explicit method (EXTUBE)	205
J.2	Cylindrical tube-implicit method (IMTUBE)	205
J.3	Chopped cone-ADI method (CONADI)	206
K	Descriptions of computer programs for rarefied gas non-obstruction factor	210
K.1	Cylindrical tube non-obstruction factor (TUBNOF)	210
K.2	Chopped cone non-obstruction factor (CONNOF)	210
L	Sublimation pressure	212
M	Nomenclature	213
N	Literature citations	216

LIST OF FIGURES

FIGURE	PAGE
1.1 Steady State Temperature Distribution Around A Bare Shell	25
1.2 Transient Maximum Temperature Of Bare Shell	26
1.3 Transient Minimum Temperature Of Bare Shell	27
1.4 Transient Phase Lag Of Bare Shell	28
1.5 Transient Normal Force Component For Bare Shell	29
1.6 Transient Parallel Force Component For Bare Shell	30
1.7 Schematics Of Microthruster	31
1.8 Optimization Of Cone Angles	32
1.9 Extrapolation Of Throat Area	33
1.10 Heated Channel Effect On Thrust Non-obstruction Factor	34
1.11 Subliming Surface Reflection Effect	35
1.12 Molecular Collision Effect On Non-obstruction Factor	36
1.13 Non-obstruction Factors Versus L/R For 45° Cone	37
1.14 Extraction Of Evaporation Coefficient From Mass Flow Data	38
2.1 Relative Motion Of Solar Probe	52
2.2 Diagram Of Torques On Spacecraft	53
2.3 Reradiative Torques On Erecting Shell	54
3.1 Schematic Of Molecular Flow Channel	77
3.2 Discretization Of Spherical Cosine Distribution	77
3.3 Reflection Coefficient Effect On Non-obstruction Factor	78
3.4 Comparison With Smoluchowski's Result On Specular Reflection Effect	79

3.5	Subliming Surface Reflection Effect	80
3.6	Curve For Interpolation Of Evaporation Coefficient	81
3.7	Molecular Collision Effect On Non-obstruction Factor	82
3.8	Subliming Temperature Effect On Molecular Collision	83
3.9	Extraction Of Evaporation Coefficient From Mass Flow Data	84
4.1	Schematic Of Erecting Shell	1 03
4.2	Transient Maximum Temperature Of Bare Shell	104
4.3	Transient Minimum Temperature Of Bare Shell	105
4.4	Transient Maximum Temperature Difference Of Bare Shell	106
4.5	Transient Phase Lag Of Bare Shell	107
4.6	Transient Normal Force Component For Bare Shell	108
4.7	Transient Parallel Force Component For Bare Shell	109
4.8	Optimum Spin And Maximum Normal Torque For A Heated Shell	110
4.9	Transient Maximum Temperature Of Coated Shell	111
4.10	Transient Minimum Temperature Of Coated Shell	112
4.11	Transient Phase Lag Of Coated Shell	113
4.12	Transient Parallel Force Component For Coated Shell	114
4.13a	Normal Force Component For Fast Spin ($\omega \gg \omega_{opt}$)	115
4.13b	Parallel Force Component For Fast Spin ($\omega \gg \omega_{opt}$)	116
4.14	Steady State Temperature Distribution Around A Bare Shell	117
4.15	Optimum Spin Rate Dependence On Bare Shell	118
4.16	Quasi-steady Temperature Distribution Around Coated Shell	119

4.17	Transient Max And Min Temperature For Thick-Coated Shell	120
5.1	Schematic Diagram Of Subliming Microthrusters	140
5.2	Non-obstruction Factors Versus L/R For 45° Cone	141
5.3	Non-obstruction Factor Of 60° Cone High Energy	142
5.4	Thrust Intensity For Pure Po-210 Deposit	143
5.5	Heated Nozzle Effect On Thrust Non-obstruction Factor	144
5.6	Regression Of Fuel In Cylindrical Microthruster (BOL)	145
5.7	Surface Temperature Of Cylindrical Microthruster (BOL)	146
5.8	Maximum Temperature In Cylindrical Microthruster (BOL)	147
5.9	Regression Of Fuel In Cylindrical Microthruster (EOL)	148
5.10	Surface Temperature Of Cylindrical Microthruster (EOL)	149
5.11	Maximum Temperature In Cylindrical Microthruster (EOL)	150
5.12	Non-obstruction Factors Versus L/R For Cylindrical Cone	151
5.13	Non-obstruction Factors Versus α For Cylindrical Cone	152
5.14	Optimization Of Cone Angles	153
5.15	Surface Temperature By ADI Method	154
5.16	Extrapolation Of Throat Area	155
6.1	Cross-sectional View Of Vane	173
6.2	Definition Of Euler's Angles	174
6.3	Graphical Representation Of Equation (6.4)	174
6.4	Cross-sectional View Of Strip Gap Vane	175
6.5	Subliming Pressure Versus Temperature	176

6.6	Subliming Rate Versus Temperature	177
6.7	Resultant Thrust For Synchronized Turning Of Microthruster (trigger $\theta=0^\circ$)	178
6.8	Resultant Thrust For Synchronized Turning Of Microthruster (trigger $\theta=90^\circ$)	179
6.9	Resultant Thrust For Synchronized Turning Of Microthruster (trigger $\theta=135^\circ$)	180

LIST OF TABLES

TABLE	PAGE
1.1 Non-obstruction Factor Of Cylindrical Tubes With Reflection Coefficient Equal To Zero	39
1.2 Non-obstruction Factor OF Cylindrical Tubes With Reflecting Walls But Non-reflecting End For $L/R=2.0$	40
3.1 Non-obstruction Factor Of Cylindrical Tubes With Reflection Coefficient Equal To Zero	85
3.2 Non-obstruction Factor Of Cylindrical Tubes With Reflecting Walls But Non-reflecting Ends For $L/R=2.0$	85
5.1 Characteristics Of Radioisotopic Heat Sources	156
5.2 Comparison Of Results From TUBNOF And CONNOF	157
5.3 Physical Properties Of Naphthalene And Biphenyl	158

CHAPTER 1

SUMMARY

1.1 Introduction

The present study was spurred by the fascination and the challenge of designing a passive attitude control scheme for small solar probes of the Sunblazer (1,3) type. The performance of the solar cells employed for electric power and of the antenna used for communications can be improved if such small probes can be oriented and the desired orientation maintained. The usual orientation directs the solar cells toward the sun and antenna toward the earth during superior conjunction, to obtain maximum power and antenna gain.

The problems of passive orientation of solar probes differ from that for passive earth satellites, since the solar gravity gradient and the solar magnetic field are too insignificant to be of practical use in attitude control. As a result, solar radiation becomes the only directional energy source available for solar probes. The approximately collimated solar radiation will induce an asymmetry of temperature distribution around a spinning spacecraft.

The two principal objectives in this work were (1) study the applications of radioisotopes and subliming materials to magnify the effect of this temperature asymmetry so that the spacecraft can be forced to orient toward the sun rapidly and reliably, and (2) the

optimization analysis of a subliming microthruster for use in the initial despinning the spacecraft after injection and in long term attitude control. Other required studies related to these objectives were: (3) the application of a modified Monte Carlo technique to Knudsen or molecular flow; (4) the various numerical solutions (involving from zero to two dimensions) of the parabolic partial differential equation for heat transfer with non-linear and moving boundary conditions.

1.2 Thermal Analysis of Erecting Shell

A spinning cylindrical shell under the solar radiation will develop an asymmetric temperature distribution around the shell as shown in Figure 1.1 due to the fact that the solar intensity on the shell surface is not uniform--rather it is nearly a half-rectified sinusoid at any point on the shell. The transient temperature solution can be approximated, depending on the problem, by ignoring the circumferential heat conduction effect, or the radial heat conduction effect, or by assuming no thermal conduction effect at all. The results obtained indicated that for a thin metallic shell, the zero-dimension, or Strip Approximation, is as good as the θ -dimension, or Thin Shell Approximation. However, if thickness increases, the smoothing effect due to the circumferential heat transfer also increases. For such cases, the Thin Shell Approximation is recommended. For a non-conductive shell of

any significant thickness, the Thick Shell, or r -dimension, Approximation is needed to account for the significant temperature gradient across the shell thickness. For the types of design investigated, the Strip Approximation is suitable for a bare shell and radioisotope-heated shell, but the Thick Shell Approximation is definitely required for a subliming material coated shell. In addition to the above transient numerical methods, first order analytic approximations to the quasi-steady state solutions were obtained. These analytic solutions have an inherent uncertainty of about twenty-five percent, but they are very useful for parametric analysis, in particular for the determination of the optimum spin rate at which the resultant force normal to the solar radiation is a maximum. The steady state temperature distribution typically resembles a skew sinusoid whose maximum lags behind the maximum solar intensity as shown in Figure 1.1. A net thermal reradiative force results, which has a component normal to the solar direction. This normal force component can be employed to erect the spacecraft, i.e., reduce the precession cone angle. The optimum spin rate is obtained by maximizing the following integral for the normal force with respect to the spin rate

$$F_N(\omega) = \int_0^{2\pi} [T(\omega, \theta)]^4 \cos\theta d\theta \quad (1.1)$$

where $T(\omega, \theta)$ is the steady state temperature distribution for spin rate ω , as shown computed for Figure 1.1 by the

numerical method or by the following approximate analytic expression,

$$T(\omega, \theta) \approx T(\omega)_{avg} [1 + M(\omega) \sin(\theta + \psi(\omega))] \quad (1.2)$$

The temperature distribution for any spin rate can be characterized by three parameters, the average temperature $T(\omega)_{avg}$, the amplitude factor, $M(\omega)$, and the phase lag, $\psi(\omega)$. Both the analytic and the numerical solutions to the above optimization have been obtained. The results are: (1) for a bare thin shell, the optimum spin is about a few tenths of a rpm (which is so slow as to be marginal from dynamics point of view); (2) for a radioisotope-heated shell, the optimum spin is about a few rpm (which is quite feasible); (3) for a subliming coated shell, the optimum spin is only a few hundredths of a rpm (which is too low to be operative). The corresponding maximum normal forces per unit height of the shell are (1) 10^{-4} dyne/cm for a bare shell; (2) about 20% higher for a heated shell; (3) in the order of few hundred dyne/cm (note that even at 3 rpm, which is well above the optimum spin, the normal force for a subliming shell is about 1 dyne/cm).

The transient behavior of these devices have been analyzed in detail. The transient temperature maximum, minimum and phase lag as well as the normal and parallel forces generated all exhibited damped oscillations such as shown in Figures 1.2, 1.3, 1.4, 1.5 and 1.6. The transient usually lasted no more than an hour provided the attitude was fixed. However, during actual stabilization, the

attitude is changing, therefore, the temperature distribution is expected to be in transient constantly.

1.3 Studies on Subliming Microthruster

To optimize the performance of an erecting shell as a passive control system for a solar probe, it is necessary to bring the spacecraft to about the optimum spin rate. However, the original fast spinning spacecraft cannot reliably be despun to the desired spin range by a Yo-Yo, which is a simple device designed to absorb the spin angular momentum from the spacecraft.

As a result, a subliming microthruster is proposed for further despin. The general configuration is shown in Figure 1.7. The sublimation heat is supplied from radioisotopic heat generated by a thin coating of long-lived radioisotope at the bottom of the cup and from a small concentration of shorter-lived radioisotope mixed in with the subliming material.

The temperature distribution is very important so that the transient solution of a heat conduction equation is necessary. The simple cylindrical cup design was analyzed by both explicit and the implicit difference schemes to obtain the transient temperature distribution. The results agreed very well. However, because of the moving boundary condition (due to surface sublimation), the implicit method appeared superior. For a sophisticated design such as the chopped cone microthruster the detailed temperature

distribution required solution of the two-dimension transient heat flow equation. An ADI (Alternate-Direction-Implicit) technique was employed. Due to the non-rectangular geometry, there was a numerical instability limitation, which however was not too serious. In general, for a rather refined mesh net, a time step of one second is quite stable.

Emphasis during the microthruster study was placed in the optimization of performance. The total thrust comes from the summation of normal momentum ($mv \cdot \cos\theta$) of all the exit molecules per unit time. By varying the nozzle cone angle and its length, the ($\cos\theta$) factor can be approached toward unity. The numerical technique developed for the molecular flow study and mentioned in Section 1.8 was adapted to analyze this problem. The results are shown in Figures 1.8 and 1.9.

To improve performance further, the ($m \cdot v$) factor offers attractive possibilities. If the nozzle wall is heated radioisotopically, the average speed of the molecules and hence the thrust can be increased because the molecules adsorbed by the wall will receive the thermal energy from the heated wall. This fact is shown in Figure 1.10. In addition, performance could in general improved by molecular dissociation, but this phenomenon was not taken into account in this study because at the temperatures considered here the dissociation effect is negligible.

A sublimation microthruster can produce thrusts of a few hundred dynes, but its effective life is quite limited. By providing a thin layer of alpha-emitting radioisotope coating to the bottom of the thruster cup, a long duration thrust, of the order of tenth of a dyne, can be provided over the life of the radioisotope.

1.4 Molecular Flow Parameters

Problems of molecular flow are implicitly related to the present study through two dimensionless quantities (1) the evaporation coefficient, which is the ratio of molecules actually sublimed from a surface to the theoretical value, and (2) the non-obstruction factor, which is the ratio of rarefied gas (mass or momentum) flow rate through a walled channel to the rate for the case no channel walls are present. The classical approach of solving Clausing's Integral equation (16,17) has limited solutions to simple channel geometries and idealized molecular behaviors.

In principle, a straightforward Monte Carlo method could be applied to this problem. However, in tracing the history of each molecule, three or four random numbers are required to determine its orientation as well as its energy, and depending on both the channel geometry and the assumed possible interactions, many more random numbers are needed. If an adequate number of case histories is to be considered, good accuracy is not obtainable within practical computation times. The complexity increases rapidly with increasing

channel length. This difficulty is very similar but not as complicated as calculation of the deep penetration of the nuclear radiation through a thick shield.

To deal with the problem, the following modified Monte Carlo method was developed. Molecules entering a channel are assumed to flow from a finite number (a few hundred) of point sources from which the molecules are emitted with a Maxwellian distribution. The total angular distribution from each point source is divided into many groups each of which is characterized by a polar angle, an azimuthal angle, and an amplitude according to the distribution function (note expected values are used). The fate of every molecular beam bundle is followed and is recorded. Those molecules adsorbed by the channel wall require further tracing because at steady state they will be reemitted as fast as they are adsorbed. A spherical cosine is assumed for these reemitted molecules. Their fate is found by considering the probabilities of the various fate of each molecule reemitted from any position in the channel.

The mathematical variance of this method is not analyzed here, but in comparison with results obtained by other methods for two simplified assumptions (16,17), this method gives excellent agreement; see Tables 1.1 and 1.2. The main advantage of the new method lies in its flexibility both to account for complex molecular interactions and reflections from surfaces and to be adapted to channels of non-uniform cross section.

The results for the sublimation surface reflection effect, the molecular collision effect, and the conic channel effect are shown in Figures 1.11, 1.12 and 1.13. Using these accurate channel obstruction effects, the raw data from mass-flow experiments (15) can be interpreted to produce accurate values for the evaporation coefficients. The result of a sample calculation is given in Figure 1.14. The evaporation coefficient is essential in determining the heat and mass transfer on a system using a subliming material such as the erecting shell and the microthruster.

1.5 Applications to Sunblazer

As a dynamical model a small solar probe such as Sunblazer is analogous to a spinning top under gravity with the exception that the solar pressure acts like a negative gravity torque. Assuming the nutation or the wobble has been taken care by a viscous damper, the attitude control is reduced to the problems of despin and precession damping.

Two pairs of microthruster cups loaded with about one pound of subliming material could despin the spacecraft from 200 rpm to few rpm in less than a day. However, if the microthruster is used to supplement the action of a Yo-Yo, the requirement for subliming material is reduced to a fraction of a pound. The long-term thrust from a coating of alpha emitter at the bottom of the cup is about a thousand times smaller than the thrust by sublimation. Unless the microthruster is mechanically turnable, the residual torque

of about 1 dyne-cm will continue to change the spin rate.

As the rate of spin is reduced to the optimum region, the erecting torque generated by an erecting cylindrical shell reaches a peak. For a shell coated with subliming material, even at the non-optimum spin of a few rpm, the resultant erecting torque is enough to erect the spacecraft in a few hours. For a bare shell, at the optimum spin rate (0.37 rpm), the erecting period is in the neighborhood of two weeks. Finally for the radioisotope-heated shell, the erecting torque is only slightly larger than that of a bare shell, but the optimum spin increases several fold. Since the rate of erection is approximately proportional to the ratio of erecting torque to spin rate, the erecting period increases to about five weeks.

Other attitude control procedures, using an erecting shell and/or microthrusters, can be designed for small space probes. They may be completely passive, semi-passive, or even active such as by synchronizing the turning of the microthrusters as the vehicle rotates so that a desirable averaged precession torque and erecting torque result.

1.6 Conclusions

(1) The asymmetric temperature distribution around a cylindrical shell is very suitable for generation of erecting torque to stabilize solar probes. Since the transient period is short compared with the despin period following exposure of the shell to the solar radiation, its

effects were ignored for the present study. In detailed dynamics analysis, the transient effect always exists during the stabilization period because the attitude of the spacecraft is continuously changing.

(2) A subliming material coated shell is by far the fastest erecting device but is also the most short-lived. The radioisotope-heated shell is capable of the least erecting rate but it is long-lived and can be operated at a higher spin rate where disturbing torques are not likely to dislodge its orientation.

(3) The numerical technique developed for the non-obstruction factor calculations of molecular flow is very flexible, accurate, and can include complex physical phenomena. It should also be applicable to the problem of calculating neutron and gamma ray streaming through gaps or beam-ports.

(4) The modified Monte Carlo technique seemed to be very appropriate for analyzing the vapor flow for the microthruster. The technique eliminates many unnecessary complex mathematics. The result clearly pointed the ways to improve the design of a microthruster.

(5) The applications of the above devices, with proper feed-back control mechanism, can be extended to a wide variety of satellites. In particular, a pair of microthrusters can produce torques in all three body axes to control the attitude of a light spacecraft.

FIG 1.1 STEADY STATE TEMPERATURE DISTRIBUTION AROUND A BARE SHELL

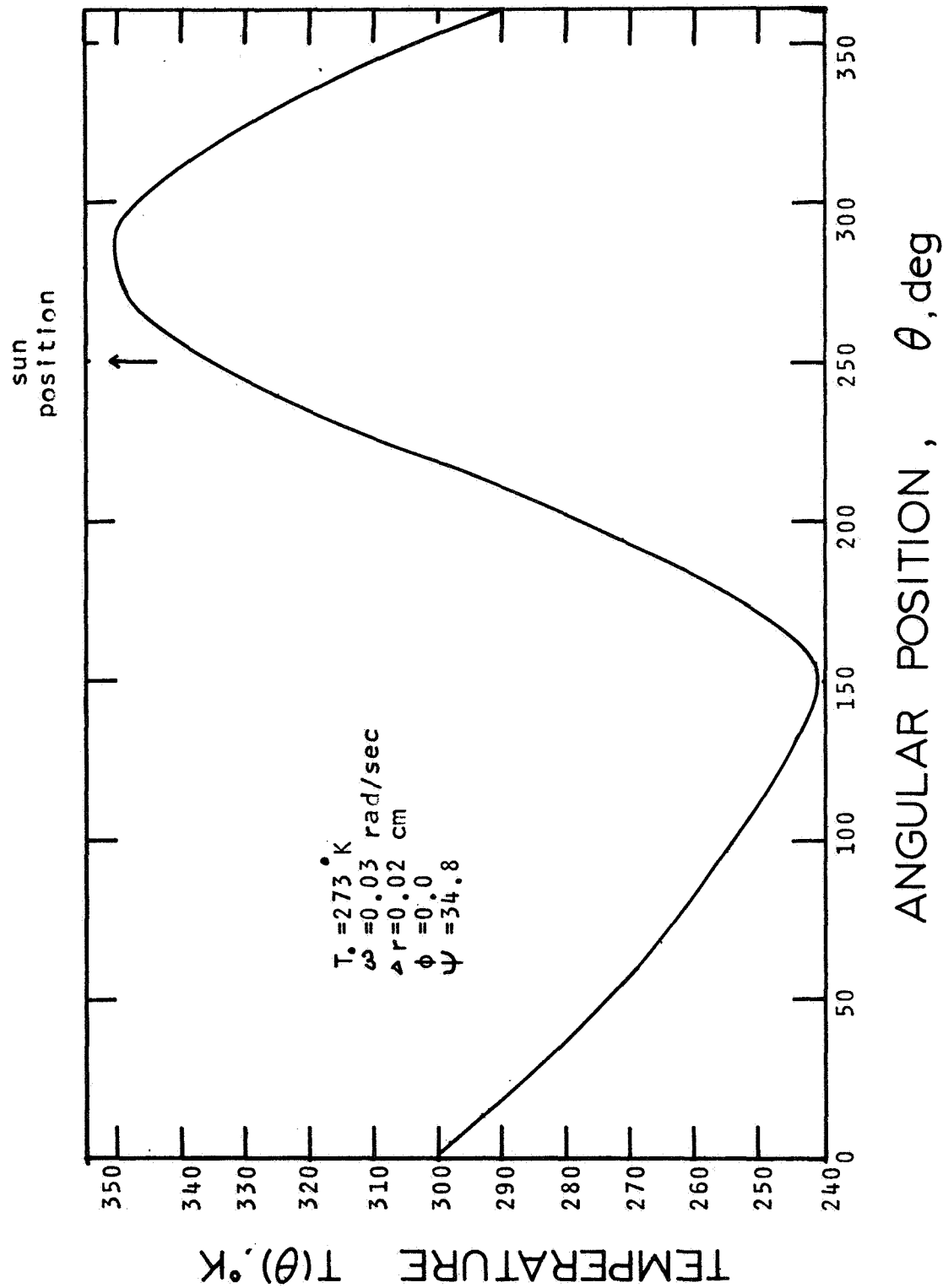


FIG 1.2 TRANSIENT MAXIMUM
TEMPERATURE OF BARE SHELL

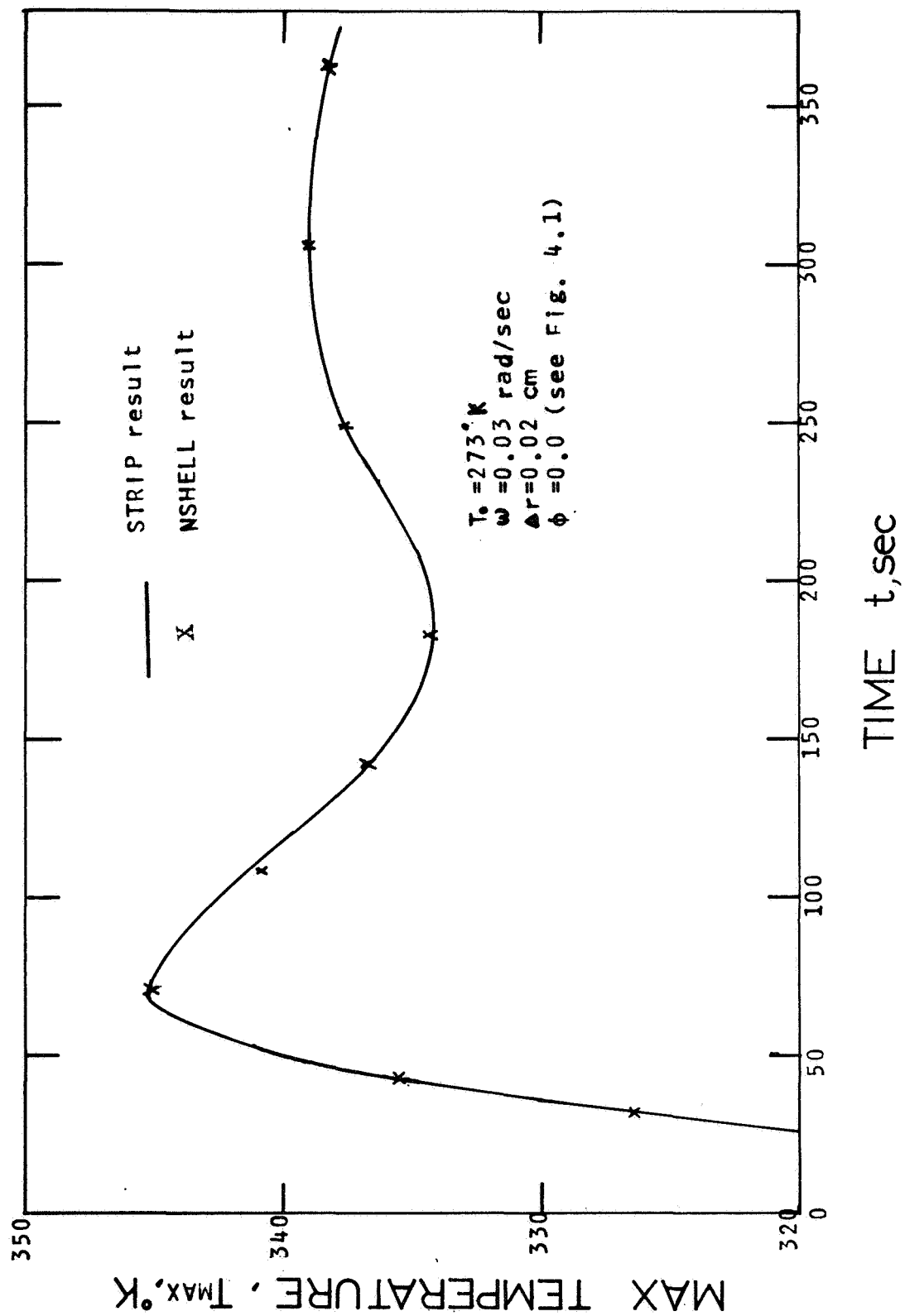


FIG 1.3 TRANSIENT MINIMUM
TEMPERATURE OF BARE SHELL

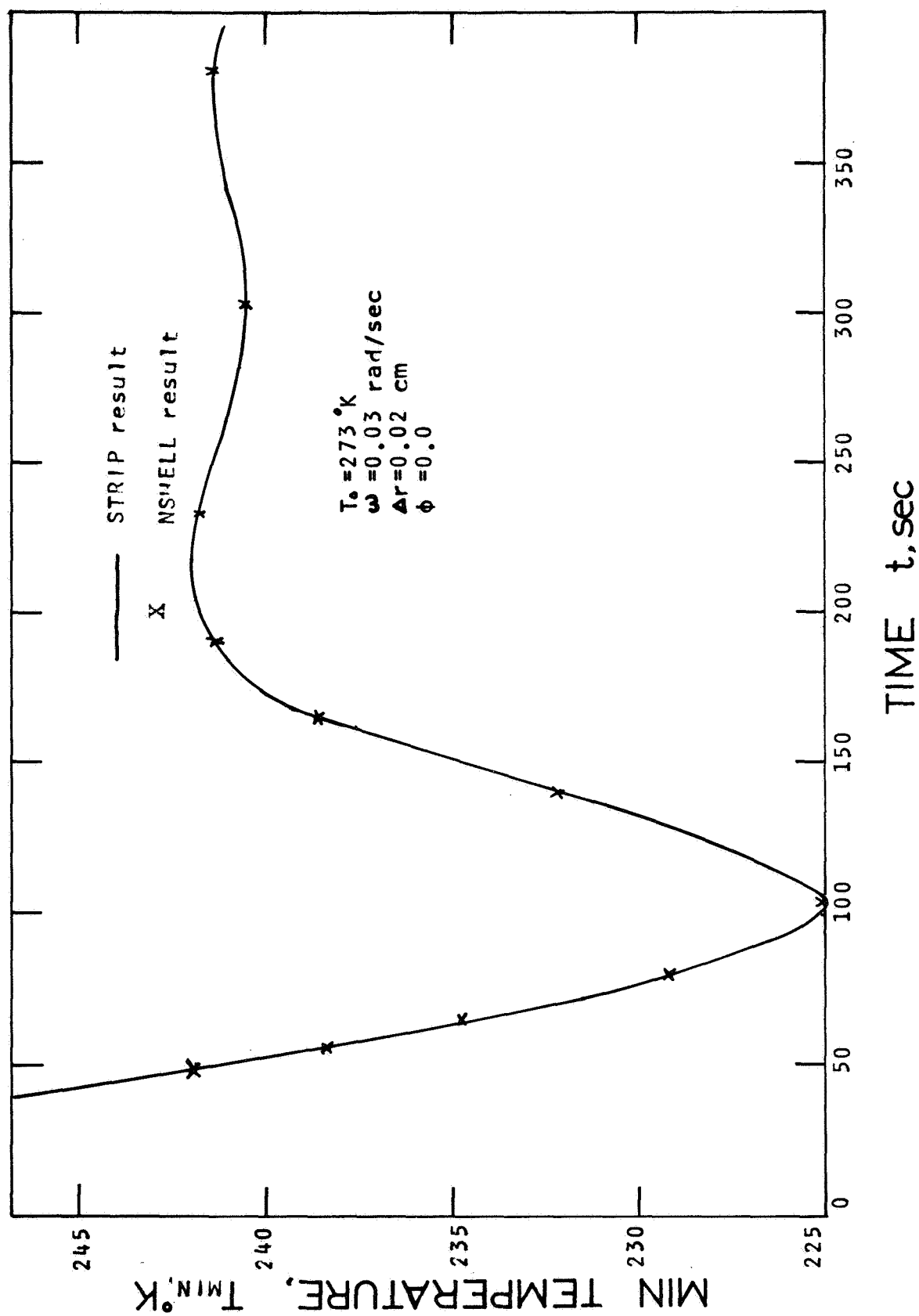


FIG 1.4 TRANSIENT PHASE
LAG OF BARE SHELL

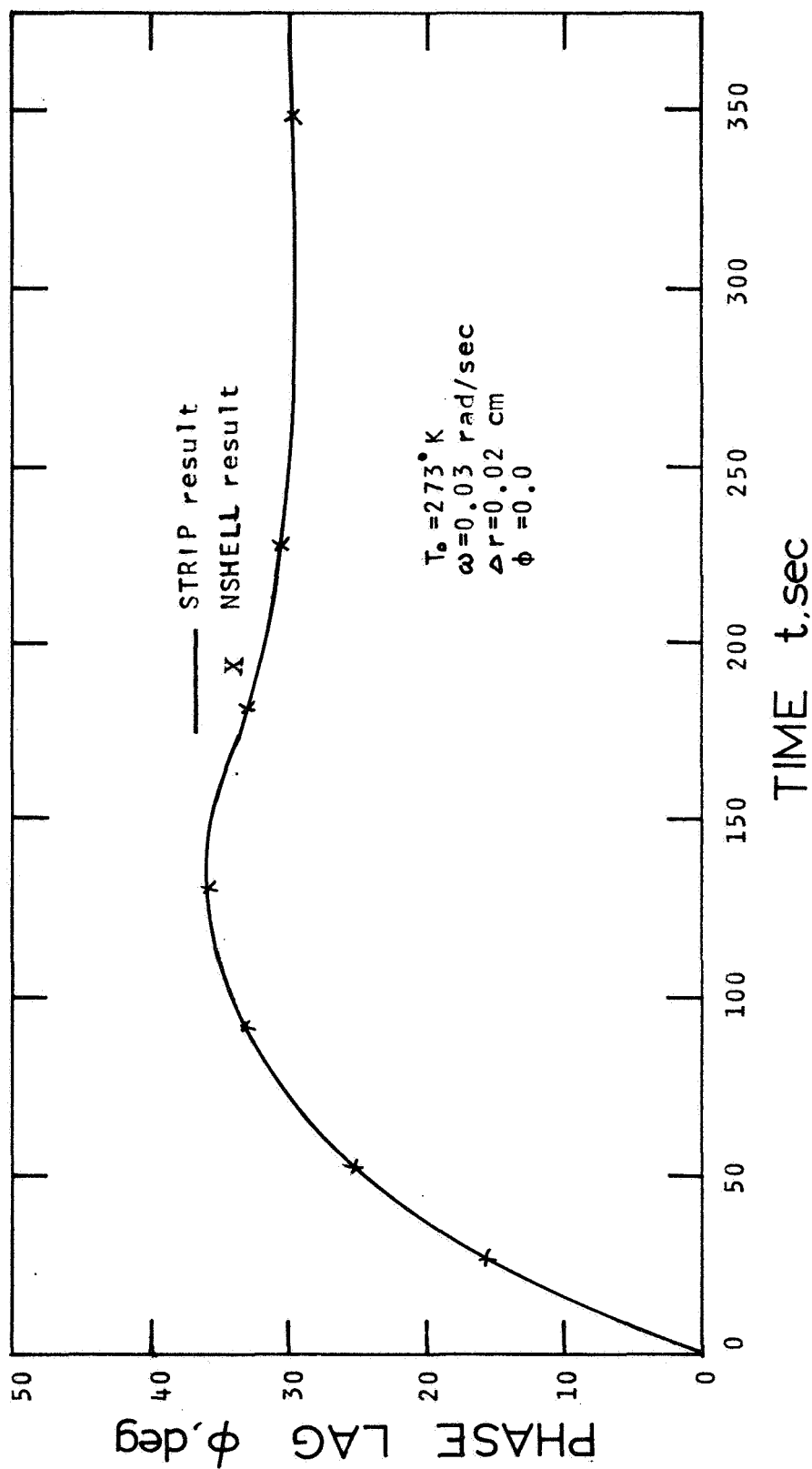


FIG 1.5 TRANSIENT NORMAL FORCE COMPONENT FOR BARE SHELL

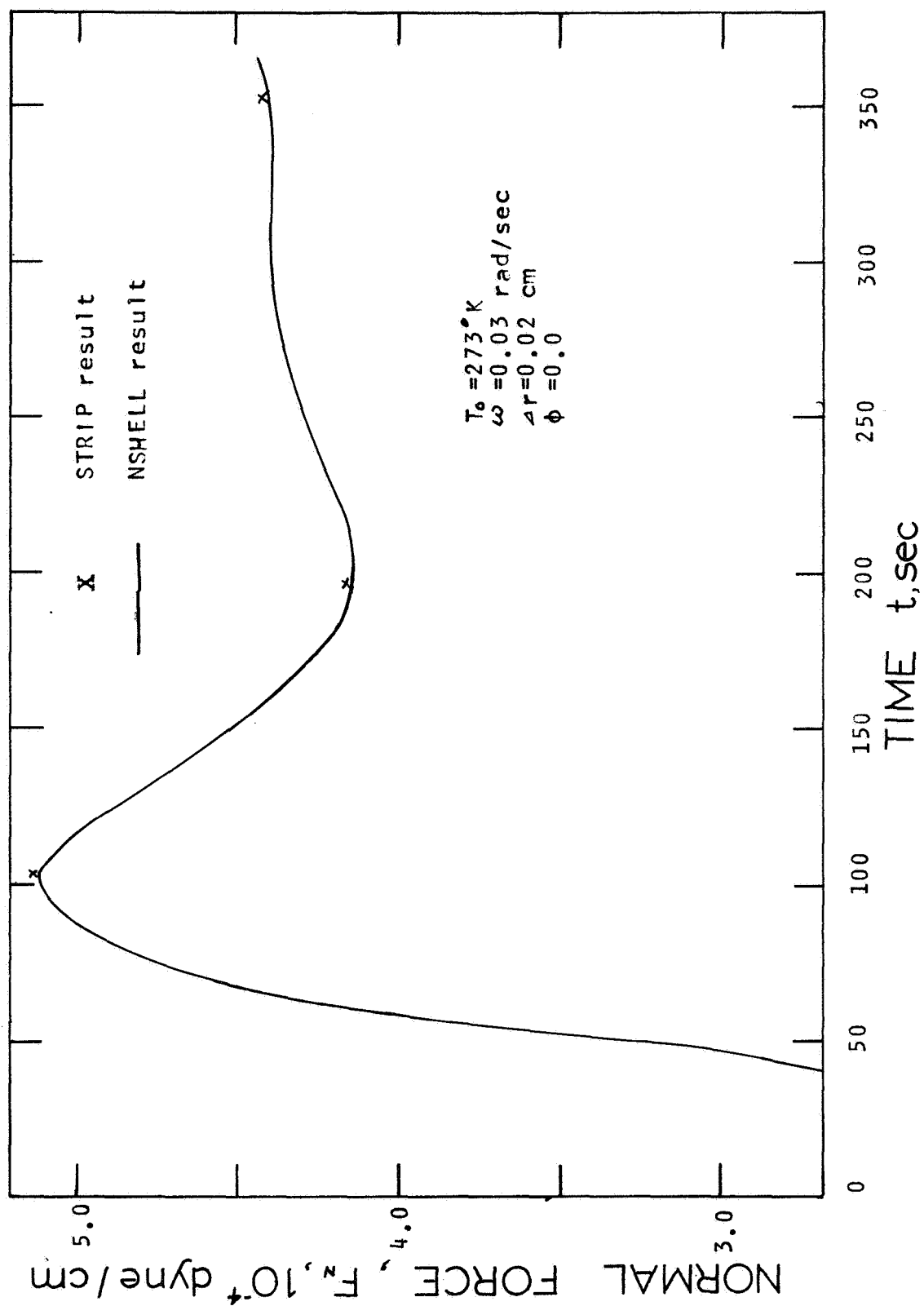


FIG 1.6 TRANSIENT PARALLEL FORCE COMPONENT FOR BARE SHELL

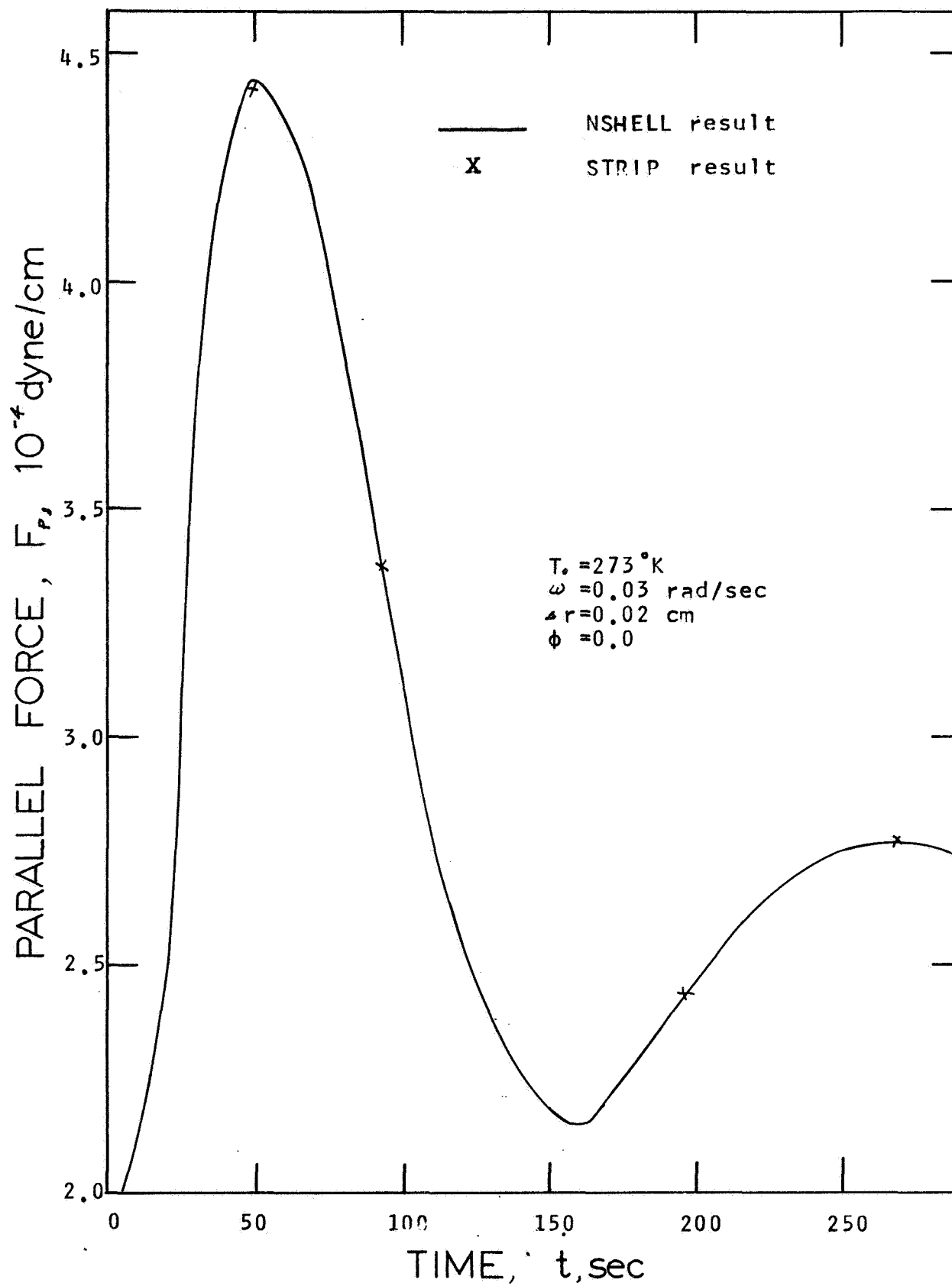
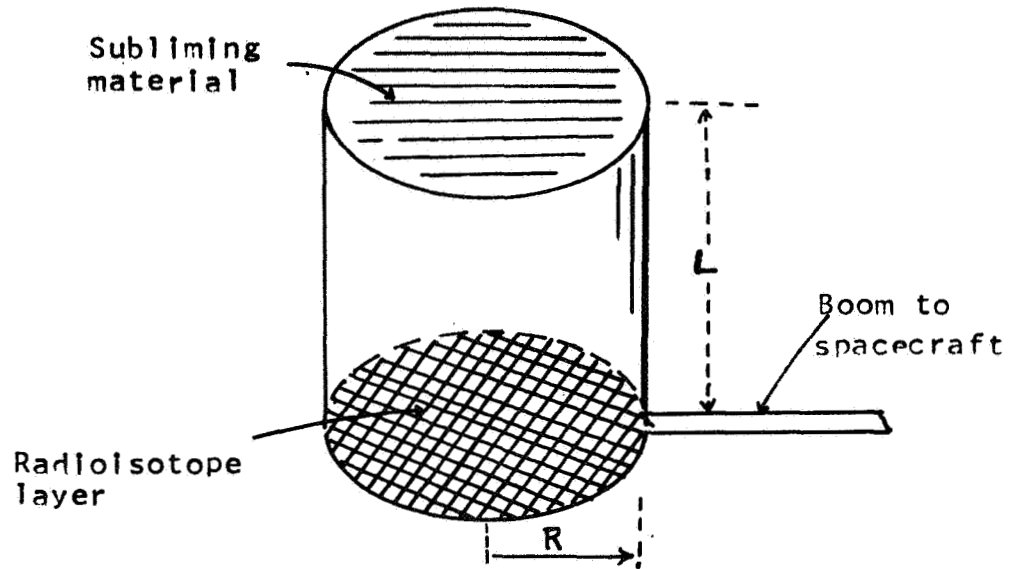
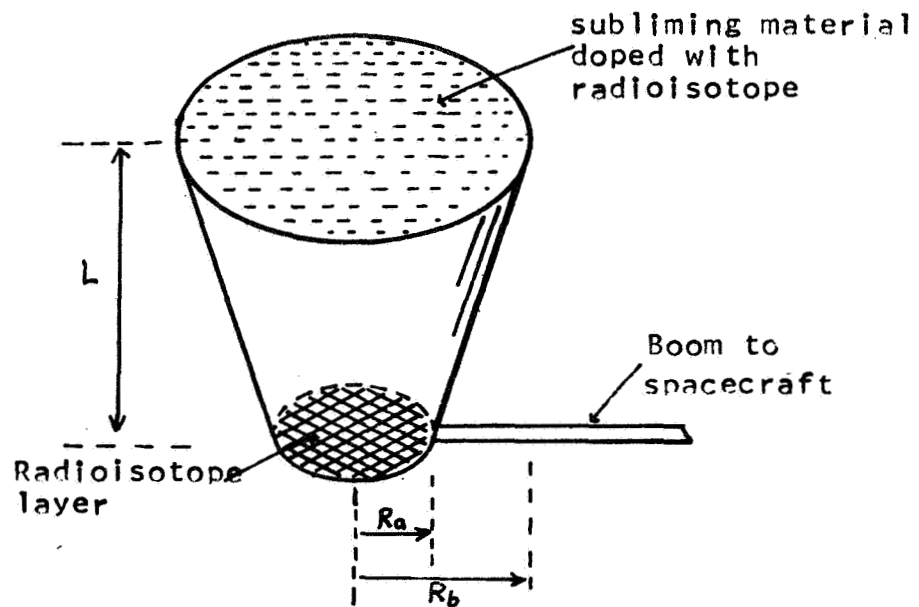


FIG 1.7 SCHEMATIC DIAGRAM OF
SUBLIMING MICROTHRUSTERS



A. Cylindrical cup



B. Chopped Cone

FIG 1.8 OPTIMIZATION OF CONE ANGLES

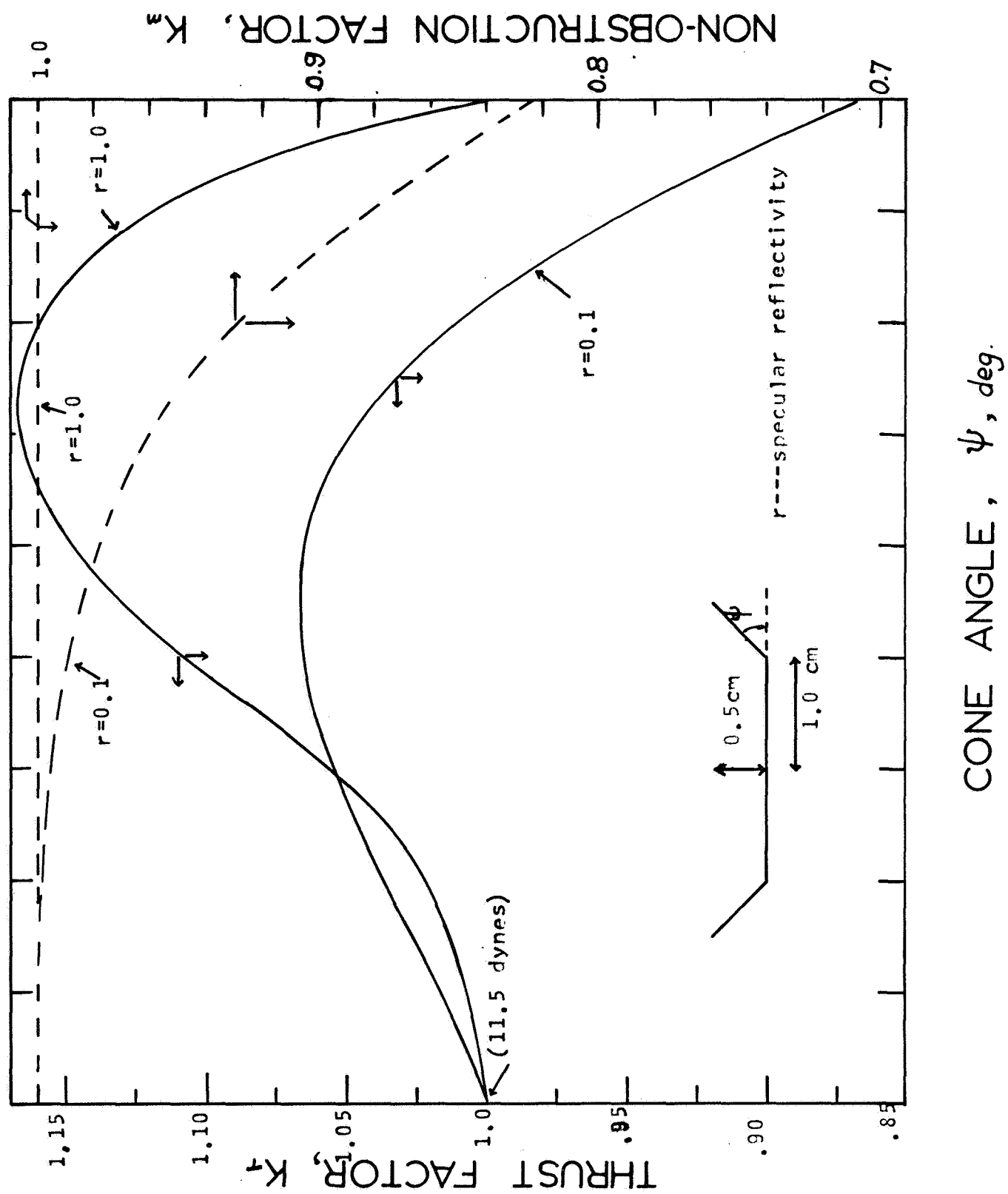


FIG 1.9
EXTRAPOLATION OF THROAT AREA

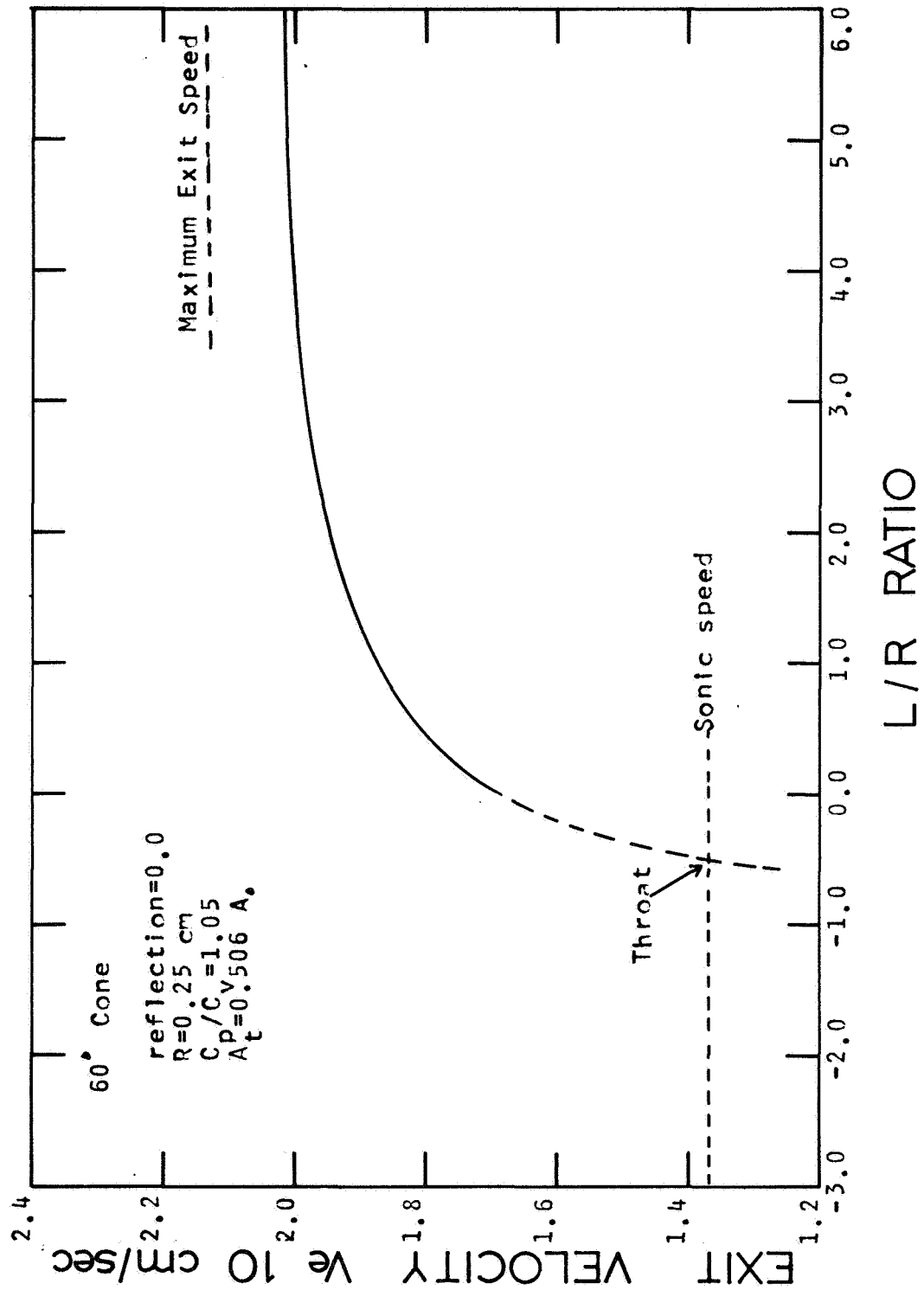


FIG 1.10
HEATED NOZZLE EFFECT ON
THRUST NON-OBSTRUCTION FACTOR

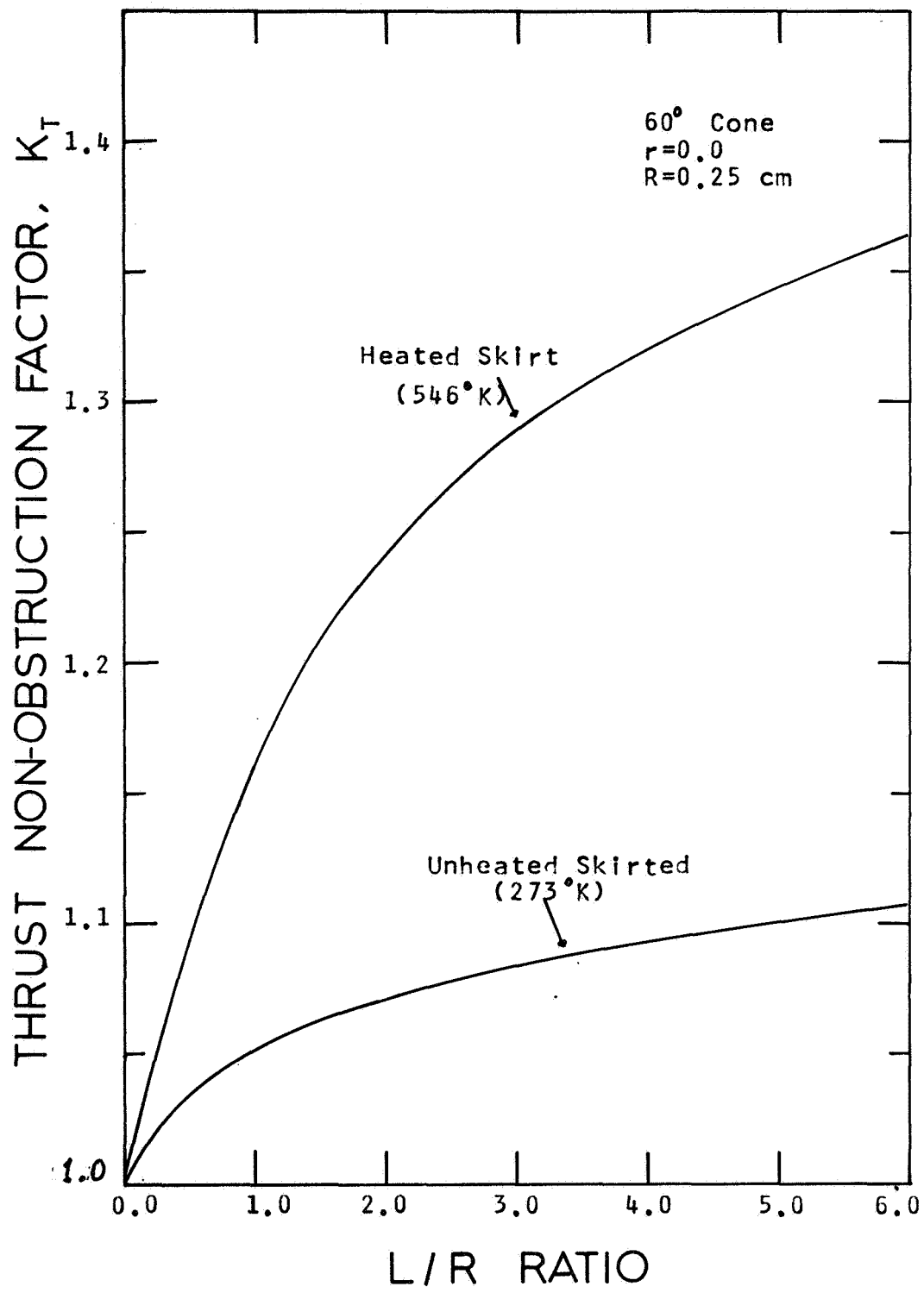


FIG 1.11 SUBLIMING SURFACE
REFLECTION EFFECT

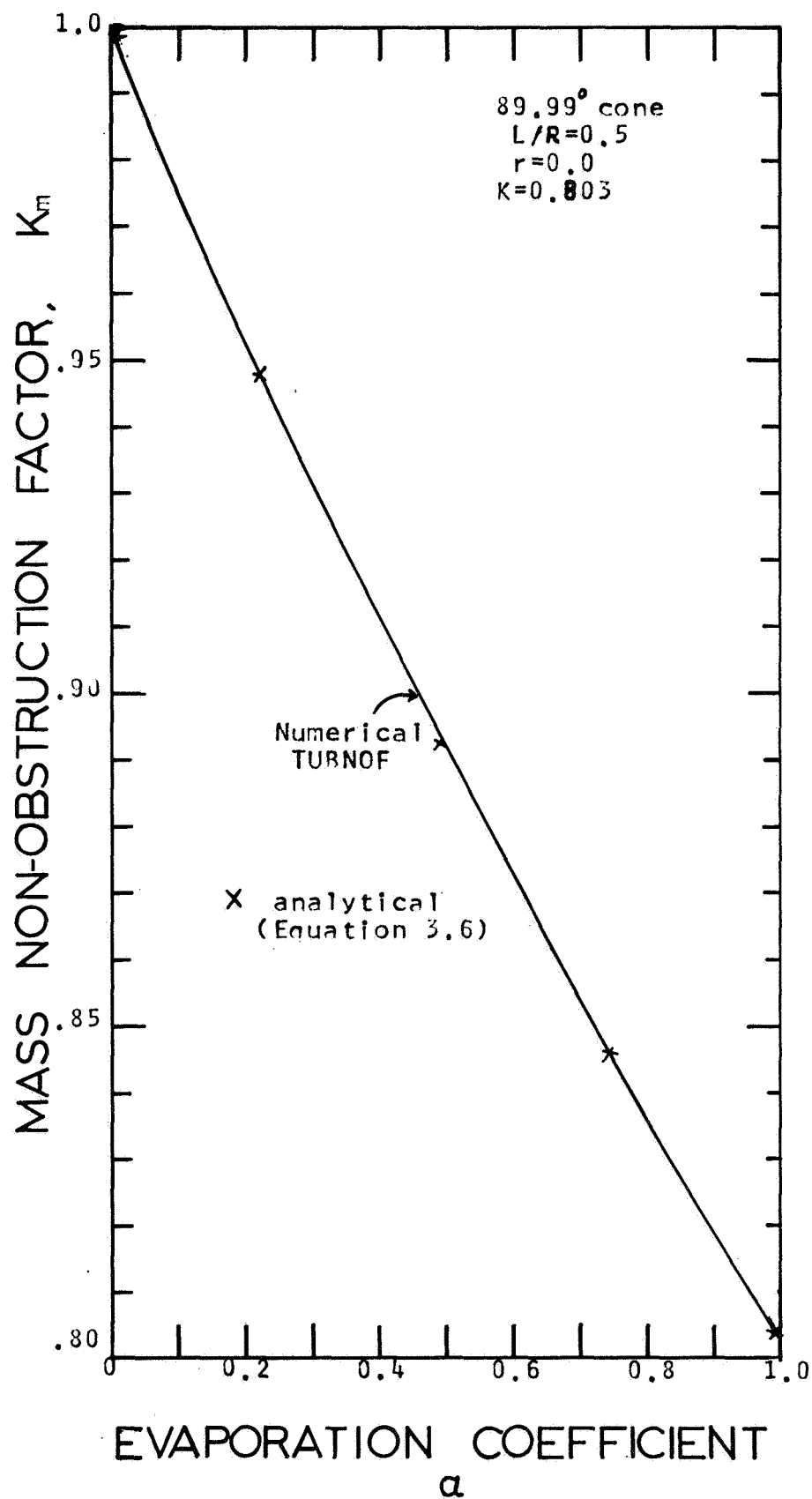


FIG 1.12 MOLECULAR COLLISION EFFECT
ON NON-OBSTRUCTION FACTOR

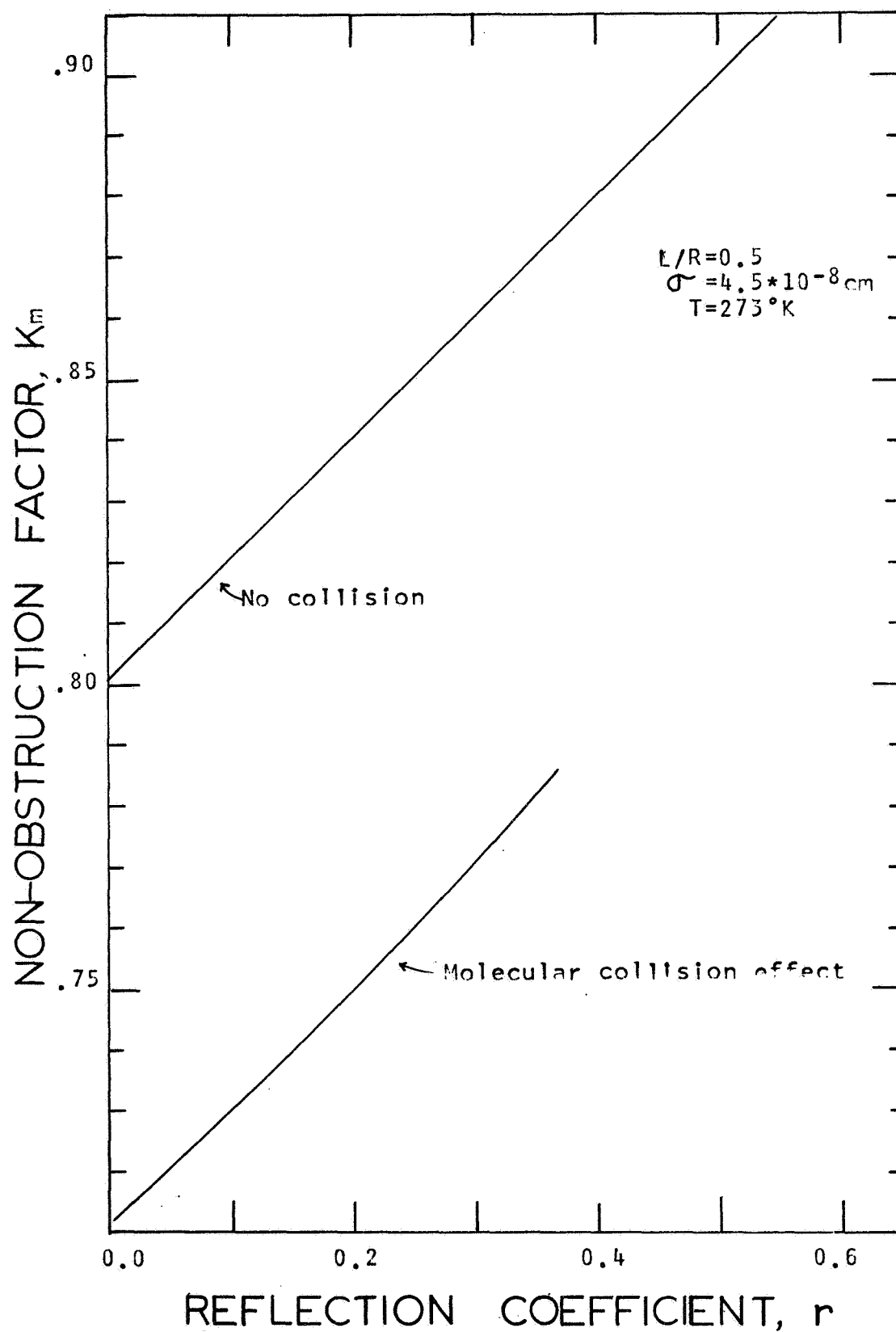


FIG 1.13
NON-OBSTRUCTION FACTORS
vs L/R FOR 45° CONE

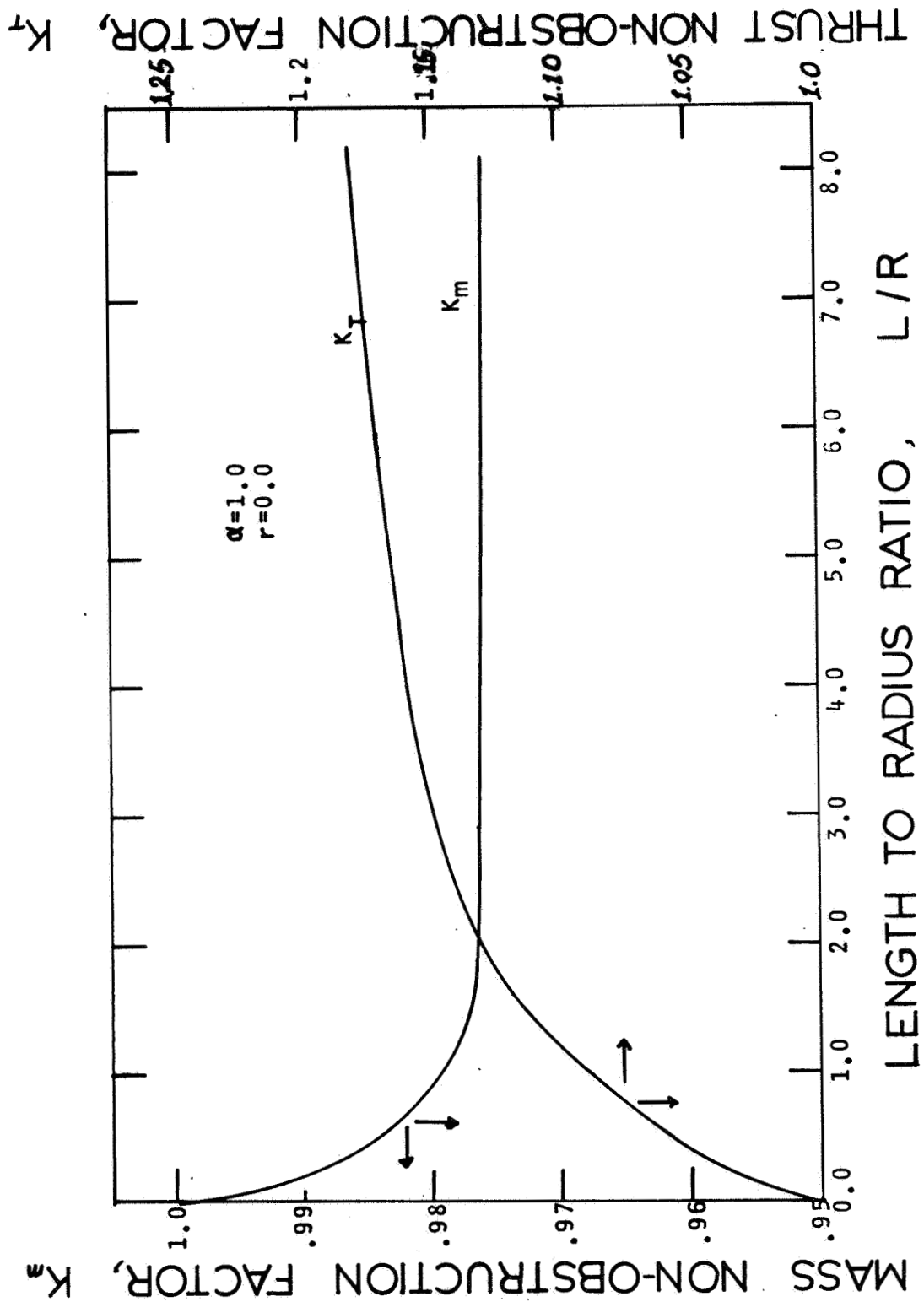


FIG 1.14

EXTRACTION OF EVAPORATION COEFF FROM MASS FLOW DATA

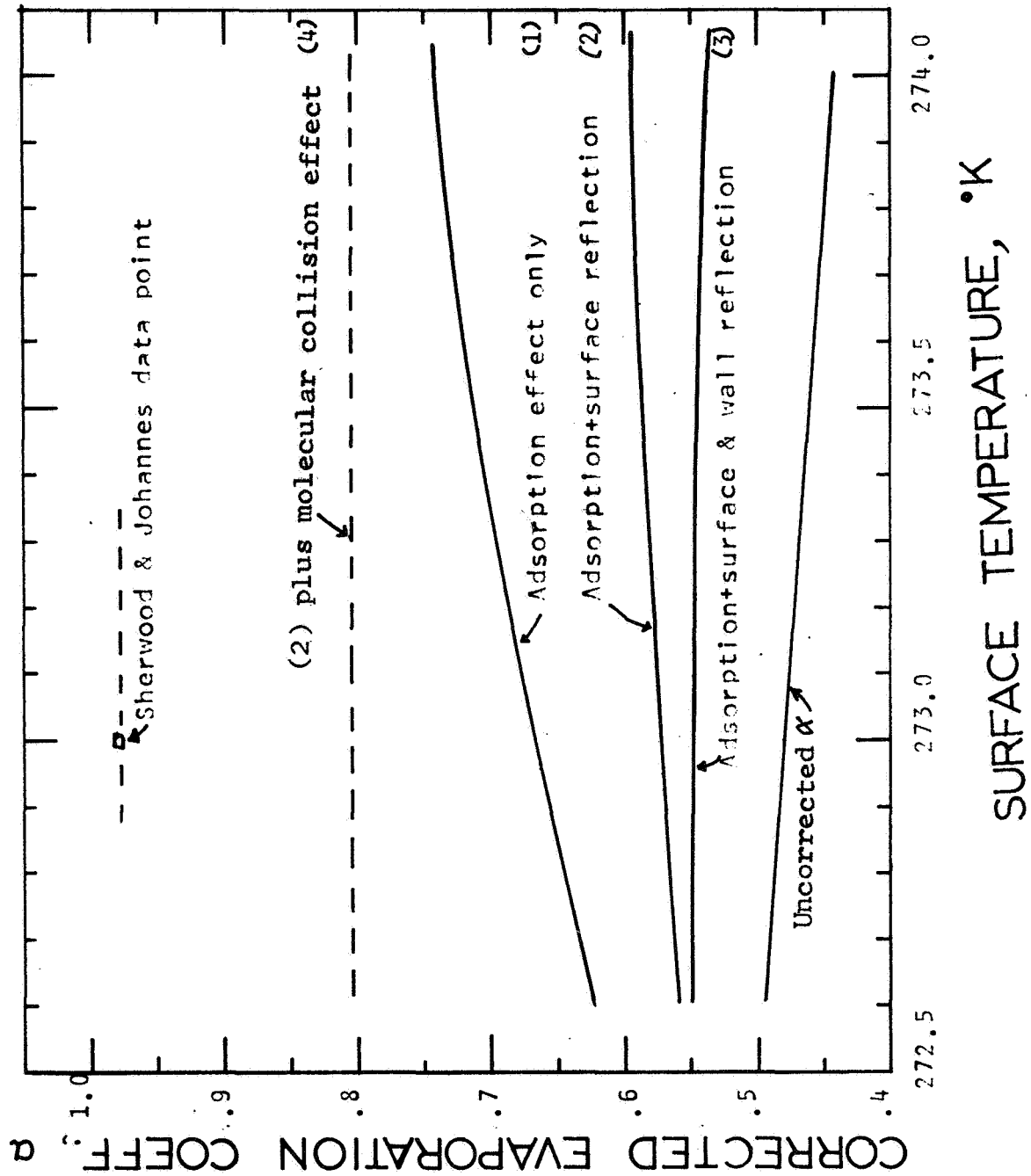


TABLE 1.1

NON-OBSTRUCTION FACTOR OF CYLINDRICAL TUBES
WITH REFLECTION COEFFICIENT EQUAL TO ZERO

L/R	K-M (THIS WORK)	K (CLAUSING)	Q (DEMARCUS)
0.5	0.80170	0.8013	0.80127
1.0	0.67192	0.6720	0.67198
1.5	0.58165	0.5810	0.58148
2.0	0.51486	0.5136	0.51423
3.0	0.41974	0.4205	0.42006
4.0	0.35619	0.3589	0.35658
5.0	0.31074	0.3146	0.31053
6.0	0.27823	0.2807	0.27547

TABLE 1.2

NON-OBSTRUCTION FACTOR OF CYLINDRICAL TUBES
 WITH REFLECTING WALLS BUT NON-REFLECTING ENDS
 For $L/R=2.0$

r	Q	K-M
	(DEMARCUS)	(THIS WORK)
0.0	0.51423	0.51486
0.2	0.58247	0.58237
0.4	0.65890	0.65651
0.6	0.74690	0.74163
0.8	0.85412	0.84483
1.0	1.00000	1.00000

K -- SEE REF. (16)

Q -- SEE REF. (17)

CHAPTER 2

INTRODUCTION

2.1 Introductory Remarks

The Sunblazer satellite (1,3), which is being designed and developed at the Center for Space Research of M.I.T. will be used to map the charged particle density in the vicinity of the sun and study the solar corona and magnetic field. This small spacecraft is to be powered by solar cells which supply an average power of about 20 watts of electricity to a multi-frequency pulsed-transmitter and other electronics. The transmitter is designed to radiate several pulsed signals simultaneously which would arrive at receivers on Earth delayed in time by different amounts due to the dispersive nature of the interplanetary charged particles.

An important characteristic of this spacecraft is its low weight so that inexpensive Scout rockets can be employed to inject several probes into heliocentric orbits per year. In doing so, systematic measurements of corona electron density fluctuations could be made. The success of the spacecraft depends upon its ability to orient itself continuously to obtain steady radiation to the solar cells, for proper thermal control of the spacecraft and for maximum transmitter antenna gain. The payload limitation of the Scout-type rocket precludes the possibility of using conventional active attitude control devices such as gas

jets or reaction wheels which require active on-board feed-back control systems. However reliability considerations dictate a system with a minimum of moving parts (passive or semi-passive) while mission requirements call for a lightweight system which has a relatively fast response-time to shorten the period of stabilization. The purpose of this work is concerned with the design of suitable devices of this type and the related physical problems.

2.2 Probe Orbit Considerations

By retrograde injection, i.e., launching the rocket directly opposite to Earth's orbital velocity, the spacecraft will fall into a heliocentric orbit with its perihelion less than 1 AU (i.e., on an inferior orbit). A typical Sunblazer orbit in an ecliptic projection in rotating and sun-oriented coordinates, such that the Earth-Sun line stays fixed, is shown in Figure 2.1. The information obtained at superior conjunction is of greatest interest, and consequently the time to superior conjunction (occultation of spacecraft by the Sun) should be made as short as possible. However, the shorter the superior conjunction time or the mission time, the larger the booster requirement and the closer the perihelion is to the sun. The small perihelion introduces problems of both spacecraft thermal control and the solar-cell degradation problems.

The transmission of pulsed signals at superior conjunction is particularly important for determining the electron densities in the solar corona. Unfortunately, a communication blackout region (2,8), which is a function of solar activity as well as the transmission power, exists near occultation. In order to minimize the blackout period, it is highly desirable to point the spacecraft directly at sun so that during superior conjunction the solar cell panel and antenna are facing the sun and earth, respectively, which will cause both the electrical power and the antenna gain towards the earth to reach a peak. The present study is concerned with passive attitude control devices suitable for this type of solar probe. The performance of the proposed devices are discussed in Chapter 4 and Chapter 5.

Under direct injection, the probe will assume a superior orbit (with the apohelion greater than 1 AU). Several difficulties arise to affect the attitude control directly or indirectly. Owing to the increasing excess velocity requirement for a superior orbit injection, the payload has to be kept small. On the other hand, because of the larger orbit and the longer mission time, the solar intensity decreases while the transmission power and the orientation requirement increase rapidly with distance. Consequently conceptual designs which depend upon solar radiation for power generation and orientation probably can not be applied for superior orbit missions. Some of the possible solutions are discussed in Chapter 6.

2.3 Spacecraft Dynamics Considerations

2.3.1 General

For a spin-stabilized spacecraft, the important dynamic motions consist of nutation, precession and spin. Nutation, sometimes referred to as the force-free precession, is that motion of a spinning body which deviates from uniform spin about a fixed axis in the absence of disturbing torques. Precession is that motion of a spinning body which results from an external torque.

The present study does not consider nutation damping because a simple, light weight, viscous liquid damper such as an annulus partially filled with mercury and mounted concentric with the spin axis, at a point off the axial center of gravity can effectively dissipate the nutational energy (4). This is true only if the spacecraft is spinning about the axis of largest moment of inertia (5) because the resulting conversion of kinetic energy into heat through viscous damping must eventually bring the body into a minimum-energy state. (Note the terminal rotational kinetic energy is $T = I\omega^2/2 = H^2/(2I)$, where H is the constant angular momentum; for minimum T , the moment of inertia I must be maximum). Unfortunately, this nutation damper is incapable of removing the precessional motion because viscous damping usually generates no external torque to change the angular momentum of the spacecraft.

Assuming the nutational motion can be rapidly damped out by an annular liquid damper, the attitude control problem is reduced to that of spin control and precession damping.

A complete attitude control system must have the capability to produce torques about all body axes of the spacecraft. These are the spin torque, the precession (or restoring) torque, and the erecting (or precession damping) torque. The positive sense of each torque is defined as shown in Figure 2.2.

2.3.2 Restoring vane

Falco vitz (5) has shown that a sun-orbiting spacecraft can be designed to take advantage of solar pressure (i.e. photon momentum) for attitude control by an ingenious arrangement of its external surface--in particular, by corrugating the optical coating on the surfaces of the restoring vane or the solar sail for generation of torques about all three body axes. Unfortunately, this technique can not produce a large non-conservative erecting torque to dissipate the kinetic energy stored in unwanted precessional mode. Furthermore, the effectiveness of this technique will be decreased by degradation of the surface radiation properties of the coated material under long-term intensive solar radiation exposure. The latest Sunblazer design (3) uses four stepping motors to rotate four big triangular vanes in order to control the resultant average torques

about all three body axes. The torques, which are time varying in each spin cycle, result from the vane surface reflection. The disadvantages of this design are: (1) necessity of deploying four large vanes when in orbit; (2) no independent control on the magnitude of each torque; (3) the capability of attitude control depends on the proper functioning of the stepping motors; and (4) out of phase electric power requirement, i.e. more power is needed to drive the motors when the solar cells produce less than normal power. Nevertheless, a restoring vane is desirable because of its contribution to the inherent stability of the spacecraft by positioning the center of pressure behind the center of mass. The resultant torque will force the spacecraft to have a retrograde precession, i.e., to precess in a direction opposite the spin direction.

2.3.3 Erecting shell

Consideration of gyroscopic action suggests that an erecting torque can be generated only if there is a force acting on a spinning body normal to both the spin axis and the axis of precession. A very clever passive device (7) is to simply place a thermally absorptive thin metallic shell in front of the spacecraft. The approximately parallel solar radiation will always introduce an asymmetry of temperature distribution around the cylindrical shell. Fortunately, the resultant reradiation force has a normal component to erect the spacecraft or to decrease the

precession cone angle as shown in Figure 2.3. In principle, this passive erecting torque should eventually damp out the precession and should orient the spacecraft to point at the sun directly. However, because of the small orbital angular velocity which is always normal to the ecliptic, it is impossible to align the spin axis with the sun axis. Hence, even at equilibrium, the spin axis will point above or below the ecliptic plane depending on the spin direction. Typically, the equilibrium canted angle is of the order of a few degrees (3).

The serious drawbacks of this simple design are: (1) In order to maximize the radiative erecting force, the shell has to be very thin and the spacecraft has to be despun to a few tenths of a rpm (18) (As a result of this small spin, the spacecraft is very vulnerable to minute disturbing forces resulted from the meteorite impacts, out-gassing, Coulomb and Lorentzian interactions.); (2) The useful reradiative energy is only a small fraction of the absorbed solar energy. Also, thermal reradiation is the most ineffective method of extracting recoil force from a given amount of energy to be radiated.

In Chapter 4, several conceptual techniques involving the use of radioisotope heating and subliming materials which are aimed at improving these shortcomings are proposed and analyzed both analytically and numerically. The analytic approach is primarily for studying the steady state behavior in a closed form. The numerical approach is to

Investigate the transient and the steady state behaviors accurately.

2.3.4 Despin microthruster

The residual spin immediately after orbit injection by a Scout rocket is about 200 rpm (3), which is too high for stabilization and perhaps for the proper functioning of instruments. A simple mechanical device, the Yo-Yo, is in theory capable of reducing the spin to any desirable value. It consists of a small mass, m , on the end of a light cord wrapped around the spinning spacecraft. As soon as the mass m is released, it will unwind at a constant rate (5) and will absorb the spin angular momentum from the spacecraft. After the cord is completely unwound (in a fraction of a second), the mass m is allowed to fly away leaving the spacecraft spinning at ω_f which is less than the initial value ω_o . The length of the cord determines the final spin and it is given by (5)

$$\ell = R \sqrt{\left(\frac{I}{m R^2} + 1\right) \frac{\omega_o - \omega_f}{\omega_o + \omega_f}} \quad (2.1)$$

where R is the radius of the spin body
 I is the moment of inertia in the spin axis

However, for a given cord, the final spin can be known only about as accurately as the initial spin is known. Unfortunately, due to the build-up of nutation during vehicle deployment, the Yo-Yo can be safely designed to despin the spacecraft only to about one tenth of its initial spin. Hence, further despin is required. In Chapter 5, use

of a sublimation microthruster to accomplish the desired residual despin is proposed and its performance analyzed. The performance of the microthruster is optimized with respect to several pertinent variables. The transient solutions of the temperature distribution in the subliming material are given for both cylindrical cup and chopped cone designs. Radioisotopes are proposed to supply the necessary heat to the sublimation process and to generate low thrust by expulsion of alpha particles so that the microthruster is capable of the short-term fast despin as well as the long-term fine spin control.

2.4 Rarefied Gas Dynamics Considerations

2.4.1 Evaporation coefficient

The evaporation coefficient is the ratio of the actual to theoretical sublimation rates. Experimental values vary significantly between different investigators (9,10,11). Many theories have been proposed to explain this phenomenon (9,12,13,14). Burrows attributed the cause to the molecular collision (12). Littlewood and Rideal blamed the discrepancies on the inaccurate thermal measurements (14). Some even went so far to suspect the irregularity of crystal surface as the main cause (11). Since the evaporation coefficient has a very important bearing on the design of sublimation devices, the theory of evaporation coefficient and a numerical calculation technique are discussed in the second half of Chapter 3.

2.4.2. Molecular flow

Sublimation usually takes place only at such a low pressures; consequently the vapor molecules have a mean free path comparable or even greater than the characteristic channel dimension. The impedance to the molecular flow through a channel is very important for proper determination of the evaporation coefficient from experimental data (15) as well as for the design analysis of a sublimation microthruster. This flow impedance effect is accounted for by dimensionless quantities such as the Clausing Factor (16), Transmission Probability (17) and in this work, the Non-obstruction Factor. These factors all represent the ratio of the outlet to inlet mass flow rates through a channel. Clausing (16), based on geometric consideration, predicted results for a very simple cylindrical case of collisionless gas in a adsorptive channel. DeMarcus (17) applied several advanced numerical techniques to solve Clausing's integral equation accurately and extended the results to include the effect of partial specular reflection of the channel. However, the integral equation approach is quite difficult to apply to a conical channel and to use in accounting for complicated processes such as molecular collision and sublimation surface reflection. A modified Monte Carlo technique was developed in this study and is reported in Chapters 3 and 5, to simulate the rarefied gas flow through both the cylindrical and the conical channels. Because of the directness of this approach, the method can

Include various gas-gas and gas-surface interactions as well as the effect of the angular distribution of the exit molecules on the net thrust.

FIG 2.1 RELATIVE MOTION OF SOLAR PROBE

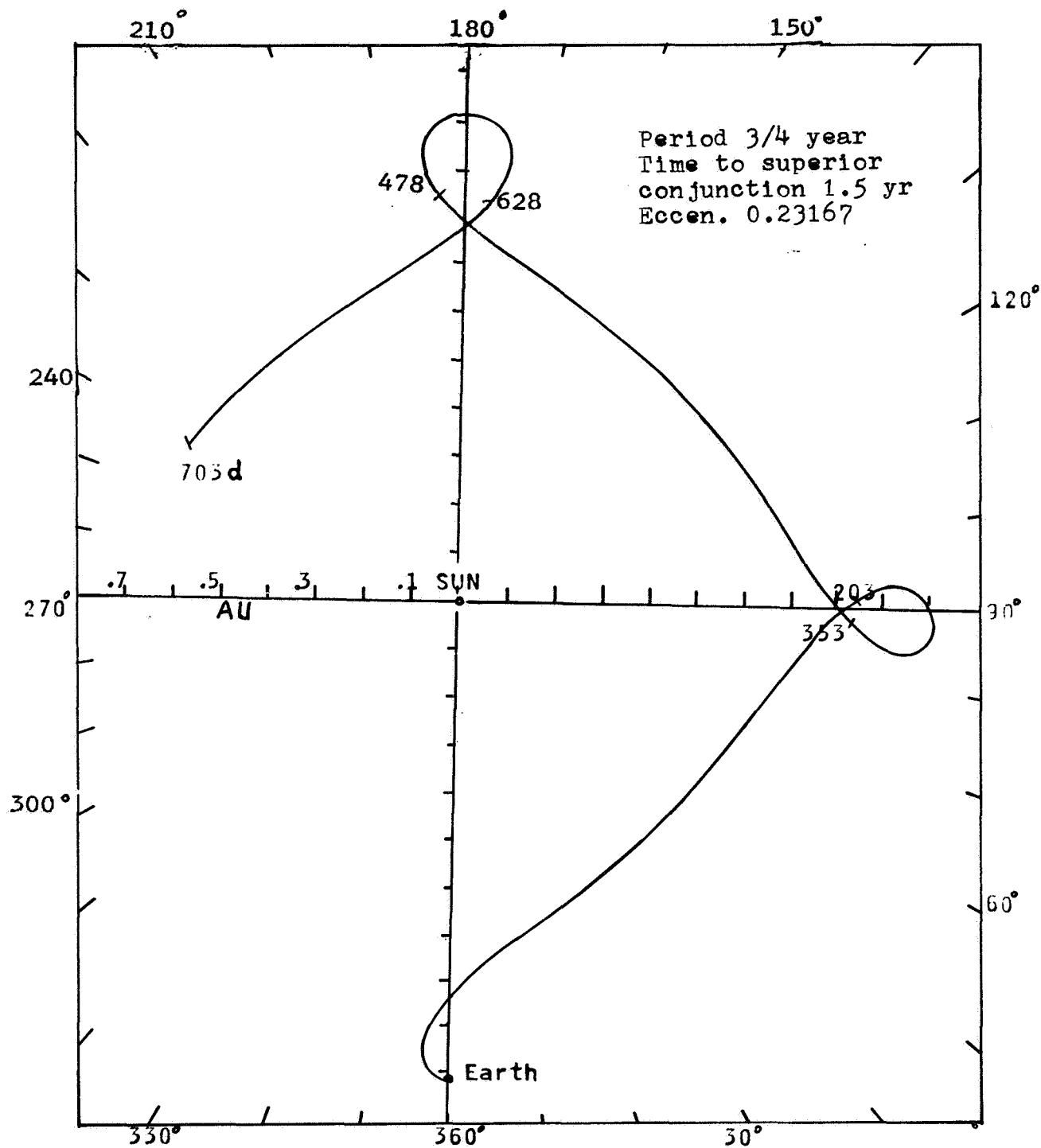


FIG 2.2 DIAGRAM OF TORQUES ON SPACECRAFT

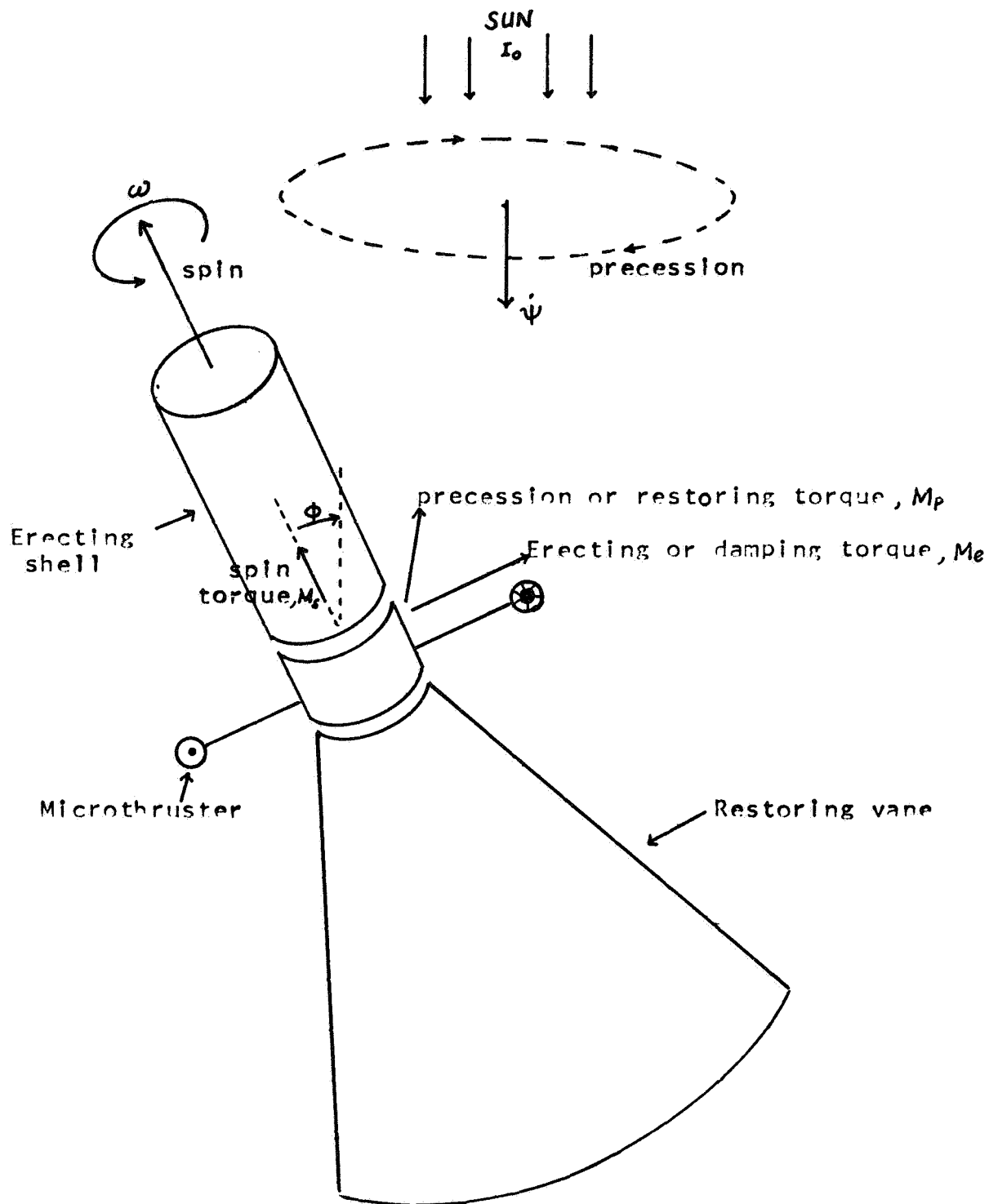
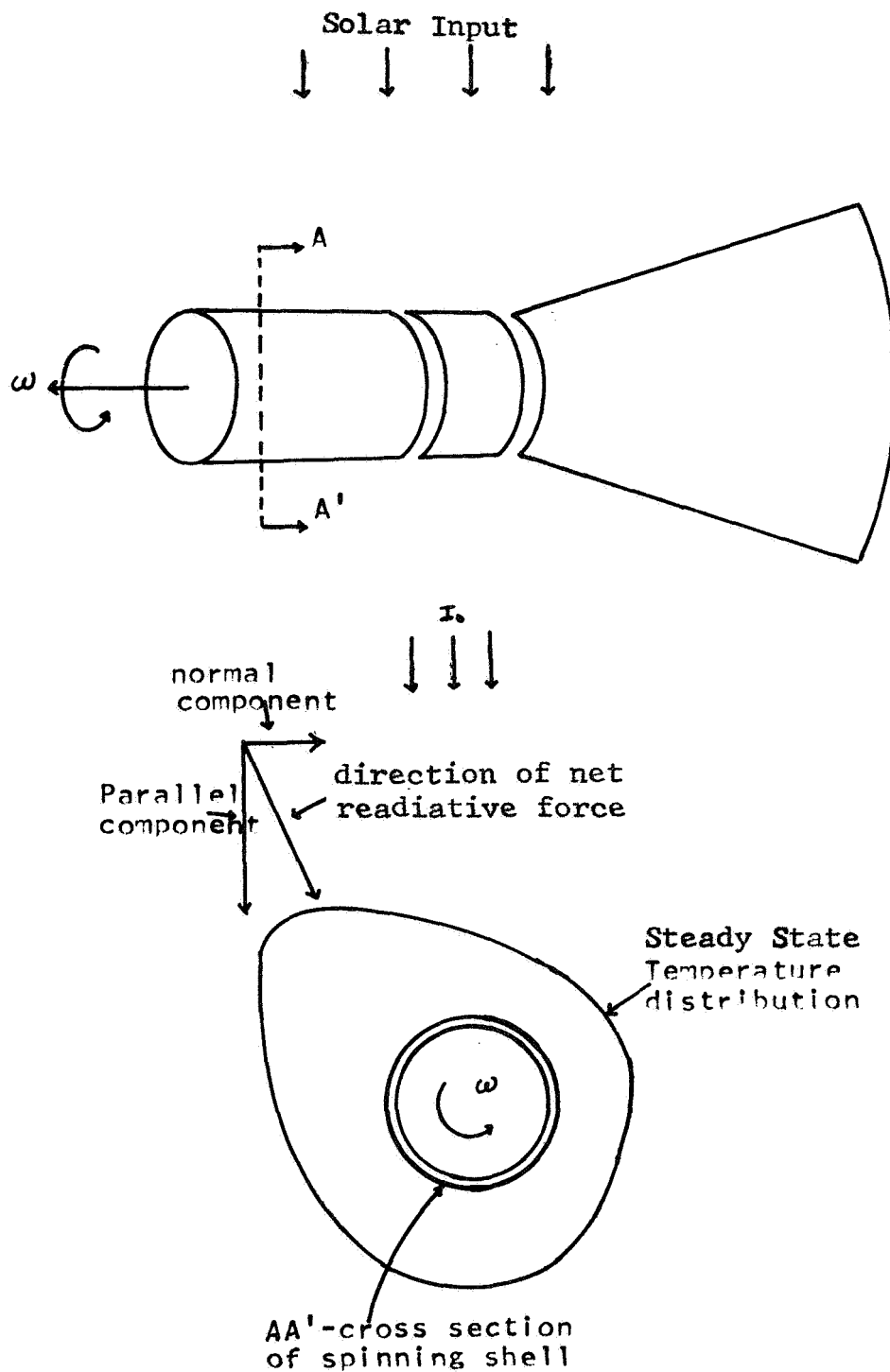


FIG 2.3 RERADIATIVE TORQUES
ON ERECTING SHELL



CHAPTER 3

SUBLIMATION AND RAREFIED GAS FLOW PARAMETERS

3.1 Introduction

The application of subliming materials is suggested in this study both as a means of improving the erecting capabilities of a spinning shell and as the fuel for a microthruster system for despinning and/or stabilizing small solar probes. In the microthruster the subliming material would vaporize in a cup and flow out of the cup to produce thrust. The net amount of material sublimed and its rate of flow from the cup are influenced (i.e., obstructed) by adsorption and reflection on the cup walls and on the surface of subliming material as well as by molecular collision between vaporized molecules. Furthermore the results of experiments conducted to determine the intrinsic rates of sublimation of various materials are also affected, to various degrees, by the same phenomena.

Consequently methods for predicting the effects of such "obstructing" phenomena are developed and discussed in this Chapter. These methods will be employed in evaluating available experimental data on sublimating rates and in the application of these evaluated experimental results to the design of the stabilizing devices discussed in this report.

3.2 Molecular Non-obstruction Factor (Modified Clausing Factor)

3.2.1 Introduction

The phenomena which affect the rate of flow of vaporized material out of a microthruster cup are: adsorption on the walls; specular and diffuse reflection from the walls and the surface of the subliming material at the bottom of the cup; and collisions between the vaporized molecules themselves. Since the quantities of interest are the rate of material actually leaving the cup and the resultant thrust, the effects of the phenomena mentioned will be evaluated in terms of "non-obstruction factors". The collective effect of the above physical phenomena on non-obstruction factors, will be referred to as the Molecular Non-obstruction Factor, by which the actual rate of vaporization from the surface of the subliming material can be multiplied to obtain the rate of flow from the exit of the microthruster cup, and as the Thrust Non-obstruction Factor (or Thrust Factor) which relates the actual thrust produced to the thrust of the molecules as they leave the subliming surface.

3.2.2 Vapor-wall collision effects

In a free molecular flow regime, the mean free path of the gas molecule is so large that intermolecular collision can be neglected. The rate of flow through a tube is limited by collision of molecules with the wall alone. The

manner of attacking this problem of flow was first suggested by Knudsen (19) whose method was to equate the rate of momentum transfer to the tube wall by molecular impacts to the difference in the pressure forces at the ends. Due to his erroneous assumption of the Maxwellian distribution for molecules in the channel in calculating the momentum, the free molecular flow equation is valid only for long tubes (proven mathematically by DeMarcus (17)). For short tubes, the end effect becomes dominant. Dushman's formula (18) takes this into account by adding the flow resistance through an orifice to Knudsen's long-tube flow formula (19), analogous to the electric resistance in series. The resultant formula is simple, but it is only approximately correct because flow resistance does not behave exactly as the electrical resistance.

Realizing the geometric nature of molecular flow, Clausing (16) derived a linear integral equation to express the surface collision density function for a cylindrical tube,

$$\psi(x) = \psi_1(x) + \int_0^L K(y, x) \psi(y) dy \quad (3.1)$$

where the quantity $\psi(x)dx$ is the total surface collision density on the wall between length x and $x+dx$ in unit of radius. $\psi_1(x)dx$ is the contribution due to particles coming directly (experiencing no previous surface collision) from the inlet and y is the dummy variable. The kernel $K(y, x)$ is the probability of particles exchange between two

differential surface areas on the wall of the tube (similar to the view factor in thermal radiation calculations). The desired normalized particle transport rate J is (17)

$$J = J_s + \int_0^L \psi(x) P(x, L) dx \quad (3.2)$$

$$J_s = (\pi/2) \left[x^2 / (x^2 + 4)^{1/2} + (x^2 + 4)^{1/2} / \pi - 2x \right] \quad (3.3)$$

The kernel $P(x, L)$ is the probability that a molecule which collides with the wall between x and $x+dx$ will leave the tube via the exit at $x=L$ without further surface collisions.

For ease of obtaining an analytical expression for $K(y, x)$ and $P(x, L)$, Clausing assumed perfect surface adsorption (i.e., no specular reflection) and infinite mean free path. The quantity J_s is the fraction of molecules streaming through the flow channel directly without suffering any surface collisions at all. Clausing obtained accurate tabulated results (16), commonly known as Clausing factors, as a function of the length to radius ratio without the help of modern computing facilities by using asymptotic power series expansions. The Clausing factor is defined as the ratio of the rate at which gas leaves the outlet of a tube to that at which gas enters the inlet, in the absence of specular reflection.

In 1955, DeMarcus (17) investigated the molecular flow problem rigorously by starting mathematical formulation from the Boltzman equation. Although he obtained essentially the same integral equation, he used different numerical approaches ('squeezing', 'scissoring' and variational

techniques) to solve this equation. According to DeMarcus, the variational result gives the upper limit for the flow conductance. He compared his results with Clausing's for the case of no specular reflection and concluded that the tabulated Clausing Factors are slightly in error because the Clausing Factors are in general somewhat higher than those of DeMarcus, especially for long tubes.

The main drawback of the integral equation method is that the formulation of the probability kernels becomes increasingly difficult for non-uniform cross-section channels and/or for molecular flow systems with finite mean free paths. The method to be discussed adopts the Monte Carlo type of approach where the actual physical processes are simulated in detail in the form of algorithm for digital computer calculation.

3.2.3 Description of numerical approach (TUBNOF)

The general description of the method proposed for use in this study follows. For a channel of arbitrary cross-section and length, as shown in Figure 3.1, the inlet is connected to a flat subliming material surface and the outlet is connected to a vacuum. (If the back-pressure is not zero, the problem can be divided into two parts and superposition applied to get the net transport.) The inlet gas is assumed to be Maxwellian and the inlet area is divided into many small pieces, each of which is considered as a point source. Knowing the angular probability

distribution (spherical cosine) for molecules leaving from a point source, the probability distribution function can be divided into differential cones as shown schematically in Figure 3.2. The fate of the particles contained in the cone (Where do they hit the wall? How many? Are they adsorbed or reflected?) is determined by the space curve of the intersection of the cone surface with the channel surface and the averaged surface reflection coefficient. The channel is divided into ring segments so that number of particles impinging on each ring segment can be calculated from the fraction of space curve intersected by each ring segment. The surface adsorption density due to only the undisturbed inlet particles as a function of down-stream distance can be obtained by summing up the contributions of all the differential cones from a point source and then all the point sources in the inlet cross-sectional area. At steady state, the rate of adsorption will balance out the rate of reemission. Assuming a known angular distribution (spherical cosine at the same temperature as the subliming surface), the probability for an adsorbed particle at $x+dx$ distance downstream to get out of the exit can be computed by keeping track of this particle until it either leaves the channel or is adsorbed by the channel wall. Doing the same for all ring segments, an 'escape' probability table is constructed which is equivalent to the Clausing's $P(x,L)$ kernel. With the surface adsorption density and the 'escape' probability table so computed, the molecular

non-obstruction factor (also referred as Clausing factor or transmission probability) is obtained by numerical integration over the length of the channel. The computer program (TUBNOF) listing with brief description is included in Appendices K.1 and P.8. The applications of this computer code to account for various molecular behaviors in the flow channel are given below.

3.2.4 Calculations of wall adsorption effect

The power of the method developed here lies in its flexibility. The method can be employed in the consideration of realistic physical phenomenon such as incident energy and angle dependences of gas-surface interaction cross sections as well as to solve for the flow in complex geometric channels, in addition to a few special cases of interest in the present study. To test the validity of the method, the first step was to check results computed by TUBNOF against those of Clausing and DeMarcus for the case of cylindrical channel, perfectly adsorptive surface, and infinite molecular mean free path. The tabulated results are given in Table 5.1. The agreement with Clausing's and DeMarcus's results is within 1%. Consequently, the method is believed to be sound. TUBNOF is capable of much higher accuracy than this, but a significant increase in computer execution time would be necessary.

3.2.5 Calculations of channel-wall reflection effect

The general theory for gas-surface interaction is still not well defined. However, drawing analogy from neutron albedo data and from some recent gas-surface experiments (20), the reflection (specular and diffuse) coefficient for sublimed molecules should be a function of incident energy and angle as well as surface properties and temperature. The effect of finite reflection on molecular flow is to increase the non-obstruction factor, i.e., to reduce the flow resistance. By using a weighted average specular reflection coefficient, the computer program TUBNOF can allow for the specular reflection effect such that whenever a beam-bundle (a group of molecules heading in a direction of $\phi+d\phi$ and $\theta+d\theta$ from a point source) hits the wall, the fraction that is reflected specularly will be traced continuously until its intensity becomes negligible due to multiple specular reflections or it leaves the channel. For a given channel length, the non-obstruction factor, K_m , increases almost linearly with specular reflection coefficient, r , as shown in Figure 3.3.

A good linear analytical fit to the TUBNOF curve of Figure 3.3 for a slightly reflective channel wall is

$$K_m(L/R) = K(L/R)(1.0-r) + r \quad (3.4)$$

where $K(L/R)$ is the non-obstruction factor for $r=0$ (i.e., $K(L/R)$ =the Clausing Factor)

The result agrees very well with that of DeMarcus as shown in Table 3.2, which suggests that Smoluchowski's correction (46)

$$K_S(L/R) = K(L/R) * (1.0 + r) / (1.0 - r) \quad (3.5)$$

is not applicable for general use as shown in Figure 3.4. In fact, Smoluchowski's correction factor for specular reflection is only approximately correct for very long tubes and for very small specular reflection coefficients.

3.2.6 Calculations of subliming surface reflection effect

For the case where the inlet molecular source is an equilibrium gas reservoir, the molecules heading back toward the source from the channel will be absorbed in the reservoir, i.e., the source appears to be black to any molecules returning from reemission or molecular collision. However, when the source is a solid subliming surface at the channel inlet, the solid subliming surface will reflect a fraction $(1-\alpha)$ of the returning molecules, where α is the evaporation or condensation coefficient (9). For a collisionless molecular flow, the fraction returning to the surface is $1-K$. Of this fraction $1-\alpha$ will be reflected back into the channel with a probability of leaving the channel through the exit of K . This effect will be compounded and if the sum of the resulting infinite series is considered, the sublimation surface reflection should increase the non-obstruction to

$$K^0 = K / (1 - (1 - K)(1 - \alpha)) \quad (3.6)$$

where K^0 is the approximate non-obstruction factor including the source reflection effect. Consequently, this surface reflection effect increases with flow channel length (since K decreases with length) and should be taken into account in the calculation non-obstruction factors.

TUBNOF therefore includes this effect. The $(1 - \alpha)$ fraction of the returning molecules is assumed specularly reflected from the subliming surface with an angular direction and intensity which are computed after each reflection. The fate of this molecular beam is accounted properly so that no particles will be tallied more than once. The result of a sample calculation is shown in Figure 3.5. The results of Equation (3.6) agree well with the 'exact' computer result.

Through the use of two experiments, it may be possible to determine if finite specular reflection of vapor molecules from the subliming materials leads to non-unity evaporation coefficients and to determine the magnitude of the evaporation coefficient. The experimental technique proposed follows. A large equilibrium reservoir with its internal surface coated with subliming material, with a tube penetrating the reservoir wall, is used to measure the mass flow rate and the non-obstruction factor K_1 . Then the same tube is connected to a subliming surface at the same temperature as the reservoir and the flow channel length is maintained constant so that a new non-obstruction factor K_2

can be measured. By using the ratio K_2/K_1 , a large portion of the experimental uncertainty should cancel. The evaporation coefficient can be obtained from the curve in Figure 3.6 which was calculated using TUBNOF or from the approximate expression (derived from Equation (3.6))

$$\alpha = 1 + (K_1/K_2 - 1)/(1 - K_1) \quad (3.7)$$

which is almost linear as shown in Figure 3.6.

3.2.7 Calculations of molecular collision effect

In the previous sections, molecules are assumed to interact with the surface only, since the mean free path is much larger than the characteristic dimension of the flow channel. This condition does not exist in the present study because the sublimation vapor pressure in the temperature range of interest (in the neighborhood of 280°K) has a mean free path comparable with the channel dimension. Burrows made an estimate of the intermolecular collision effect which surprisingly was very significant. Burrows in his paper (12) tried to attribute the cause of the existence of evaporation coefficient to the molecular collision. It should be noted that Burrows' evaporation coefficient

$$\alpha = K \left\{ \frac{a^2}{\ell^2 + a^2} \left[e^{-\frac{\ell+a}{\lambda}} + \frac{a}{a + (\ell^2 + a^2)^{1/2}} (1 - e^{-\frac{\ell+a}{\lambda}}) \right] + \frac{\ell^2}{\ell^2 + a^2} \left[e^{-\frac{2a}{\lambda_E}} + \frac{2}{3} (1 - e^{-\frac{2a}{\lambda_E}}) \right] \right\} \quad (3.8)$$

where

K--tube Clausing factor

a--tube radius

l--tube length

λ_e --equilibrium vapor mean free path

λ --effective mean free path

is different from the the conventional evaporation coefficient by just the Clausing factor. In other words, the quantity in the square bracket which accounts for the molecular collision effect is Burrows' estimate of the conventional evaporation coefficient. Burrows' explanation appears inconclusive based on the experimental results of Sherwood and Johannes (10) whose sophisticated experimental setup should minimize the molecular collision effect. Nevertheless, the effect of molecular collision should not be ignored.

A numerical scheme was developed to estimate the molecular collision effect so that the evaporation coefficient can be evaluated from the experimental data. The first step is to calculate the molecular density and flux (track length density) as a function of radial and axial distances (see Appendix G for detailed description). Only the contributions from the subliming source and diffuse reflection from the wall surfaces are considered. For the cases of interest in this study, the effects of specular reflection and molecular collision on density and flux are small and are therefore neglected for the sake of simplicity. Due to the lack of knowledge on the dynamics of molecular collision, the direction of motion after a collision is assumed random. One further assumption is

required for the molecular interaction cross section which is related to the effective diameter of sublimed molecule. Many well-known techniques (18,26,31,46) of extracting molecular size from viscosity, critical temperature and pressure and diffusion coefficient measurements are available in the literature. Additionally, different assumed molecular force fields will also yield different expressions for the molecular diameter. Since the viscosity data is most readily available, it is used as a basis for molecular cross section calculation. The effect of molecular collision on the gas flow is computed in the following manner.

The collision density as a function of radial and axial distances is calculated from the result of density, flux and molecular cross sections. The solid angles subtended at each differential volume by the inlet and exit determine the fractions of the collided molecules in the channel heading back and streaming out respectively. However, in the process of heading back or streaming out, the probability of further collisions is governed by an exponential function $\exp(-S/\lambda)$, where S is the distance travelled in a particular direction and λ is the average mean free path in this direction. The concept here is analogous to the neutron diffusion calculation in a source free medium. Since a fraction of the molecules collided was originally streaming toward the exit, the net effect is the difference between the fraction heading outward before and after collisions in

each differential volume. The molecular density at each position is computed, but the angular distribution is not known; in particular, the fraction of the molecules heading out is not readily obtained. This fraction is assumed in the coding of TUBNOF to increase linearly with axial distance and is constant in radial direction. The rest of the molecules after collision are adsorbed by the channel wall in a ratio proportional to the solid angles subtended at the collision point by each of the channel ring segments. The calculated result for the molecular collision effect are shown in Figure 3.7. Evidently, the molecular collision greatly increases the flow impedance.

Also, since the molecular collision density is proportional to the square of particle density, at low sublimation temperature or at low vapor pressure the collision effect should be negligible. The computed result is shown in Figure 3.8.

In passing it should be pointed out that Burrows' expression, Equation (3.7) probably overestimates the molecular collision effect, because based on Rossmann and Yarwood's experimental data (12), Burrows' corrected evaporation coefficients for mercury in many cases were greater than unity (which is not realistic).

3.3 Evaporation Coefficient Theory

3.3.1 Introduction

In principle, all material will sublime from a solid phase to a gaseous phase bypassing liquefaction, if the transition occurs below the triple point. The theoretical derivation of the expression for sublimation rate was developed by Hertz, Knudsen, and Langmuir (19). The ratio of the experimental to theoretical sublimation rate is commonly known as the evaporation coefficient. The evaporation coefficient, which is involved directly in calculating the heat and mass transfer rates for the subliming microthruster and erecting shell discussed in this study, is therefore an experimental correction factor for the Hertz-Kundsen-Langmuir equation (19).

Since the experimental subliming rate is always less than or equal to the theoretical rate (9), many scientists had attempted to give a satisfactory explanation. One explanation has been that the theory is in error by assuming that all collisions with a surface result in condensation (the theory assumes that the rates of sublimation and condensation in a system at equilibrium are equal and that the rate of condensation can be equated to the rate of collision on the surface calculated from the known vapor properties). There is also the probability of experimental errors. Littlewood and Rideal (14) went so far to claim that evaporation coefficient should be unity if the thermal

measurement is performed properly. Burrows (12) implied in his paper that material really sublimed at the theoretical rate, while in actual experiments molecular collisions caused the reduction in the subliming rate. Their assertions can not be supported by the recent experimental evidences of Paul and Lyon (15) as well as Sherwood and Jonannes (10) whose experiments minimized the molecular collision effect and the temperature measurement error. The concept of equating the evaporation coefficient to the condensation coefficient has been rejected in the past. However, Paul and Lyon's recoil pressure experiment gave a favorable support of this concept because the result (based on Miescher's (9) derivation) agreed well with that of mass flow. However, it appears that Miescher's derivation requires further refinement which is given in the following section.

3.3.2 Evaporation dependence on reflection

The detailed theory of gas surface interaction is still not well understood. However, the interactions of vapor molecules and their parent solid generally consist of diffuse and specular reflections and condensation. The condensation process can be understood as a delayed reemission because molecules condensed will evaporate diffusely at a later time and this process is different from the prompt diffuse reflection which accompanies the specular reflection. In experiment, the prompt diffuse reflection

and delayed reemission are difficult to separate. However, in the following derivation of the mathematical dependence of evaporation coefficients on the reflection (diffuse and specular) coefficients, the reflection coefficients as functions of surface temperature, incident angle and speed are assumed known. Also the vapor and solid are assumed to be at thermal equilibrium so that surface cooling or surface heating effects are avoided. Let the total reflection coefficient of the vapor molecules on the subliming solid be

$$r(\theta, v, T) = \delta(\theta, v, T) + s(\theta, v, T) \quad (3.9)$$

where $\delta(\theta, v, T)$ is the diffuse reflection
 $s(\theta, v, T)$ is the specular reflection
 θ is the incident angle
 v is the incident speed
 T is the surface temperature

The fraction of the molecules which do not reflect are assumed condensed and is given by $1-r(\theta, v, T)$. Since at kinetic equilibrium, the fraction condensed would be exactly equal to the fraction evaporated, the total number of the molecules evaporated from a unit surface exposed to vacuum is given by the integral

$$G = m \int_{\theta=0}^{\pi/2} d\theta \int_{v=0}^{\infty} dv [1 - r(\theta, v, T)] f(\theta, v) \quad (3.10)$$

where $f(\theta, v)dv d\theta = 1/2 \cdot v dn_v \sin\theta \cos\theta d\theta$ is the number of molecules per unit time leaving a unit surface with speed v and making angle with the normal between θ and $d\theta$. For Maxwellian distribution, the number of molecules per unit volume with speed between v and $v+dv$, dn_v is

$$dn_v = \frac{4n}{\pi^{3/2}} (2kT/m)^{-3/2} v^2 \text{EXP}(-mv^2/2kT) dv \quad (3.11)$$

The theoretical mass evaporation rate or the Hertz-Knudsen-Langmuir equation is

$$\begin{aligned} G_m &= m \int_0^{\pi/2} d\theta \int_0^{\infty} dv f(\theta, v) \\ &= P_v / (2\pi RT)^{1/2} \\ &= 0.0583 P_v (M/T)^{1/2} \end{aligned} \quad (3.12)$$

where n is molecular density
 m is the molecular mass
 \bar{v} is average speed
 P_v is vapor pressure in mm of Hg
 M is molecular weight
 T is vapor temperature in °K
 R is gas constant per unit mass

The evaporation coefficient α is then

$$\begin{aligned} \alpha &= \frac{G}{G_m} = \frac{\int_0^{\pi/2} d\theta \int_0^{\infty} dv [1 - r(\theta, v, T)] f(\theta, v)}{\int_0^{\pi/2} d\theta \int_0^{\infty} f(\theta, v) dv} \\ &= 1 - \overline{r(\theta, v, T)} \end{aligned} \quad (3.13)$$

In special case, when diffuse reflection is zero, the evaporation coefficient is just $1 - \overline{s(\theta, v, T)}$.

3.3.3 Ratio of recoil pressure to vapor pressure

At thermodynamical equilibrium, the vapor pressure (or the total force acting on the subliming surface) due to the gas-surface interactions, consists of four components.

$$P_v = P_e + P_d + P_s + P_c \quad (3.14)$$

where subscript v----vapor
e----evaporation
d----diffuse reflection
s----specular reflection
c----condensation

At equilibrium, the molecular condensation rate is equal to the evaporation rate, so P_e is equal to P_c .

However, in vacuum, no particles will return to the subliming surface (assuming molecular interaction is negligible); therefore the force acting on the surface is due to P_v alone. Under this circumstance, P_e is the recoil pressure which is a physical property of the subliming surface temperature and is independent of the equilibrium condition or the ambient pressure. The expression of P_e in terms of P_v is derived in Appendix E.

$$P_e = P_v \cdot \frac{\frac{P_v}{2G_m} - \overline{r(\theta, v, T) v \cos \theta}}{\frac{P_v}{G_m} + \frac{P_v}{2G_m} \cdot \overline{s(\theta, v, T) - r(\theta, v, T) v \cos \theta} + \overline{s(\theta, v, T) v \cos \theta}} \quad (3.15)$$

The barred quantities are the Maxwellian distribution weighted averages and G_m is the maximum mass flux as defined in Equation (3.12). If there is no diffuse reflection, the expression becomes,

$$P_e = \frac{1}{2} P_v - G_m \overline{s(\theta, v, T) v \cos \theta} \quad (3.16)$$

Furthermore, if the specular reflection is independent of incident angle and energy, the expression reduces to (using Equation (3.13))

$$P_e/P_v = \frac{1}{2} (1 - S(T)) = \alpha/2 \quad (3.17)$$

This is the expression on which Paul and Lyon (15) based in their recoil pressure experiment. The validity of their result is dependent upon the condition that the diffuse reflection is negligible and the specular reflection is independent of angle and energy. Consequently, the P_e/P_v ratio from Equation (3.15) is a function of surface

temperature, but, in general, is not a simple function of the evaporation coefficient as given by Equation (3.17).

3.4 Evaporation Coefficient Calculation Techniques

3.4.1 Introduction

Precise calculation of the evaporation coefficient from experimental data is a very difficult task. Experimentally, accurate subliming surface temperature measurement has plagued researchers for years. Paul, Lyon (15) and others (9) had developed ingenious surface temperature measurement techniques. However, in computing evaporation coefficient from mass-flow experimental data, they generally neglected the gas-gas and gas-surface interaction effects on the mass flow rate, which are quite significant as indicated in Section 3.2. In the following sections, two possible techniques for accurate calculation of evaporation coefficients from experimental data are discussed.

3.4.2 Extraction from mass-flow data

In mass-flow experiments such as described by Paul and Lyon (15), both the surface temperature and mass flow channel length are a function of time. These two time variables as well as the gas-surface interaction effect have to be taken into account properly before precise evaporation coefficients can be obtained. The experimental quantities available are the surface temperature and surface position as a function of time. The mass flow rate $G(t)$ is

$$G(t) = \rho \, dx/dt \quad (3.18)$$

and the evaporation coefficient $\alpha(t)$ is

$$\alpha(t) = \frac{G(t)}{G_m(t)} \frac{1}{K(t)} = \rho \frac{dx/dt}{G_m(t) K(t)} \quad (3.19)$$

Where ρ is the density
 dx/dt is the rate of surface regression
 $G_m(t)$ is the maximum mass flow rate
 $K(t)$ is the non-obstruction factor

The evaporation coefficient as a function of time and hence a function of temperature was calculated. Using Paul and Lyon's experimental data (apparent evaporation coefficient) for naphthalene, the results are shown in Figure 3.9 for four cases in which the experimental data (bottom curve) were corrected for: (1) wall adsorption effect only or exact Clausing factor correction; (2) wall adsorption and subliming surface reflection effect; (3) correction (2) plus finite wall reflection effect ($r=0.1$); and (4) correction (3) plus the molecular collision effect. Since the higher the non-obstruction factor, the lower the corrected evaporation coefficient, it is quite evident that Clausing factor correction (1) is not adequate to describe molecular flow accurately. The effects of the subliming surface and channel wall reflections increase the non-obstruction factor and hence decrease the corrected evaporation coefficient, as shown in Curves 2 and 3. The molecular collision effect as indicated by Curve 4 is responsible for further increase of the corrected evaporation coefficient. Even so the result is lower than

the experimental values of Sherwood and Johannes (10) which indicates there may be a residual underestimation of the molecular collision effect in the present study.

3.4.3 Extraction from recoil-pressure data

One of the objectives of Paul and Lyon (15) was to take advantage of the simple relation of Equation (3.17) to calculate evaporation coefficients.

In Section 3.3.3, the ratio of recoil pressure to vapor pressure was shown to be a complicated function of temperature as given in Equation (3.15). This ratio, in general, is not equal to the half of the evaporation coefficients as given by Equation (3.17). Consequently, the recoil pressure method described by Paul and Lyon could give erroneous results. Their recoil pressure results did show some discrepancies. It is tentatively concluded that the recoil pressure experiment is not suitable for extraction of evaporation coefficients for the present study. Nevertheless, their experimental technique is very useful for determination of the thrust non-obstruction factor which resembles the mass non-obstruction factor in many ways. The thrust non-obstruction factor will be discussed in some detail in Chapter 5.

FIG 3.1 SCHEMATIC OF MOLECULAR
FLOW CHANNEL

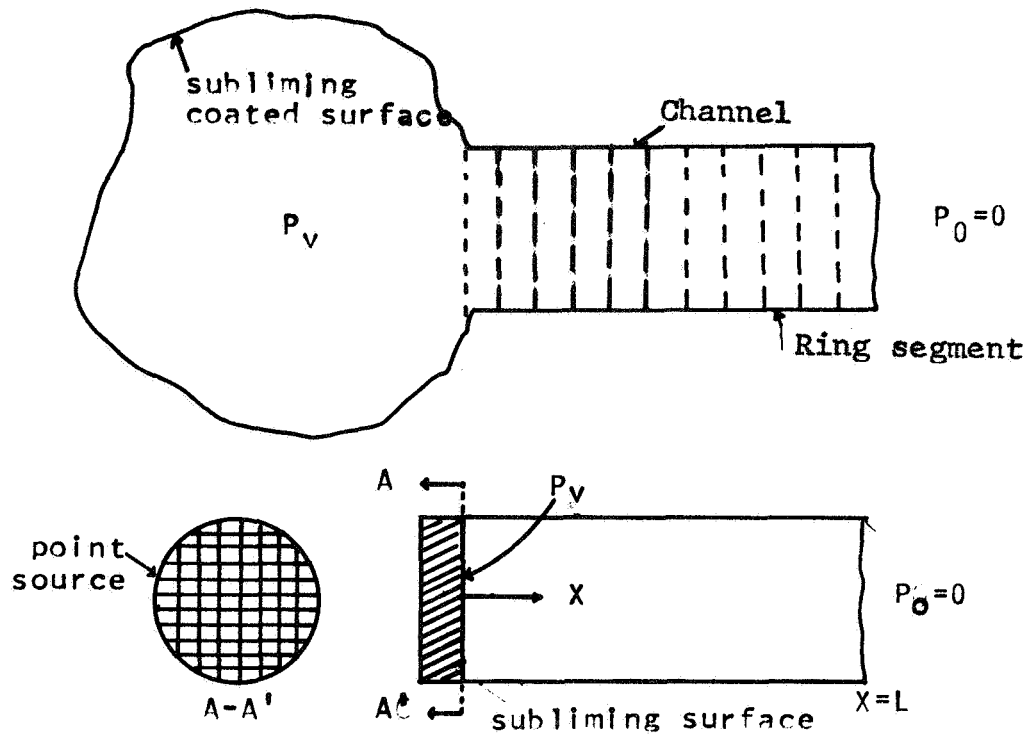


FIG 3.2 DISCRETIZATION OF SPHERICAL
COSINE DISTRIBUTION

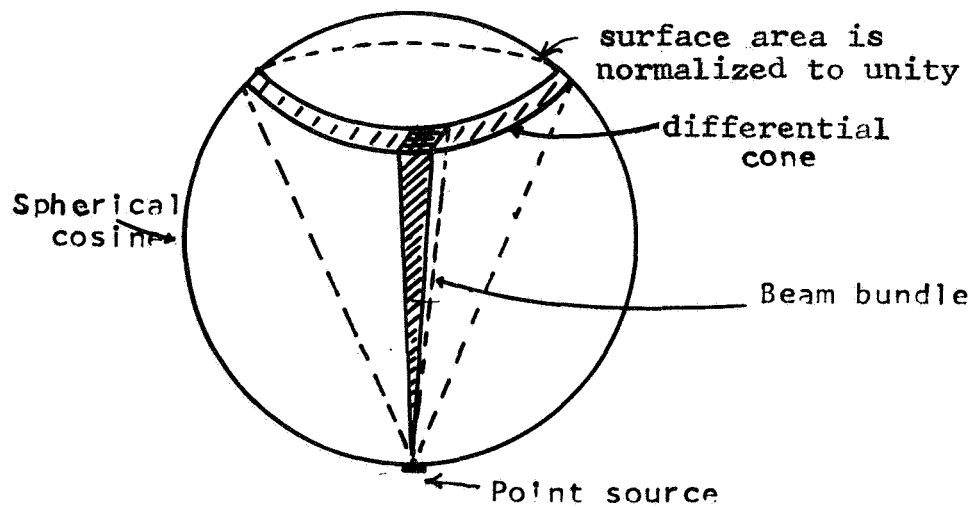


FIG 3.3 REFLECTION COEFFICIENT
EFFECT ON NON-OBSTRUCTION FACTOR

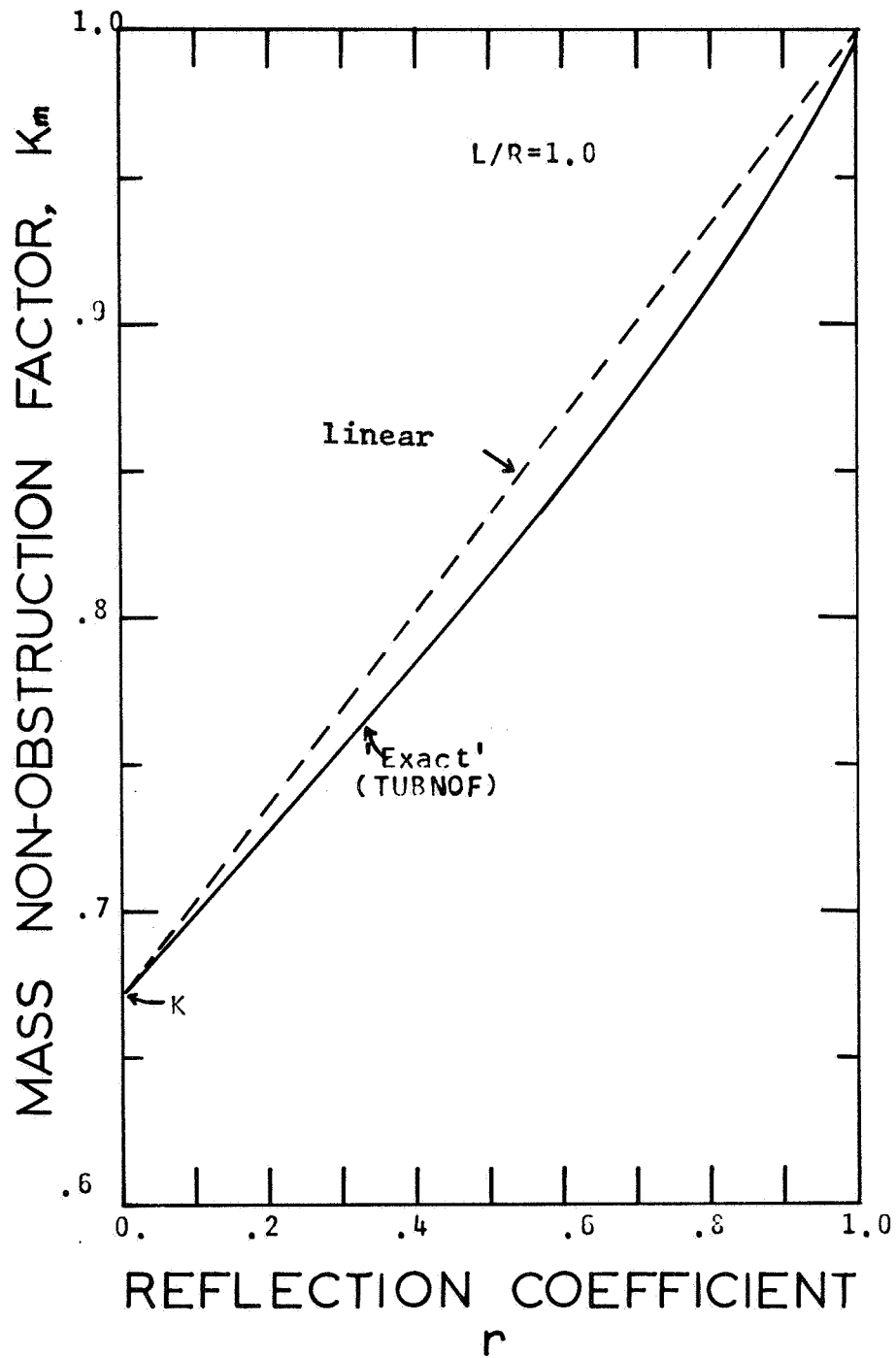


FIG 3.4 COMPARISON WITH SMOLUCHOWSKI'S
RESULT ON SPECULAR REFLECTION EFFECT

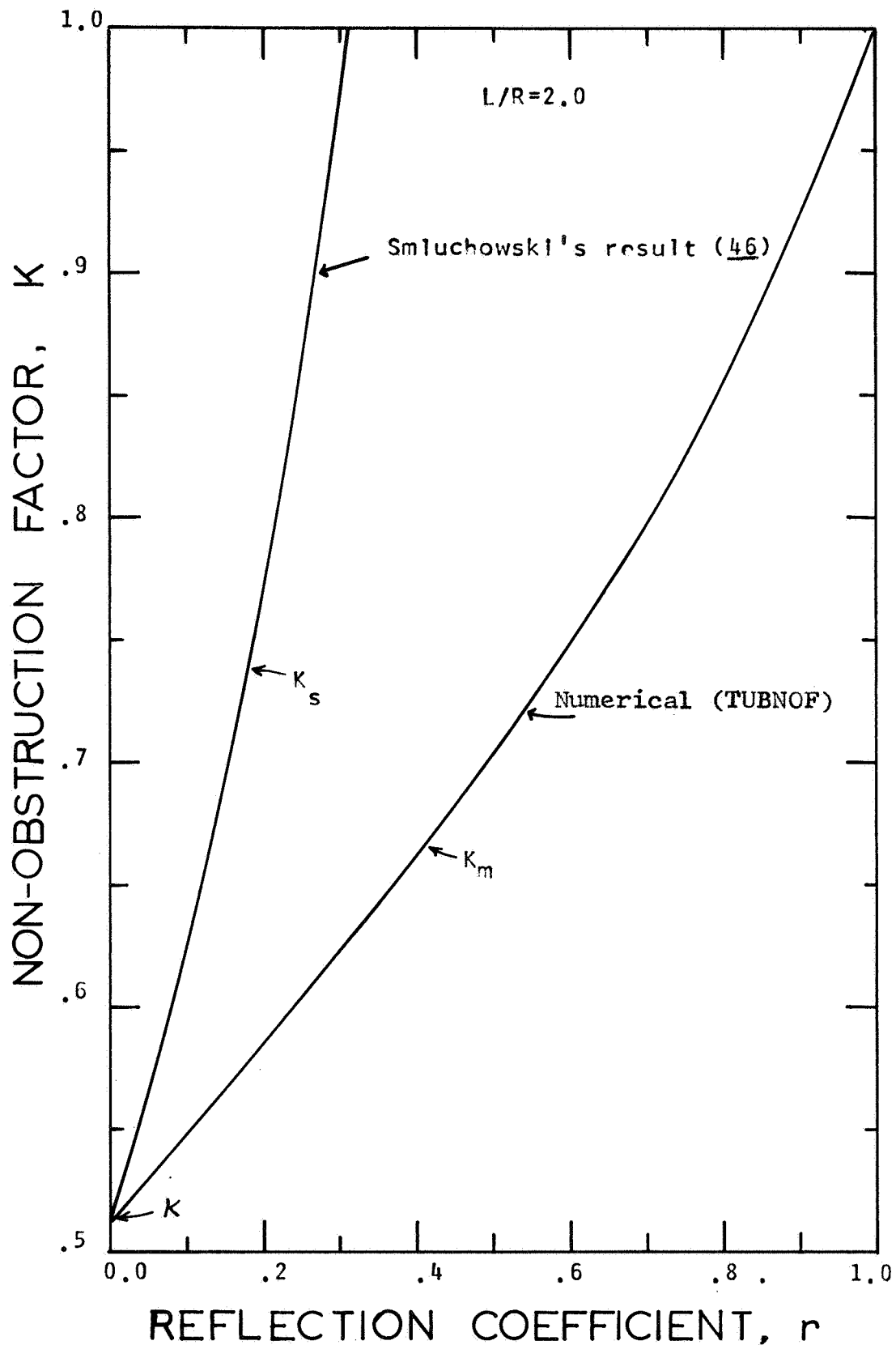


FIG 3.5 SUBLIMING SURFACE
REFLECTION EFFECT

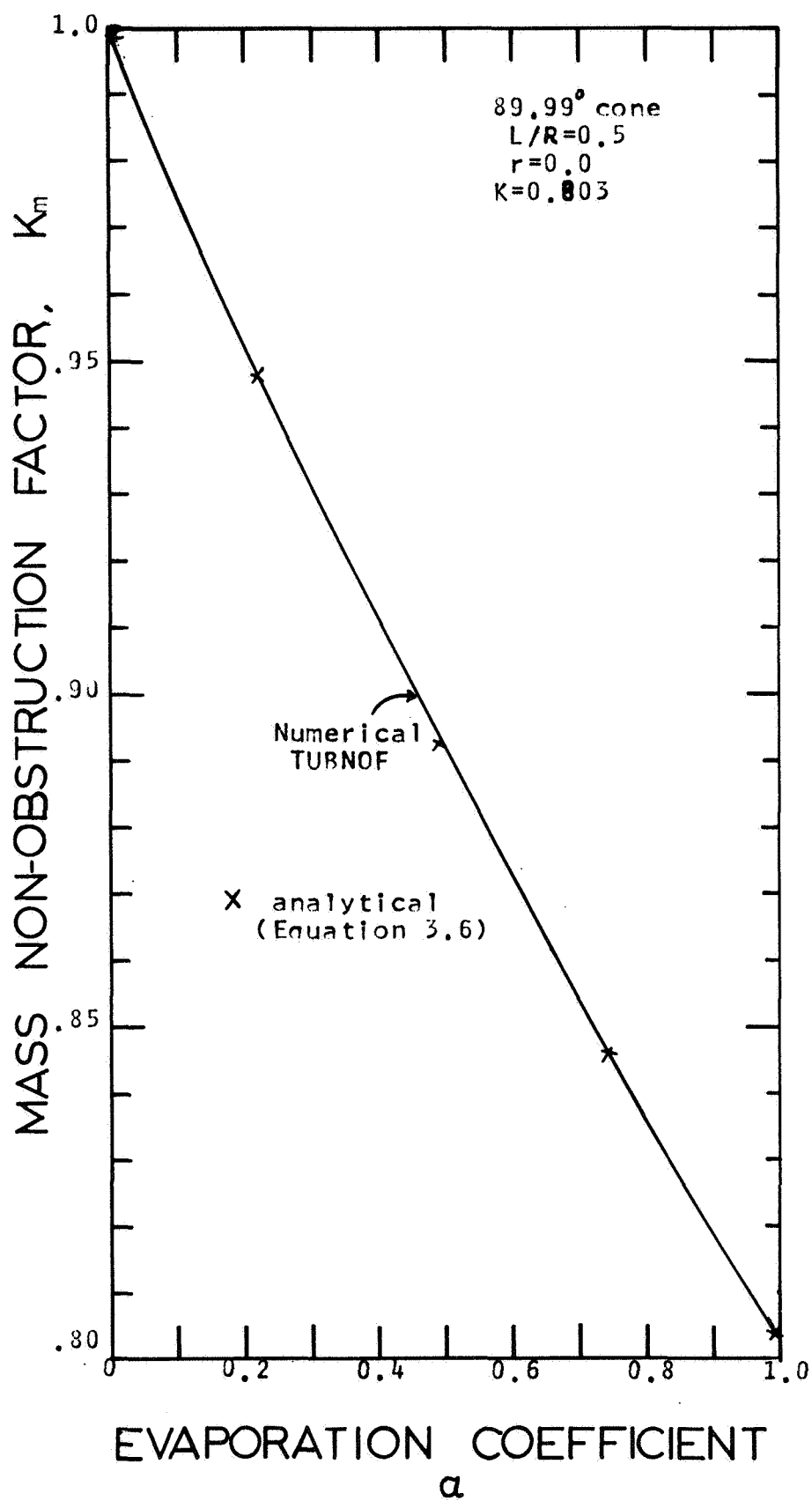


FIG 3.6 CURVE FOR INTERPOLATION
OF EVAPORATION COEFFICIENT

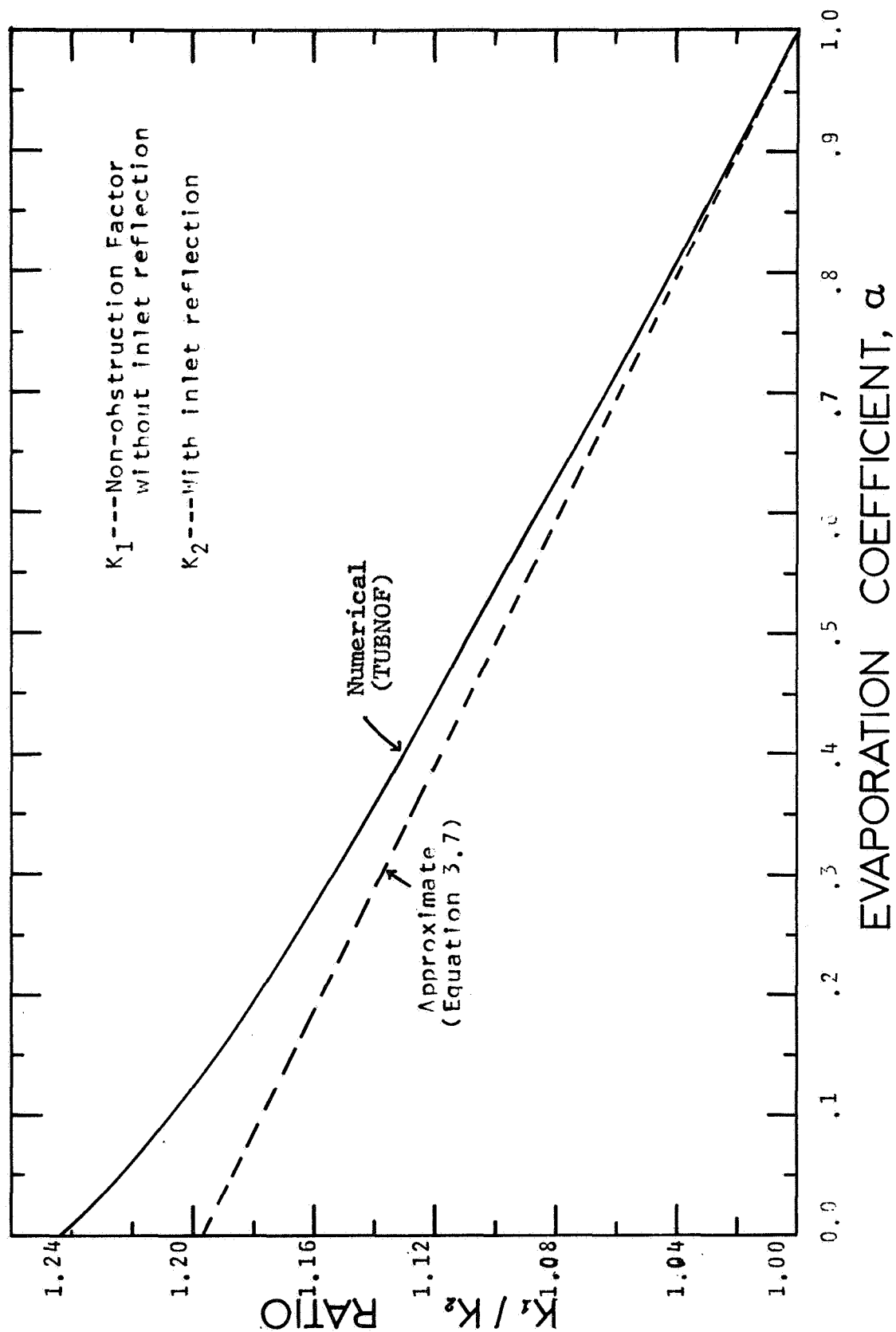


FIG 3.7 MOLECULAR COLLISION EFFECT
ON NON-OBSTRUCTION FACTOR

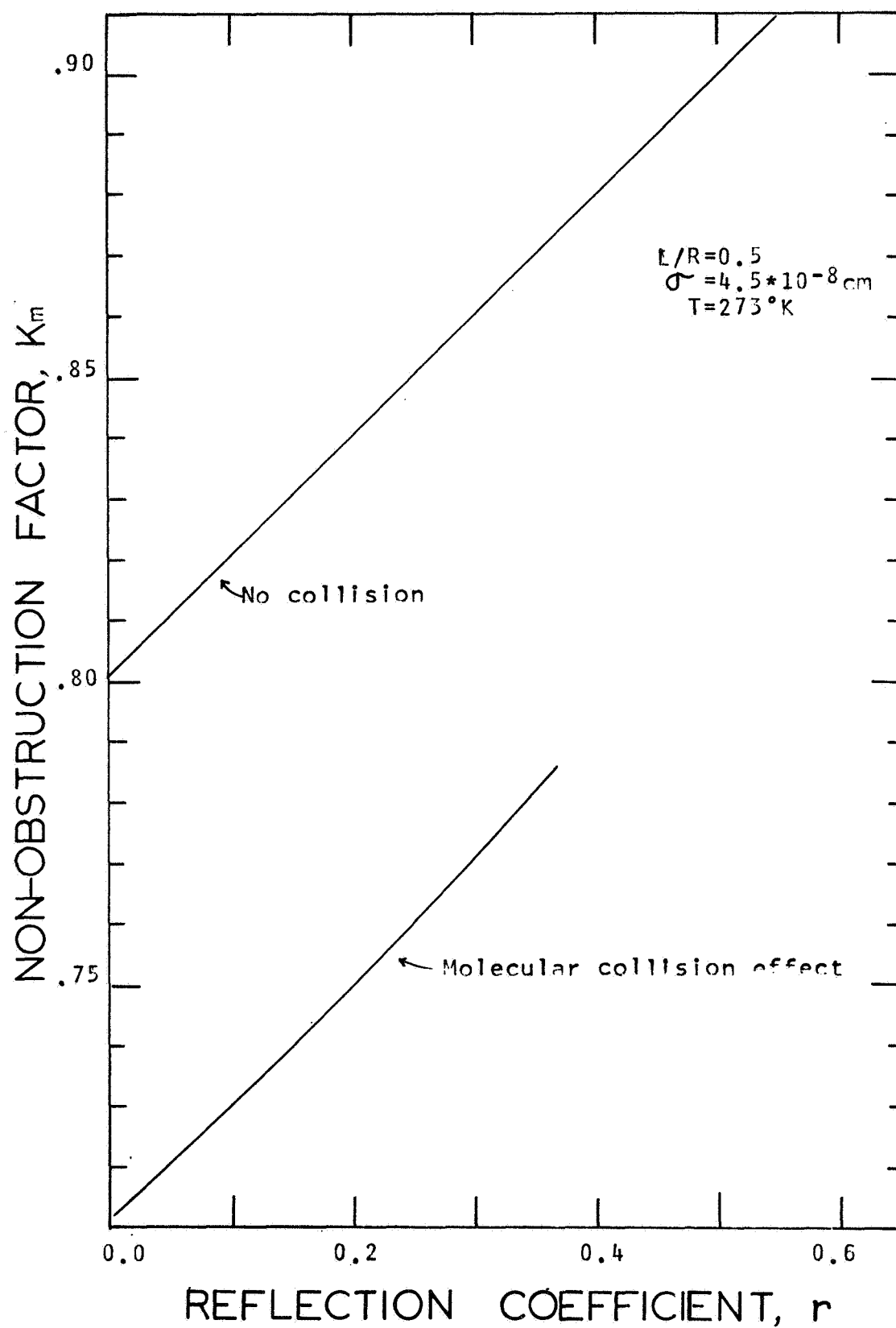


FIG 3.8 SUBLIMING TEMPERATURE EFFECT
ON MOLECULAR COLLISION

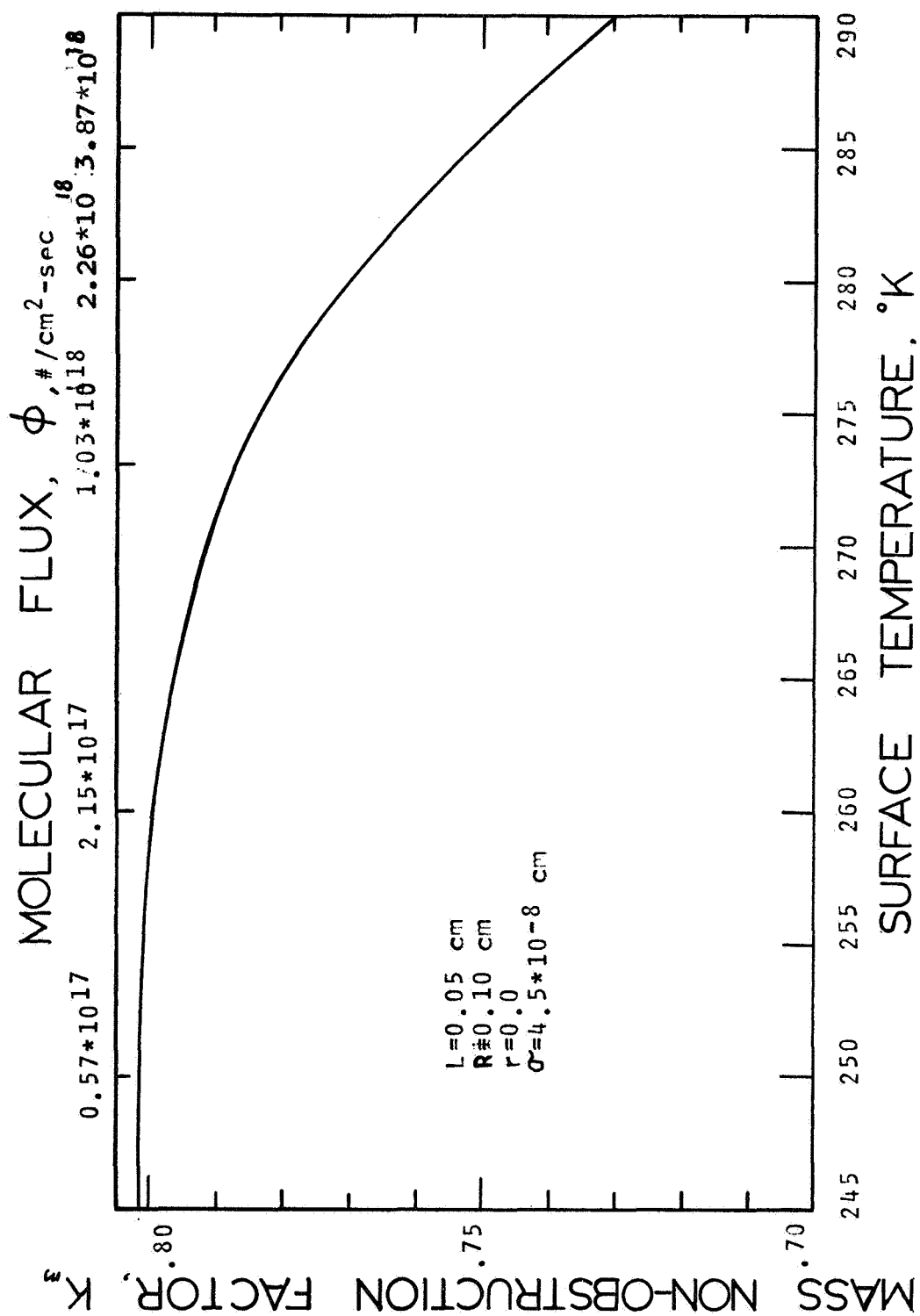


FIG 39

EXTRACTION OF EVAPORATION
COEFF FROM MASS FLOW DATA

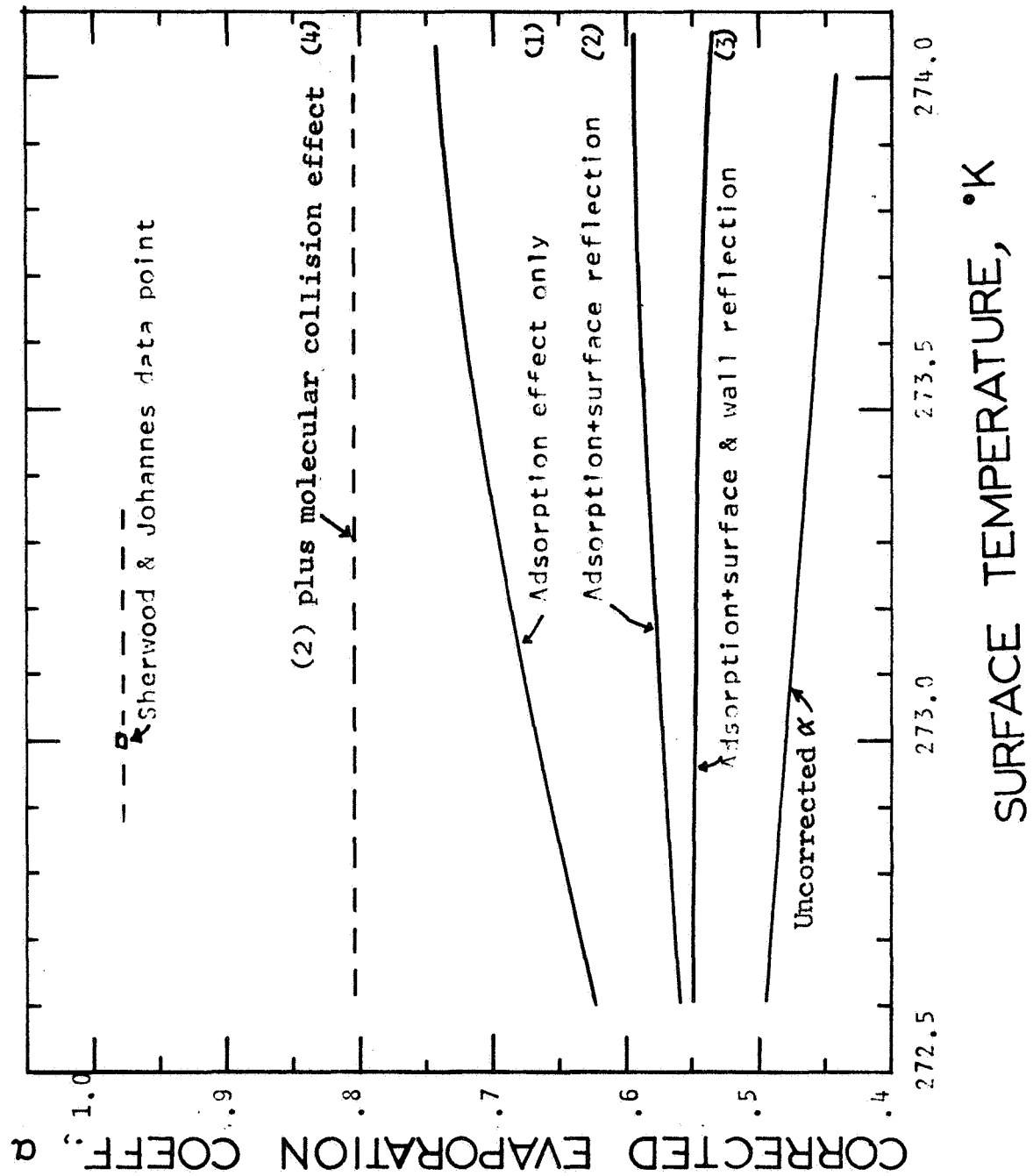


TABLE 3.1

NON-OBSTRUCTION FACTOR OF CYLINDRICAL TUBES
WITH REFLECTION COEFFICIENT EQUAL TO ZERO

L/R	K-M (THIS WORK)	K (CLAUSING)	Q (DEMARCUS)
0.5	0.80170	0.8013	0.80127
1.0	0.67192	0.6720	0.67198
1.5	0.58165	0.5810	0.58148
2.0	0.51486	0.5136	0.51423
3.0	0.41974	0.4205	0.42006
4.0	0.35619	0.3589	0.35658
5.0	0.31074	0.3146	0.31053
6.0	0.27823	0.2807	0.27547

TABLE 3.2

NON-OBSTRUCTION FACTOR OF CYLINDRICAL TUBES
WITH REFLECTING WALLS BUT NON-REFLECTING ENDS
FOR $L/R=2.0$

r	Q (DEMARCUS)	K-M (THIS WORK)
0.0	0.51423	0.51486
0.2	0.58247	0.58237
0.4	0.65890	0.65651
0.6	0.74690	0.74163
0.8	0.85412	0.84483
1.0	1.00000	1.00000

K -- SEE REF. (16)

Q -- SEE REF. (17)

TRANSIENT THERMAL ANALYSIS OF ERECTING SHELL

4.1 Introduction

The surface temperature of a cylindrical shell such as an erecting shell attached in front of a spinning solar probe will in general have a non-uniform temperature distribution around the shell. It is this asymmetric temperature distribution which gives rise to a net radiative and (or) subliming force to dissipate the precession kinetic energy. To analyse the temperature distribution as a function of time, a time dependent two dimension heat flow equation of the form (assuming constant material properties)

$$\frac{\partial^2 T}{\partial r^2} + \frac{1}{r} \frac{\partial T}{\partial r} + \frac{1}{r^2} \frac{\partial^2 T}{\partial \theta^2} = \frac{\rho c}{K} \frac{\partial T}{\partial t} \quad (4.1)$$

$$T(r, 0, t) = T(r, 2\pi, t); \quad \left. \frac{\partial T}{\partial r} \right|_{r=R+\Delta r} \neq 0$$

$$\left. \frac{\partial T}{\partial \theta} \right|_{\theta=0} = \left. \frac{\partial T}{\partial \theta} \right|_{\theta=2\pi}; \quad \left. \frac{\partial T}{\partial r} \right|_{r=R} = 0$$

has to be solved numerically because the boundary conditions resulted from the thermal radiation and sublimation are, in general, non-linear in T . The schematic diagram of an erecting shell is shown in Figure 4.1. In order to avoid numerical instability, an implicit difference formulation has to be used. Consequently the problem is reduced to solving a large matrix equation which is very time consuming. In the following sections various assumptions are made to simplify the partial differential equation,

under the condition that the results will not be seriously compromised. To facilitate comparisons, the calculations in the following sections are based on the input conditions of steady precession (no erecting torque) and uniform initial temperature. The order of development is: (1) completely neglected the heat conduction effects (Strip Approximation); (2) allowed for only the circumferential heat conduction effect (Thin Shell Approximation); (3) allowed for only the radial heat conduction effect (Thick Shell Approximation).

4.2 Strip Approximation Method

4.2.1 Description of strip model

The crudest approximation is that the cylindrical shell is so thin that the radial temperature gradient through the shell is negligible, and the shell is assumed to consist of strips with infinitesimal insulation gaps between strips so the circumferential (or tangential) heat conduction is also ignored. The above partial differential equation is simplified to a set of ordinary differential equations of the form

$$\rho c \frac{\partial T}{\partial t} = \frac{1}{\Delta r} \left[I_0 F(\theta_i, t) \cos \phi - \epsilon \sigma T_i^4 \right] \quad (4.2)$$

$$i=1, 2, 3, \dots, J$$

T_i and θ_i are the temperature and angular position for each strip. Therefore if the shell is divided into J strips, there will be J equations to be solved per time step. The $F(\theta_i, t)$ in the Equation (4.2) is the

half-rectified sinusoid characterizing the solar input to the shell as a function of time and angular position of the strip.

4.2.2 Bare thin shell system

To maximize the thermal reradiative effect, i.e., the erecting torque, one of the criteria is to make the shell as thin as possible so the solar input can give rise a maximum temperature change. In this thin shell design, the strip approximation should hold because the radial temperature gradient and the circumferential heat transfer would be small due to the thin shell thickness. A computer program (STRIP) is written to solve the entire set of Equation (4.2). The description and listing of STRIP are included in Appendices H.1 and P.1.

The angular temperature distribution gradually changes from its initial uniform shape to skew sinusoid which travels around the shell at the angular rate of the spin. The instantaneous maximum and minimum temperatures around the shell are shown in Figures 4.2 and 4.3 and the instantaneous maximum temperature difference, ΔT_m , which is the difference of the maximum and minimum temperatures is shown in Figure 4.4. Immediately after exposure to the solar radiation the amplitude of the temperature exhibits a damped oscillation character which reaches a steady state amplitude after a few spin cycles.

The initial temperature distributions all have the damped oscillation character which can be explained graphically by comparison of the steady state distribution with the initial distribution. A detailed explanation is given in Appendix C where three types of damped oscillation are analysed for three classes of initial condition. These are (1) the initial temperature T_0 is greater than the steady state maximum temperature; (2) T_0 is less than the steady state minimum temperature; (3) T_0 is in between the steady state maximum and minimum temperatures.

Another important quantity, which is plotted in Figure 4.5, is the angular phase lag of the instantaneous maximum temperature from the maximum solar intensity direction. As will become clear later, this phase lag is a major factor in determining the normal component of the reradiative force, and equivalently the erecting torque.

For fast spin such as the residual spin after the Yo-Yo despin operation (see Section 2.3.4), the transient behaviors will be noticeably different. The most outstanding feature is that the damped oscillation will persist for many spin cycles, but the total transient time span is increased only moderately. Also, if the initial temperature is too high above the equilibrium maximum, the damped oscillation behavior does not exist at all because the shell is always losing energy during the entire spin cycle. As a result, the damped oscillation will degenerate to a slanted stair shape which continuously decreases toward

an asymptotic value.

4.2.3 Optimum spin rate

Ideally, to realize the largest normal force component, the phase lag, ψ should be as close to $-\pi/2$ as possible and the maximum temperature difference, ΔT_m should be as large as possible. Unfortunately for a given configuration at zero spin, ΔT_m is maximum but ψ is zero; and for fast spin, ΔT_m approaches zero but ψ is close to $-\pi/2$. Consequently, there must be an optimum spin rate at which the resultant normal force is maximum. Trial-and-error solution would certainly give an answer, but it could be very time-consuming, especially without a prior knowledge of the optimum spin region.

For a reradiative erecting shell, an analytic expression for the optimum spin can be obtained by maximizing the following integral

$$F_N(\omega) = \int_0^{2\pi} [T(\omega, \theta)]^4 \cos \theta d\theta \quad (4.3)$$

where $T(\omega, \theta)$ is the temperature distribution shown in Figure 4.1.

The normal and parallel forces resulting from the transient temperature distribution of a bare thin shell of unit height are presented in Figures 4.6 and 4.7. The oscillations have damped out after about 300 seconds for the conditions given.

4.2.4 Radioisotope-heated thin shell system

Without the solar heat flux, the above thin shell will gradually reach a very low uniform temperature. The solar input not only heats up the shell but also creates an asymmetry of temperature distribution so that a net reradiative force will act on the shell to generate a torque. If the shell is internally heated to an elevated temperature, the superposition of the skew sinusoid (due to the solar input) on the elevated uniform temperature will increase the net reradiative force because of the higher energy of the reradiative photons.

Practically, all alpha energy can be absorbed by a very thin layer of material, therefore alpha-emitting radioisotopes are good internal heat sources. Po-210, Pu-238, Cm-242 and Cm-244 are some of the possible candidates because they give the low radiation hazard. To analyze this design proposal numerically, a radioisotopic heat flux which corresponds to the amount of radioisotope deposited per unit shell area is added to Equation (4.2). The results of the optimum spin rates and the maximum erecting forces (normal component of the net force) as functions of radioisotopic heat flux are shown in Figure 4.8. The addition of uniform heat flux favorably increases the optimum spin rate but unfortunately, the associated increase in the steady state erecting force is only about twenty percent as shown on Figure 4.8. (Note that the amount of isotope required varies with isotopes. For

Po-210, the typical isotope requirement using Table 5.1 for conversion is about a few mg/cm² of shell surface area.)

4.3 Thin Shell Approximation Method

4.3.1 Description of Thin Shell model

In the Strip Approximation method, both the radial and circumferential heat conductions are neglected. Since the circumferential heat conduction will tend to smooth out the asymmetric angular temperature distribution, the Strip Approximation may overestimate the maximum and minimum temperature and hence the performance, (i.e., the torque generated). To account for circumferential heat conduction, the governing differential equation becomes

$$\rho c \frac{\partial T}{\partial t} = k \frac{\partial^2 T}{R^2 \partial \theta^2} + \frac{1}{\Delta r} [I_0 F(\theta, t) \cos \phi - \epsilon \sigma T^4] \quad (4.4)$$

where ρ , c , k , ϵ , σ , I_0 , Δr , and R are the density, heat capacity, conductivity, emissivity, Boltzmann constant, solar constant, shell thickness and radius respectively. $F(\theta, t)$ is the half-rectified sinusoid which characterizes the solar intensity around a cylinder; ϕ is the complement angle between the spin axis and sun-line.

This semi-linear partial differential equation is solved numerically and analytically in the following sections.

4.3.2 Semi-implicit numerical solution

The implicit difference formulation of the above partial differential equation requires linearization of the radiation term i.e. $[T^{n+1}]^4 \cong T^{n+1} (T^n)^3$. This non-linear term is not expected to introduce serious numerical instability problems, but the resultant coefficient matrix is not exactly tridiagonal because there are two non-zero terms on the extreme corners of the matrix due to the closed-loop nature of the circumferential heat conduction. As a result, the matrix factorization technique cannot be applied and the Gaussian reduction method is used instead, which is more time-consuming. The numerical results for the thin metallic shell using Thin Shell Approximation agreed to about one percent of the results of the Strip Approximation (see Figures 4.2, 4.3, and 4.4).

Two of the by-products of this computation are the parallel and the normal force components (relative to the sun axis line) as functions of time. They both exhibit damped oscillation as shown in Figures 4.6 and 4.7 (for a shell length of a centimeter). From the spacecraft dynamics viewpoint, the absolute magnitude of the normal force component is just as important as its magnitude relative to the parallel force component, because the parallel and the normal forces are directly related to the precession torque and the erecting torque respectively. The following section discusses a proposed scheme to increase the normal force.

4.3.3 Subliming material coated shell system

The thermal force on the shell originates from the recoil momentum of photons which have a spectrum of energy characterized by the temperature of the radiative surface. At steady state, any unit surface on the shell will radiate as much energy as it receives during one spin cycle. The scalar momentum is directly proportional to the energy radiated but inversely proportional the particle expulsion speed. Consequently, if sublimation of a solid material is employed as the mode of removing energy, the expulsion speed ($\sim 3 \cdot 10^4$ cm/sec) is about a million times lower than the speed of radiated thermal energy ($3 \cdot 10^{10}$ cm/sec); the momentum resulting from sublimation is therefore about a million times the thermal radiative momentum. Thus, there is quite an incentive to coat the thin shell with subliming material. The heat flux carried by sublimation can be derived (see Appendix L) as

$$q_{sub} = - \frac{H_s}{17.14} \sqrt{\frac{wt}{T}} \text{EXP}[2.303 \cdot (A - B/T)] \quad (4.5)$$

where H_s is heat of sublimation
wt is molecular weight
A, B are the sublimation constants
T is the sublimation temperature

which is added into the bracket of Equation (4.4) to account for sublimation.

The resulting temperature distributions are shown in Figures 4.9, 4.10 and 4.11. The important features are (1) the damped oscillations of the instantaneous maximum and minimum temperatures are essentially suppressed by the

sublimation heat loss for wide range of spin rate, however, the instantaneous phase lag still retains a small damped oscillation; (2) the steady state temperature distribution is lower than the results from a bare shell; (3) the phase lag is not as large as in the case of a bare shell. For fast spin rate ($\omega \gg \omega_{opt}$), the instantaneous normal and parallel force components will tend to oscillate for a very long time because the surface temperature does not have sufficient time during each cycle to equilibrate. There are two interesting features worth mentioning: (1) for fast spin, the restoring torque can actually switch polarities as shown in Figure 4.12; (2) as shown in Figures 4.13 (a and b), the amplitudes of the force components for low initial temperature will have growing oscillation for many cycles before the amplitudes of oscillation start to decrease. The initial maximum temperature oscillates with damping, but its mean value continues to rise toward the equilibrium maximum temperature. Since the net reradiative and subliming forces are proportional to the exponential power of temperature, the amplitude of the oscillation attains a peak.

4.3.4 Approximate analytical solution

At steady state, the angular temperature distribution for a bare thin shell as shown in Figure 4.14 has a remarkable resemblance to a sinusoid. This temperature profile travels around the shell with an angular speed of the spin. The Fourier expansion of this wave form for

constant spin ω is

$$\begin{aligned} T(t, \theta) = & 290.9 + 21.55 \cdot \cos(\omega t + \theta) - 45.16 \cdot \sin(\omega t + \theta) \\ & - 12.65 \cdot \cos 2(\omega t + \theta) + 1.40 \cdot \sin 2(\omega t + \theta) \quad (4.6) \\ & + 0.43 \cdot \cos 3(\omega t + \theta) + 0.25 \cdot \sin 3(\omega t + \theta) + \dots \end{aligned}$$

which indicates that the steady state temperature distribution can be approximated by

$$\begin{aligned} T(t, \theta) \cong & T_{avg} [1 + M_1 \cos(\omega t + \theta) + M_2 \sin(\omega t + \theta)] \\ = & T_{avg} [1 + M \sin(\omega t + \theta + \psi)] \quad (4.7) \end{aligned}$$

Here, T_{avg} is the average temperature, M is related to the maximum temperature difference and ψ is the phase lag of the maximum temperature from the direction of maximum solar intensity. The half rectified sinusoid $F(\theta, t)$ and T^4 in Equation (4.4) are approximated by

$$F(t, \theta) = \frac{1}{\pi} + \frac{1}{2} \sin(\omega t + \theta) - \frac{2}{\pi} \sum_{n=1}^{\infty} \frac{\cos 2n(\omega t + \theta)}{4n^2 - 1} \quad (4.8)$$

$$T^4 \cong T_{avg}^4 [1 + 4M_1 \cos(\omega t + \theta) + 4M_2 \sin(\omega t + \theta)] \quad (4.9)$$

Substituting the above expressions into Equation (4.4) and equating the coefficients of the constant, sine, and cosine terms, the solution of the resultant simultaneous equation is

$$T_{avg}^4 = [-D/(\pi C)]^{1/4} \quad (4.10)$$

$$M = 0.5 D / [T_{avg} (A^2 \omega^2 + B^2 + 16 C^2 T_{avg}^6 - 8 B C T_{avg}^3)^{1/2}] \quad (4.11)$$

$$\psi = \tan^{-1} [A \omega / (A C T_{avg}^3 - B)] \quad (4.12)$$

and the constants in Equations (4.10), (4.11) and (4.12) are defined in Equations (4.17) through (4.22).

For the radioisotope-deposited thin shell, a constant heat flux term G is added to Equation (4.4) as proposed in Section 4.2.4. The expressions for M and ψ are the same as above, however the expression for T_{avg} is

$$T_{avg} = [-(D/\pi + G)/C]^{1/4} \quad (4.13)$$

In the case of the subliming material coated shell, a sublimation heat flux term $E T^{1/2} \exp[(A_c - B_c/T_{avg})^{2.3}]$ is added to Equation (4.4). The above parameters become

$$C T_{avg}^4 + D/\pi + T_{avg}^{-1/2} \cdot E \cdot 10^{A_c - B_c/T_{avg}} = 0 \quad (4.14)$$

$$M = D/(2 T_{avg}) \cdot \left\{ A^2 \omega^2 + [-B + 4C T_{avg}^3 + E \cdot \left(\frac{B_c}{T_{avg}^{2.5}} - \frac{1}{2 T_{avg}^{1.5}} \right) \cdot 10^{A_c - B_c/T_{avg}}]^2 \right\}^{-1/2} \quad (4.15)$$

$$\psi = \tan^{-1} \frac{A T_{avg} \omega}{-B T_{avg} + 4C T_{avg}^4 + E T_{avg}^{-1/2} 10^{A_c - B_c/T_{avg}} \cdot \left(\frac{B_c}{T_{avg}^{2.5}} - \frac{1}{2} \right)} \quad (4.16)$$

The constant A, B, C, D, E, G are the coefficients of the partial differential equation. They are

$$A = \rho C \quad (4.17)$$

$$B = k/R^2 \quad (4.18)$$

$$C = -\epsilon \sigma / 4r \quad (4.19)$$

$$D = I_0 \cos \phi / 4r \quad (4.20)$$

$$E = H_s W t^{1/2} / (17.14 4r) \quad (4.21)$$

$$G = R I_{HS} / 4r \quad (4.22)$$

where H_s is the heat of sublimation
 Rl_{H_s} is the radioisotopics heat flux
 and the rest are defined in Eq.(4.3)

These approximate analytical expressions of the form of Equation (4.7) are capable of representing the true (numerical) temperature distributions within about 20% accuracy. In general, Equation (4.7) should be used with caution because it could introduce large errors in computing other quantities such as the reradiative force components (note the reradiative force is proportional to the 4th power of temperature).

When the approximate analytic expression for temperature, Equation (4.7), is substituted in the normal force expression, Equation (4.3), the resultant expression is a sixth order polynomial in terms of the spin rate ω . Applying the Descartes Rule of Sign, it can be shown that there is one and only one real positive root in the solution. Analytically this root is found by transforming the sixth order polynomial to a cubic equation before using the Cardan's formula to get an explicit expression (37). The result is

$$\omega_{opt}^2 = \frac{1}{12\pi_2} \left\{ 2(64\pi_3^2 + 81\pi_1^4)^{1/4} \cos \left[\frac{1}{3} \tan^{-1} \left(-1 + \frac{4}{27} * \right. \right. \right. \\ \left. \left. * \frac{(64\pi_3^2 + 81\pi_1^4)^3}{192 \left(-\frac{56}{9}\pi_3^3 + 18\pi_1^2\pi_3^2 + \frac{81}{4}\pi_1^6 \right)^2} \right)^{1/2} \right] - (4\pi_3 + 9\pi_1^2) \right\} \quad (4.23)$$

$$\text{where, } \pi_1 = I_0 \cos \phi / (2\Delta r T_{avg})$$

$$\pi_2 = \rho^2 c^2$$

$$\pi_3 = \frac{k}{R^4} + 8 \frac{k \epsilon \sigma}{R^2 \Delta r} T_{avg}^3 + 16 \frac{\epsilon^2 \sigma^2}{\Delta r^2} T_{avg}^6$$

For the bare and the heated shells the numerical results from this expression agreed almost exactly with the only positive root of the original sixth order polynomial. For a bare thin shell, the optimum spin is nearly inversely proportional to the shell thickness and is only a few hundredths of a radian per second as shown in Figure 4.15. For the radioisotope-heated thin shell, the optimum spin is greater by an order of magnitude as shown in Figure 4.6. Again, the approximate solution checked out well ($\pm 25\%$) with the exact (numerical trial-and-error) solution.

For the case of the subliming material coated shell, the approximate optimum spin is not obtainable because the subliming force is a complicated function of temperature. As a result, the integral of Equation (4.3) is very difficult to obtain analytically. However, based on the reradiative force results, the optimum spin is at least an order of magnitude less than that of a bare thin shell. From a practical point of view, the coated shell functions best if the spin is about a few rpm because at this spin rate, the average parallel force is quite small and yet the normal force for erecting the spacecraft is still appreciable as indicated in Figures 4.13 (a and b).

4.4 Thick Shell Approximation Method

For a thin shell, the radial temperature variation is negligible. However for a shell coated with subliming material, the above assertion is not true anymore, because

the thermal conductivity of the subliming material is about a thousand times smaller than the metal and its thickness has to be at least ten times as thick as the metal in order to be practical. Fortunately, due to the low thermal conductivity of the subliming material, the circumferential heat conduction effect can still be ignored as in the Strip Approximation method (see Section 4.2). The resultant governing differential equations and boundary conditions are

$$\frac{\partial^2 T_i}{\partial r^2} + \frac{1}{r} \frac{\partial T_i}{\partial r} = \frac{\rho c}{k} \frac{\partial T_i}{\partial t}$$

$$k \frac{\partial T_i}{\partial r} \Big|_{R+dr} = -\sigma \epsilon T_i^4 - H_s \frac{(Wt/T)^{1/2}}{17.14} 10^{A_c - B_c/T_i} + I_0 F(\theta, t) \cos \phi$$

$$k \frac{\partial T_i}{\partial r} \Big|_R = 0 \quad ; \quad T_i(r, 0) = \text{CONSTANT} \quad (4.24)$$

$$i=1, 2, 3, \dots, J$$

Since the shell is divided into J strips, for a complete angular temperature distribution at any time t , the above differential equation has to be solved J times. Obviously, this is a very time-consuming process. As a matter of fact, the number of operation steps will exceed the solution of the original two-dimension parabolic partial differential equation (Equation 4.1) by ADI (Alternate Direction Implicit) scheme (see Section 5.4.3) for each time step because the number of radial mesh points is generally less than the number of circumferential mesh points. The important difference is that the proposed method is very stable numerically. On the contrary, the ADI method will likely introduce a severe numerical stability limitation due

to the non-rectangular geometry of this problem (20). As a result, the present numerical method will probably require less computer time for a complete transient solution in comparison with the ADI method because the present method can utilize a large time step.

There are many interesting features contained in the numerical solution as displayed in Figures 4.16 and 4.17.

(1) The temperature gradient across the shell is usually very significant (about $12^{\circ}\text{C}/\text{cm}$).

(2) For each strip, this gradient will switch signs for each spin cycle.

(3) The phase lag of the maximum temperature on the subliming surface is less than the phase lag on the metallic surface by above 50%.

(4) The temperature distribution at any instant resembles a sinusoid as shown in Figure 4.16.

(5) The maximum and the minimum temperatures as functions of time shown in Figure 4.17 are similar in shape to the curves from the Thin Shell Approximation. (see Section 4.3.3)

(6) Finally, the computer execution time is about five times greater than that for the similar calculation by the Thin Shell Approximation.

4.5 Comparison of Results

The original two dimension time dependent heat flow equation has been solved with varying degrees of

sophistication. It is obvious that as each assumption is removed, the fine structures of the 'exact' solution will begin to unfold, and the computer execution time will also increase. In general, the Strip Approximation is very accurate for thin metallic shell. If the metallic shell is not very thin, then the smoothening effect due to the circumferential heat conduction should be taken into account by the Thin Shell Approximation. When the shell exhibits poor thermal conduction such as with subliming material, the Thick Shell Approximation should be used in order to yield accurate surface temperature, because the sublimation process is very strongly dependent upon the surface temperature. Only under extreme conditions, such as a thick metallic shell coated with organic subliming material, must the original two-dimension differential equation be solved rigorously. Fortunately this situation does not exist in this study.

FIG 4.1 SCHEMATIC OF ERECTING SHELL

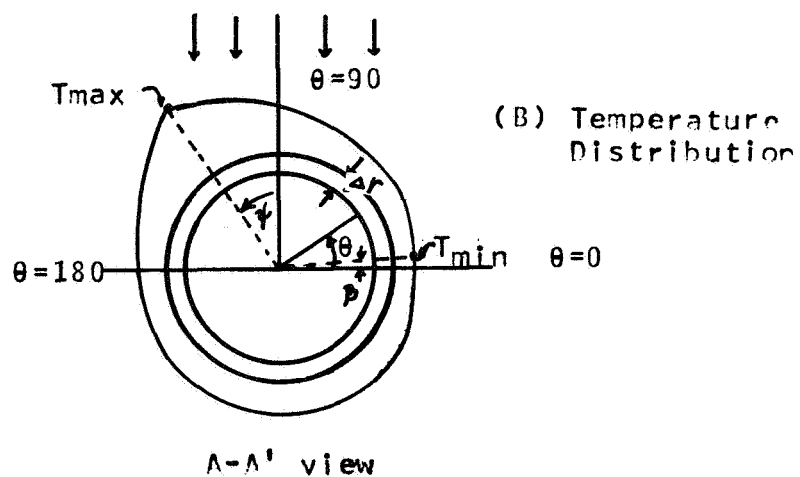
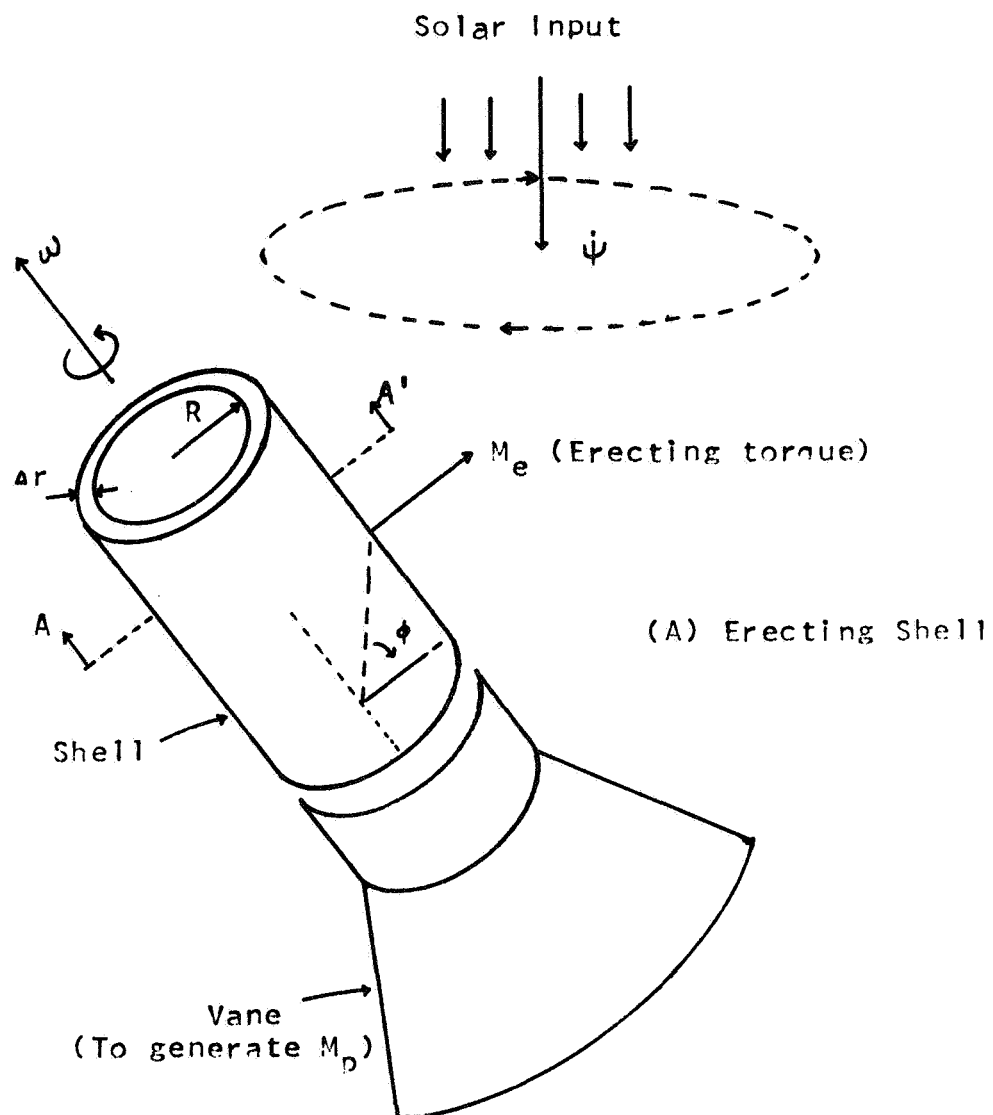


FIG 4.2 TRANSIENT MAXIMUM
TEMPERATURE OF BARE SHELL

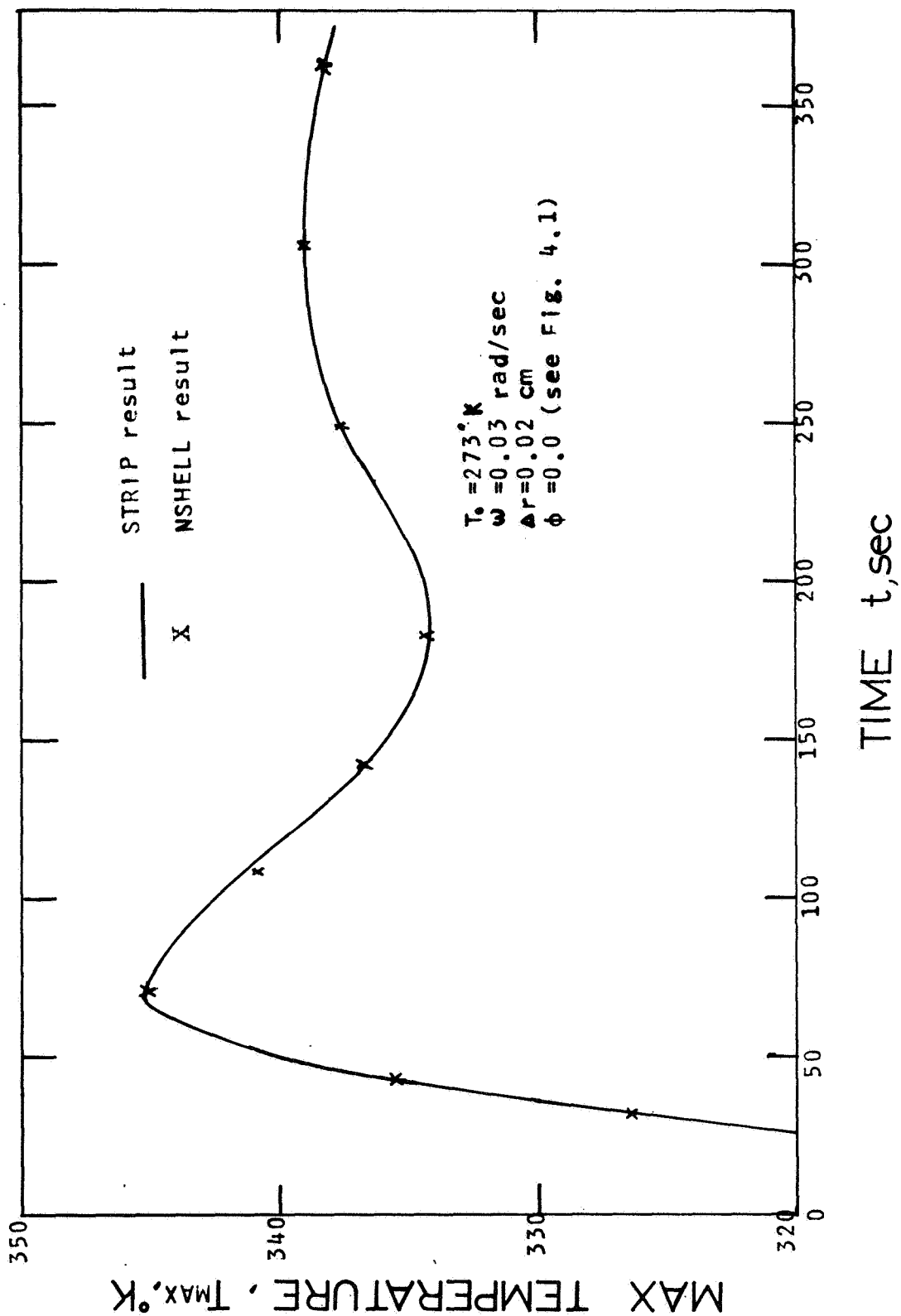


FIG 4.3 TRANSIENT MINIMUM
TEMPERATURE OF BARE SHELL

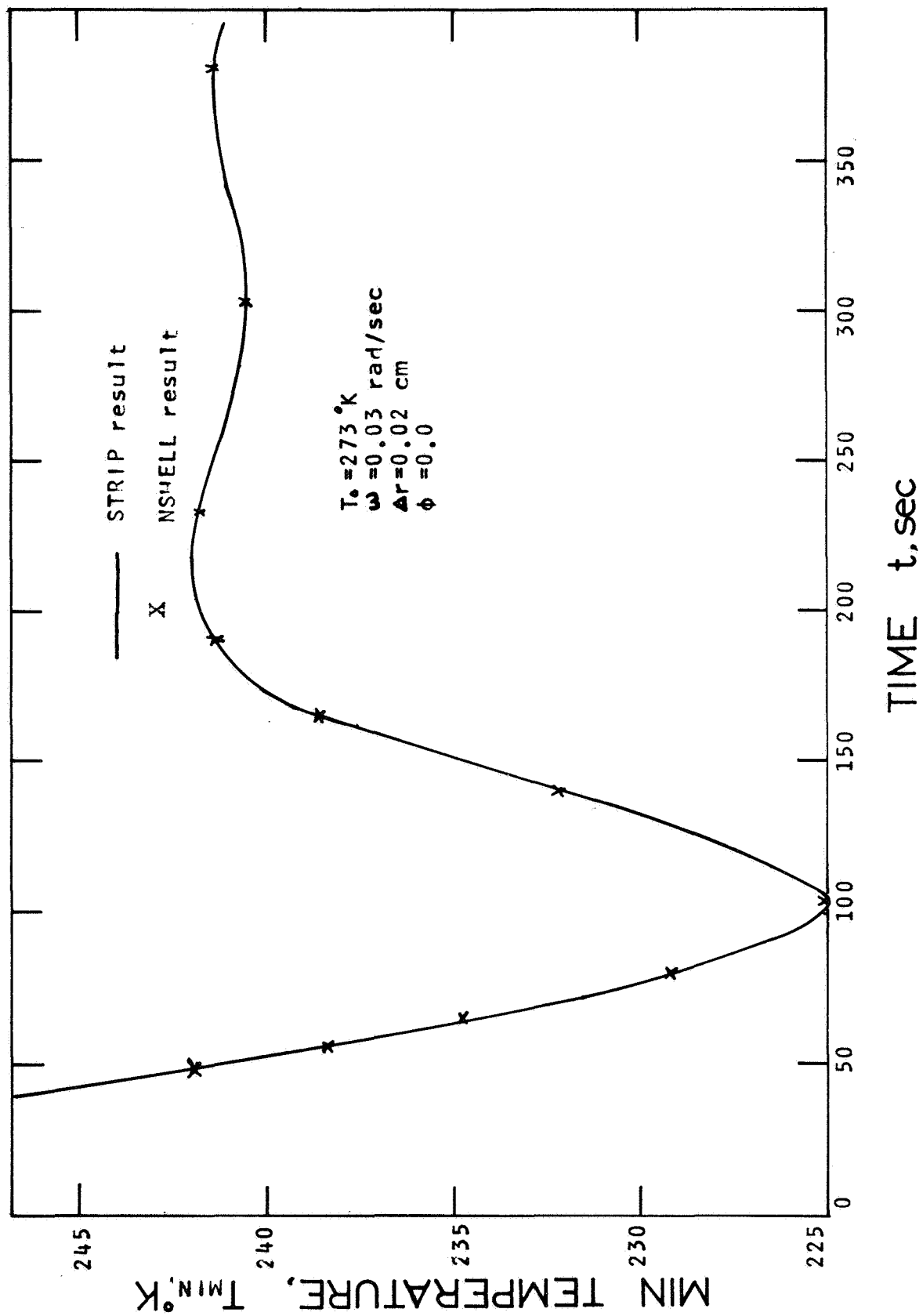


FIG 4.4 TRANSIENT MAXIMUM TEMPERATURE
DIFFERENCE OF BARE SHELL

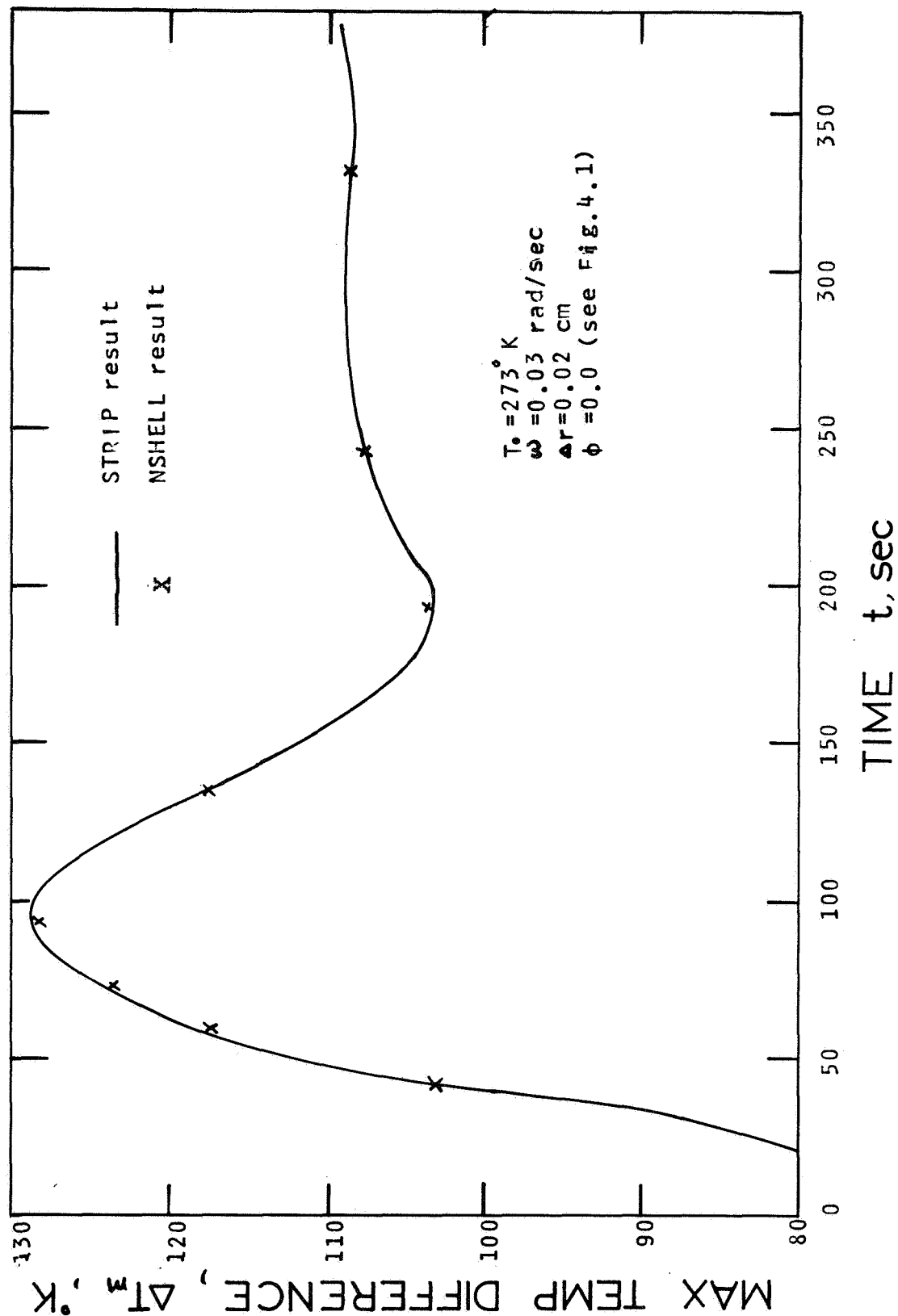


FIG 4.5 TRANSIENT PHASE
LAG OF BARE SHELL

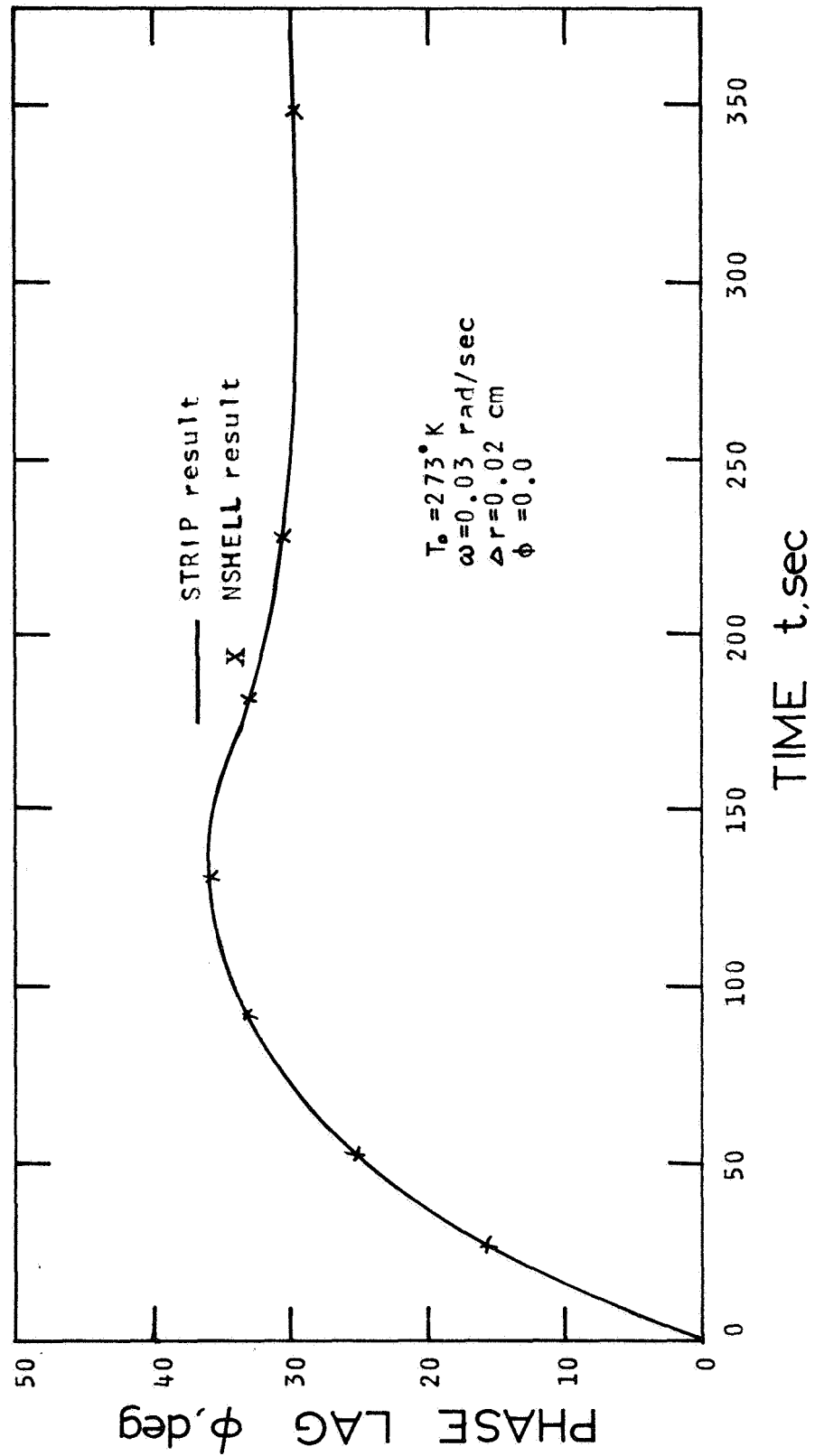


FIG 4.6 TRANSIENT NORMAL FORCE COMPONENT FOR BARE SHELL

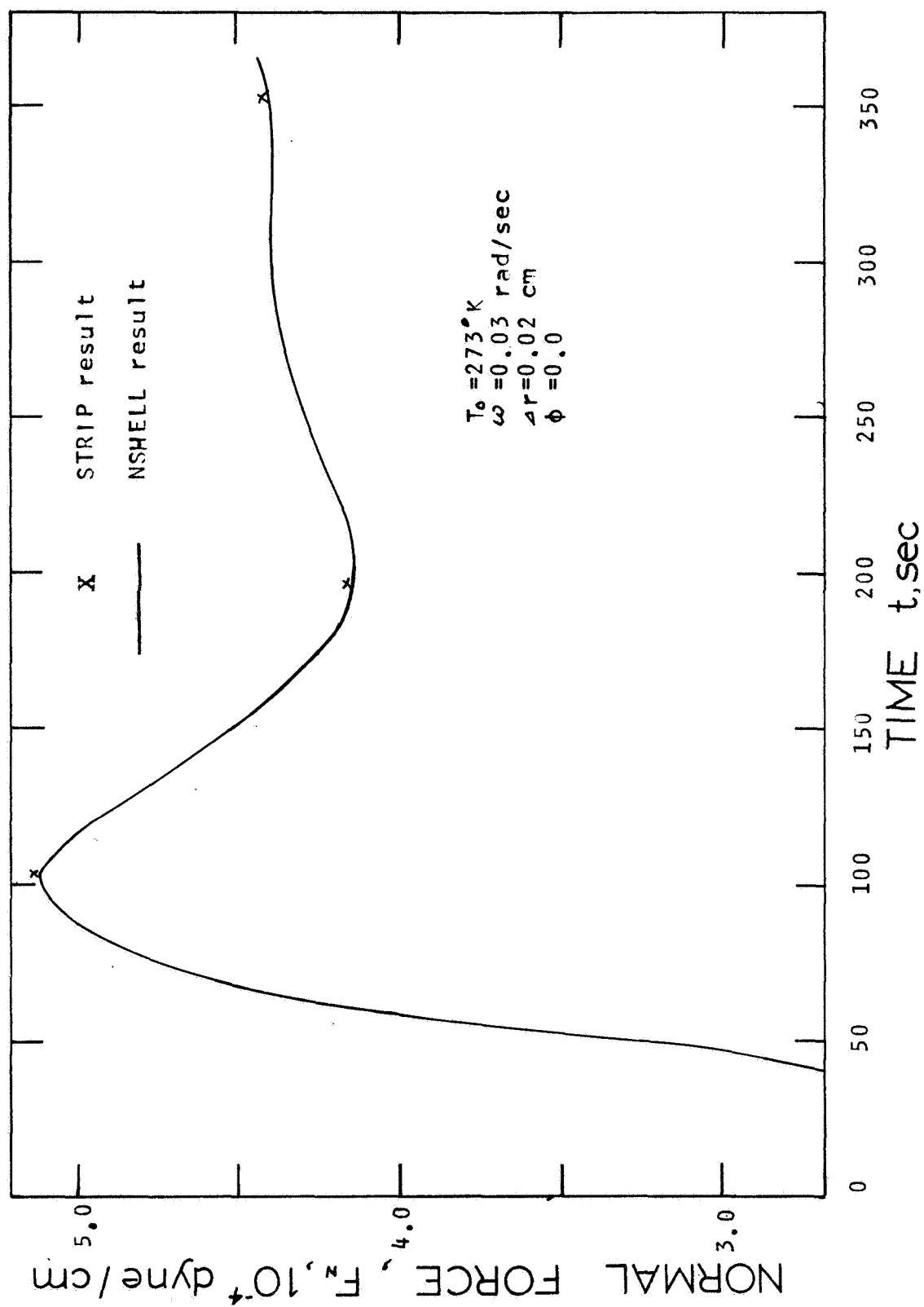


FIG 4.7 TRANSIENT PARALLEL FORCE COMPONENT FOR BARE SHELL

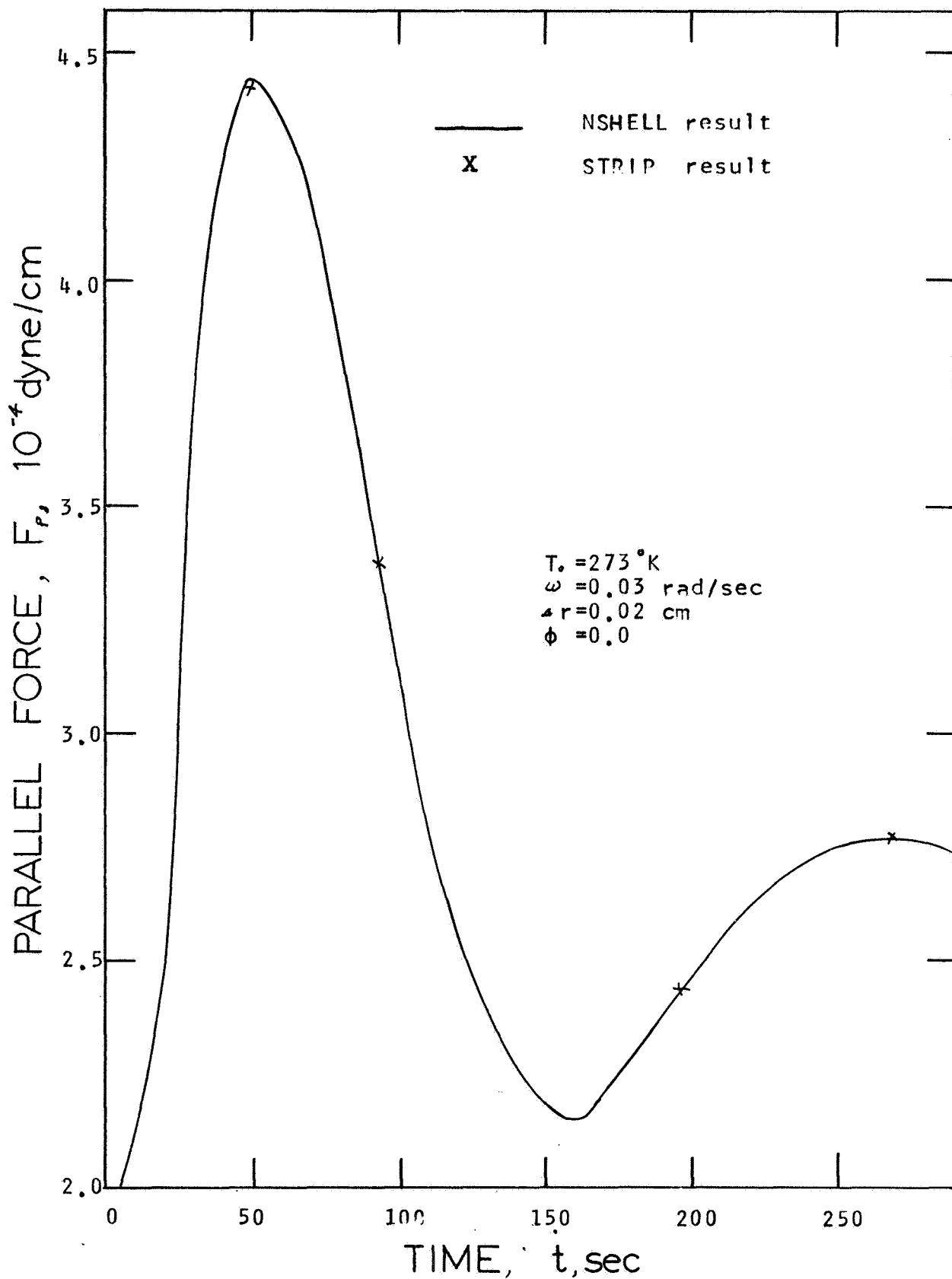


FIG 4.8
OPTIMUM SPIN AND MAXIMUM NORMAL
TORQUE FOR A HEATED SHELL

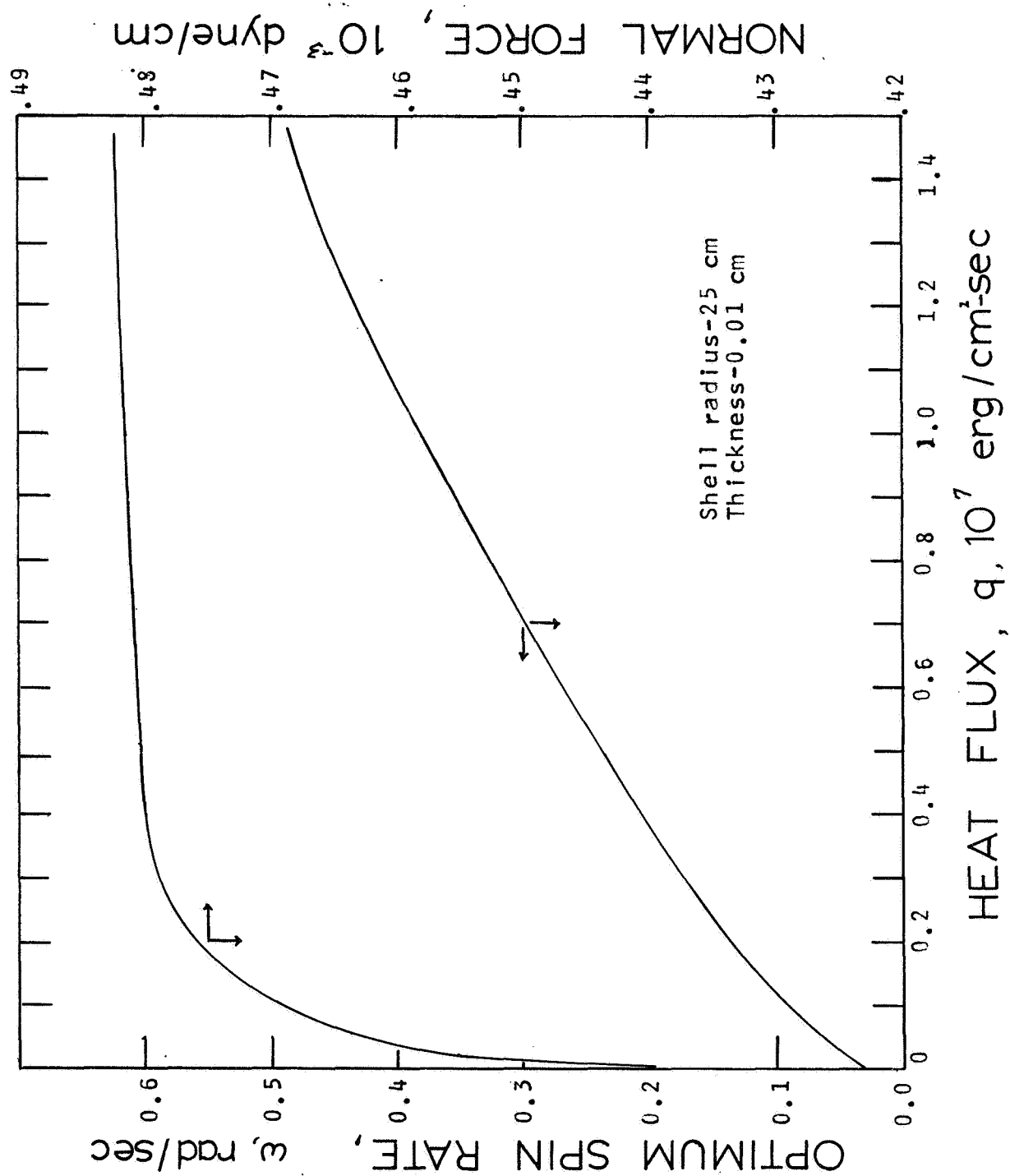


FIG 4.9 TRANSIENT MAXIMUM
TEMPERATURE OF COATED SHELL

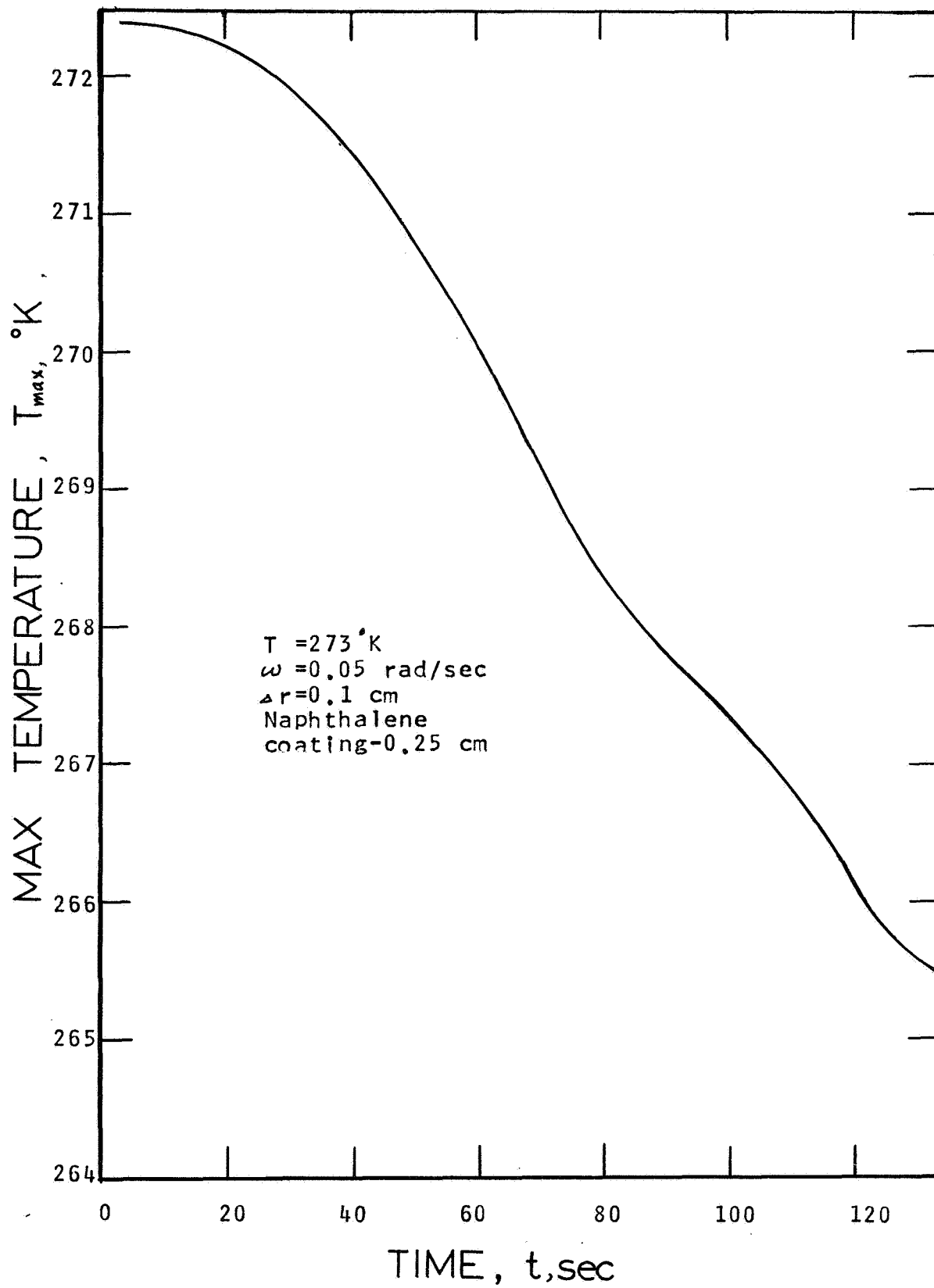


FIG 4.10 TRANSIENT MINIMUM
TEMPERATURE OF COATED SHELL

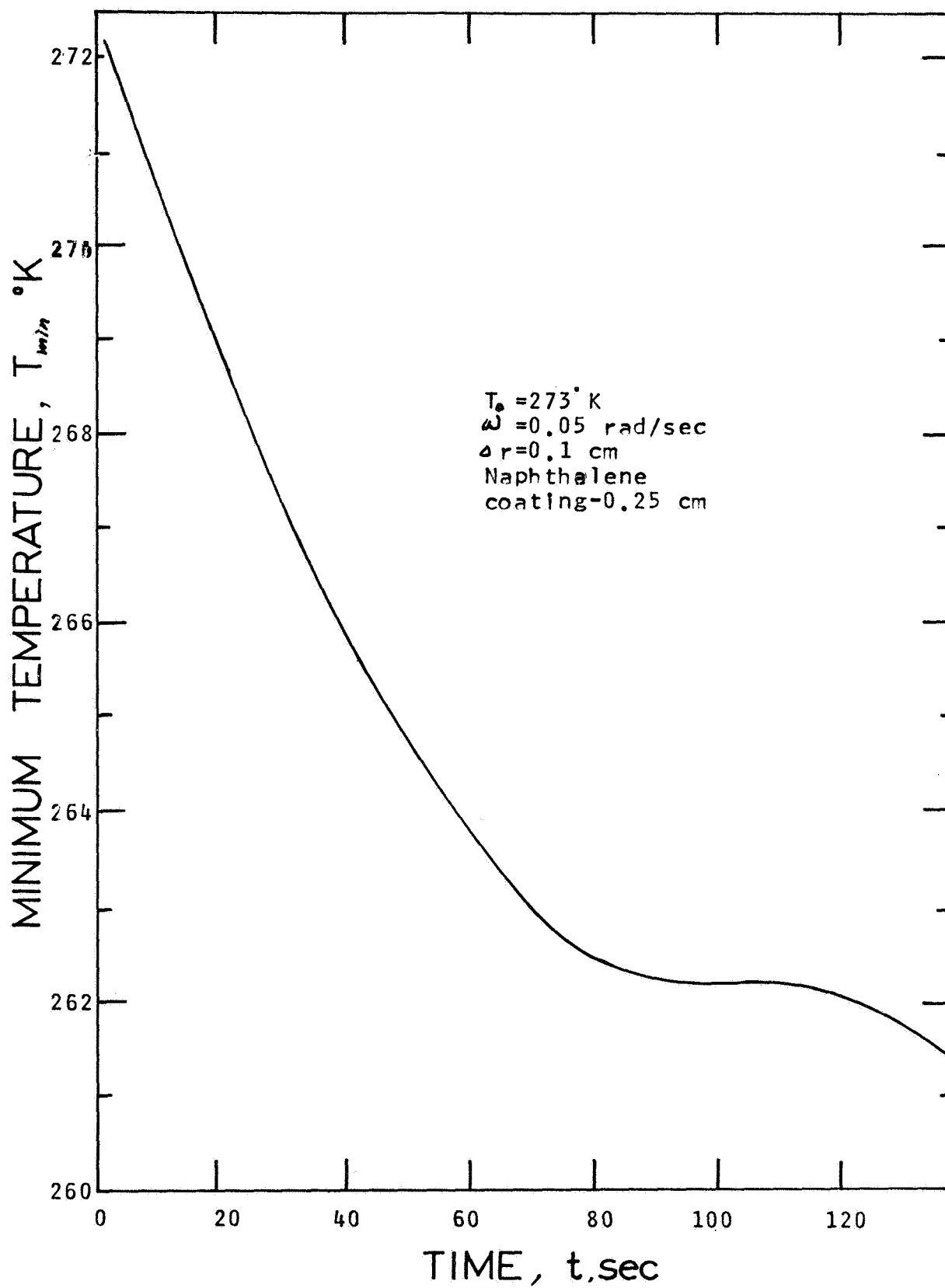


FIG 4.11 TRANSIENT PHASE
LAG OF COATED SHELL

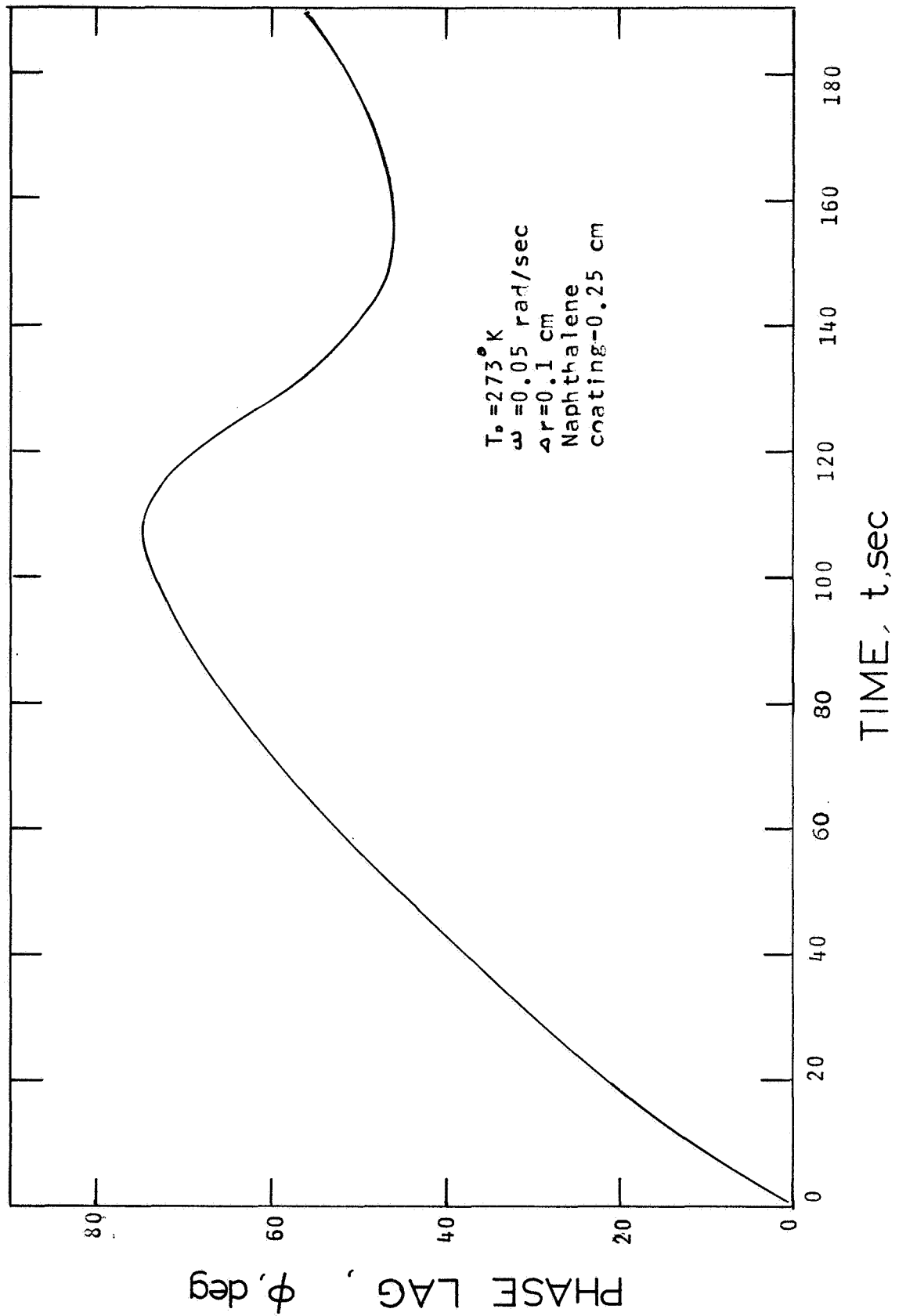


FIG 4.12 TRANSIENT PARALLEL FORCE COMPONENT FOR COATED SHELL

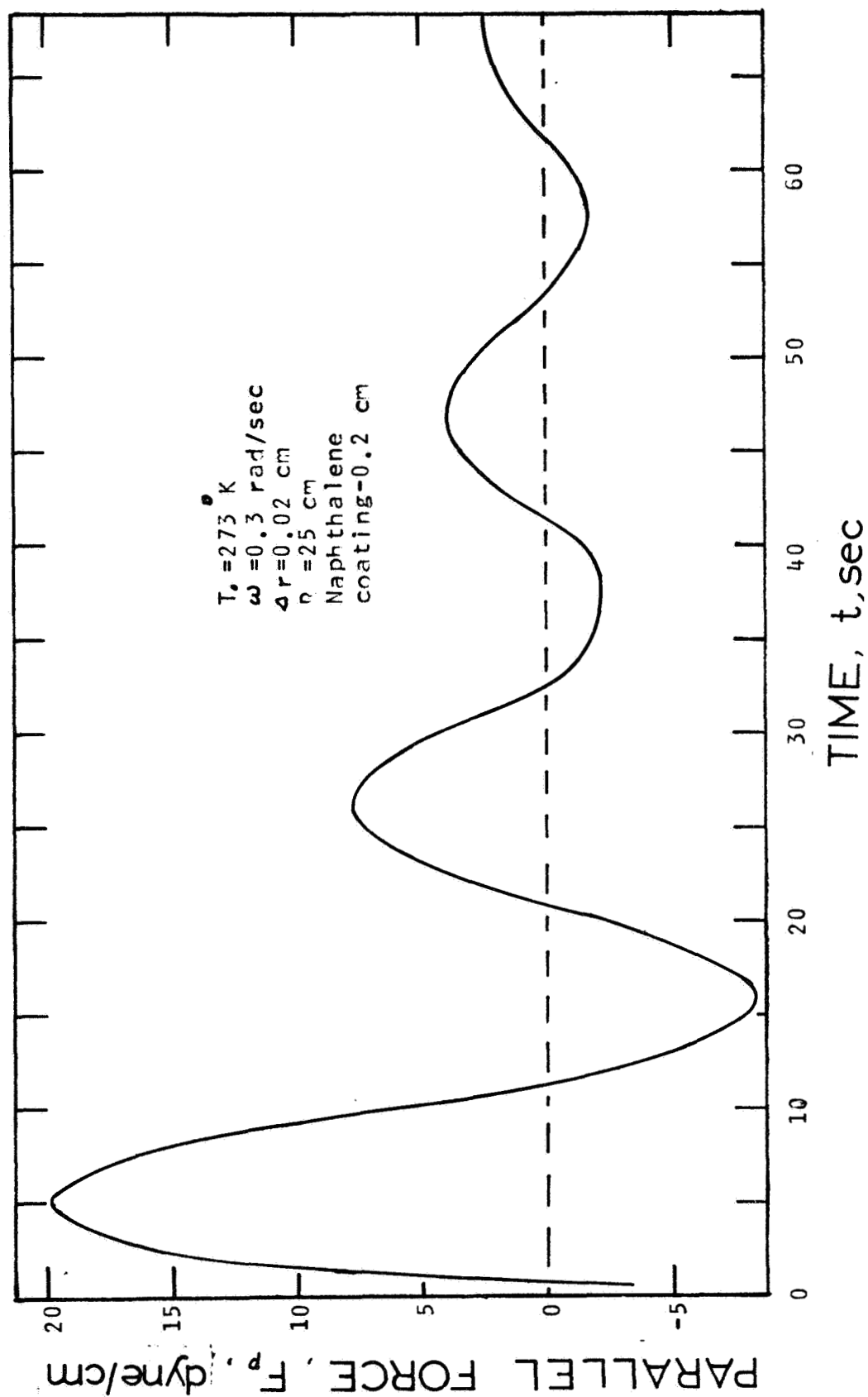


FIG 4.13a NORMAL FORCE COMPONENT
FOR FAST SPIN ($\omega \gg \omega_{pt}$)

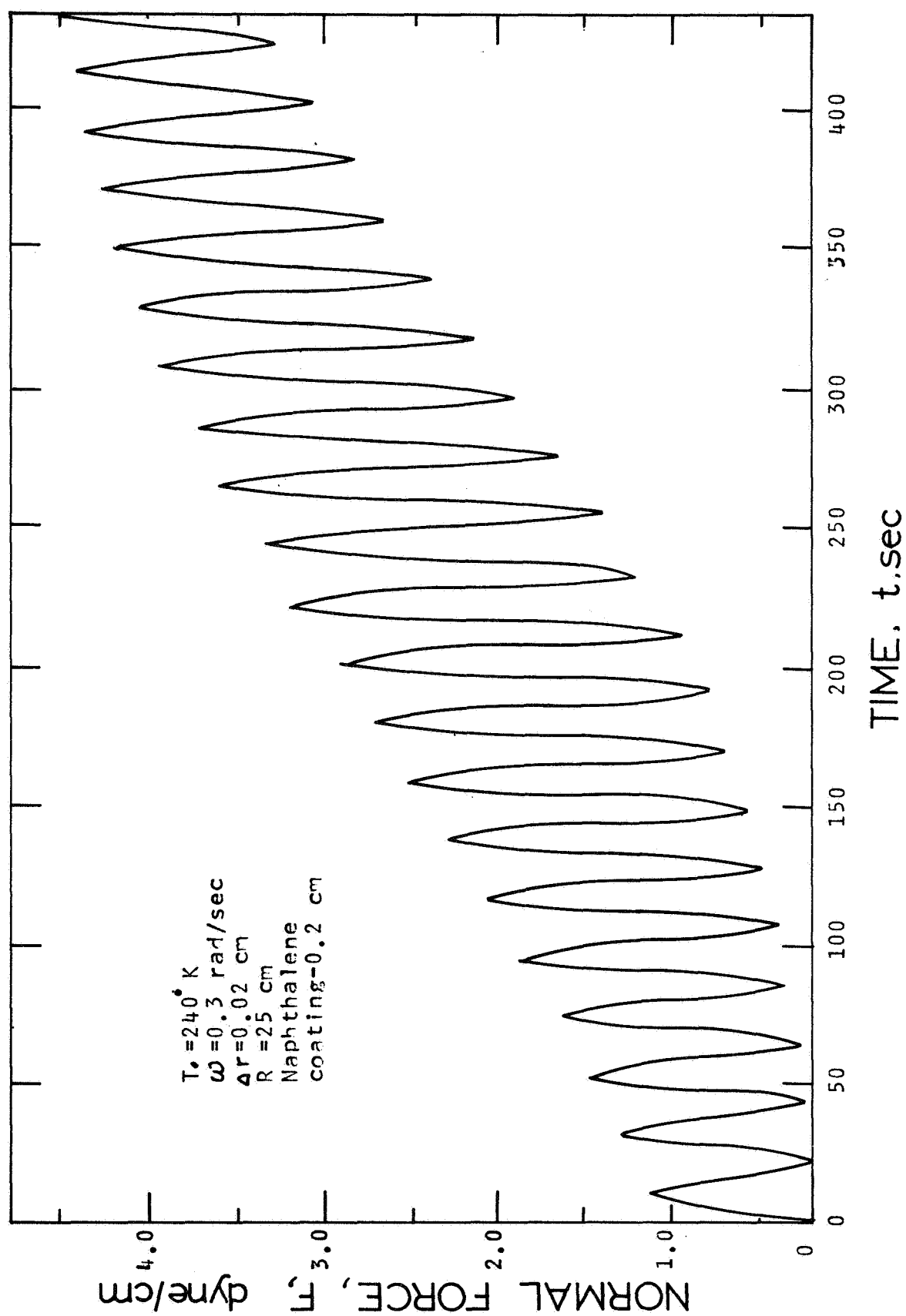


FIG 4.13b PARALLEL FORCE COMPONENT
FOR FAST SPIN ($\omega \gg \omega_{opt}$)

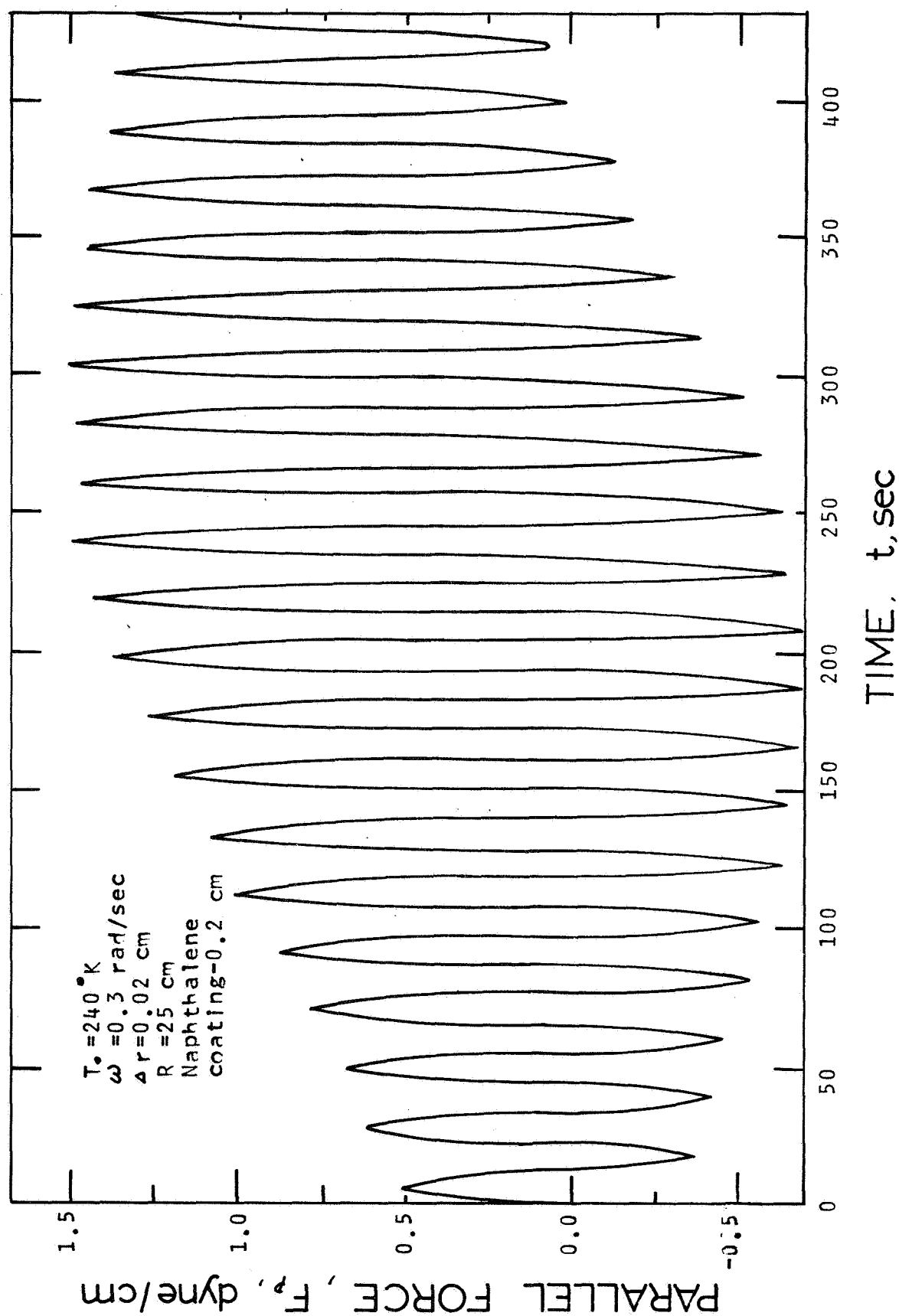


FIG 4.14 STEADY STATE TEMPERATURE DISTRIBUTION AROUND A BARE SHELL

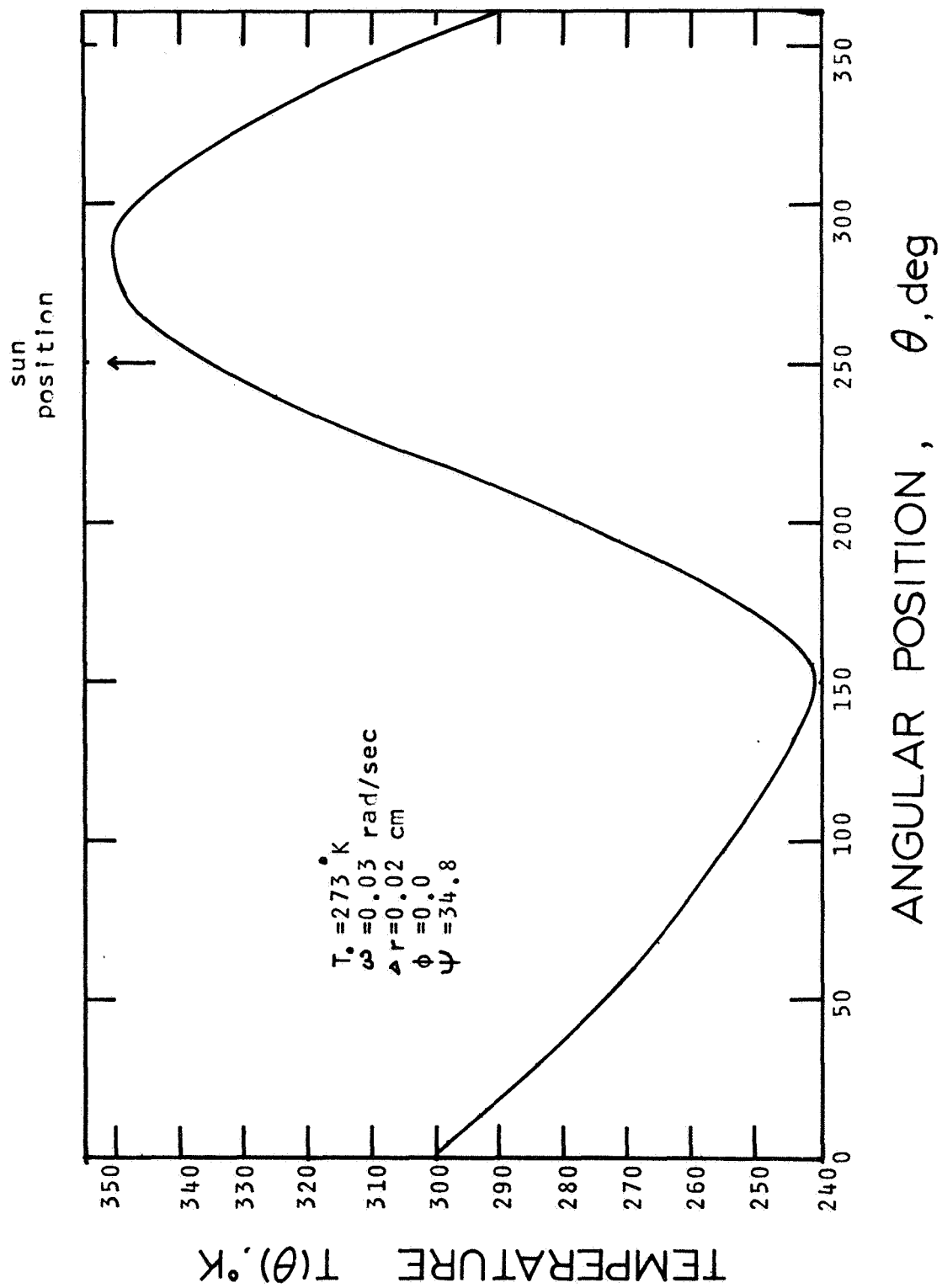


FIG 4.15 OPTIMUM SPIN RATE DEPENDENCE
ON BARE SHELL THICKNESS

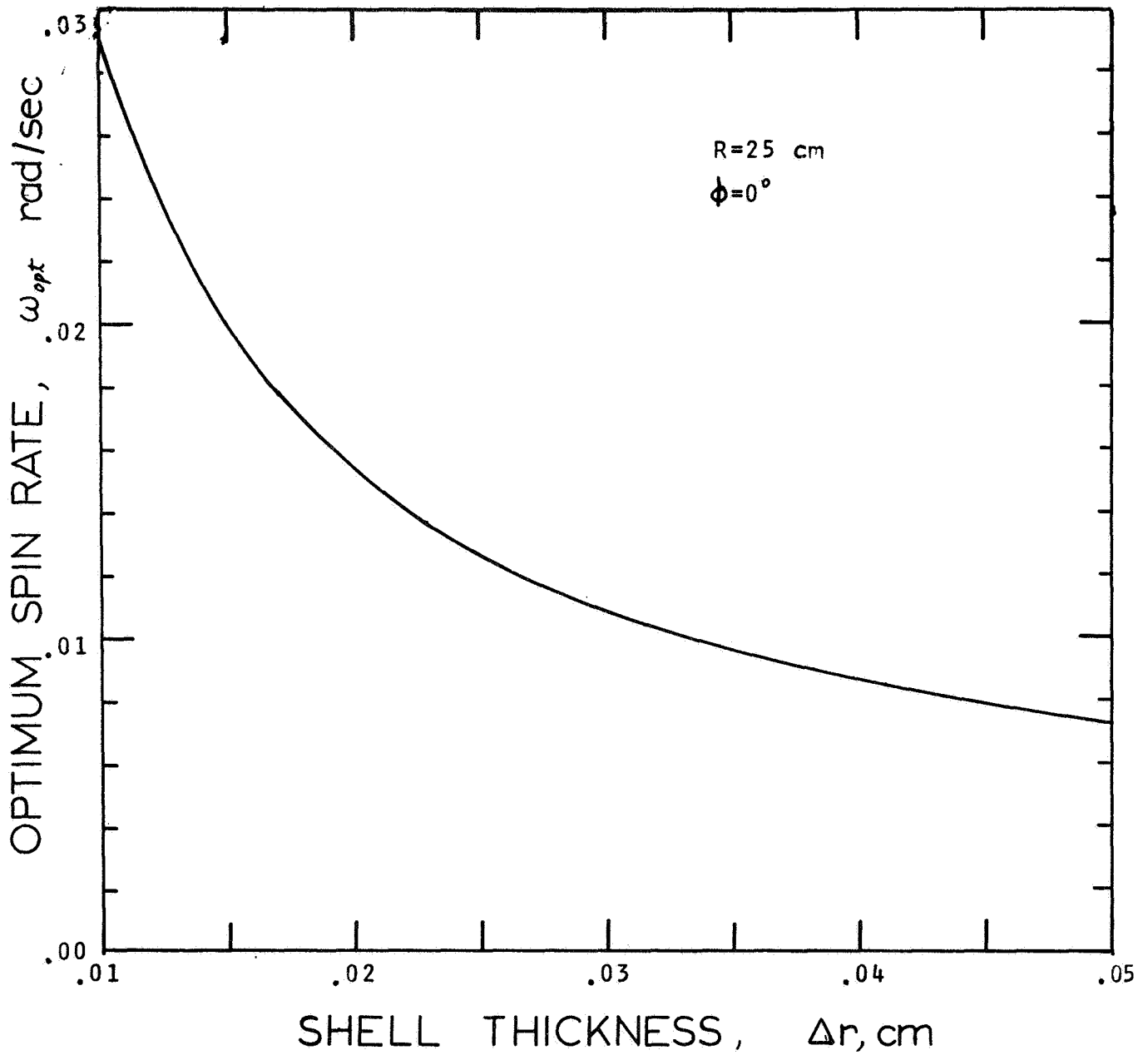


FIG 4.16 QUASI-STEADY TEMPERATURE DISTRIBUTION AROUND COATED SHELL

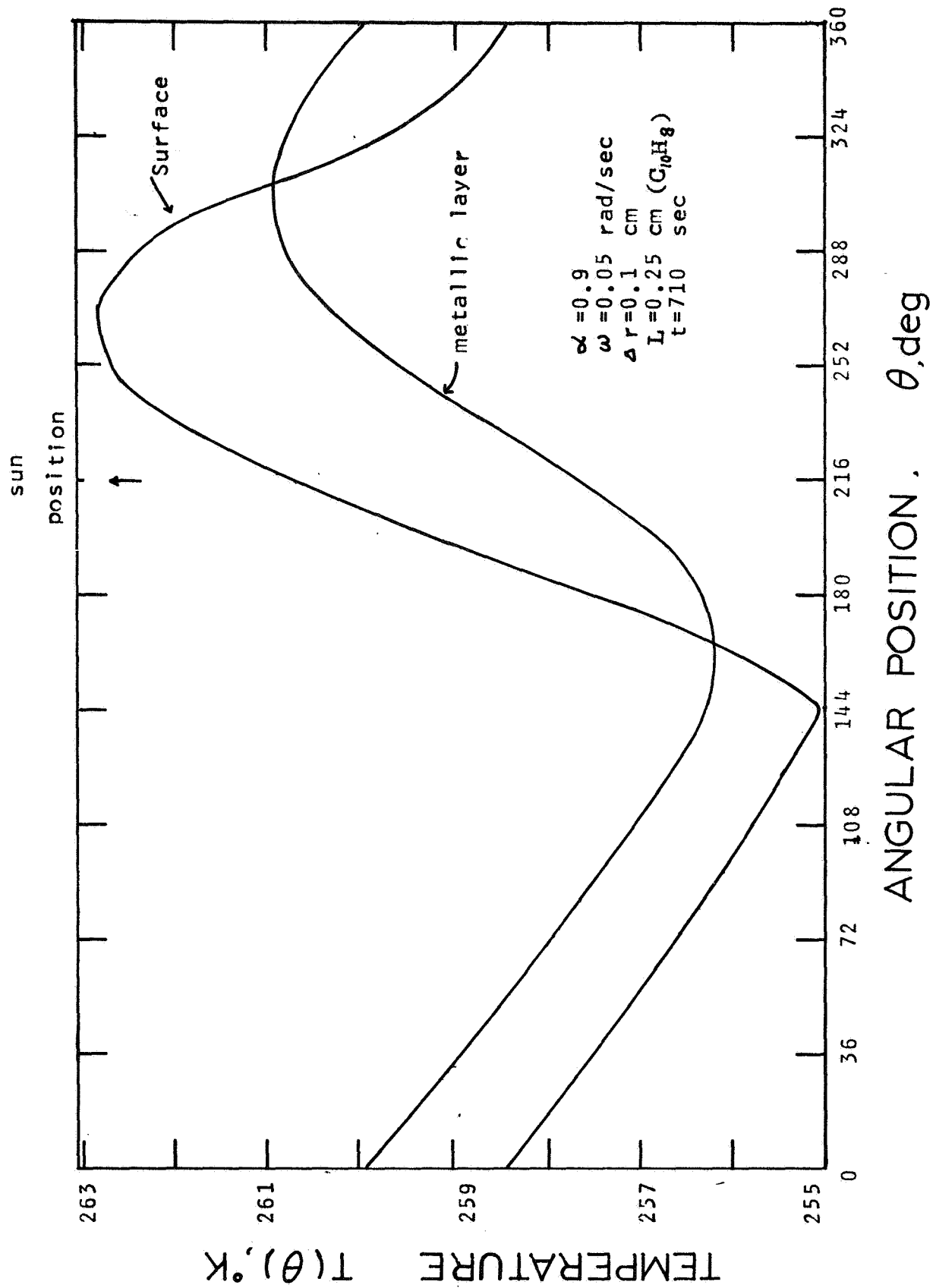
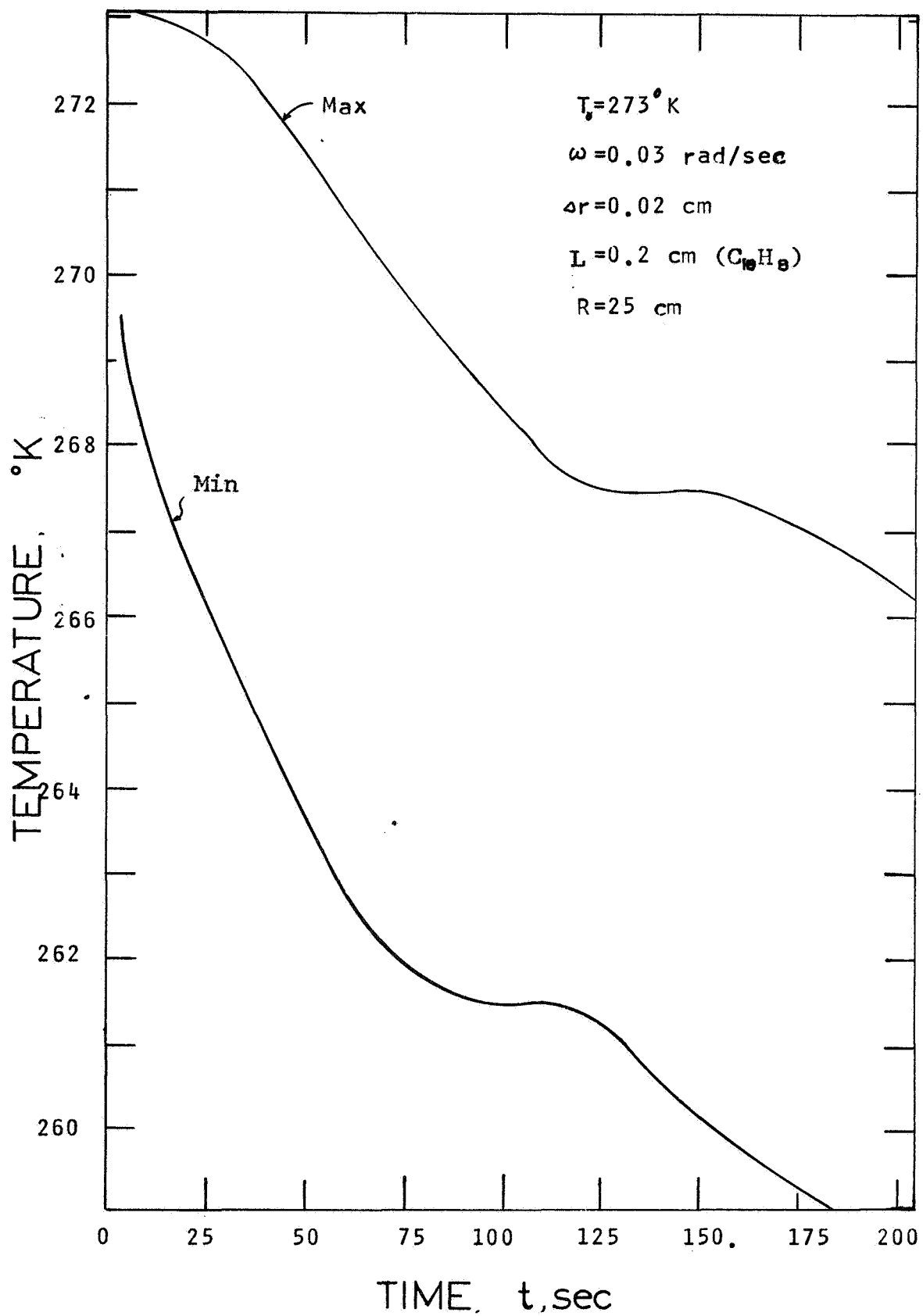


FIG 4.17 TRANSIENT MAX AND MIN TEMPERATURE FOR THICK-COATED SHELL



CHAPTER 5

PERFORMANCE ANALYSIS OF MICROTHRUSTER

5.1 Microthruster Design Considerations

In conventional chemical or nuclear rockets, the thermal power from chemical reactions or nuclear fission reactions is imparted to the propellant in the form of random gaseous kinetic energy which is transformed to directional kinetic energy by means of convergent-divergent nozzle to produce thrust. Theoretically, if all the gaseous molecules are expelled exactly in parallel with the thrust axis, the resultant thrust will be the maximum attainable for a given chamber stagnation condition.

In the subliming microthruster, this maximum can be achieved in principle if the subliming solid is placed at the focal point of a perfectly reflective parabolic nozzle. In reality, this is not a practical system because the subliming surface has to be very small at the focus and also the practical parabolic surface is far from being reflective. Nevertheless, a simple system, such as a cylindrical cup filled with subliming material as shown in Figure 5.1A, can realize about half of the theoretical maximum thrust. The performance of this simple design can be easily improved by connecting a divergent conical nozzle to the cylindrical cup (Figure 5.1B). The plausible reason is that gas molecules sublime, on the average, with a speed of $\left(\frac{\pi k T}{2m}\right)^{1/2}$ (31) which is higher than the sonic (pressure wave) speed of $\left(\frac{\gamma k T}{m}\right)^{1/2}$ (for complex molecules $\gamma=1.0$), so that the

nozzle has to be divergent to increase the resultant thrust. Physically, the molecular interactions with nozzle wall are conveniently divided into specular and diffuse reflections. In a divergent nozzle, the wall is slanted outward. From a simple geometric consideration, it can be shown that after either type of interaction with a divergent wall, the average final normal velocity component (parallel to the conic axis) is always greater than the initial. Consequently, the longer the nozzle, the higher the thrust will be. However, the net mass flow, due to the nozzle obstruction, is decreased to an asymptotic value as shown in Figure 5.2. To increase the thrust further, the alternative is to increase the mean speed of the molecules by heating the nozzle skirt so the molecules adsorbed by the wall will be evaporated with a higher average energy than their initial average energy.

5.2 Radioisotope Applications

5.2.1 Radioisotope properties

There are at least two areas where radioisotopes can contribute. These are as the heat source for the sublimation process and as propellant for thrust generation by the decay particle recoil momentum. Unlike Joule heating (electric resistance heating), the radioisotopic heating cannot be turned on and off so that it imposes a design problem. On the other hand, it is very reliable in generating a predetermined thermal energy. Considering

decay recoil momentum, the heavy particle emitter is very attractive for generating small thrust as will be shown in Section 5.2.2. In the present study, only alpha-emitters appear to be useful because of both their ease of converting the decay energy to heat and their availability. The selection of a particular alpha-emitter depends on many factors such as half-life, radiation hazard, cost, and material compatibility.

In Table 5.1, a few radioisotopes of interest are listed along with their physical properties. These isotopes are formed by capture of one or more neutrons. The nuclear radiations given off by them emanate directly from their natural decay scheme or from interaction of primary radiation with other materials. Usually, only gamma rays and neutrons are important in the required shielding considerations since they are more penetrating than both beta and alpha particles. Although the isotopes of importance in this study decay by emission, gamma rays and neutrons are present due to impurities, (α, n) threshold reactions with low atomic weight elements (e.g., O-17 and O-18), spontaneous fission (except Po-210), and induced fission (e.g., Pu-238 and Cm-244). The effects of neutron multiplication (34) in Pu-238 and Cm-244 are negligible for the present applications, however, the effects of impurities are sometimes unavoidable. Incidentally, Th-228 is an excellent propulsion isotope; the half-life is 1.9 year and its decay causes emission of five energetic alpha particles.

Unfortunately, it is not on the AEC isotope production list.

5.2.2 Radioisotope-doping for fast despin

Sublimation processes, as with other phase transition, require thermal energy. For materials of interest, the sublimation heat is of the order of 15 Kcal/mole (33). Unfortunately, subliming material are usually very poor thermal conductors, so that to supply a large amount of heat by way of conduction through these materials is very undesirable because of the associated large temperature gradients and the non-uniform subliming surface temperature. Radioisotope-doping seems to offer an excellent solution. Minute amount of alpha-emitting radioisotopes could be mixed in with the subliming material to form an internal heat source so that the sublimation heat is readily available and the surface temperature can be made fairly uniform radially. The resultant thrust would be about a few dynes per square-centimeter (based on the vapor pressure of Figure 6.5 at $\approx 273^\circ\text{K}$), which is sufficiently large to rapidly despin an initially fast spinning spacecraft.

5.2.3 Radioisotopic decay for long term spin-control

If the microthruster cup bottom is coated with a thin layer of an alpha-emitting radioisotope, then a small thrust will act on the cup due to the alpha recoil force as soon as the subliming material is depleted. The purpose of this film of radioisotope is to generate a long-term despin

thrust for the correction of any unexpected spin-drift. Since the alpha particles have such a low penetration capability, half of them are absorbed by the bottom of the cup and the other half are assumed to escape through the flow channel. The thrust non-obstruction factor for these high energy particles is very much different from that of the thermal energy molecules (see Section 3.2.2) because interactions with channel surface by these high energy particles will heat up the surface and the subsequent reemission will account for only a very small fraction of their initial momentum (less than a thousandth of the original). These high-energy charged particle interactions with the channel surface will contribute negligible recoil force. Consequently, as a good approximation, the thrust for high energy particles can be assumed to come from the direct streaming alone (those experiencing no channel surface obstruction). The thrust non-obstruction factor for high-energy charged particles (see Figure 5.3) is a function of both nozzle length and nozzle cone angle and is always less than that for the thermal energy subliming vapor.

The absolute thrust due to alpha particle emission is about three to four orders of magnitude smaller than the sublimation thrust. This is obtained in the following manner. The relativistic expression for the recoil momentum of an alpha decay is

$$P = \frac{KE}{c} \left(1 + \frac{2M_{\alpha}c^2}{KE} \right)^{1/2} \quad (5.1)$$

where KE is the alpha kinetic energy
 C is the speed of light
 M_α is the rest mass of alpha particle

The total number of alpha emissions per second is equivalent to the activity of the radioisotope and it is given by

$$\frac{dN}{dt} = -\lambda N e^{-\lambda t} \quad (5.2)$$

where N is $\#/cm^2$

Taking into account the factors of 1/2 for the absorption loss and 1/2 for surface normal component correction (not all particles leave the surface vertically), a useful expression for a thin-layer nuclear (neglecting self absorption) disintegration recoil force is

$$F\left(\frac{\text{dyne}}{\text{cm}^2}\right) = 0.83 \times 10^{-4} \times e^{-\lambda t} \left(1 + \frac{2M_\alpha C^2}{KE}\right) * WPA \quad (5.3)$$

where WPA is watts of radioisotope deposited on a cm^2 of surface

For $WPA \approx 0.1 \text{ W/cm}^2$, the recoil force is about $4.7 \times 10^{-4} \text{ dyne/cm}^2$. With inclusion of the nozzle skirt this force will be reduced by a factor equal to the thrust non-obstruction factor.

However, as the thickness of the isotope layer (or WPA) increases further, the above expression will overestimate the thrust because of the self-shielding. In principle, the thrust will reach a plateau for isotope thickness beyond its alpha range. If the isotope thickness x , is less than the range r_α , the thrust is given by (36)

$$T = \left(\frac{m}{8E}\right)^{1/2} * WPA * 6.23 \times 10^{12} * (1 - x/2r_\alpha) \quad (5.4)$$

For Po-210, the graph of thrust versus the dimensionless thickness x/r_α is shown in Figure 5.4. It is evident that the self absorption limits the maximum thrust intensity to about $5 \cdot 10^{-3}$ dyne/cm². In other words, the thickness of deposited layer should not exceed the alpha range of about $1.7 \cdot 10^{-3}$ cm.

For available radioisotopes such as Po-210, Cm-242, Cm-244 and Pu-238, the life span of their decay thrust, which is proportional to the half-lives, vary from about a year to several hundreds years, so that this type of nuclear disintegration thrust is suitable for long-term spin control.

5.2.4 Radioisotopic heating of nozzle wall

For a given mass flow rate, in order to increase the thrust and hence the specific impulse, more energy has to be imparted to the vapor. In an advanced nuclear rocket, seeded propellant can absorb thermal radiation from the divergent nozzle to increase the exhaust velocity, but here the sublimed vapor is so rarefied that the molecules do not interact with themselves or with thermal radiation. However, if the nozzle wall is heated by radioisotope decay to a temperature much higher than the sublimation temperature, molecules adsorbed by the surface will be reemitted with a higher average speed. Only the adsorbed molecules will benefit from the heated wall, but for a nozzle of moderate length the majority of the molecules will

indeed interact with nozzle surface. The results of the heated-wall effect is shown in Figure 5.5, for the case where the wall temperature is maintained at twice the subliming temperature. For the unheated-wall case, the wall temperature was assumed to be the same as the subliming temperature, but in reality the wall temperature would be lower so that the relative effect of having a heated wall is actually higher than that shown in Figure 5.5. The wall temperature is dependent upon amount of radioisotope deposited, surface emissivity, radiation view factor and the heat loss to the reemitted molecules.

5.3 Cylindrical-cup Microthruster

5.3.1 Description of governing equation

The schematic diagram of this device is shown in Figure 5.1A. The sublimation heat is supplied from the cup bottom where the heat is generated by a few layers of radioisotope. The outside cup surface is assumed to be thermally insulated (i.e., negligible surface emissivity). Since sublimation involves both the heat transfer and the mass transfer, the temperature distribution is always in transient state. The subliming surface temperature, and hence the resultant thrust, as a function of time must be obtained from the solution of time dependent one-dimension heat flow equation. The governing equations are the following.

$$k \frac{\partial^2 T}{\partial x^2} = \rho c \frac{\partial T}{\partial t} \quad (5.5)$$

$$dX_0/dt = -G(t)/\rho \quad (5.6)$$

The associated boundary conditions are

$$T(x, 0) = f(x)$$

$$-k \frac{\partial T}{\partial x} \Big|_{x=0} = q(t) - \epsilon_2 \sigma T^4(0, t)$$

$$-k \frac{\partial T}{\partial x} \Big|_{x=x_0(t)} = \epsilon_1 \sigma T^4(x_0, t) + G(t) * H_s$$

(5.7)

$$x_0(0) = \text{CONSTANT}$$

where $G(T)$ is the sublimation rate
 $q(t)$ is the radioisotope heat flux
 $f(x)$ is the initial temperature profile
 ρ, c, k, H_s are the density, heat capacity,
thermal conductivity, and heat of
sublimation respectively

Two numerical approaches, the explicit and the implicit difference methods, have been tried.

5.3.2 Explicit solution of temperature distribution

The difference formulation is such that the future temperature at any point is simply dependent upon the past temperature only; however, the numerical stability criteria requires the time step and the mesh size to be chosen in such a way that $\Delta t / \Delta x^2$ is always less than or equal to $(0.5)(\rho c) / k$ (about 200 in cgs unit). This limitation complicates the problem somewhat, because physically the outermost mesh will always decrease in size due to continuous sublimation process. This difficulty is resolved by starting with a larger than minimum outermost mesh; then as soon as the outermost mesh reaches the minimum allowed size, it is combined with its neighboring mesh to form a new outermost mesh.

The result of computation for one design is shown in Figures 5.6, 5.7, and 5.8. The initial temperature was assumed to be uniform (not true in reality). The surface temperature dipped to a minimum at the beginning because the heat losses through sublimation and radiation are larger than the heat supply through conduction (almost zero) and then started to rise to a quasi-equilibrium value because the resultant large temperature gradient due to initial dip increased the conduction heat transfer. The surface temperature crept up slowly to a maximum as a result of the reducing thermal resistance to the flow of heat from the radioisotope layer to the surface. As soon as all subliming material was evaporated, the temperature of the bottom of the cup rose quickly as shown in Figures 5.9, 5.10, and 5.11, because the only heat removal mode was then thermal radiation. However, an elevated equilibrium temperature was rapidly reached.

5.3.3 Implicit solution of temperature distribution

To avoid the restriction on small time steps and the coarse mesh size, the implicit difference formulation is employed. However, the temperature at a point depends upon both the past temperatures around this point and the current temperatures around this point which are unknown. Consequently, the spatial temperature distribution at any time is the solution of simultaneous linear algebraic equations. Fortunately, the coefficient matrix of these

simultaneous equations is tridiagonal so that the very efficient matrix factorization technique can be employed. The solution is very stable in general. Externally introduced disturbances such as the rearrangement of boundary and mesh net are usually damped out in a fraction of a minute (real time). The results of a sample calculation based on the same conditions as in the case of the explicit solution are shown in Figures 5.9, 5.10, and 5.11 for the time period during which the subliming material is about to disappear completely.

5.3.4 Comparison of results

The results of the above two methods agree very well throughout the tested time span except at a few transition instants when the mesh net was rearranged. As long as the surface was coated with subliming material, the surface temperature remained relatively constant after the initial fast transient because of the large damping effect of the sublimation process (see Figures 5.7 and 5.10). Since the thrust increases exponentially with the surface temperature, a small variation in temperature can be important. Consequently, accurate prediction of the temperature is a prerequisite for accurate evaluation of the thrust. Between these two numerical methods the implicit scheme is preferred on this count. An interesting fact found in testing the above two programs was that the explicit computer coding required many checking calculations to prevent instability

and as a result actually required more computer time than the implicit program under more or less the same conditions.

5.3.5 Thrust non-obstruction factor

By analogy with the mass non-obstruction factor, the thrust non-obstruction factor is the ratio of real thrust from a channel to the thrust from a plain subliming surface. Unlike the mass non-obstruction factor, the thrust non-obstruction factor can be, and is desirably, greater than unity. These two non-obstruction factors are different because the thrust factor involves a $(v \cos \theta)$ weighting factor in the integration of the Maxwellian distribution. Physically, molecules specularly reflected from a vertical wall do not affect the normal force component. However, those adsorbed and subsequently reemitted diffusely will lose some initial normal momentum on the average, so that the thrust non-obstruction factor for a cylindrical channel will be less than unity in general (except when the evaporation coefficient is very small). Also, since the average wall-incident angle (with respect to channel axis) is larger than the average angle for molecule escape from the channel wall, the thrust non-obstruction factor is expected to be larger than the corresponding mass non-obstruction factor. These effects are shown in Figures 5.12 and 5.13 where non-obstruction factors are plotted as functions of the L/R ratio and the evaporation coefficient, (for $\alpha=1.0$, the sublimation surface specular reflection is

zero). It is interesting to note that for small evaporation coefficients (large subliming surface reflection) the thrust non-obstruction factor can actually be greater than unity due to the large subliming surface reflection.

5.4 Chopped-cone Microthruster

5.4.1 Introduction

To significantly increase the thrust non-obstruction factor, the flow channel (or nozzle) has to be modified. Intuitively, a divergent nozzle should increase both the mass flow and thrust because the slanted channel wall helps to reflect molecules outward. Considering fluid dynamics, there is also a plausible reason. Vapor molecules leave the subliming surface with an average speed of $(\pi kT/2m)$ which is greater than the sonic or pressure wave speed $(\gamma kT/m)$ of any non-monoatomic gas (noting the specific heat ratio $= 1 + 2/f$, where f is the number of degrees of freedom)(31). The flow speed in this supersonic region can only be increased if it is expanded through a divergent nozzle. Of course the equations developed in fluid dynamics cannot be applied directly to the present pressure range, but apparently, useful qualitative conclusions can still be drawn from them. If the above deduction is correct then, a thrust engine design involving the heating a subliming material in a coated chamber to produce vapor to be passed through a nozzle (33) would not result in an efficient design.

The simplest design of a divergent nozzle is probably a chopped cone. However, it will be shown that proper design can improve its performance significantly such that the thrust does actually approach the theoretical maximum. Two of the most important geometric design parameters are the optimum cone angle and the optimum nozzle skirt length. In theory, the longer the skirt length the higher the exhaust speed (or the better the propellant expansion), however, "diminishing returns" will limit the length. In Figure 5.2, it is obvious that contributions to the thrust are decreasing for L/R greater than about six for a 45° -cone nozzle. A schematic diagram of a cylindrical-cup microthruster is shown in Figure 5.1B.

5.4.2 Optimum cone angle calculation

The optimum cone angle is very difficult to obtain analytically from Clausing's integral equation (see Section 3.2). The main difficulty lies in the formulation of the probability kernels, especially for slightly complicated assumptions on gas-surface interactions. However, numerically the non-obstruction factors for a chopped cone geometry pose no additional problems other than those described in Chapter 3. In the cylindrical tube case, the point sources from the inlet (apparent throat) were divided into differential cones, which intersect the channel wall or trace space curves on the wall. The number of molecules contained in each cone are proportional to the spherical

cosine distribution so that the surface adsorption density in each channel ring is the properly weighted summation of all intercepted space curves from all cones of the point sources.

Unfortunately, truncation errors introduce an uncertainty by at least a fraction of a percent. The major portion of the uncertainty probably comes from the numerical treatment of the interceptions of differential cones by each channel ring. The computer program (CONNOF) for solving the chopped cone geometry treats the differential cones in a slightly different fashion from the cylinder case (TUBNOF) so that a direct comparison can be made with the cylindrical-tube solution (noting a 90 degree chopped cone is equivalent to a cylinder).

In this computer program (CONNOF), the circumference of each individual differential cone is equally divided into about one hundred equal groups such that each group is considered as a beam bundle characterized by a set of polar and azimuthal angles. The trajectory of this beam bundle is traced until it is adsorbed by the channel wall. Adopting the same procedure as in the cylindrical tube case (see Section 3.2.2), the mass non-obstruction factor is computed. Since the polar angle of each escaping beam is known, the normal momentum and hence the thrust non-obstruction factor can also be computed. For a given nozzle length, the non-obstruction factors are calculated for different cone angles.

The results are shown in Figure 5.14. For maximum thrust, there is an optimum cone angle which is strongly dependent on the gas-surface properties, in particular, the specular reflectivity. In Figure 5.14, although the thrust reaches a peak, the mass flow monotonically increases as the cone angle is widened. Also in comparison with the results from TUBNOF, it is surprising that the two results agreed very well (see Table 5.2). By manipulating the cone angle of a short nozzle the thrust level can be increased by about twenty-five percent as shown in Figure 5.14. In Figure 5.2, it is shown that by lengthening the nozzle, the thrust can be increased by about twenty percent. Consequently, it pays to design a chopped cone microthruster properly because it is capable of improving the efficiency over the cylindrical-cup design by about fifty percent. With a radioisotope-heated nozzle skirt as described in Section 5.3.3, the performance can be increased further by about another twenty-five percent as shown in Figure 5.5.

5.4.3 ADI solution of temperature distribution

In Section 5.3, the temperature distribution in a cylindrical cup was obtained from the solution of the one dimension parabolic partial differential equation by assuming negligible radial heat transfer. The same assumption is not reasonable for a chopped cone geometry, because the radioisotope heat flux will funnel out from the bottom and introduce radial heat flux component even with

perfect thermal insulation of the external cone surface. Consequently, the temperature distribution in a chopped cone microthruster must include the effect of radial heat conduction. A straight implicit difference scheme would require an inversion of about 100×100 matrix for each time step. This method is certainly not practical because of the enormous computer time needed as well as the large but unknown numerical error associated with this type of operation (inversion of large matrix). A relatively new technique called ADI (Alternate-Direction-Implicit) was developed for fast convergence (30) of parabolic partial differential equations. This technique makes full use of the fast matrix factorization operation for solving the resultant matrix equation and is unconditionally stable for any mesh size or time step provided rectilinear coordinates are used for the partial differential equation. However, the geometric symmetry of the chopped cone demands use of cylindrical coordinates. The ADI method was chosen for solution using cylindrical coordinates with the understanding that the method might not be unconditionally stable in this coordinate system. The description and listing of the computer code are given in Appendices J.3 and P.7.

While testing the computer program, the implicit solution of the center-line in the axial direction exhibited an irregularity whose cause has not been determined, but by a parabolic interpolation of the center-line temperature,

this difficulty has been bypassed. As suspected, the numerical scheme is not unconditionally stable. For a reasonable fine mesh net ($0.1 \times 0.1 \text{ cm}^2$), the corresponding maximum time step should be less than about 1.0 second. As a result, the computer execution time on IBM 360/65 is comparable to the real time (total subliming time) thus for a propellant (subliming material) thickness of a few centimeter, several hours of computer time will be required to complete the transient temperature solution. The typical temperature distribution shown in Figure 5.15 suggests that the one-dimension solutions of Section (5.3) may be used as a first approximation because the temperature varies very little radially except in the vicinity of boundary. Only for the detailed design calculation will the computer program need to be executed in its entirety.

5.4.4 Performance parameters

In general, the thrust level for this type of microthruster is less than a hundred dynes or a few hundred micro-pounds. For ease of comparison with other thruster systems, the parameters characteristic of a thruster were calculated.

Neglecting the pressure differential effect at the exit, the exit velocity is just the ratio of thrust to mass flow rate. The exit velocity as a function of the nozzle length is plotted in Figure 5.16. Since the exit velocity is supersonic throughout the nozzle length, the throat

cross-section is not a real quantity, but its effective location can be found by extrapolating the exit velocity until the sonic velocity is reached as shown by dashed line in Figure 5.16. The corresponding fictitious throat area A_t , the thrust coefficient C , and the specific impulse I_{sp} , are (naphthalene)

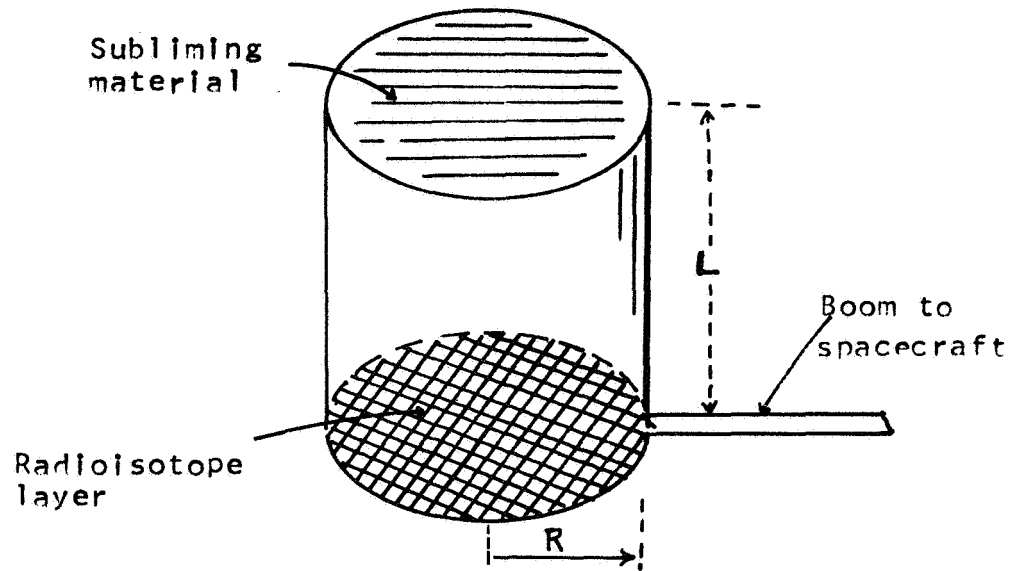
$$A_t = \pi(R-1/\tan\psi)^2 \cong 0.5 A_0 \quad (5.8)$$

$$C = T/(P_0 \cdot A_t) = 1.8 \quad (5.9)$$

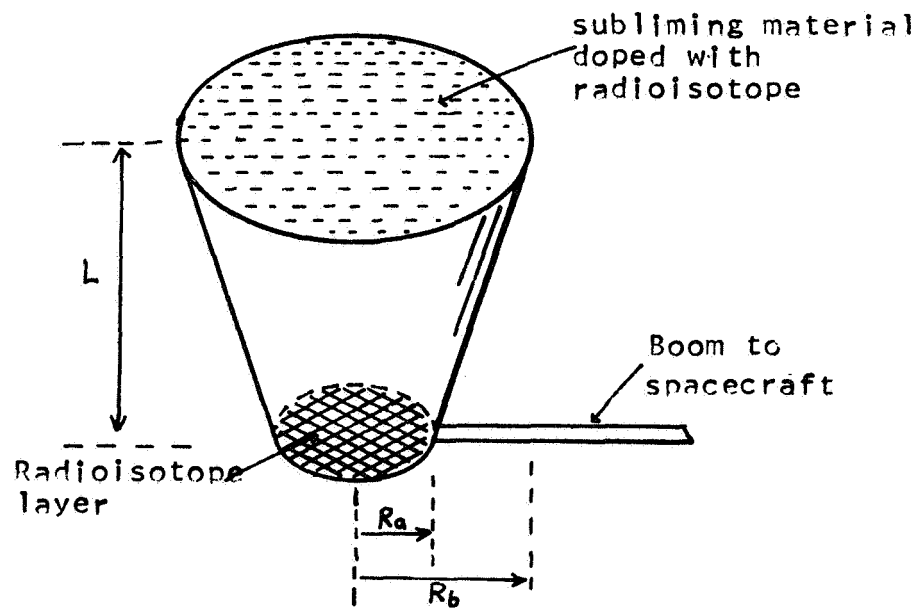
$$I_{sp} = V_e/g_0 = 21. \quad (5.10)$$

Since the performance is strongly dependent upon the propellant molecular weight and the temperature range over which the microthruster can be properly operated, the selection of a suitable subliming material is important. In this study only the biphenyl and naphthalene are considered because of their adequate vapor pressures in the vicinity of 273°K and their relatively high melting points. Some of their physical properties are given in Table 5.3.

FIG 5.1 SCHEMATIC DIAGRAM OF
SUBLIMING MICROTHRUSTERS



A. Cylindrical cup



B. Chopped Cone

FIG 5.2

NON-OBSTRUCTION FACTORS
vs L/R FOR 45° CONE

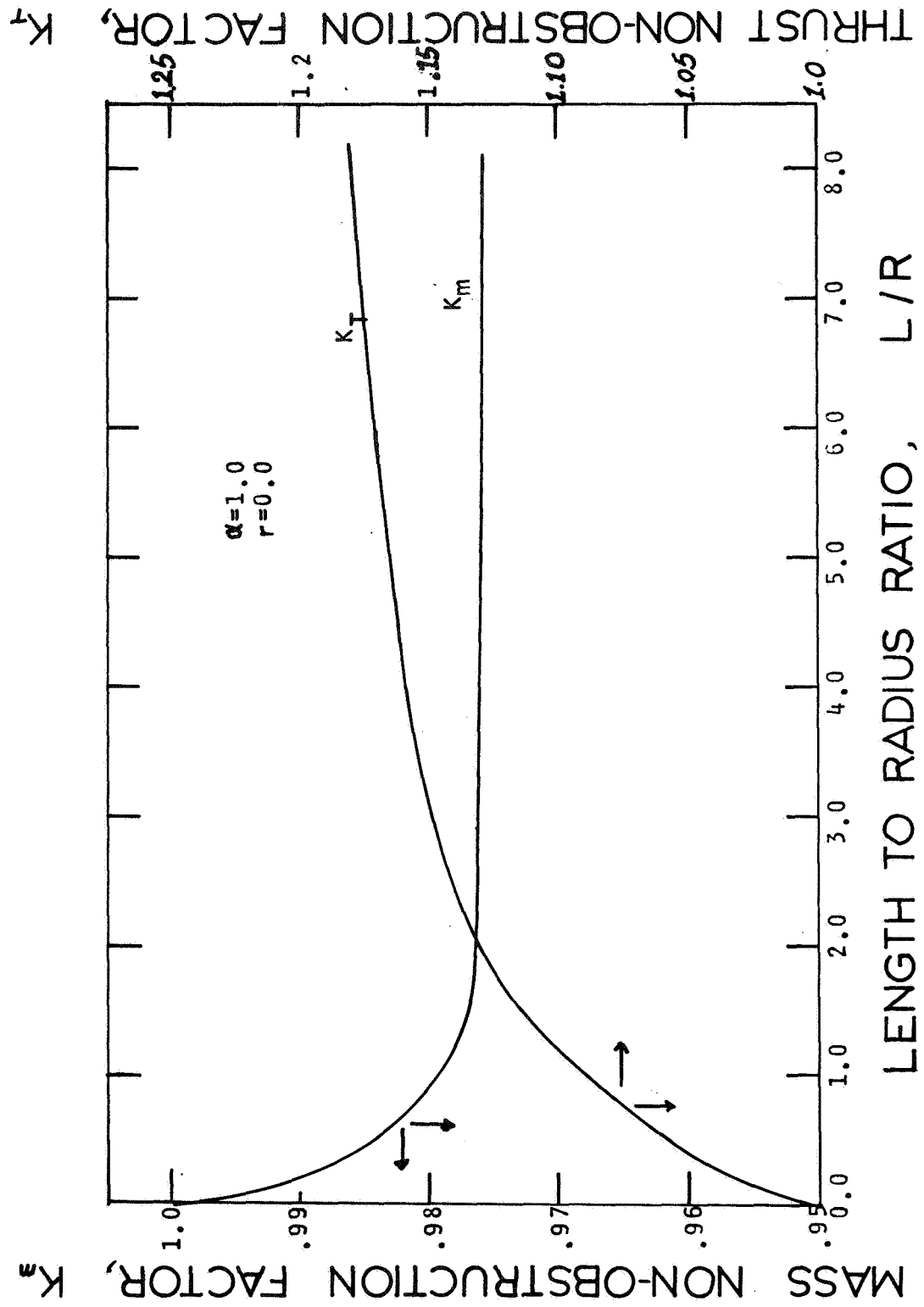


FIG 5.3
NON-OBSTRUCTION FACTOR OF
60° CONE FOR HIGH ENERGY α

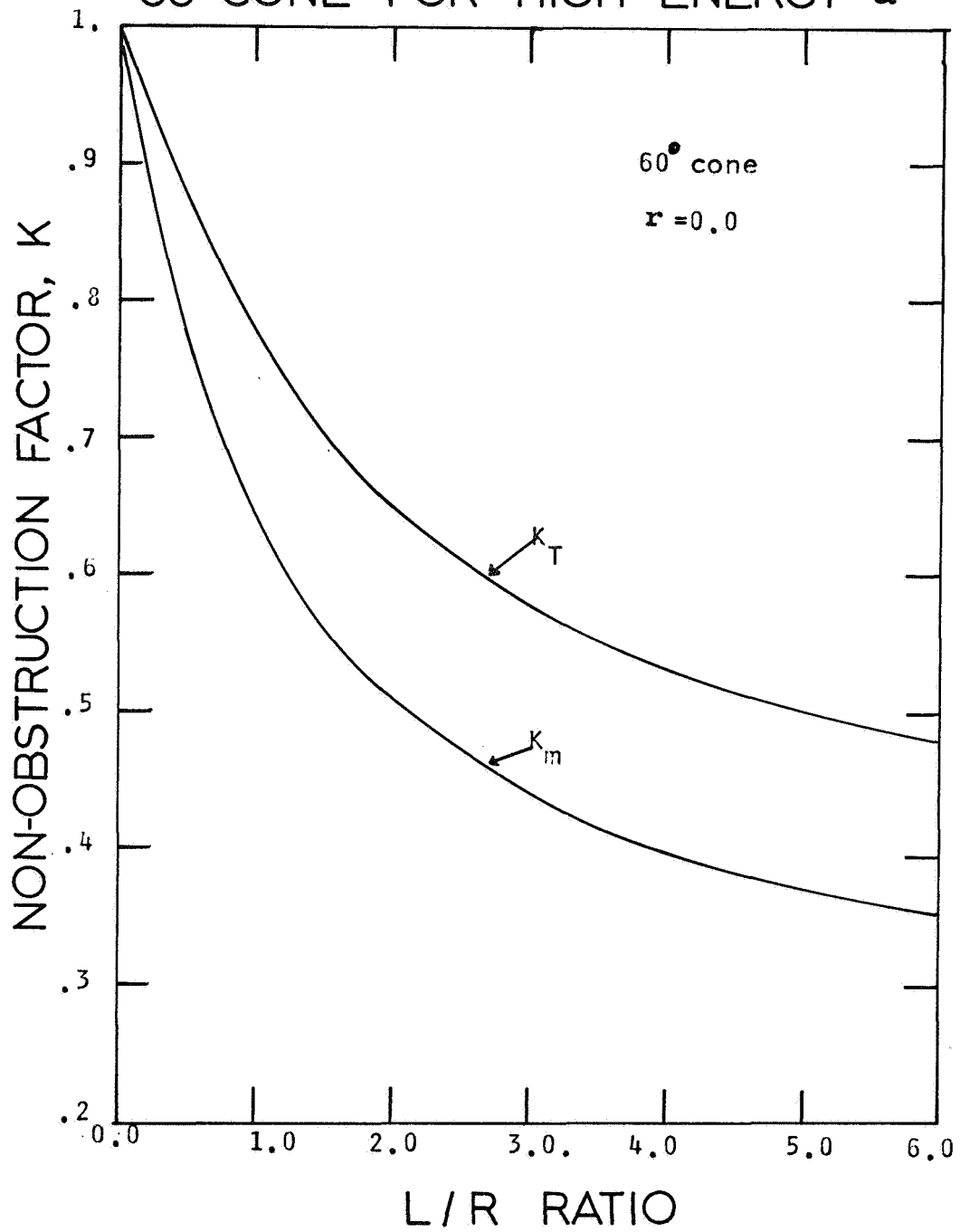


FIG 5.4 THRUST INTENSITY FOR
PURE Po^{210} DEPOSIT

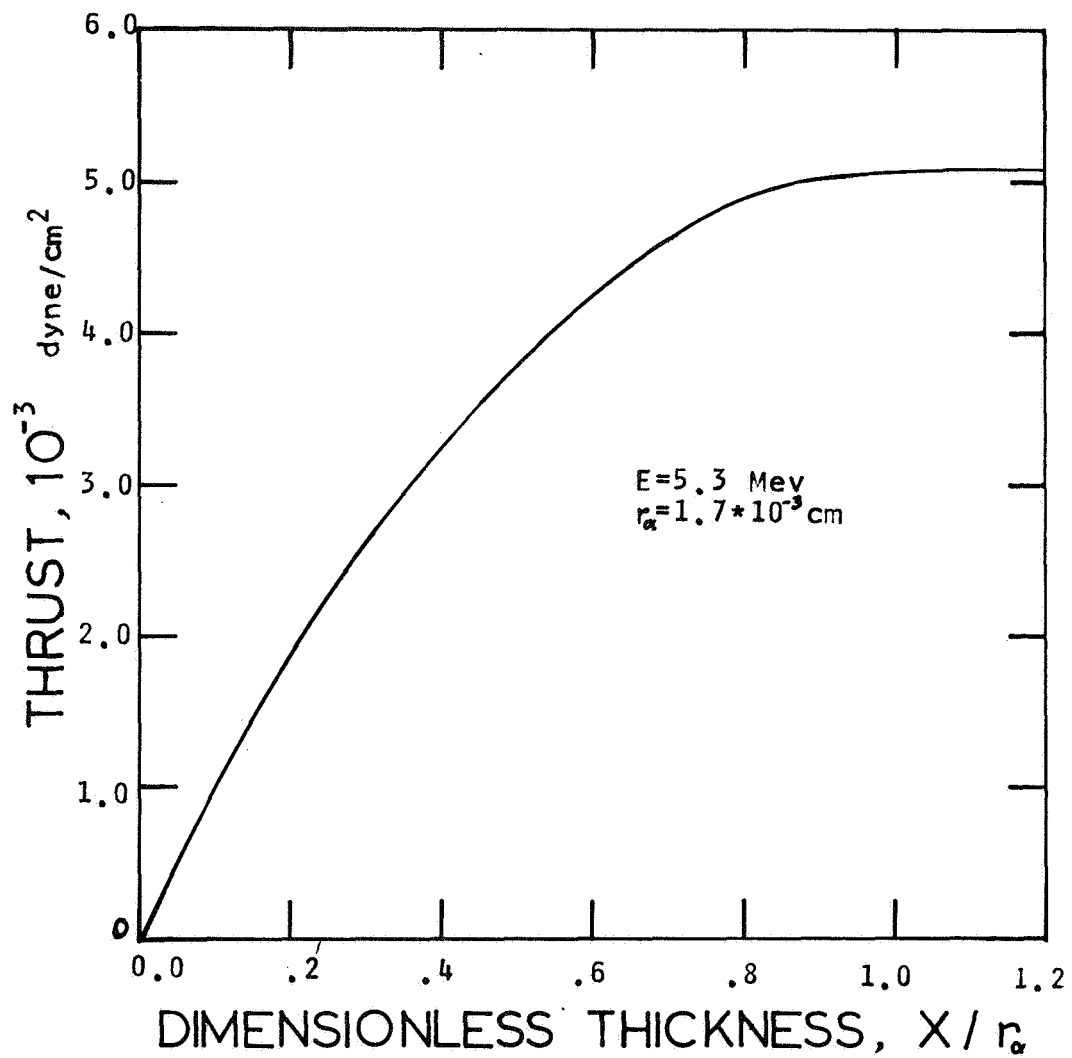


FIG 5.5
HEATED NOZZLE EFFECT ON
THRUST NON-OBSTRUCTION FACTOR

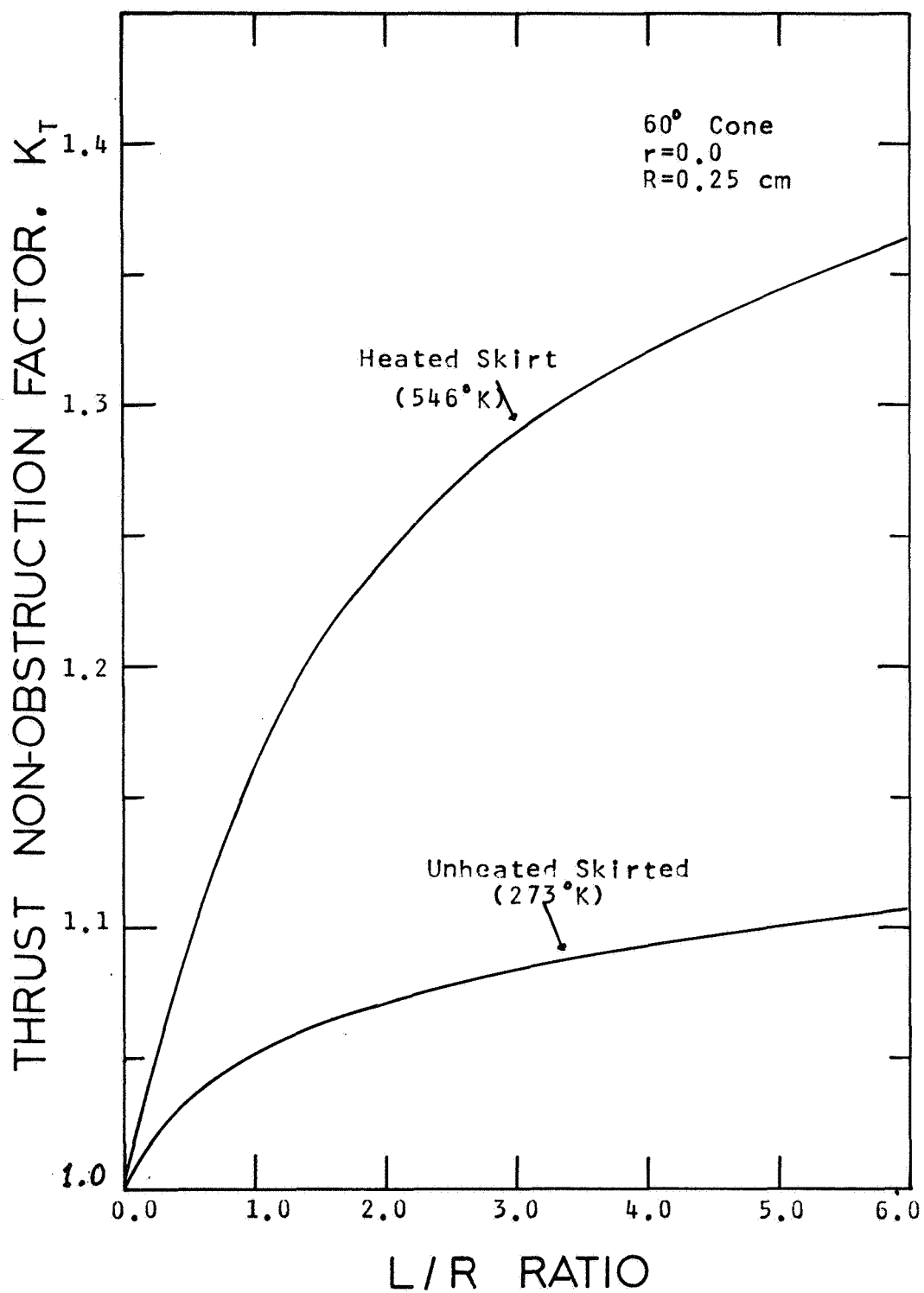


FIG 5.6 REGRESSION OF FUEL IN
CYLINDRICAL MICROTHRUSTER (BOL)

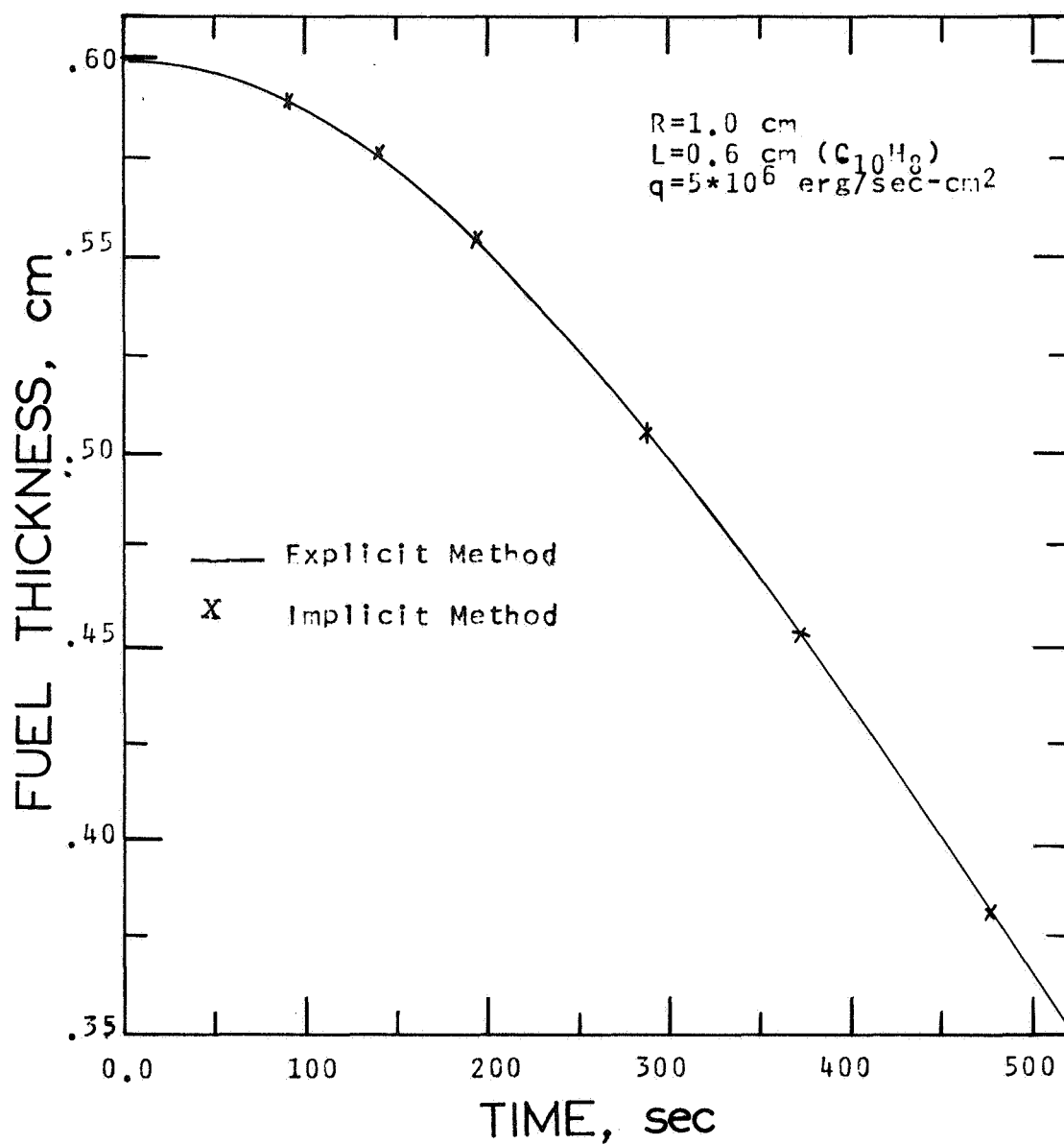


FIG 5.7 SURFACE TEMPERATURE OF
CYLINDRICAL MICROTHRUSTER (BOL)

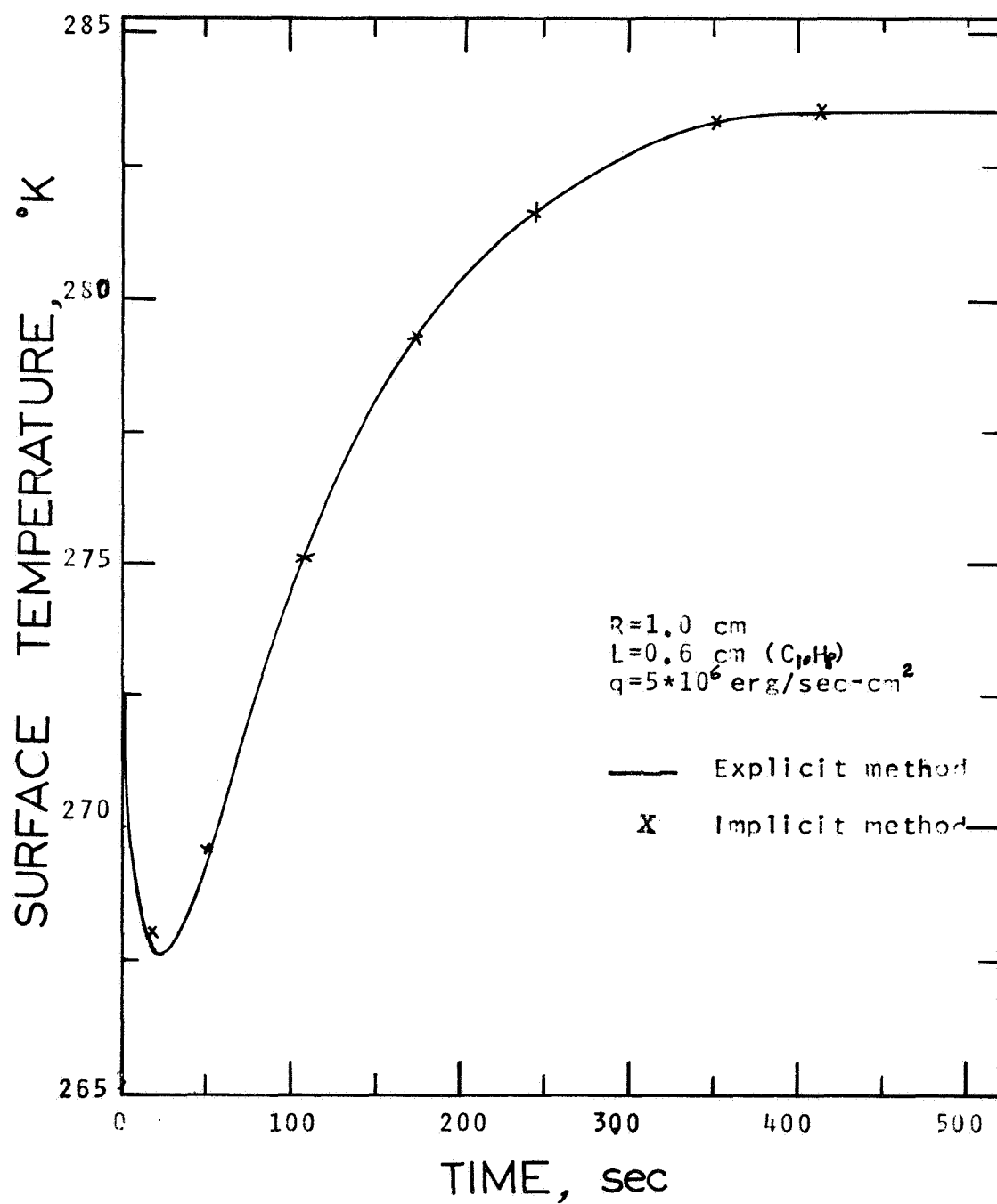


FIG 5.8 MAXIMUM TEMPERATURE IN
CYLINDRICAL MICROTHRUSTER (BOL)

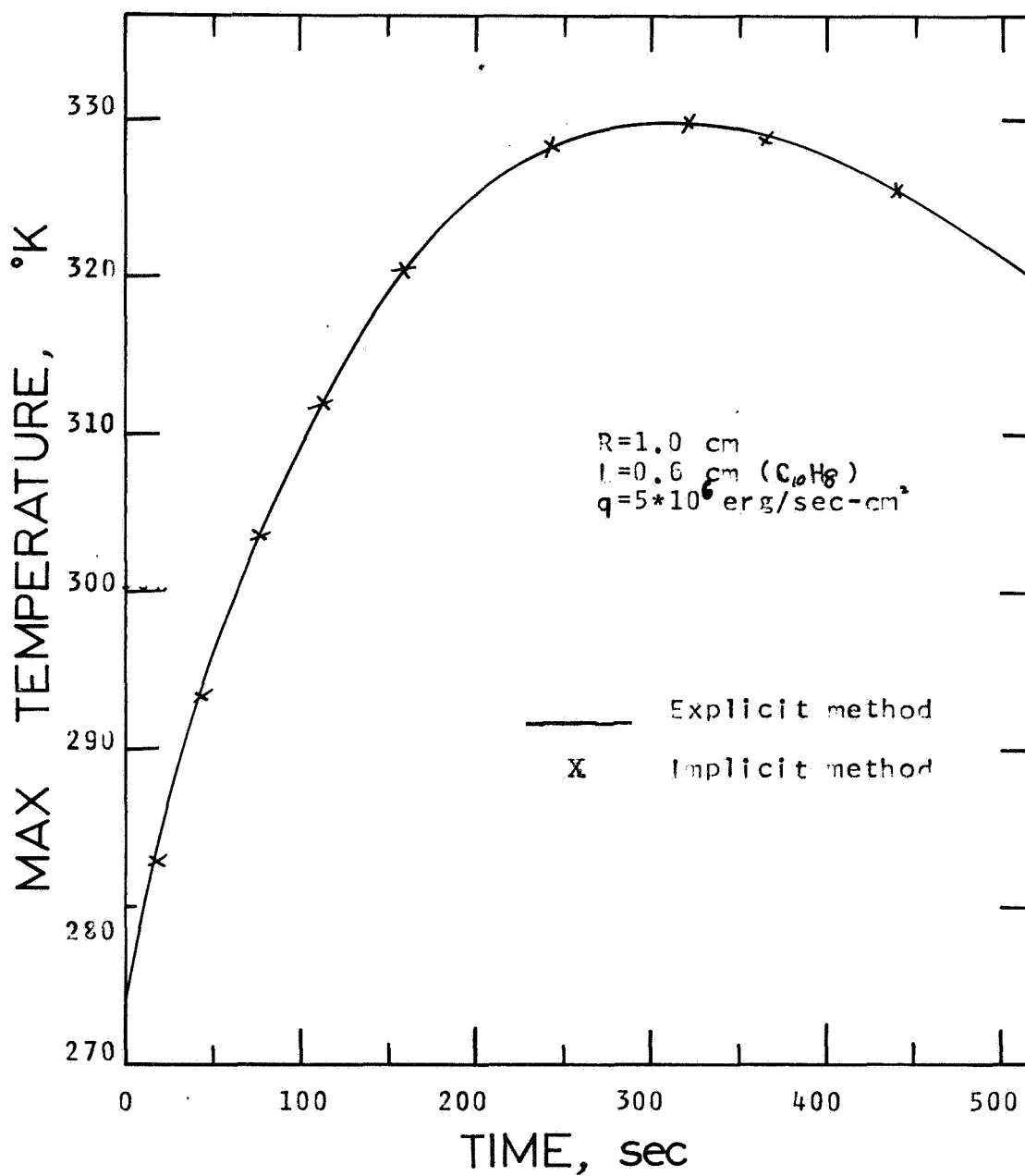


FIG 5.9 REGRESSION OF FUEL IN
CYLINDRICAL MICROTHRUSTER (EOL)

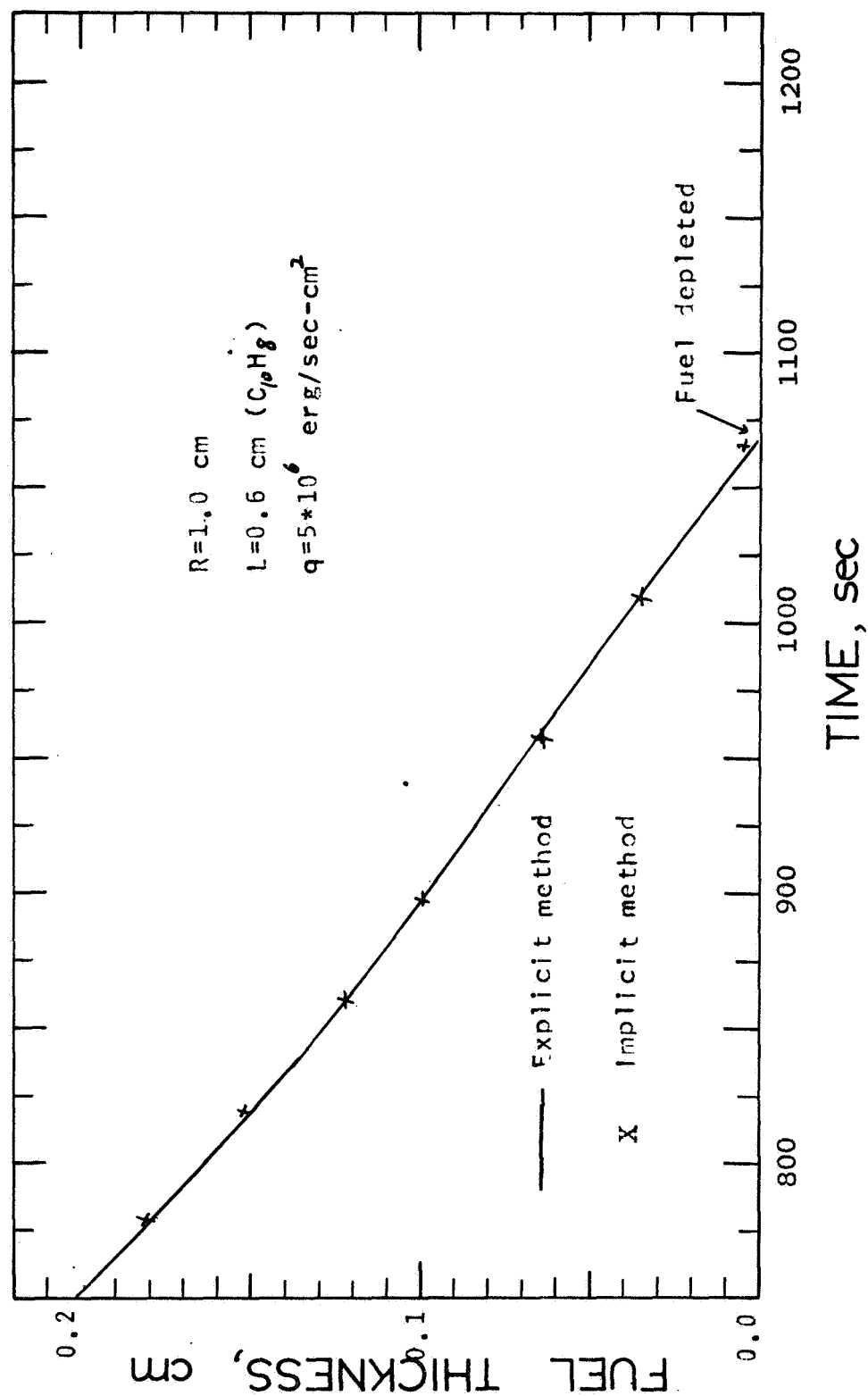


FIG 5.10 SURFACE TEMPERATURE OF
CYLINDRICAL MICROTHRUSTER (EOL)

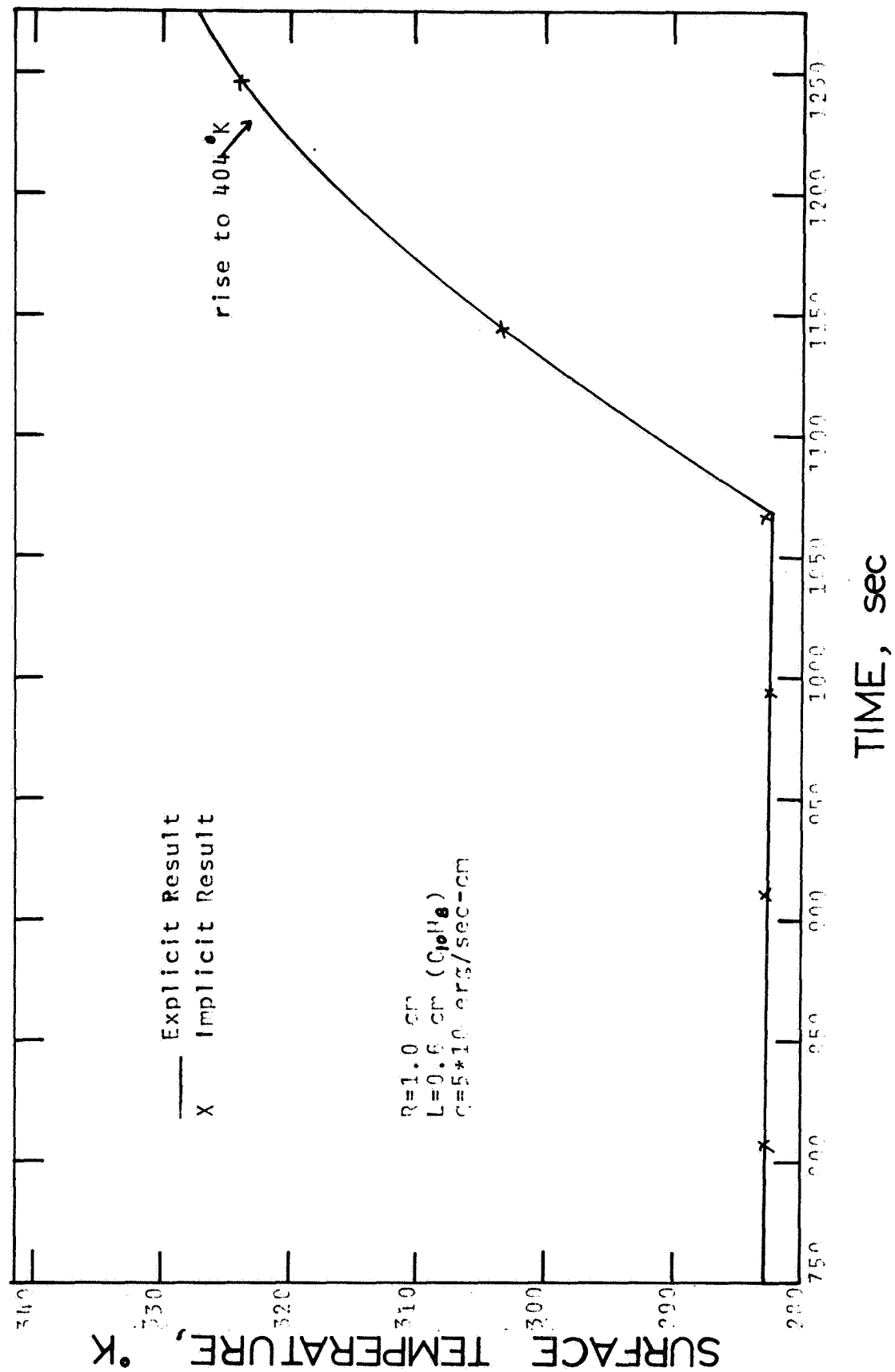


FIG 5.11 MAXIMUM TEMPERATURE IN
CYLINDRICAL MICROTHRUSTER (EOL)

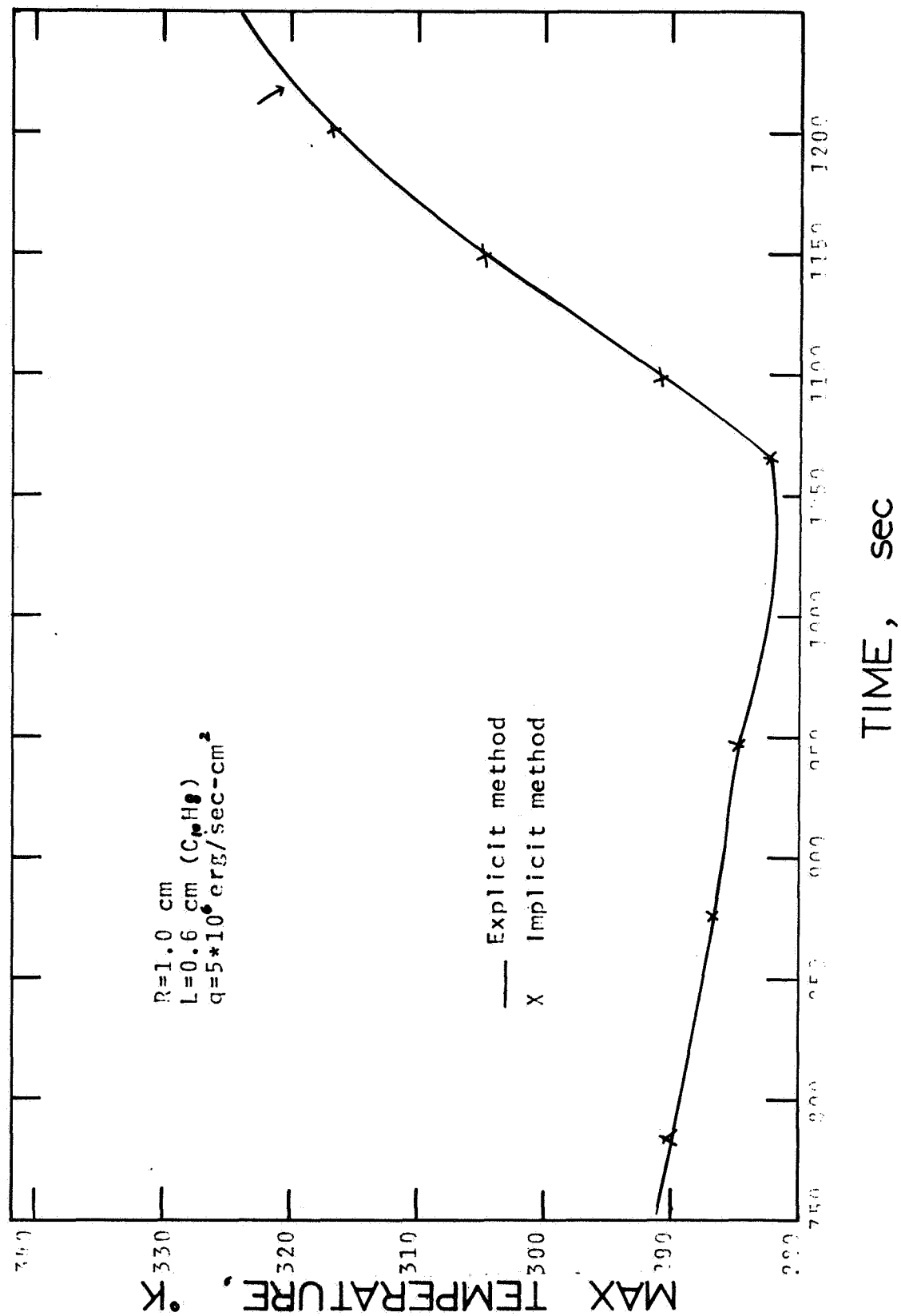


FIG 5.12
NON-OBSTRUCTION FACTORS vs
L/R FOR CYLINDRICAL CONE

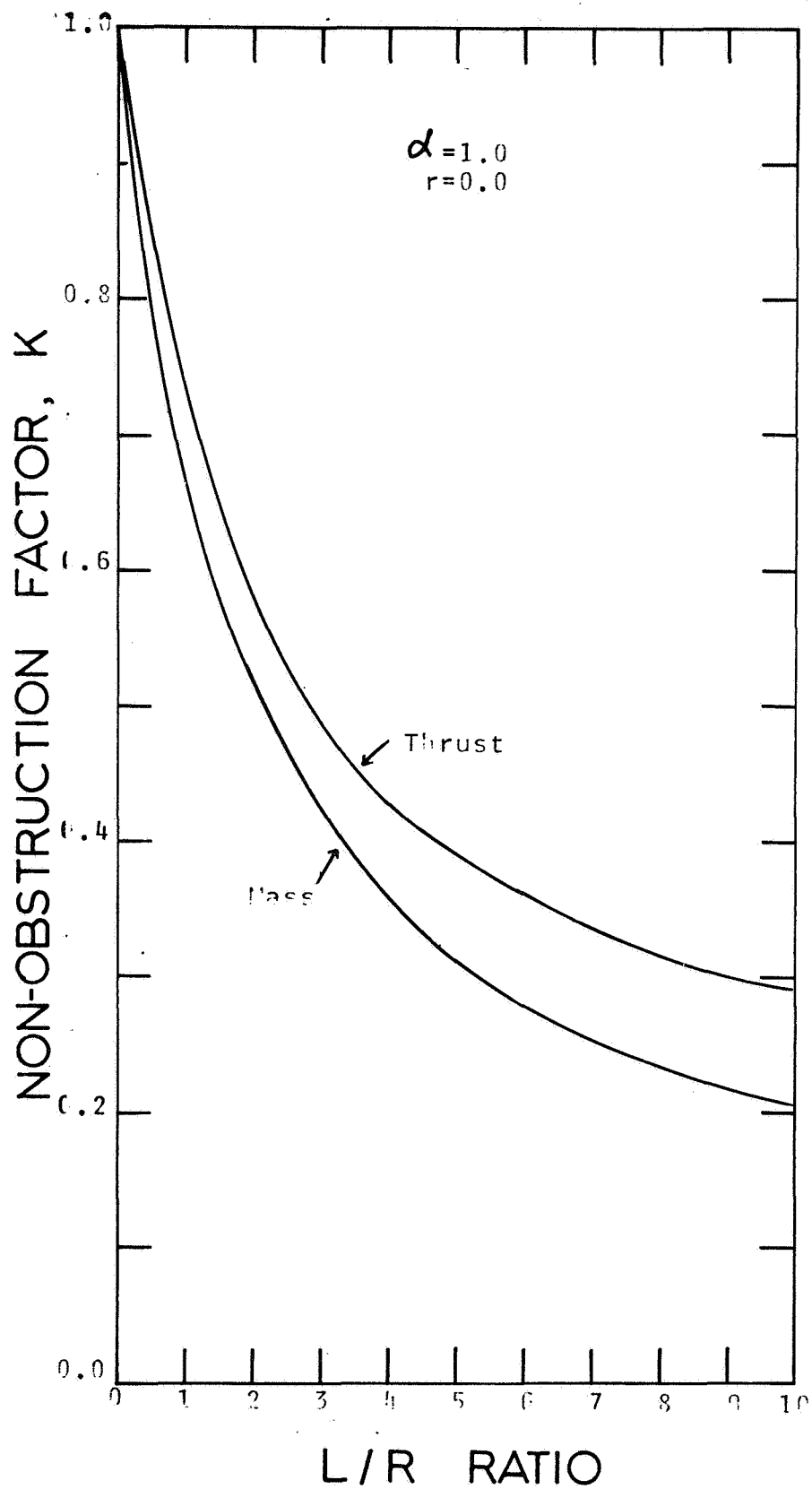


FIG 5.13 NON-OBSTRUCTION FACTORS
vs α FOR CYLINDRICAL CONE

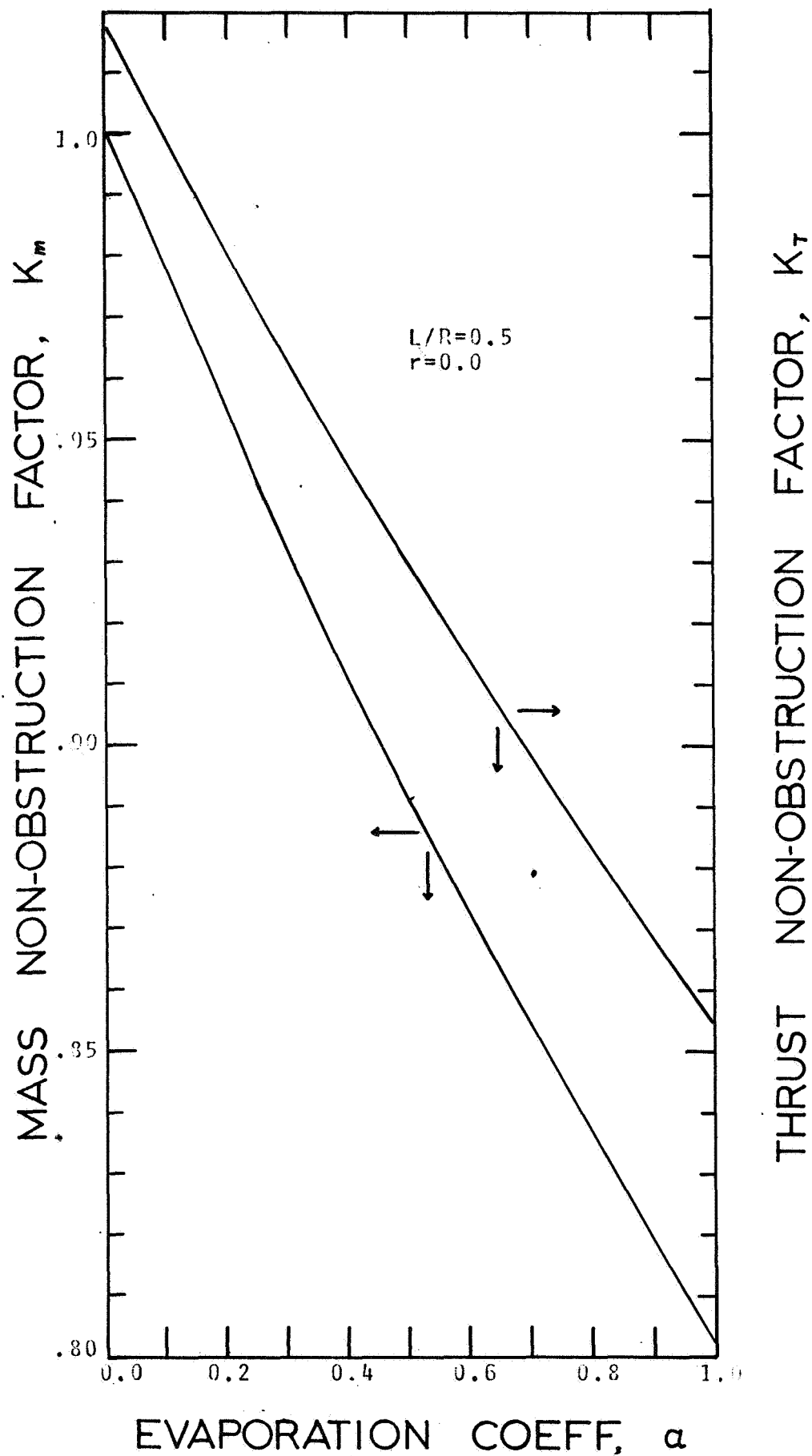


FIG 5.14 OPTIMIZATION OF CONE ANGLES

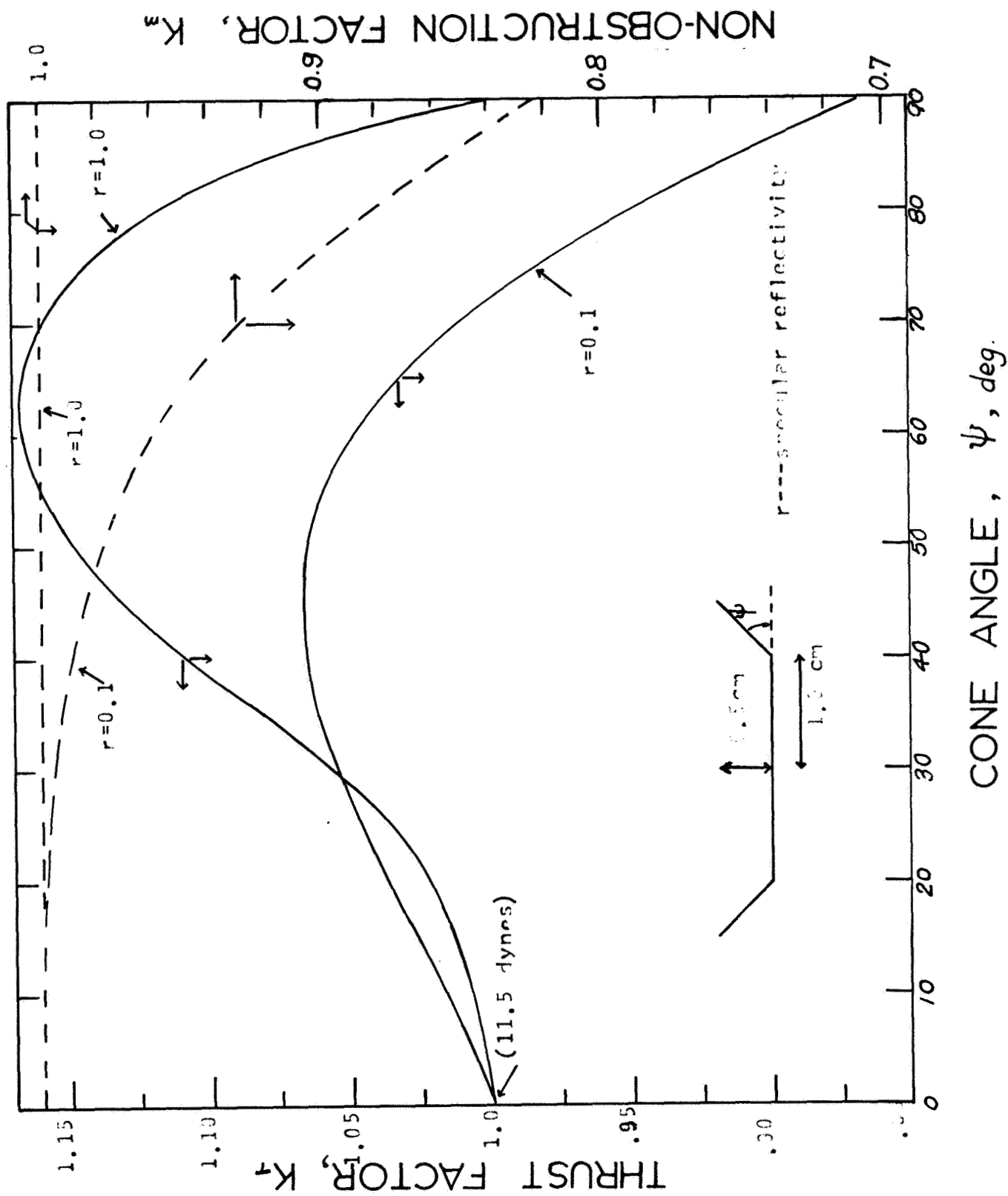


FIG 5.15 SURFACE
TEMPERATURE BY ADI METHOD

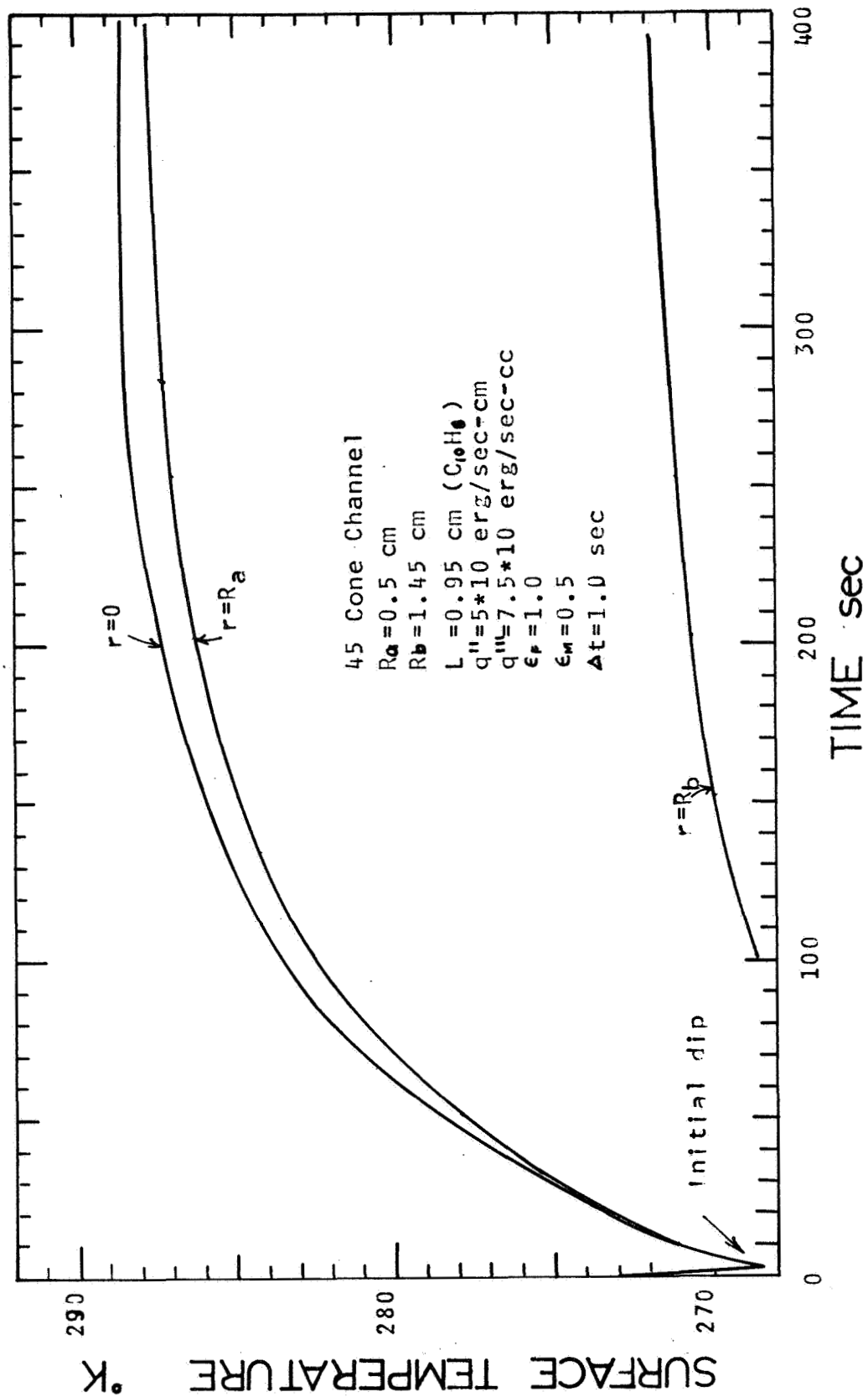


FIG 5.16
EXTRAPOLATION OF THROAT AREA

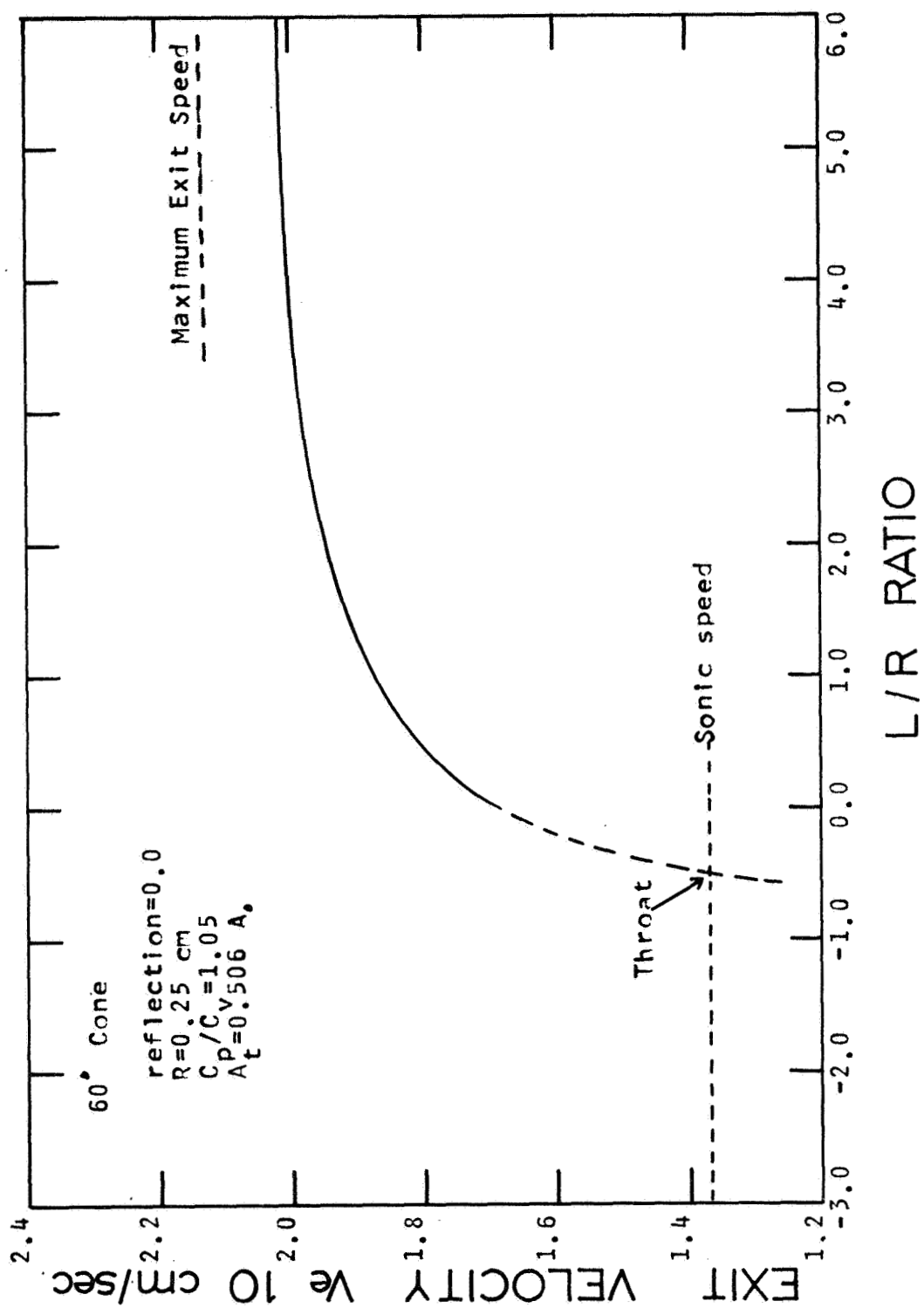


TABLE 5.1

CHARACTERISTICS OF RADIOISOTOPIC HEAT SOURCES

	POLONIUM	PLUTONIUM	CURIUM	CURIUM
	PO-210	PU-238	CM-242	CM-244
HALF-LIFE (YR)				
ALPHA DECAY	0.38	86	0.45	18
FISSION	∞	4.9×10^{10}	7.2×10^6	1.4×10^7
DECAY (MEV)				
ALPHA	5.3	5.49	6.11	5.80
GAMMA	0.8	0.044	0.04	0.04
FUEL FORM	METAL	OXIDE	OXIDE	OXIDE
DENSITY (G/CC)	9.9	10	9	9
W/GM (PURE)	141.	0.56	120	2.65
PURITY	0.95	0.80	0.90	0.95
W/CC (FUEL)	815	3.9	882	20.4
CI/W	32	30	28	29
SHIELDING	MINOR	MINOR	MINOR	MODERATE
CAPACITY (KG/YR)	1	15	0.15	3
SOURCE STRENGTH				
(N/SEC-W)	3.2×10^3	5.2×10^4	4.0×10^5	4.6×10^6
FUTURE COST				
(\$/W)	20	540	17	64

*REFERENCES (34), (35)

TABLE 5.2

COMPARISON OF RESULTS FROM TUBNOF AND CONNOF

L/R	γ	K_m	K_m
	(REF)	(TUBNOF)	(CONNOF)
0.5	0.0	0.80291	0.8023
1.0	0.0	0.67293	0.6728
1.0	0.1	0.69910	0.6988
1.0	0.2	0.72630	0.7261
2.0	0.0	0.51486	0.5150
3.0	0.0	0.41974	0.4211
4.0	0.0	0.35619	0.3589
5.0	0.0	0.31074	0.3138

*NOTE THE CONE ANGLE FOR CONNOF CALCULATION
IS FOR 88.99 DEGREES RATHER THAN 90 DEGREES.

TABLE 5.3

PHYSICAL PROPERTIES OF NAPHTHALENE AND BIPHENYL

	NAPHTHALENE	BIPHENYL
FORMULAR	C ₁₀ -H ₈	C ₁₂ -H ₁₀
M.P. (°C)	80.3	68.8
SPEC. HT.		
(CAL/GM-°C)	0.315	0.307
TH. COND.		
(W/CM-°C)	0.0038	0.0037
MOLE. WT.	128.2	154.2
HT. OF SUB.		
(KCAL/MOLE)	14.23	17.37
DENSITY		
(GM/CC)	1.145	1.18
CONST. A	11.45	10.38
CONST. B	3729	3799
SONIC SPEED		
AT 0 °C (CM/SEC)	1.367×10^4	1.243×10^4

*NOTE THE ABOVE CONSTANTS WERE OBTAINED PARTLY FROM
 PHYSICAL-CHEMICAL CONSTANTS OF PURE ORGANIC COMPOUNDS,
 VOL II.

CHAPTER 6

APPLICATIONS TO SUNBLAZER-TYPE SOLAR PROBE

6.1 Spacecraft Dynamics

6.1.1 Passive attitude control system

A complete passive attitude control system for the present Sunblazer probe would consist of an erecting shell, a restoring vane, an annular viscous damper and two pairs of microthrusters. The reason to have two pairs instead of one pair is mainly to maintain the axisymmetry of the moment of inertia.

However, a requirement for both the erecting shell and the restoring vane may be questionable. In principle, either the erecting shell or the restoring vane should be able to provide the necessary erecting and precession torques to stabilize the spacecraft. The net reradiative force acting on the erecting shell is shown in Chapter 4 to have a normal component and a parallel component. The normal component is capable of aligning the spacecraft with the sun line such that the solar panel at one end of the probe will face the sun. The parallel component will cause the spacecraft to precess about the sun-pointing axis. Even if the initial precession angle (angle between the sun-pointing vector and the spin vector) is greater than 90° , the normal force component will, due to the erecting shell, increasingly reduce the cone angle to less than 90° . Before

the cone angle is reduced below 90° , the precession is retrograde and thereafter, the precession becomes direct (precess in the same sense as the spin). This direct precession is similar to a spinning top under a gravity torque (36). As long as the precession torque does not exceed a limit (see Section 6.1.3), the spacecraft will be very stable. In the meantime, the erecting torque, though diminishing in magnitude, will gradually reduce the cone angle toward zero.

On the other hand, a restoring vane can be designed to accomplish the same task. This is done by making the external surface of the vane, which will 'see' the sun, a moderate absorber of solar radiation and a poor thermal radiation emitter. The internal surface, however, is coated with a highly emissive material so that the absorbed energy is radiated away from the sun by the internal surface of the vane as shown in Figure 6.1. In this manner, the solar pressure on the external surface of the vane, due to the absorption and the reflection, will always sustain a stable retrograde precession because of the negative precession torque (see Figure 6.2). The thermal reradiation from the internal surface of the vane will have the same function as the erecting shell. The net reradiative force has a normal component to erect the spacecraft and a parallel component to cancel only a portion of the solar pressure force acting on the external surface.

As a result, both the erecting shell and the restoring vane are able to erect the spacecraft. The main differences between them are: (1) the erecting force from the erecting shell will always be larger than that from the restoring vane on per unit surface area basis; (2) The erecting shell will force the spacecraft to have direct precession rather than retrograde precession as in the case of using restoring vane.

6.1.2 Euler's dynamical equations

The extension of Newton's law to rotational motion is that the time rate of change of angular momentum is equal to the applied moment, i.e.

$$\vec{M} = d\vec{H}/dt + \vec{\Omega} \times \vec{H} \quad (6.1)$$

where $\vec{\Omega}$ is the angular velocity for axis system.

In an axisymmetric spacecraft, $I_z = I_y = I_T$ (subscript T for transverse axis) and the relation between the absolute angular velocity of the body $\vec{\omega}$, and that of the body axis, $\vec{\Omega}$ is

$$\Omega_y = \omega_y ; \quad \Omega_z = \omega_z ; \quad \Omega_x \neq \omega_x$$

The corresponding component form of the above moment's equation, or the Euler's dynamical equations, are

$$\begin{aligned} M_x &= I_x d\omega_x/dt \\ M_y &= I_y d\omega_y/dt - \Omega_x I_T \Omega_z + \Omega_z I_x \omega_x \\ M_z &= I_T d\Omega_z/dt - \Omega_y I_x \omega_x + \Omega_x I_T \Omega_y \end{aligned} \quad (6.2)$$

The ω 's are not angular velocity components in the ordinary sense of being derivatives of some spatial coordinates which describe the position of the body at time t . To describe the orientation of the spacecraft, Euler's angles are used as shown in Figure 6.2. In terms of Euler's angle, the Euler's dynamical equations become (37)

$$\begin{aligned} M_x &= I_x d\omega_x/dt \\ M_y &= I_T \ddot{\theta} - I_T \dot{\psi} \sin\theta \cos\theta + I_x \omega_x \dot{\psi} \sin\theta \\ M_z &= I_T d(\dot{\psi} \sin\theta)/dt - \dot{\theta} I_x \omega_x + \dot{\theta} I_T \dot{\psi} \cos\theta \\ \text{where } \omega_x &= \dot{\phi} + \dot{\psi} \cos\theta \end{aligned} \quad (6.3)$$

In principle, the spin moment M_x , the precession moment M_y and the erecting moment M_z as a functions of time can be found, so that the orientation of the spacecraft at any time t is the solution of the above nonlinear coupled differential equations. The difficulties are: (1) the large amount of computer time required to obtain the moment components as a function of time: (2) too many initial conditions involved. Consequently, the numerical integration solution will be very time-consuming and the result will be difficult to analyse and to draw useful conclusions from. The following sections deal with only the specialized solutions to Euler's dynamical equation.

6.1.3 Effect of various moments on precession

For steady precession as shown in Figure 6.2, θ and ω_x are constant, so the the precession is given by

$$\dot{\psi} = \frac{I_x \omega_x}{2I_T \cos \theta} \pm \left[\left(\frac{I_x \omega_x}{2I_T \cos \theta} \right)^2 - \frac{M_y}{I_T \sin \theta} \right]^{1/2} \quad (6.4)$$

For a given θ and ω_x , the precession-torque plot is shown in Figure 6.3. There is a maximum allowable precession (restoring) torque M_y^m , above which steady precession is impossible because the spacecraft will flip upside down, where

$$M_y^m = \frac{1}{4} \frac{I_x^2 \omega_x^2}{I_x} \tan \theta \quad (6.5)$$

The positive precession torque will force the spin axis to precess about the preferred axis 1 (i.e., the sun-pointing axis) in the same sense as the spin, as long as the torque is less than M_y^m . The net force acting on the spinning spacecraft due to temperature asymmetry on the erecting shell will always have a positive precession torque component. Thus a solar vane or solar sail might have to be added to insure a stable precession, i.e., to balance out all or part of the positive precession torque.

In addition to the positive precession torque component, a highly desirable erecting torque is also present. This erecting torque will force the spin axis to spiral into the preferred axis or the axis of precession, in other words, the precession cone angle is continuously diminishing. However, unless the restoring torque decreases as fast as $\sin \theta$, a possibility exists that the precession becomes unstable.

Also, during the stabilization period, the spin rate slows down, which has two serious implications. First of all, the precession torque will increase with decreasing spin because the parallel force component of the thermal radiation reaches a maximum at zero spin. Secondly, as shown in Equation (6.5) the maximum allowable precession torque decreases in direct proportion to the square of the spin. As a result, to maintain a stable precession, the despin microthruster has to be designed carefully, i.e., it should not despin the spacecraft rapidly to zero.

6.1.4 Despin rate

The spin behavior of an axisymmetric spacecraft is essentially dependent upon the microthruster spin moment alone. Its governing differential equation is simply

$$M_s = I_x d\omega_x/dt \quad (6.6)$$

For an estimate, assume there are two pairs of (i.e., a total of four) microthrusters, each of which has a throat radius of a centimeter; the microthruster has a moment arm of 20 cm and its surface is maintained at about 273°K. The despin moment is about

$$M = -4 * 20 \text{ cm} * 15 \text{ dyne} = -1200 \text{ dyne-cm} \quad (6.7)$$

A typical small satellite has an axial (or largest) moment of inertia of about

$$I_x = 5 * 10^6 \text{ gm-cm} \quad (6.8)$$

Consequently, the despin rate is of the order of $2.4 * 10^{-4}$ rad/sec which is large enough to despin the Sunblazer

satellite from 200 rpm to few rpm in 20 hours without the help of a Yo-Yo device. However, about a pound of subliming material (obtained by multiplying the total subliming surface area, surface regression rate, despin time and material density) is required to accomplish the task, so that integration with a Yo-Yo is needed to reduce the fuel requirement to a tenth of a pound. As to the residual spin torque from the alpha emission at the bottom of the cup after the material had sublimed away, for saturated deposition (see Section 5.2.2) the spin torque is about 1 dyne-cm which is quite appreciable for long term spin control because the life span of this thrust is about two to three half-lives of the alpha-emitter.

6.1.5 Erecting rate

During the despinning period, the erecting shell will nearly attain the equilibrium temperature distribution, and the nutation will be damped out by the annular viscous damper (see Section 2.3.1). Assuming the transient precession and erecting torques do not affect the attitude significantly, the initial motion of the spacecraft is simply a slow retrograde precession about the sun axis. Since the precession torque and the spin remain relatively constant, the effect of the erecting torque on the spacecraft can be found from the M_z expression of Equation (6.3). The resultant erecting rate in terms of the erecting torque is

$$\dot{\theta} = -M_z / (I_x \omega_x - 2 I_T \dot{\psi} \cos \theta) \quad (6.9)$$

For a practical design, the net precession torque (algebraic sum of the solar pressure torque and the parallel torque component from the erecting shell) is very small, hence the precession rate is usually very much smaller than the spin rate. The erecting rate is further simplified to

$$\dot{\theta} = -M_z / (I_x \omega_z) \quad (6.10)$$

A shell (thickness=0.01 cm, radius=25 cm, length=25 cm) will yield an erecting force of 0.01 dyne at the optimum spin of 0.037 rad/sec, so an erecting torque of 0.25 dyne-cm is achievable. As a result, the erecting rate for the bare shell is about 1.3×10^{-6} rad/sec and this rate will decrease as the spacecraft precession cone angle is decreased because of the reducing solar input to the shell surface. Therefore, it will take on the order of two weeks to stabilize the spacecraft.

The main drawback of the above scheme is the vulnerability to small perturbation torques because of its low spin rate. A radioisotope-heated shell can resolve this difficulty. For a surface heat flux of 0.2 watt/cm, the optimum spin rate is 0.14 rad/sec and the corresponding erecting torque is about 0.27 dyne-cm. Due to this large jump on the spin, the erecting rate is down to 4.1×10^{-7} rad/sec. Consequently, the stabilization time increase to about one month.

For short-term stabilization, the subliming material coated shell is really the best performer. Even at a spin of 0.3 rad/sec (way above the optimum spin), the erecting force is nearly 20 dynes and the erecting torque is about 450 dyne-cm. The erecting rate is 3×10^{-4} rad/sec which can damp out the precession in a few hours at most.

6.2 Possible Applications

6.2.1 Introduction

In general, any of the above erecting shells can be made to work for a solar probe, like the present Sunblazer satellite, if the spin is controlled actively. For instance, a stepping motor may be used in conjunction with an attitude sensor to switch the spin torque by turning the microthrusters such that the spin of the spacecraft can be increased, kept constant and decreased.

Disregarding the present Sunblazer attitude-control design philosophy, the erecting shell and the microthruster are able to fulfill the stabilization requirements for future solar probe missions. Three conceptual light-weight attitude control systems are described in the following sections.

6.2.2 Passive systems for inferior orbit probes

For inferior orbit probes, the solar input is quite adequate so the pure reradiative torques from a thin metallic shell and a restoring vane (reradiative internal

surface) can be acceptable in the following passive system design.

The chopped-cone microthruster is designed to have enough subliming material such that the spacecraft is very rapidly despun shortly after launch to the vicinity of optimum spin. In this low spin range, the erecting torques from the thermal reradiations (summation of the effects of the shell and vane) are most effective in reducing the precession cone angle and even at zero spin, the reradiative force is still capable of damping out the resultant librational motion (7). During this erecting period, the small recoil thrust due to the radioisotopic emission of alpha particles from the depleted microthruster despins the spacecraft to zero and then starts to spin up in the negative direction so the effects of the perturbing torques due to the interspace magnetic field, meteorites bombardments and outgassing from leak-joints can gradually be reduced. This is by no means a fool-proof system because the exact dynamical behavior of the spacecraft near zero spin is still not well understood.

6.2.3 Semi-passive system for inferior orbit probes

The disadvantages of the passive system are mainly the slow response and the inflexibility. The above passive system can be improved by installing a motor which, on command from the attitude sensor, is able to switch the spin moment from positive to zero or negative and vice versa.

One scheme which can make good use of this 'switching' motor and attitude sensor combination is the following. A cylindrical strip-gap vane as shown in Figure 6.4 with the internal surface coated with subliming material is placed at the rear of the spacecraft. At any instant, the attitude sensor detects a deviation from a preset precession cone angle, the microthrusters will be positioned properly by the switching motor to despin the spacecraft toward a predetermined spin rate where the undesired positive precession torque due to the parallel component is insignificant yet the erecting torque due to the normal component is still quite appreciable to stabilize the spacecraft. As soon as the desired attitude is attained again, the microthrusters will be switched so the spin will go back to the original steady state value at which small disturbing torques are not likely to upset the attitude of the spacecraft. In the event the attitude is thrown off, the above procedure is repeated. Since subliming materials on the vane and in the microthruster must be present throughout the mission, the sublimation rate during inactive period should be less than one cm/year. As a result, the steady state surface temperatures have to be less than 225°K in order to reduce the weight penalties for the subliming materials. The sublimation rate and pressure as functions of temperature are shown in Figures 6.5 and 6.6 for naphthalene and biphenyl. For long missions, biphenyl is a suitable material because of its low subliming rate.

Intuitively, the thrust level is dependent on the surface radiation properties as well as the gap-strip ratio. The cylindrical vane shown in Figure 6.4 should reduce the steady state fuel loss through continuous sublimation.

6.2.4 Active system for superior orbit probes

For probes designed to explore the electron density and interspace magnetic field beyond the Earth's orbits and up to 50 AU distance such as pioneer scouting satellites for the Grand Tour mission, almost all present systems have to be modified. Because of the $1/r^2$ attenuation on the solar flux, the electric power generation will have to turn to nuclear devices such as the radioisotope thermoelectric generator (RTG) or the radioisotope thermionic devices. Also, as result of long transmission path, a high-gain antenna is necessary which makes the attitude control requirements quite formidable.

Although, the erecting shell and the restoring vane will lose their appeals, the microthruster can still be used to supplant their original functions (generation of the erecting torque and the negative precession torque and the despin torque). This task is accomplished through an active coupling of the microthruster and the attitude sensor system.

The sequence of interactions to stabilize the attitude is the following. From Figure 6.7, the spin rate and the relative angular positions of each pair of microthrusters

with respect to the precession axis (i.e., the angle between the line connecting each pair of microthrusters and the precession plane or the plane of the sun-point axis and the body axis) can be determined by the attitude sensors. Then a trigger signal delayed by a preset spin angle starts the turning of each pair of microthrusters at the same rate as the spin. In each spin cycle all three moments are generated as shown in Figure 6.7. The direction of turning will only affect the erecting torque and the precession torque but not the spin torque which is always averaged to zero. The time-delay on triggering the turning will affect the waveforms of the precession torque and the erecting torque as shown in Figures 6.8 and 6.9.

The maximum averaged precession or erecting torques are only a half of the maximum spin torque. These torques are independent of the spacecraft attitude, in particular the precession cone angle, with an exception that as the cone angle reduces to zero the attitude sensor will not be able to trigger the turning properly (assuming the sensor is attached at the periphery of the spacecraft). Since the precession is a function of time, the attitude sensors may have to trigger frequently for instance, one trigger for every two or three spin cycles during the stabilization period. Once the desired attitude is attained, all torques can be reduced to zero by turning the microthrusters such that the spin torque is zero. Whenever the attitude sensors detects large deviations, this stabilization system will be

activated again.

In principle, heat-pipes can be used to control the heat flux supply for sublimation by mechanically causing the heat-pipes to contact a heat source whenever heat is required. In so doing, the fuel requirement can significantly be reduced. Alternatively, the long-lived radioisotopic recoil momentum can be used for generation of thrust, however, the stabilization time will have to increase because of the low thrust. The stabilization time can be shortened if the spacecraft is despun whenever stabilization is called for, and as soon as the stabilization is attained, the spacecraft is spun up to a steady state spin, at which the spacecraft is relatively immune to external torques.

FIG 6.1 CROSS-SECTIONAL VIEW OF VANE

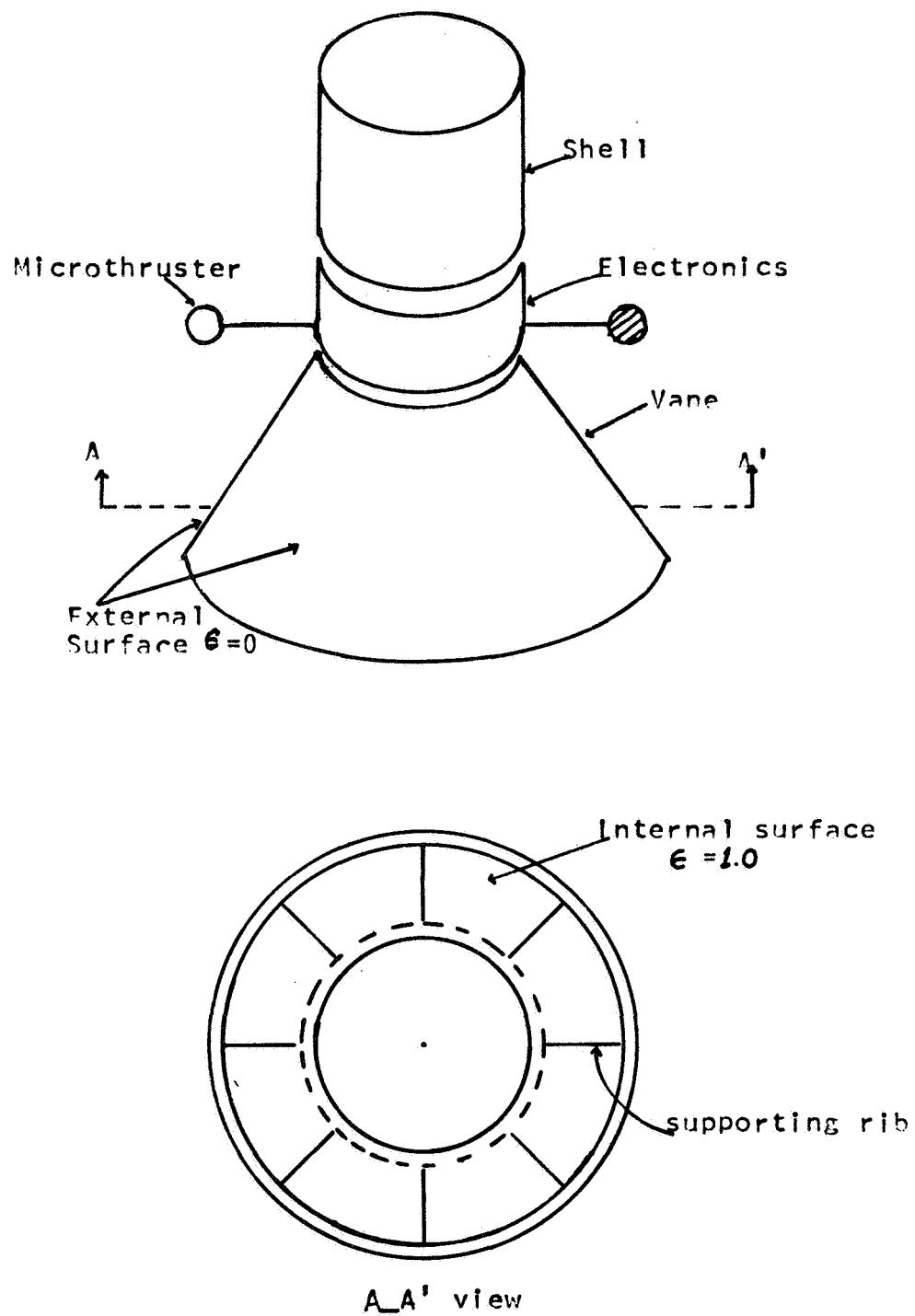


FIG 6.2 DEFINITION OF EULER'S ANGLES

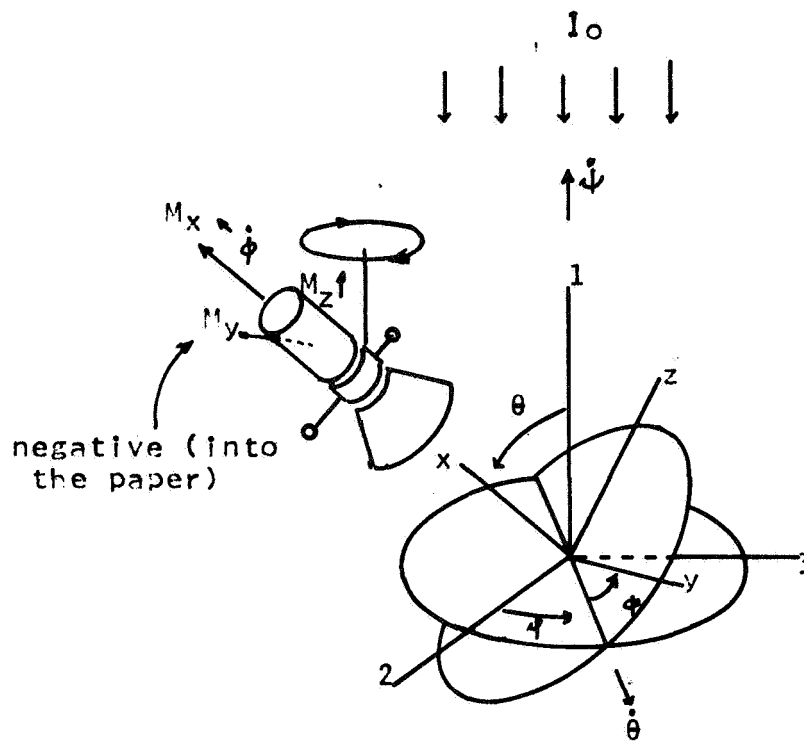


FIG 6.3 GRAPHICAL REPRESENTATION OF Eq (6.4)

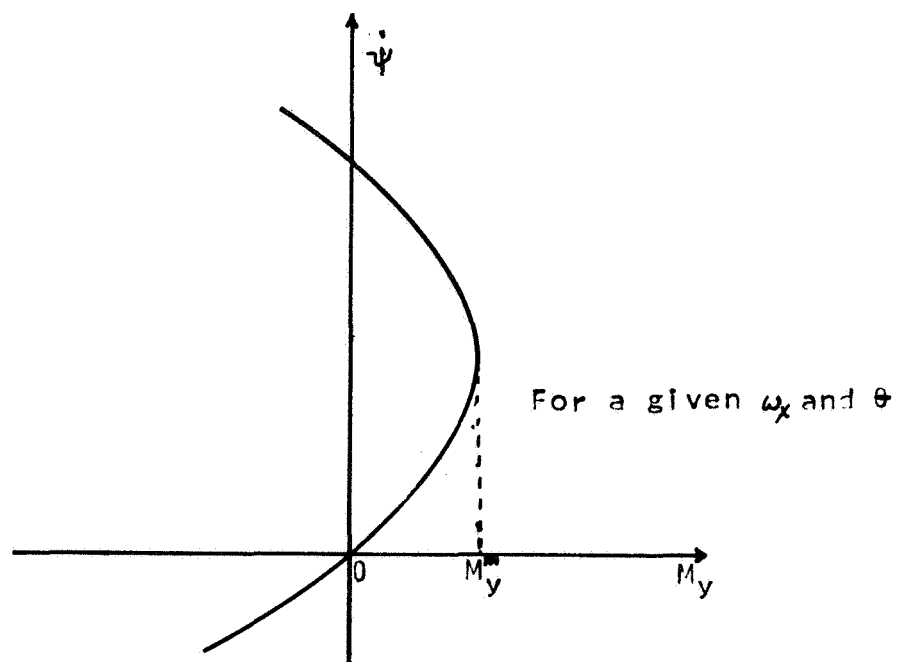


FIG 6.4 CROSS-SECTIONAL VIEW
OF STRIP GAP VANE

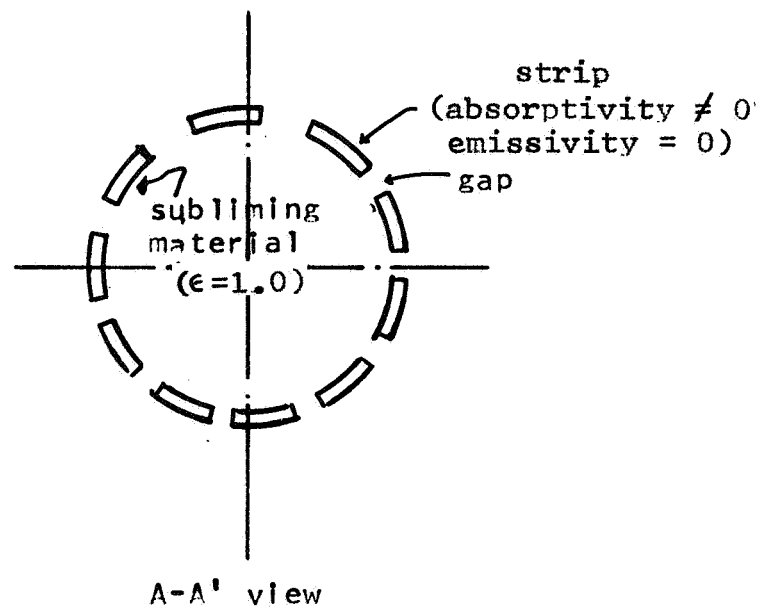
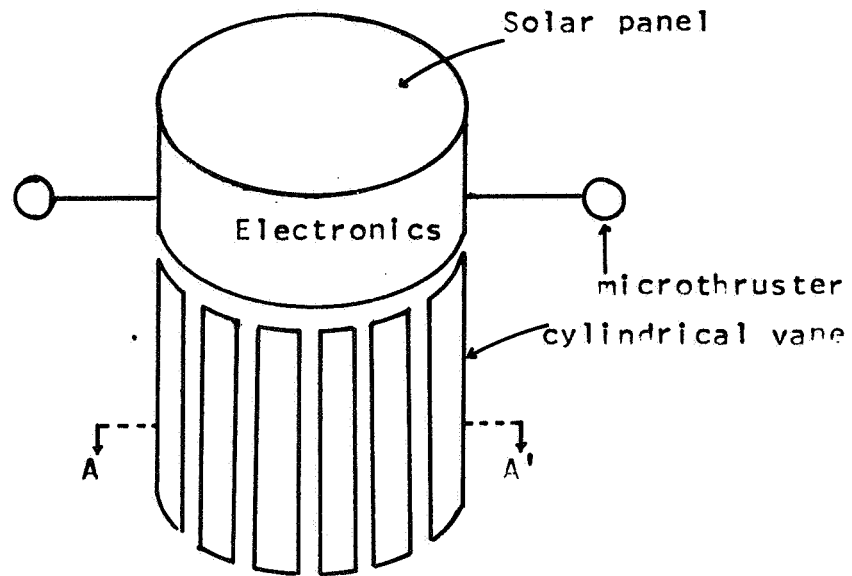


FIG 6.5 SUBLIMING PRESSURE
vs TEMPERATURE

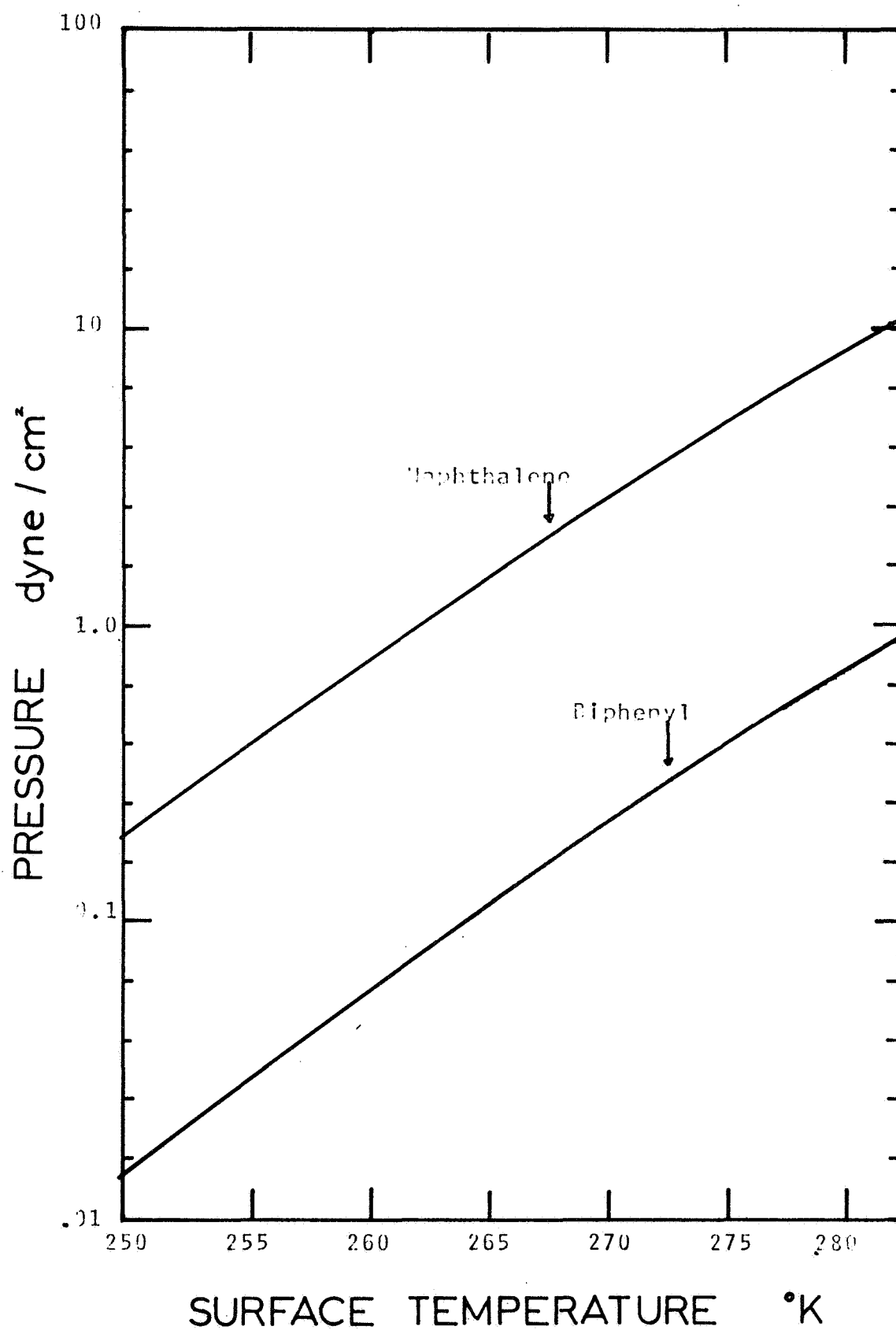


FIG 6.6 SUBLIMING RATE
vs TEMPERATURE

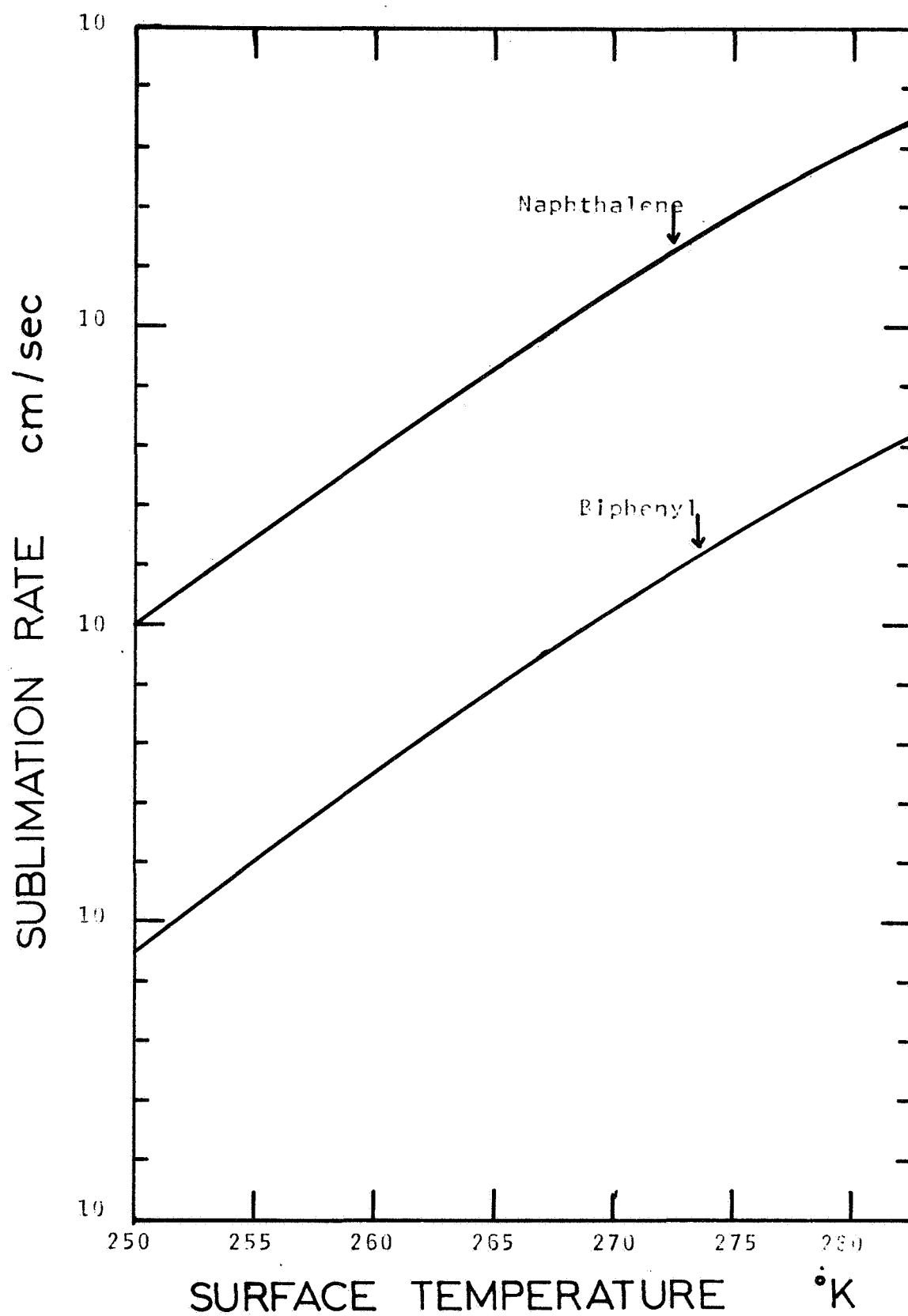


FIG 6.7
RESULTANT THRUSTS FOR SYNCHRONIZED
TURNING OF MICROTHRUSTER (trigger $\theta=0$)

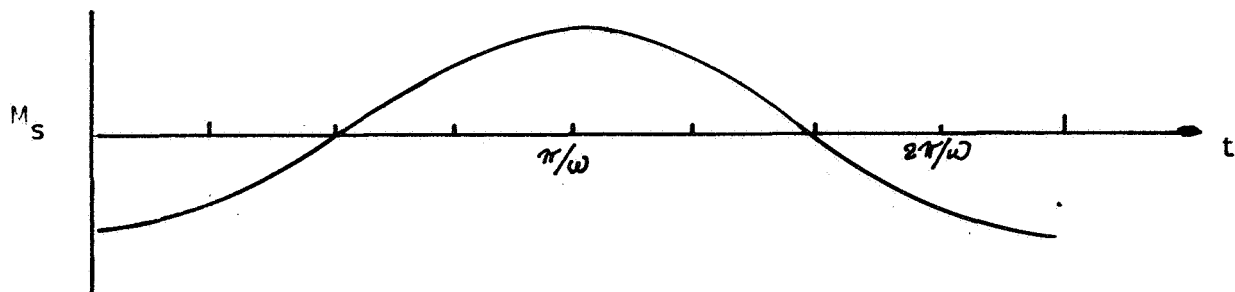
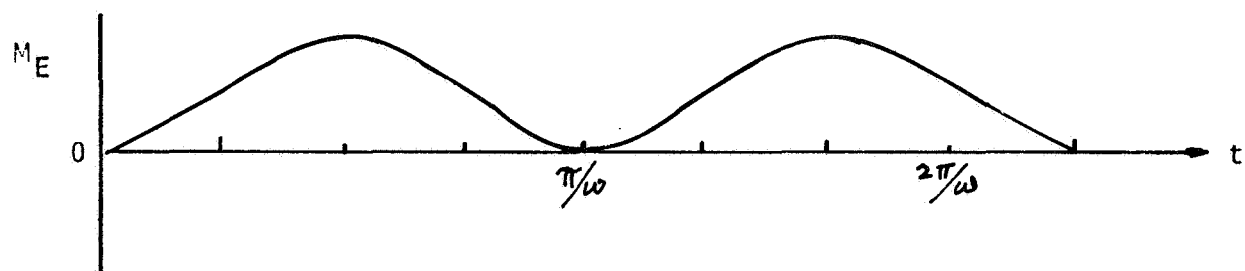
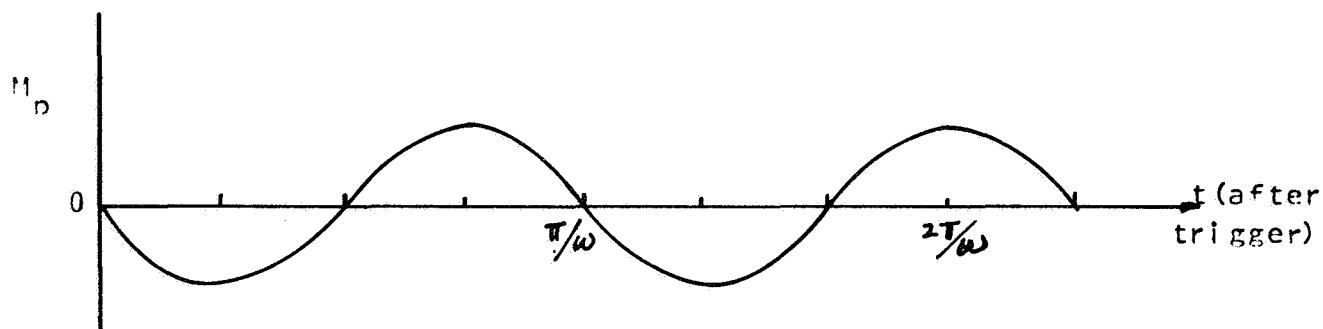
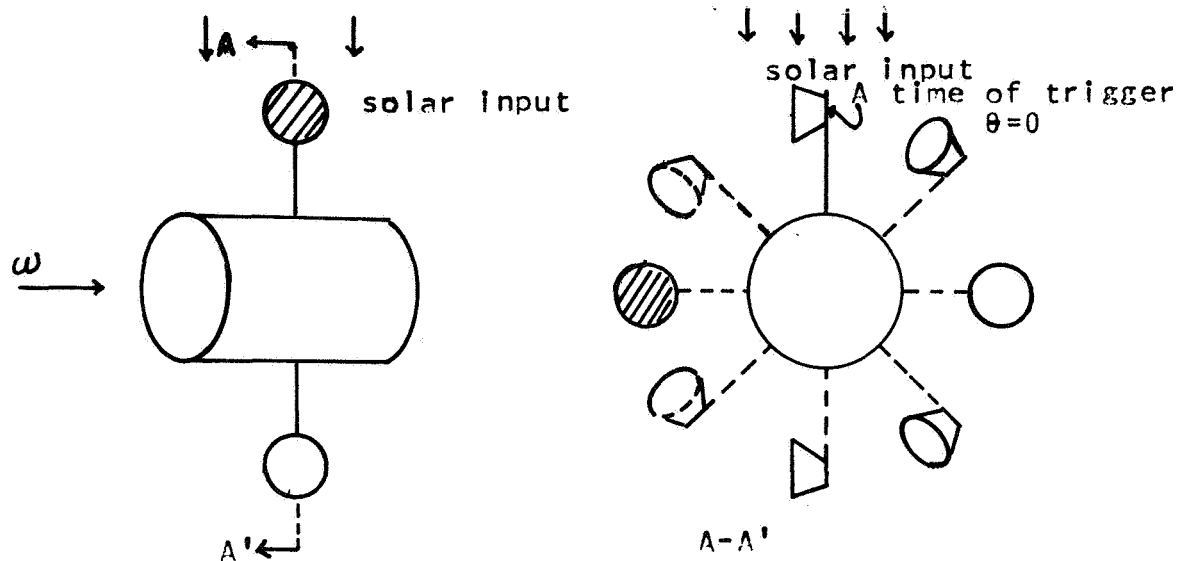


FIG 6.8
RESULTANT THRUSTS FOR SYNCHRONIZED
TURNING OF MICROTHRUSTER (trigger $\theta = 90^\circ$)

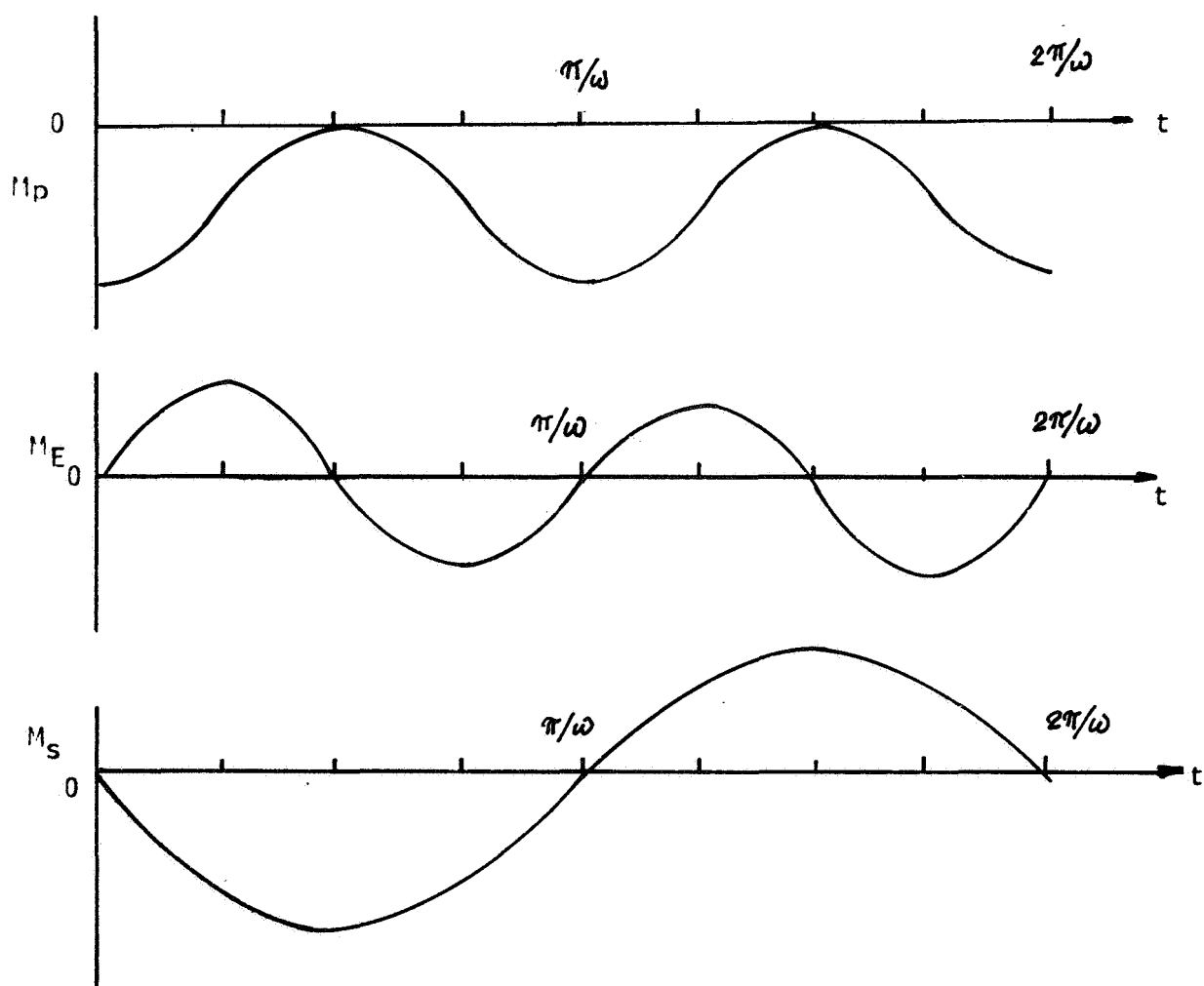
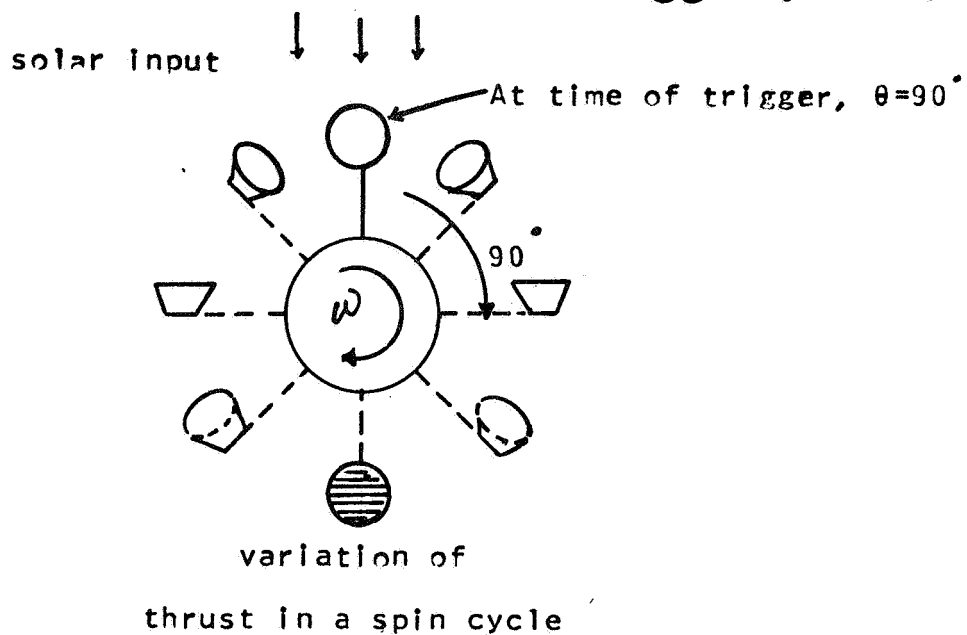
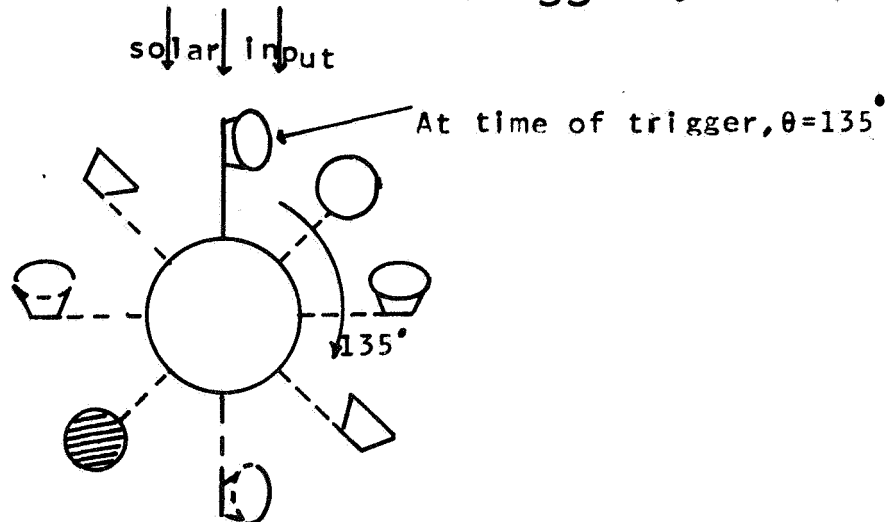
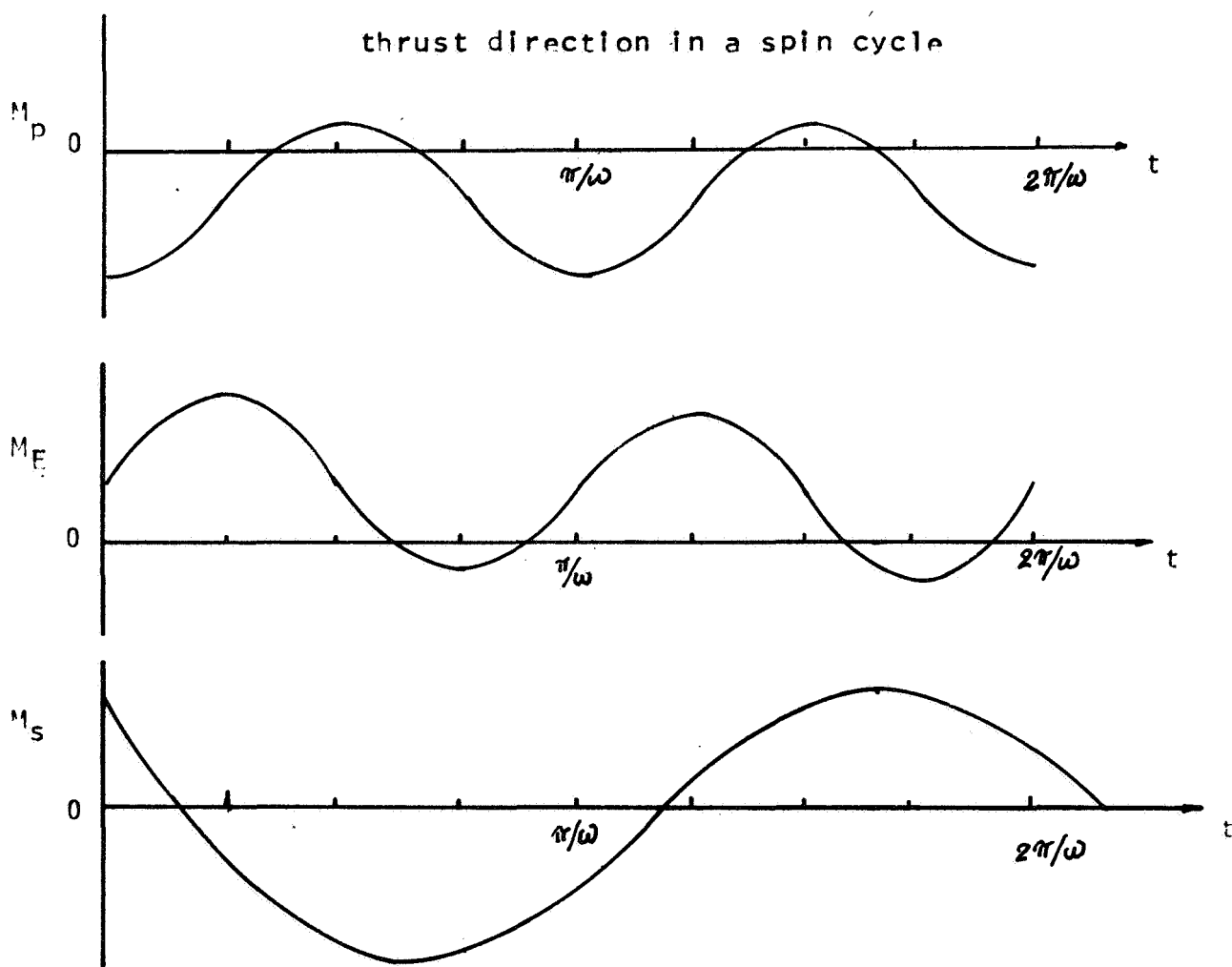


FIG 6.9
RESULTANT THRUSTS FOR SYNCHRONIZED
TURNING OF MICROTHRUSTER (trigger $\theta=135^\circ$)



Variation of
thrust direction in a spin cycle



CHAPTER 7

CONCLUSIONS AND RECOMMENDATIONS

7.1 Conclusions

The conclusions reached in studying the applications of radioisotopes and subliming materials for attitude control of small solar probes are listed below.

(1) Alpha-emitting radioisotopes with moderate half-lives are much superior to beta and gamma emitters in applications for attitude control. These isotopes can readily increase the optimum spin of an erecting shell so that the spacecraft is more immune to disturbing torques. Furthermore, they are indispensable in supplying uniform thermal energy to a subliming microthruster for fast spin control. Additionally, they are useful to generate small recoil thrust for long term, fine spin control.

(2) Organic subliming materials are found to be very suitable for use in magnifying the erecting torque from an coated erecting shell by several orders of magnitude over a wide range of spin in comparison with a bare thin metallic shell. As a result, the erecting shell can still function effectively even at a relative high spin rate.

(3) A microthruster fueled with subliming material can convert almost all the thermal energy imparted to the sublimed molecules into useful thrust by proper design of the nozzle cone angle and length.

(4) At a given sublimation rate, the thrust can be further increased if a portion of the nozzle skirt is heated radioisotopically.

(5) The applications of microthrusters and/or erecting shell are found to be attractive for stabilizing the Sunblazer probe. With proper feed-back control mechanisms, the applications of the above devices are able to be extended to a wide variety of satellites. In particular, a pair of microthrusters can produce torques in all three body axes to control the attitude of any light spacecraft.

Investigations on other required studies led to the following conclusions.

(1) In many cases of interest, the transient thermal analyses of erecting shells and microthrusters, can be carried out by considering only zero or one spatial dependence without appreciable loss of accuracy. Numerical instability is found to limit the time step for ADI solution of a subliming microthruster where both radial and axial heat conduction effects are accounted for.

(2) The transient period for an erecting shell is short (less than an hour) if the attitude of the spacecraft is fixed. However, during stabilization, the attitude constantly changes, so the transient effect should be included in detailed dynamic analyses.

(3) The numerical technique (modified Monte Carlo) developed for the non-obstruction factor calculations of molecular flow is very flexible, accurate, and can include

complex physical phenomena. The results were applied to study the evaporation process and found to be useful.

(4) The above numerical technique was adapted to analyze the gas dynamic aspect of the subliming microthruster. The result clearly paved the way to an improved design of the microthruster.

7.2 Recommendations for further studies

The present study is by no means complete. Several areas are open for immediate further research.

(1) The method of calculation of the molecular collision effect on the non-obstruction factor needs refinement, since the evaporation coefficients derived from existing experimental data of mass flow experiments appear to be low thus suggesting that the molecular collision effects used in obtaining the evaporation coefficients have been underestimated.

(2) The technique developed for non-obstruction factor calculation should be applicable to shielding calculations involving neutron and gamma ray streaming through a gap or a beam-port.

(3) The assumption that the sublimation surface reflection coefficient is one minus the evaporation coefficient can be tested experimentally as outlined in Section 3.2.3. If it is verified, the evaporation coefficient theory will be placed on a firmer base.

(4) In the chopped-cone microthruster analysis, the sublimation surface is assumed flat, but in reality the surface becomes concave. The effects of this curved subliming surface on the thrust are yet to be investigated.

(5) Utilization of molecular dissociation may offer a means for a marked increase in microthruster performance, but a radical change in the design proposed here would be required in order to provide the few electron-volts of energy required per molecule to induce molecular dissociation.

(6) Detailed analyses should be carried for the dynamic behavior of solar probes which incorporate the various erecting shell and microthruster designs proposed here in order to determine the specific design requirements for specific missions.

APPENDIX A

APPROXIMATE ANALYTIC SOLUTION OF $t-\theta$ PARABOLIC PARTIAL DIFFERENTIAL EQUATION

The partial differential equation is of the form

$$A \frac{\partial T}{\partial t} = B \frac{\partial^2 T}{\partial \theta^2} + C T^4 + D F(\theta, t) \quad (A.1)$$

where symbols are defined in Appendix M, is used for Thin Shell Approximation in Section 4.3.4. At steady state, the temperature distribution has the approximate form of

$$T(\theta, t) = T_{avg} [1 + M \sin(\theta + \omega t + \psi)] \quad (A.2)$$

By trigonometric expansion, $T(\theta, t)$ becomes

$$T(\theta, t) = T_{avg} [1 + M_1 \cos(\omega t + \theta) + M_2 \sin(\omega t + \theta)] \quad (A.3)$$

and

$$\frac{\partial T}{\partial t} = T_{avg} [-M_1 \omega \sin(\omega t + \theta) + M_2 \omega \cos(\omega t + \theta)] \quad (A.4)$$

$$\frac{\partial^2 T}{\partial \theta^2} = T_{avg} [-M_1 \cos(\omega t + \theta) - M_2 \sin(\omega t + \theta)] \quad (A.5)$$

$$T^4 \cong T_{avg}^4 [1 + 4M_1 \cos(\omega t + \theta) + 4M_2 \sin(\omega t + \theta)] \quad (A.6)$$

The solar input $F(\theta, t)$ is a half-rectified sinusoidal and can be expanded as

$$F(\theta, t) \cong \left[\frac{1}{\pi} + \frac{1}{2} \sin(\omega t + \theta) \right] \quad (A.7)$$

Substituting the above quantities into the governing differential equation and neglecting the higher order terms.

$$\begin{aligned} A T_{avg} \omega [-M_1 \sin(\omega t + \theta) + M_2 \cos(\omega t + \theta)] = \\ -B T_{avg} [M_1 \cos(\omega t + \theta) + M_2 \sin(\omega t + \theta)] + C T_{avg}^4 [1 + \\ 4M_1 \cos(\omega t + \theta) + 4M_2 \sin(\omega t + \theta)] + D \left[\frac{1}{\pi} + \frac{1}{2} \sin(\omega t + \theta) \right] \end{aligned} \quad (A.8)$$

Since the above identity is forced to hold for all t and θ , the coefficients of the sine, cosine and constant terms must be zero, i.e.,

$$C T_{avg}^4 + D/\pi = 0 \quad (A.9)$$

$$A T_{avg} \omega M_1 - B T_{avg} M_2 + 4 C T_{avg}^4 M_2 + D/2 = 0 \quad (A.10)$$

$$-A T_{avg} \omega M_2 - B T_{avg} M_1 + 4 C T_{avg}^4 M_1 = 0 \quad (A.11)$$

The solution is

$$T_{avg}^4 = -D/(\pi c) \quad (A.12)$$

$$M_1 = \frac{0.5 A T_{avg} \omega D}{-A^2 T_{avg}^2 \omega^2 - 16 C^2 T_{avg}^8 - B^2 T_{avg}^2 + 8 B C T_{avg}^5} \quad (A.13)$$

$$M_2 = \frac{0.5 D (-B T_{avg} + 4 C T_{avg}^4)}{-A^2 T_{avg}^2 \omega^2 - 16 C^2 T_{avg}^8 - B^2 T_{avg}^2 + 8 B C T_{avg}^5} \quad (A.14)$$

So that

$$M = \sqrt{M_1^2 + M_2^2} \quad (A.15)$$

$$= \frac{I_0 \cos \phi}{2 \Delta r T_{avg} [\rho^2 c^2 \omega^2 + K^2/r^4 + 8 \frac{K \epsilon \sigma}{r^2 \Delta r} T_{avg}^3 + 16 \frac{\epsilon^2 \sigma^2}{\Delta r^2} T_{avg}]}^{1/2}$$

and

$$\begin{aligned} \psi &= \tan^{-1} \left(\frac{M_1}{M_2} \right) \\ &= \tan^{-1} \left(\frac{-\rho c r^2 \Delta r \omega}{4 \epsilon \sigma r^2 T_{avg}^3 + K \Delta r} \right) \quad \dots (A.16) \end{aligned}$$

For subliming material coated shell, a heat loss term $ET \exp(A_c - B_c/T)$ is added to the differential equation. The expansion for this term is

$$\begin{aligned} T^{-1/2} \exp(A_c - B_c/T) &= \exp(A_c - B_c/T_{avg}) T_{avg}^{1/2} * \\ &[1 + (B_c M_2/T_{avg} - M_2/2) \sin(\omega t + \theta) \\ &+ (B_c M_1/T_{avg} - M_1/2) \cos(\omega t + \theta)] \quad (A.17) \end{aligned}$$

Substituting back, T_{avg} , M_1 and M_2 are solutions of the following equations

$$CT_{avg}^4 + D/\pi + ET_{avg}^{-1/2} \exp(A_c - B_c/T_{avg}) = 0 \quad (A.18)$$

$$AT_{avg} \omega M_2 = -BT_{avg} M_1 + ET_{avg}^{1/2} * \\ \exp(A_c - B_c/T_{avg})(B_c M_1/T_{avg} - M_1/2) \\ + 4CT_{avg}^4 M_1 \quad (A.19)$$

$$-AT_{avg} M_1 \omega = -BT_{avg} M_2 + 4CM_2 T_{avg}^4 + D/2 + \\ ET_{avg}^{1/2} \exp(A_c - B_c/T_{avg})(B_c M_2/T_{avg} - M_2/2) \quad (A.20)$$

The results for M and are given in Section 4.3.4.

APPENDIX B

APPROXIMATE ANALYTIC SOLUTION OF OPTIMUM SPIN RATE

In Section 4.3.4, the approximate analytic optimum spin is obtained as following. At the steady state, the temperature distribution is approximately given by

$$T(\theta, t) = T_{avg} [1 + M \sin(\omega t + \theta + \psi)] \quad (B. 1)$$

In an inertial fixed coordinate, the temperature distribution is fixed as shown in Figure B.1 and is reduced to

$$T(\theta, \omega) = T_{avg} [1 + M(\omega) \sin(\theta + \psi(\omega))] \quad (B. 2)$$

The net force component in θ direction (or normal to solar ray) is proportional to the following integral

$$F_N(\omega) = - \int_0^{2\pi} [T(\theta, \omega)]^4 \cos \theta d\theta \quad (B. 3)$$

Taking the derivative with respect to ω , and setting the result equal to zero, the result is

$$\begin{aligned} & 4\pi_2^2 \pi_4^2 \omega^6 + [6\pi_3 \pi_4^2 \pi_2 + 9\pi_1^2 \pi_2 \pi_4] \omega^4 \\ & + [6\pi_1^2 \pi_2 - 4\pi_2 \pi_3] \omega^2 - 4\pi_3^2 - 3\pi_1^2 \pi_3 = 0 \end{aligned} \quad (B. 4)$$

where parameters are defined in Section 4.3.4 and Appendix M. This is a 6th order equation from which a positive real root is to be solved. There should be only one real root which is the optimum spin speed for a maximum erecting force.

The method of analytic solution to this 6th order algebraic equation follows. Transform the equation to

cubic (by setting $\omega^2 = y$, then eliminate the quadratic term by a linear transformation ($y = x + K$), where $K = -(2\pi_3\pi_2\pi_4^2 + 3\pi_1^2\pi_2\pi_4^2)/(4\pi_2^2 + \pi_4^2)$). The cubic has the form of

$$X^3 + PX + Q = 0 \quad (B.5)$$

Now, the three roots are by Cardan's Formula (37)

$$X_1 = A + B$$

$$X_2 = \omega A + \omega^2 B$$

$$X_3 = \omega^2 A + \omega B \quad (B.6)$$

where

$$\omega = [-1 + \sqrt{3}i]/2$$

$$A^3 = -Q/2 + \sqrt{Q^2/4 + P^3/27}$$

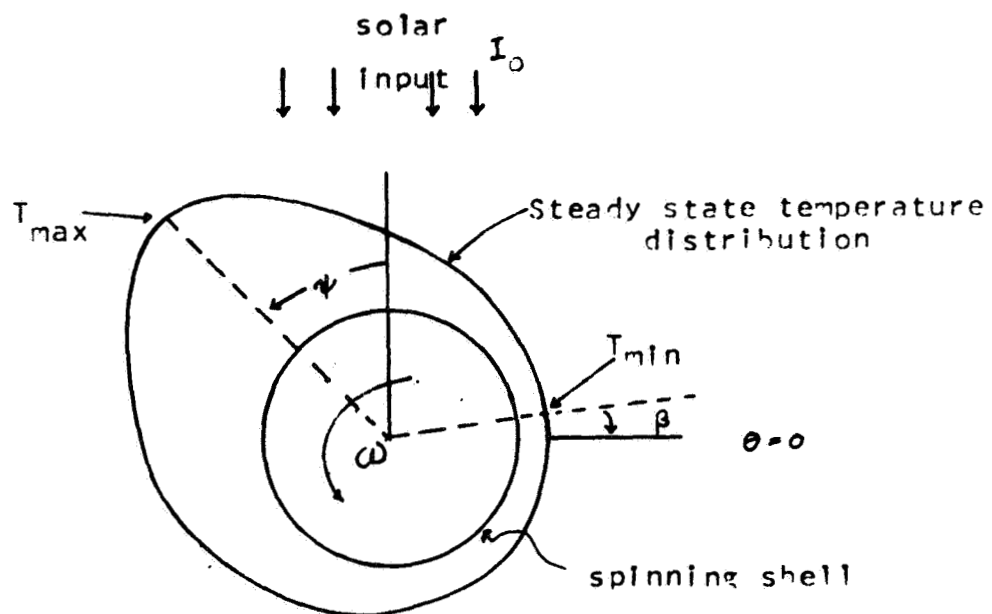
$$B^3 = -Q/2 - \sqrt{Q^2/4 + P^3/27} \quad (B.7)$$

Since the discriminant is negative, all three roots are real. From the DesCartes' Rule of Sign (37), the original 6th order polynomial and its transformed cubic equation have one and only one variation of sign, so that the equation can have at most one positive real root. On the other hand, the cubic equation can have at most two negative real roots, hence the original equation can only have one positive real root which is the desired optimum spin. The closed form of this root given in Section 4.3.4 was obtained by means of the complex variable identities manipulation of Equation (B.6).

The numerical results from the analytic expression Equation (B.6) have been checked against the direct

numerical solution of the original polynomial. The six roots indeed contained only one positive root which agreed to four or five significant figures with the closed form solution.

FIG B.1 STEADY STATE
TEMPERATURE PROFILE



APPENDIX C

GRAPHICAL EXPLANATIONS FOR NSHELL SOLUTION

For a given configuration of the erecting shell, the steady state temperature profile around the shell with respect to the sun is independent of time, however, the transient behavior is very much dependent upon the initial conditions. The steady state temperature profile is characterized by the maximum T_{max} , the minimum T_{min} and the phase lags ψ and β as shown in Figure C.1. To a good approximation, their relations are

$$I_0 \sin \beta = \epsilon \sigma T_{min}^4 \quad (C.1)$$

$$I_0 \cos \psi = \epsilon \sigma T_{max}^4 \quad (C.2)$$

Case 1 $T_{min} < T_0 < T_{max}$

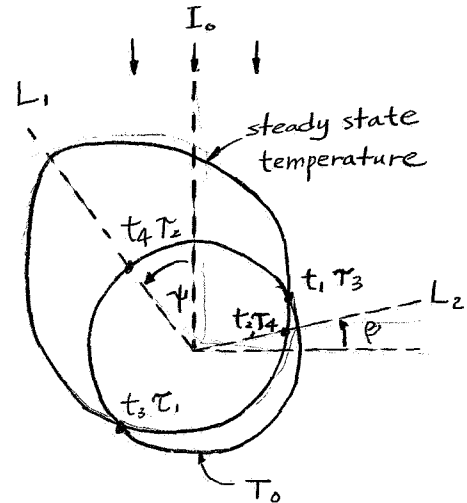
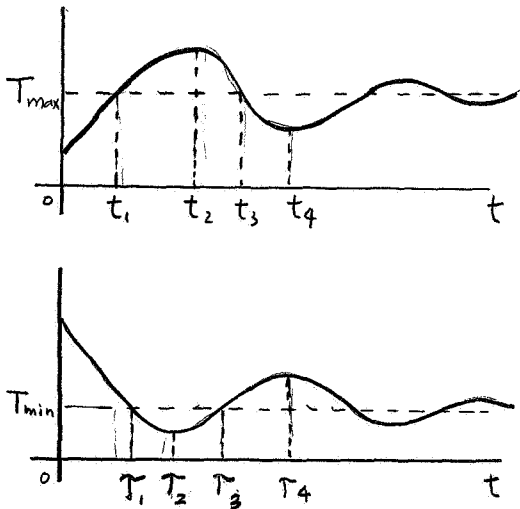
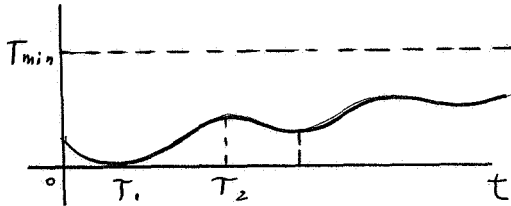
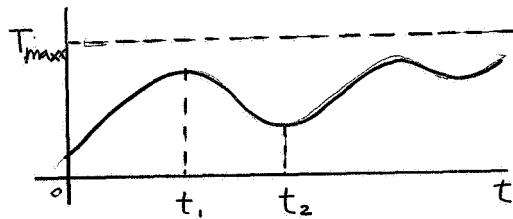


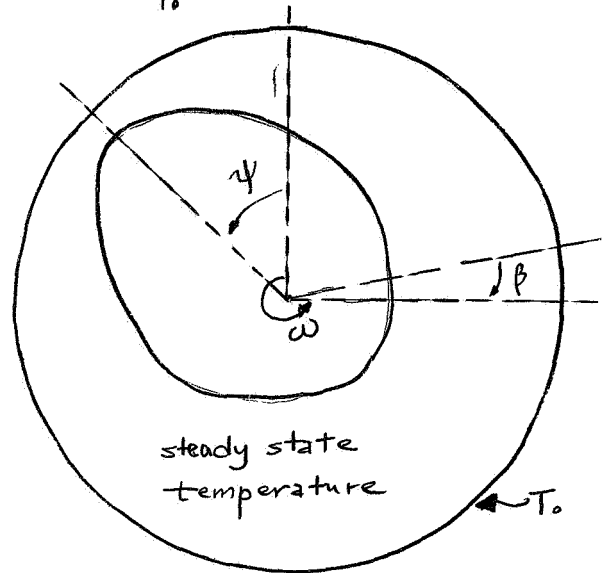
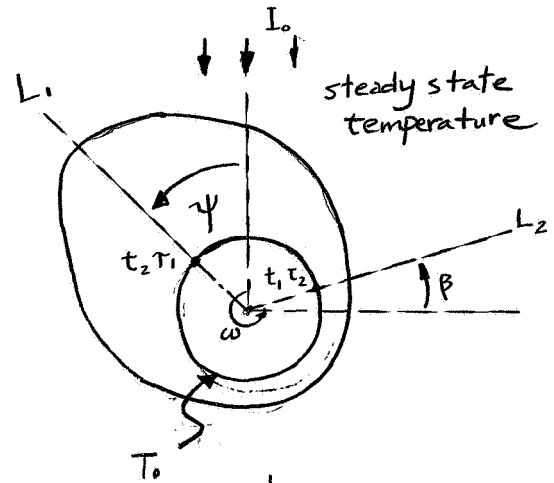
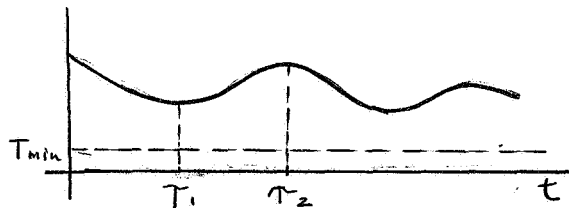
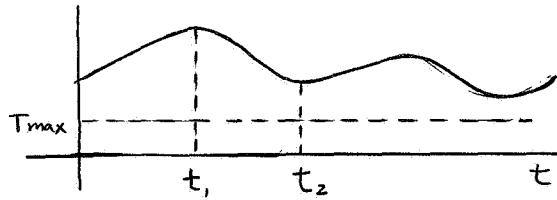
Fig C.1

where t_1 is the time required to rotate to L_1 and τ_1 is the time required to rotate to L_2 from the positions shown in the figures.

Case 2 $T_o < T_{min}$



Case 3 $T_o > T_{max}$



However, if T_o is very much larger than T_{max} , the oscillation will disappear, instead the transient distribution will look like a slanted stair.

APPENDIX D

RECOIL PRESSURE OF PHOTONS, NUCLEAR DECAY AND SUBLIMING PARTICLES

(i) Solar pressure on a projected surface is

P_{sun} = direct solar pressure + reflected solar pressure

$$\begin{aligned} P_{sun} &= I_0/c + 2/3 * (1 - \epsilon) I_0/c \\ &= I_0/c * [1 + 2/3 * (1 - \epsilon)] \end{aligned} \quad (D. 1)$$

where I_0 is the solar flux at a distance 1 AU

c is the speed of light

ϵ is the emissivity

(ii) Thermal radiation pressure:

For a diffuse surface the total emissive power is $E = \pi I$.

The time rate of change of normal momentum is

$$\begin{aligned} dP_n &= E \cos^2 \phi * (2\pi r^2 \sin \phi d\phi) / (\pi c r^2) \\ &= 2E \cos^2 \phi \sin \phi d\phi / c \\ P_n &= 2E/c * \int_0^{\pi/2} \cos^2 \phi \sin \phi d\phi \\ &= 2E/3c \\ &= 2\epsilon \sigma T^4 / 3c \end{aligned} \quad (D. 2)$$

(D. 3)

(iii) Nuclear disintegration pressure:

The recoil momentum due to a relativistic particle is $E/c * (1 + 2mc^2/E)^{1/2}$. The number of disintegration per unit area is

$$N = \text{disintegration per Watt} * \text{Watt per area} \\ = 3.7 * 10^{10} * 1.686 * 10^2 / E(\text{mev}) * \text{WPA} \quad (\text{D.4})$$

The disintegration pressure is then

$$P_{\alpha} = 0.832 * 10^{-4} \text{ wPA} * \exp(-\lambda t) (1 + 2M_{\alpha} c^2 / E)^{1/2} \quad (\text{D.5})$$

*This expression is good only if the deposited layer thickness is much smaller than the alpha range in the material, i.e., self absorption is negligible.

(iv) Sublimation pressure:

The recoil pressure due to sublimation is quite complex, but as a definition (9)

$$P_s = \alpha P_v / 2 \\ = \frac{\alpha}{2} 10^{A-B/T} \\ = 666.6 * \alpha * \exp(2.303 (A - B/T)) \quad (\text{D.6})$$

where P_v is the sublimation vapor pressure

α is evaporation coefficient

T is the subliming temperature

* The expression is good only if the reflection is specular and constant.

APPENDIX E

DERIVATION OF THE RELATIONS BETWEEN RECOIL PRESSURE AND REFLECTION COEFFICIENT

Let the interactions of vapor molecules with solid surfaces, i.e., the reflection (diffuse+specular) coefficient as a function of the incident angle θ , speed v and surface temperature T be $r(\theta, v, T)$. The fraction of the molecules which do not reflect are assumed to be condensed. The fraction which does not reflect is assumed to be condensed. At kinetic equilibrium, the fraction condensed is equal the fraction evaporated. Therefore, the total number of molecules evaporated from a plain surface is proportional to

$$\int_0^{\pi/2} \int_0^{\infty} [1 - r(\theta, v, T)] f(\theta, v) dv d\theta$$

where $f(\theta, v)$ is the number of particles reaching a unit surface area per unit time and solid angle with speed between v and $v+dv$

At thermal equilibrium, the vapor-pressure acting on a surface consists of the contributions from evaporation, condensation, diffuse and specular reflections. That is

$$P_v = P_e + P_c + P_d + P_s \quad (E.1)$$

$$P_e = P_c \quad (E.2)$$

$$\frac{P_d}{P_c} = \frac{\overline{\delta v \cos \theta} + \overline{\delta \cdot v \cos \theta}}{\overline{v \cos \theta} - \overline{r v \cos \theta}} \quad (E.3)$$

$$\frac{P_s}{P_c} = \frac{\overline{s \cdot v \cos \theta} + \overline{s \cdot v \cos \theta}}{\overline{\bar{v} \cdot \cos \theta} - \overline{r v \cos \theta}} \quad (E.4)$$

where the barred quantities are the Maxwellian distribution weighted averages. The reflection coefficients are functions of the surface temperature, the incident angle and speed. The total reflection \bar{r} is the sum of the specular s and the diffuse reflection δ . Substituting the above expression into Equation (E.1), the relationship between P_v and P_e is

$$\frac{P_v}{P_e} = 2 + \frac{\overline{rv \cos \theta} + \overline{\delta \cdot v \cos \theta} + \overline{sv \cos \theta}}{\overline{v \cos \theta} - \overline{rv \cos \theta}} \quad (E.5)$$

Only if δ is zero and s is independent of both the incident angle and speed will the above expression reduce to

$$\begin{aligned} P_v/P_e &= 2/(1-r) \\ &= 2/(1-s) = 2/\alpha \end{aligned} \quad (E.6)$$

where α is the evaporation coefficient

APPENDIX F

GEOMETRIC RELATIONS FOR SPECULAR PARTICLE REFLECTION IN SPACE

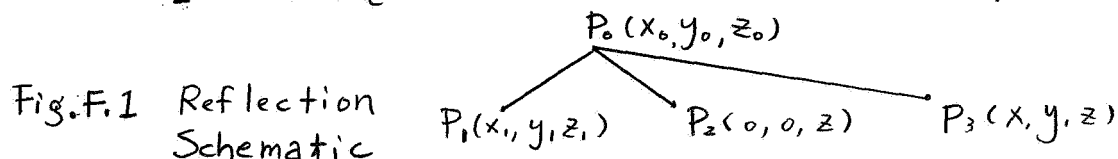
F.1 Cylindrical Wall

A particle originating from $P_1(x_1, y_1, z_1)$ and impinging the wall at $P_0(x_0, y_0, z_0)$ will be reflected and will pass $P_3(x, y, z)$. The other point lying on the normal of the surface of reflection is $P_2(0, 0, z)$. Since P_0, P_1, P_2, P_3 are in a same plane and P_3 is a mirror image of P_1 , a plane equation and two sphere equations can be written to solve for $P_3(x, y, z)$. The results are

$$x = [2y_1y_0x_0 + x_1(x_0^2 - y_0^2)] / R^2 \quad (F.1)$$

$$y = [2y_1y_0x_0 + x_0(x_0^2 - y_0^2)] / R^2 \quad (F.2)$$

$$z = 2z_0 - z_1 \quad (F.3)$$



If P_1 is on the wall, so will be P_3 . But if P_1 is not on the wall, the intersection point has to be solved from the line (passing through P_0, P_3) and the cylindrical surface simultaneously.

F.2 Chopped Cone Wall

The specular reflection from a chopped cone wall is more complex because the surface normal is not readily obtainable. The procedure to calculate the reflected beam is similar to that of a cylinder, but the resultant expressions are very complicated. They are used directly in Subroutine CONREF in program CONNOF (see Appendix K.2).

APPENDIX G

DERIVATION OF PARTICLE FLUX DUE TO SUBLIMATION

The angular mass flow rate from a differential area dA for molecules having velocity in v and $v+dv$ is $(m\alpha/4\pi)v dn_v \cos\theta dA$. The number of these molecules streaming through a unit sphere is $(\alpha/4\pi)v dn_v \cos\theta (dS/l^2) dA$ per unit time. The average residence time of these molecules inside the unit sphere is $4r/3v$. At any instant, the number of these molecules stationed in the sphere is $(\alpha/4\pi)v dn_v \cos\theta dS/l^2)(4r/3v)dA$. The flux or track length due to these molecules is $(\alpha r^3/3l^2)v dn_v \cos\theta dA$ or $(\alpha/4\pi l^2)v dn_v \cos\theta dA$. The flux from molecules of all speed is just $(\alpha n/(4\pi l^2))\bar{v} \cos\theta dA$ or $(\alpha \bar{n}\bar{v}/4\pi l^2) dA$. Summation of contributions of all the elemental area dA will yield the flux at the location of the sphere due to the sublimation only. The corresponding particle density is $n = \Sigma(dA\alpha n_z/l^2)$. Contributions from channel wall reflection and reemission are not included in the above summation.

APPENDIX H

DESCRIPTIONS OF COMPUTER PROGRAMS FOR THERMAL ANALYSIS OF THE ERECTING SHELL

H.1 Strip Approximation

This program (STRIP) solves for the temperature distribution around a shell by neglecting the effects of thermal conductions. The shell divided into JM strips. At each time step (is fixed by JM), the temperature is set to be uniform; however it can be very easily modified for any initial distribution. The maximum, minimum temperatures and phase lag at each time step are computed and recorded for plotting at the end of the computation determined by TMAX in seconds.

Subroutines: ARRAY, PLOT, FORCOM, CURVE.

Functions: FUN, DIFQ2, FH, FN

Compiler: WATFOR

Execution time: 0.7 minute

H.2 Thin Shell Approximation

The complexity of the coding increases significantly by including the tangential heat conduction effects. The coefficients of the difference equation for each strip are computed and stored in the coefficient matrix. The number of strips, JM, is preferred to be odd and less than 50. For each time step, the matrix is solved by Gaussian reduction method, the reradiative force components, maximum, minimum temperatures and phase lag are computed and recorded. The interaction is terminated as soon as the NMAX (<200) time

steps or the steady state has been reached. The stored informations are plotted out and the steady state temperature distribution is expanded numerically into Fourier sine and cosine series. The approximate analytic results are computed for comparison.

Subroutines: RECOIL, FORIT, RGRAPH, PLOT,
ARRAY, CURVE, APPROX, SIMQG

Function: SINHR

Compiler: WATFOR, FORTRAN G

Execution time: 1.5 minute

H.3 Thick Shell Approximation

By considering the radial heat conduction alone, the partial differential equation remains one dimensional. However, for each time step, the equation has to be solved as many times as JM (number of strips). The difference equation for each concentric layer yield a tridiagonal matrix which are stored in AA and solved by the fast matrix factorization method. The surface temperatures are plotted out occasionally both in rectilinear form and in polar form. The maximum, minimum, and phase lag for the internal and the external surface are plotted out every 100 time steps.

Subroutines: OUTPT2, STRIP, MATFAC, PHASE, MAXMIN,
ARRAY, PLOT, CURVE, DIFQ2, POLAR

Functions: FUN, SINHR

Compiler: WATFOR

Execution time: 3 min./100 time steps

H.4 Optimum Spin Rate

This program is relatively simple. The coefficients in the partial differential equation are computed first. The average temperature is solved by system subroutine RTWI (using the Weigstein's method). Then the coefficients for the sixth order algebraic equation are computed. The six roots are solved by another system subroutine POLRT. The numerical value of the analytic optimum spin expression is also calculated.

Subroutines: RTWI, POLRT

Functions: FCT, FCN

Compiler: FORTRAN G and H

Execution time: 0.3 minute

APPENDIX I

SPACE CURVE TRACED BY CONIC-PARTICLE BEAMS ON CYLINDRICAL TUBE

1.1 Inlet Sublimation

The equation for a conic surface is obtained by rotating a straight line about an axis. This conic surface can describe the sublimation from a tube inlet.

A line in X-Z plane is

$$Z = x \cdot \tan \theta - h \cdot \tan \theta$$

The surface generated about $x=h$ is

$$Z^2 = \tan^2 \theta ((x-h)^2 + y^2)$$

The equation for a cylindrical tube is

$$x^2 + y^2 = R^2$$

With the above relations, the parametric equations for the space curve of intersection are

$$x = (R^2 - t^2) / 2h$$

$$y = (R^2 - x^2)^{1/2}$$

$$Z = (h^2 + t^2)^{-1/2} \tan \theta$$

where t is the parameter

These three equations yield the coordinates of a point on the space curve of intersection.

1.2 Channel Wall Reemission

In this case, the reemission is originated from the tube wall. The conic surface

$$(R-x)^2 = \tan^2 \theta ((z-z_0)^2 + y^2)$$

comes from the revolution of the line

$$R-z=(z-z_0)\tan\theta$$

Where $(R, 0, z_0)$ is the apex of the cone and θ is the angle between the generating line and the z axis. The cylindrical surface of radius R is

$$x^2+y^2=R^2$$

The resultant parametric equations for the space curve of intersection are

$$Z = t^{1/2} + Z_0$$

$$(R-x)^2 = t \tan^2 \theta - (x^2 - R^2) \tan^2 \theta$$

$$y = (R^2 - x^2)^{1/2}$$

Again, t is the parameter. This result is useful for computation of the fate-probability of reemitted particles.

APPENDIX J

DESCRIPTIONS OF COMPUTER PROGRAMS FOR THERMAL ANALYSIS OF THE MICROTHRUSTER

J.1 Cylindrical Tube--Explicit Method

Since the temperature on any mesh point at any time step depends only on the temperatures of previous time step, The transient solution is obtained by marching-out in time. However, due to sublimation, the extreme mesh always decreases in size. As soon as the numerical stability criterion is violated, the mesh net is rearranged. Toward the end of sublimation, the rearrangement will introduce a large disturbance. Also, the time step has to reduce frequently to insure stability. The surface and the bottom temperature and the fuel thickness are displayed graphically by PLOT.

Subroutines: OUTPT1, CURVE1, ARRAY, PLOT

Function: G

Compiler: WATFOR

Execution time: 2.5 min.

J.2 Cylindrical Tube--Implicit Method

Unlike the explicit method, the temperature distribution in the fuel at any time has to be solved simultaneously. Since the coefficient matrix is tridiagonal, a fast matrix factorization method is adopted. The initial temperature distribution is arbitrary set to be linear. The method is numerically stable for any mesh size. However, toward the end, the mesh net has to be modified to

two-point difference. A temporary disturbance did show up in the surface temperature. As usual, the results are plotted out.

Subroutines: MACFAC, OUTPUT, CURVE1, PLOT, ARRAY

Compiler: WATFOR

Execution time: 2min.

J.3 Chopped Cone-ADI Method

In the analysis of a subliming microthruster, due to the cylindrical symmetry, the temperature in a chopped cone microthruster is a function of r and z . The physical problem is best described by the following diagram, Figure J.1. The presence of sublimation, which involves both heat and mass transfer, prevents the temperatures from reaching steady state. To apply the ADI technique, the cone cylinder is divided into convenient mesh as shown in the cross-sectional diagram. Difference equations implicit in r -direction are required for each row as well as similar difference equations implicit in z -direction for each column. The diagram shows that there are only 13 distinct difference equations for each direction (i.e., temperature at other mesh point can be expressed by one of the 13 equations). Their formulations are strictly based on energy balance (first law of thermodynamics) and with proper care no problem should arise for difference equations in the center region.

The general heat conduction is $Q = -K \cdot S \cdot D \cdot \Delta T$. For rectangular mesh $S \cdot D$ is $0.5A/\Delta x$ (note: D is depth, $S = 0.5 \cdot \cot \theta$

, where θ is the angle subtended by the heat flow path (24)).

The temperature at any mesh point can be described by one of the 26 (2*13) difference equations. At each time step, the temperature distribution in the plane is obtained by solving the temperature in the line repeatedly until the plane is covered. The direction of the lines alternate for each time step. The representative temperature profile is shown in Figure J.2. The iteration in z-direction is performed in Subroutine ZITER and the iteration in R-direction is performed in Subroutine RITER.

Subroutines: RITER, ZITER, MATFAC, PARAS, PARAD,
RADFOR, CURVE

Function: SUBM

Compiler: WATFOR

Execution time: 1/3 real time

FIG J.1 SCHEMATIC OF CHOPPED
CONE MICROTHRUSTER

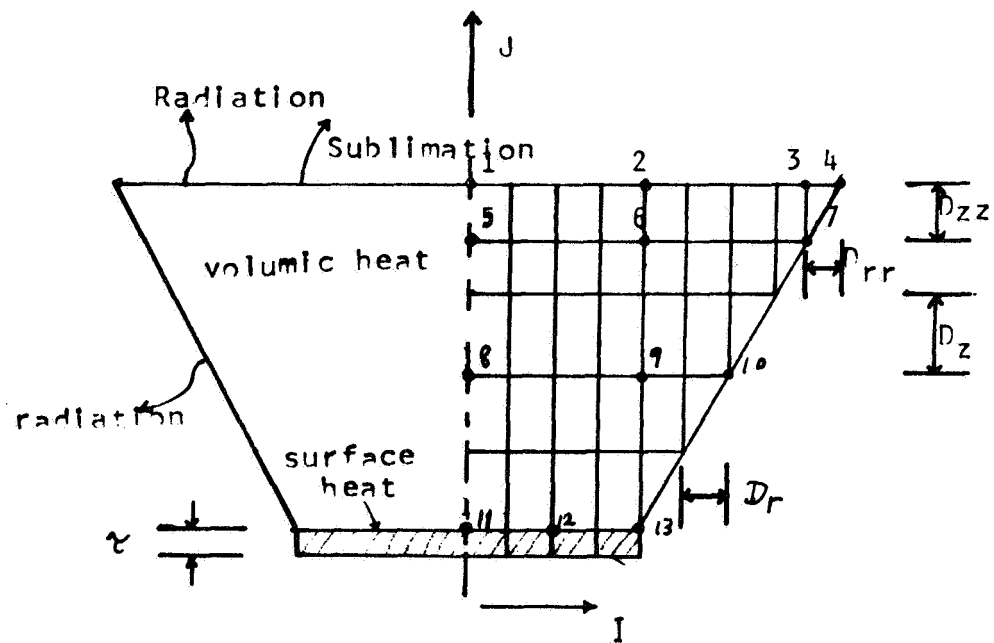


Fig. J.2 Numerical Display of CONADI Solution

45 degree cone; radius=0.5 cm; time step=1 second
 fuel=naphthalene; thickness=0.95 cm; emissivity=1.0; heat source=0.75E 07 erg/cc-sec.
 cup material=Be; thickness=0.05 cm; emissivity=0.5; heat flux=0.5E 07 erg/cc-sec.
 Initial temperature=273.0 K (uniform)

t=50 seconds

r=0 cm

r=0.5 cm

Subliming surface

r=1.45 cm

278.4	278.3	278.2	278.1	278.0	277.8	277.5	277.2	276.8	276.2	275.3	274.2	272.6	270.4	276.7
284.8	284.8	284.7	284.5	284.3	283.9	283.5	282.9	282.2	281.3	280.1	278.5	276.4	273.5	
289.2	289.2	289.0	288.8	288.5	288.0	287.4	286.7	285.8	284.6	283.2	281.3	278.9		
293.1	293.0	292.9	292.5	292.0	291.4	290.6	289.6	288.5	287.1	285.4	283.3			
296.8	296.7	296.5	296.0	295.4	294.5	293.4	292.1	290.7	289.0	287.1				
300.7	300.6	300.3	299.7	298.8	297.6	296.1	294.4	292.6	290.6					
305.3	305.1	304.8	304.0	302.9	301.3	299.1	296.7	294.3						
310.7	310.6	310.2	309.4	308.1	306.0	302.6	299.2							
317.2	317.1	316.8	316.3	315.2	312.8	307.0								
324.7	324.7	324.6	324.7	324.6	324.4									

isotope layer

t=100 seconds

283.3	283.3	283.2	283.0	282.7	282.4	282.0	281.4	280.7	279.9	278.8	277.3	275.3	272.6	268.8
292.8	292.7	292.5	292.1	291.6	291.0	290.2	289.2	288.0	286.5	284.8	282.5	279.7	276.0	
300.9	300.8	300.4	299.9	299.2	298.2	297.1	295.6	294.0	292.0	289.6	286.8	283.3		
308.0	307.9	307.5	306.8	305.8	304.6	303.0	301.1	298.9	296.5	293.6	290.2			
314.7	314.5	314.0	313.2	311.9	310.3	308.2	305.9	303.2	300.2	296.8				
321.2	321.0	320.4	319.4	317.8	315.8	313.2	310.2	307.0	303.4					
327.9	327.6	327.0	325.9	324.1	321.5	318.1	314.4	310.4						
334.9	334.7	334.1	332.9	331.0	328.0	323.4	318.4							
342.2	342.1	341.7	340.9	339.4	336.3	329.2								
349.8	349.8	349.7	349.7	349.7	349.4									

APPENDIX K

DESCRIPTION OF COMPUTER PROGRAMS FOR RAREFIED GAS NON-OBSTRUCTION FACTOR

K.1 Cylindrical Tube Non-obstruction Factor

After initialization of the necessary parameters, the relative amplitudes for all angular groups in the spherical cosine are computed and stored, then a probability 'table' for reemitted molecules is constructed. Now, molecules leaving the point sources are traced successively. Symmetric properties are utilized in order to save execution time whenever possible. The molecular collision effects are estimated by calculating the molecular flux and density in the channel first and then approximated the fate of the collided molecules. Finally, the fate of the adsorbed molecules are computed with the aid of the probability 'table'. The total exit molecules to the initial inlet molecules ratio is the desired mass non-obstruction factor.

Subroutines: ANGP, COLISN, XY, MOLCOL, DELAY, REEMIT,
XYZ3, ITER, TABLE, RGRAPH, XYZ2, XATER,
RFLUX, DFLUX, REFLET, BISRCH, SCATTER,
CONE

Compiler: WATFOR

Execution time: 1 min.

K.2 Chopped Cone Non-obstruction Factor

The basic technique in this program is essentially the same as the previous one. However, the molecular collision option is replaced by the subliming surface reflection and

the thrust coefficient. Also, the mesh cone is divided into many equal azimuthal segments which are different in the cylindrical case where the mesh cone is divided according to the intersection of the mesh cone with the wall ring segment rings. For 90° cone angle (i.e., cylinder), the result can check against those of previous calculations.

Subroutines: HIT, CONREF, CONCON, ANGPR, CONCEN,
BISRCH, CONEMI

Functions: CNITER, CENTER

Compilers: FORTRAN G, H and WATFOR

Execution time: 0.7 min.

APPENDIX L

SUBLIMATION PRESSURE

In calculating the sublimation heat flux or mass flow, the pressure term always arises. The pressure dependence on temperature is derived below. The free energy change is constant for both the solid and the gas phases at sublimation for small changes in P and T , therefore

$$dG = V_v dP - S_v dT = V_s dP - S_s dT$$

$$\text{or } dP/dT = \Delta S / \Delta V$$

If the latent heat of sublimation is H_s , ΔS is simply H_s/T . Assuming the ideal gas law, the following approximation can be obtained.

$$dP/dT = H_s / (T \Delta V)$$

$$= H_s / TV_g$$

$$dP / (P dT) = H_s / (RT^2)$$

$$d \ln P / dT = H_s / (RT^2)$$

$$\ln P = -(H_s / RT) + C$$

$$P = \exp(H_s / RT + C) = 10^{A - B/T}$$

This is the common pressure-temperature relationship for sublimation. A and B are empirical constants.

APPENDIX M

NOMENCLATURE

A ,B	---sublimation constants
AU	---astronomical unit (radius of earth orbit)
A	--- ρc
B	--- K/R^2
c	---speed of light; heat capacity
C	--- $(-\epsilon\sigma/\Delta r)$
d	---diameter
D	--- $I_0 \cos\phi/\Delta r$
E	--- $(-H_s \sqrt{\omega t}/(17.14 \Delta r))$
G	--- $R_{HS}/\Delta r$; mass flow rate
H	---angular momentum
H_s	---heat of sublimation
I_0	---moment of inertia
I_{sp}	---solar constant (heat flux)
I	---specific impulse
k	---thermal conductivity; Boltzmann's constant
K	---non-obstruction factor
l	---channel length
L	---subliming fuel height
m	---particle mass
M	---molecular weight; temperature amplitude factor
M_i	---moment or torque component in i-direction
n	---particle density; neutron

P ---pressure; momentum
 q'' ---heat source
 q'', q ---heat flux
 r_α ---alpha range
 R ---cylindrical radius
 R_{Hs} ---radioisotopic heat flux
 s ---specular reflection coefficient
 t ---time
 T ---temperature; kinetic energy
 T_{avg} ---average temperature
 v ---particle speed
 W_t ---molecular weight
 α ---evaporation coefficient; alpha particle; absorptivity
 γ ---reflection coefficient; specific heat ratio
 δ ---diffuse reflection coefficient
 ϵ ---emissivity
 ρ ---density
 σ ---Stefan-Boltzmann constant; molecular cross-section
 $\dot{\psi}$ ---precession
 ψ ---maximum temperature phase lag
 ϕ ---angle between figure axis and the sun-line
 ω ---spin rate; angular speed of body
 β ---minimum temperature phase lag
 Ω ---angular speed of body axes
 λ ---mean free path; decay constant
 π_1 --- $I_0 \cos \phi / (2 \Delta r T_{avg})$

$$\pi_2 \quad \text{---} (\rho c)^2$$

$$\pi_3 \quad \text{---} K^2/R^4 + 8K\epsilon\sigma/(R^2 \Delta r) T_{avg}^3$$

$$\pi_4 \quad \text{---} A/\sqrt{\pi_3}$$

$$\beta_0 \quad \text{---} \text{minimum temperature point from the twilight}$$

$$\theta \quad \text{---} \text{position of strip on the shell}$$

APPENDIX N

LITERATURE CITATIONS

1. Harrington, J. V., "Study of a Small Probe", MIT, Center for Space Research, PR-5255-5 (1965)
2. Dugan, D. W., "A Preliminary Study of a Solar Probe Mission", NASA Ames Research Center TN D-783 (1963)
3. Baker, R. H., D. H. Galvin, "The Conceptual Design of a Small Solar Probe", Laboratory for Space Experiment, Center for Space Research, MIT, TR-69-1 (1969)
4. Singer, S. F., "Torques and Attitude Sensing in Earth Satellites", Academic Press, N. Y. (1964)
5. Thomson, W. T., "Introduction to Space Dynamics", Johns Wiley and Sons, Inc., London (1961)
6. Falcovitz, J., "Attitude Control of a Spinning Sun-orbiting Spacecraft by Means of a Grated Solar Sail", MIT, CSR TR-66-17 (1966)
7. Peterson, C. A., "Use of Thermal Reradiative Effects in Spacecraft Attitude Control", MIT, CSR T-66-3 (1966)
8. Galman, B. A., M. M. Levinson, and J. J. Weinstein, "Solar Probe Orbit Design", J. Spacecraft and Rockets, 3, 1002 (1966)
9. Paul, B., "Compilation of Evaporation Coefficients", ARS J. 32, 1321 (1962)
10. Sherwood, T. K., and C. Johannes, "The Maximum Rate of Sublimation of Solids", A.I.Ch.E.J., 8, 590 (1962)
11. Alty, T., "The Interaction of Vapor Molecules with a Crystal Surface", Proc. Roy. Soc. (London), A, 161, 68

(1937)

12. Burrows, G., "Evaporation at Low Pressures", J. Appl. Chem., (London) 7, 375 (1957)
13. Melville, H. W., "A Note on Evaporation from Irregular Surfaces", Trans. Faraday Soc., 32, 1017 (1936)
14. Littlewood, R., and R. Rideal, "On the Evaporation Coefficient", Trans. Faraday Soc., 52, 1598 (1956)
15. Paul, B., and L. G. Lyon, "Evaporation Coefficients and Recoil Pressure for Biphenyl and Naphthalene", AIAA 3, 1067 (1965)
16. Clausius, P., Physica. Eindhoven, 9, 65 (1929)
17. DeMarcus, W. C., "The Problem of Knudsen Flow", K-1302, Oak-Ridge Gaseous Diffusion Plant (1955)
18. Dushman, S., "Scientific Foundations of Vacuum Technique", edited by J. M. Lafferty, John Wiley, London (1962)
19. Knudsen, M., "The Kinetic Theory of Gases", John Wiley, London (1953)
20. Brundin, C. L., "Rarefied Gas Dynamics", Vol. 1. Academic Press, N. Y. (1967)
21. Evans, R. D., "The Atomic Nucleus", McGraw-Hill, N. Y. (1955)
22. Bussard, R. W., R. D. DeLauer, "Fundamentals of Nuclear Flight", McGraw-Hill, N. Y. (1965)
23. Churchill, R. V., "Fourier Series and Boundary Value Problems", McGraw-Hill, N. Y. (1962)

24. Dushnberg, G. M., "Heat Transfer Calculations by Finite Differences", Int. Text. Co., N. Y. (1961)
25. Kreith, F., "Principles of Heat Transfer", International Textbook, N. Y. (1964)
26. Rohsenow, W. M., and H. Y. Choi, "Heat, Mass, and Momentum Transfer", Prentice-Hall, N. J. (1961)
27. Arpaci, V. S., "Conduction Heat Transfer", Addison-Wesley, London (1966)
28. Shreider, Yu. A., G. J. Tee, "The Monte Carlo Method", Pergamon Press, N. Y. (1966)
29. Forsythe, G. E., W. R. Wasow, "Finite-Difference Methods for Partial Differential Equations", John Wiley, London (1965)
30. Clark, M., K. F. Hansen, "Numerical Methods for Reactor Analysis", Academic Press, N. Y. (1964)
31. Sears, F. W., "Thermodynamics, The Kinetic Theory of Gases, and Statistical Mechanics", Chapter 12, Addison-Wesley, London (1956)
32. Fishell, R. E., and L. Wilson, "Spacecraft Application of Subliming Materials", J. Spacecraft and Rockets, 2, 376 (1965)
33. Hardt, A. P., W. M. Folly, and R. L. Brandon, "The Chemistry of Subliming Solids for Micro Thruster Engines", Astronautica Acta, 11, 340 (1965)
34. Diekamp, H. M., "Nuclear Space Power System", (Atomic International, 1967)

35. Corliss, W. R., and D. G. Harvey, "Radioisotopic Power Generation", Prentice Hall, N. J. (1964)
36. Short, W., and C. Sabin, "A Radioisotope Propulsion System", J. of the British Interplanetary Soc., London, 17, 453 (1960)
37. Lin, J. P., High School Algebra, Cheng Chun Book Co., Taiwan (1953)
38. Halfman, R. L., "Dynamic", Addison-Wesley, London (1962)
39. McCuskey, S. W., "An Introduction to Advanced Dynamics", Addison-Wesley, Mass. (1958)
40. Carrol, J. R., R. G. Limburg, "Dynamics of a Solar Pressure Stabilized Satellite", MIT, CSR T-65-1 (1965)
41. Cloutier, G. J., "Attitude Perturbation of Space Vehicles by Meteoroid Impacts", J. Spacecraft and Rockets, 3, 523 (1966)
42. Dixon, W. J., "Major System Design Problems for Deep Space Probes", J. Spacecraft and Rockets, 4, 1121 (1967)
43. Scott, D. S., and F. A. L. Dullien, "The Flow of Rarefied Gases", A.I.Ch.E. J., 8, 293 (1962)
44. Hirth, J. P., and G. M. Pound, "Coefficients of Evaporation and Condensation", J. Chem. Physics, 64, 619 (1960)
45. Leob, B. L., "The Kinetic Theory of Gases", Dover Pub. Inc. N. Y. (1961)
46. Kennard, E. H., "Kinetic Theory of Gases", McGraw-Hill, N. Y. (1938)

LISTINGS OF SOURCE PROGRAMS

The computer codes developed for the present studies were all programmed using the FORTRAN-IV language. Except for the Optimum Spin Rate program, all codes have been successfully run under the WATFOR compiler. However, the present FORTRAN G and H compilers have shown difficulties to accept the codes which are usually not optimized. They contain some redundant statements left over during debug-period. The listing of the codes and some sample data are included in the original thesis on file in MIT Library. All codes were punched by the IBM 029 key punch and they were run on the IBM 360/65 processor.